



The Journal of **Gemmology**

Volume 38 / No. 6 / 2023



Age Dating of
Sapphires from
Muling, China

More on
Emeralds from
Chitral, Pakistan

Forsterite-Serpentine
from North-eastern
China

Portraits
Engraved on
Diamond



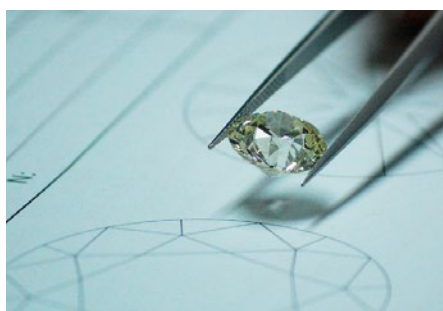
SCHWEIZERISCHES GEMMOLOGISCHES INSTITUT
SWISS GEMMOLOGICAL INSTITUTE
INSTITUT SUISSE DE GEMMOLOGIE



ORIGIN DETERMINATION · TREATMENT DETECTION

DIAMOND GRADING · PEARL TESTING

EDUCATION · RESEARCH



THE SCIENCE OF GEMSTONE TESTING™



Cover photo: A new emerald deposit was discovered in 2021 in the Chitral region of north-western Pakistan. Following an earlier description of pale-coloured emerald that was initially mined there (see *The Journal*, Vol. 38, No. 3, 2022), an article on pp. 582–599 of this issue characterises some more deeply coloured samples, and compares them to emeralds from Afghanistan and elsewhere in Pakistan. The Chitral emerald specimen shown here measures 12.5 cm tall. Photo by Federico Picciani; courtesy of MCP (www.mcp-italy.com).

COLUMNS

What's New

539

GemID Diamond Fingerprinting Instrument | Carbon Footprint of Pandora Laboratory-grown Diamonds | Europa Star 'Digital Books' | *Gemmes* French Online Journal | Gemstone Supplier Conversations Guide | JNA's *Lab-Grown Diamond Special 2023* | Natural Diamond Council's Report on Education in Retail Settings | *Platinum Jewellery Business Review 2023* | *SSEF Facette Magazine*

Gem Notes

542

Benitoite Beads | Surface Structures on Beryl Crystals | Morganite from Numbi, Democratic Republic of the Congo | Colour-Change Garnet Showing Blue Colouration from Kamtonga, Kenya | Red Musgravite | Rhodonite from Italy and Indonesia | Three-Ray Asterism in Quartz: A Multi-Star Network | Quartz with Kyanite Inclusions from Brazil | Ruby from Central Madagascar | Spessartine from Engare Naibor, Tanzania | Update on Colourless HPHT-grown Synthetic Diamonds Testing as Synthetic Moissanite | Polymer Carving Imitating Dickite | Kyropoulos Synthetic Ruby and Sapphire

546



Photo by C. Schwarzing

ARTICLES

Characterisation and *In Situ* Age Determination of Zircon Inclusions in Sapphires from Muling, North-east China
By Yimiao Liu, Ren Lu and Shaokui Pan

564

Comparison of Emeralds from the Chitral District, Pakistan, with other Pakistani and Afghan Emeralds
By Carina S. Hanser, Tom Stephan, Bilal Gul, Tobias Häger and Roman Botcharnikov

582

Mineralogical and Gemmological Characteristics of Gem-quality Forsterite-Serpentine from North-eastern China
By Bijie Peng, Mingyue He, Mei Yang, Xi Liu and Xinhao Sui

600

565

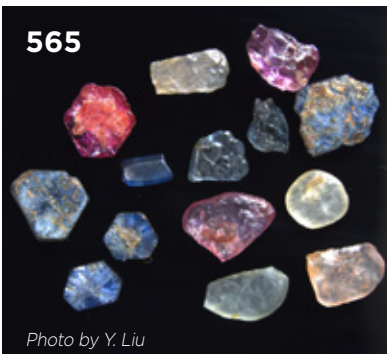


Photo by Y. Liu

601



Photo by Mingyue He

GEMMOLOGICAL BRIEF

Late Nineteenth-Century Portraits Engraved on Diamond
By Erik Schoonhoven

616

Conferences

Gem-A Midlands Conference | Nineteenth Annual Sinkankas Symposium: San Diego County Gems and Minerals

621

Learning Opportunities

625

New Media

628

Literature of Interest

636

The Journal is published by Gem-A in collaboration with SSEF.



The Journal of Gemmology

EDITORIAL STAFF

Editor-in-Chief
Brendan M. Laurs
brendan.laurs@gem-a.com

Executive Editor
Alan D. Hart

Editorial Assistant
Carol M. Stockton

Editor Emeritus
Roger R. Harding

ASSOCIATE EDITORS

Ahmadjan Abduriyim
Tokyo Gem Science LLC,
Tokyo, Japan

Raquel Alonso-Perez
Harvard University,
Cambridge, Massachusetts,
USA

Edward Boehm
RareSource, Chattanooga,
Tennessee, USA

Maggie Campbell Pedersen
London

Alan T. Collins
King's College London

Alessandra Costanzo
National University of
Ireland Galway

John L. Emmett
Crystal Chemistry, Brush
Prairie, Washington, USA

Emmanuel Fritsch
University of Nantes,
France

Rui Galopim de Carvalho
Gem Education Consultant,
Lisbon, Portugal

Al Gilbertson
Gemological Institute
of America, Carlsbad,
California

Lee A. Groat
University of British
Columbia, Vancouver,
Canada

Thomas Hainschwang
GGTL Laboratories,
Balzers, Liechtenstein

Henry A. Hänni
GemExpert, Basel,
Switzerland

Jeff W. Harris
University of Glasgow

Alan D. Hart
Gem-A, London

Ulrich Henn
German Gemmological
Association, Idar-Oberstein

Jaroslav Hyršl
Prague, Czech Republic

Brian Jackson
National Museums
Scotland, Edinburgh

Mary L. Johnson
Mary Johnson Consulting,
San Diego, California, USA

Stefanos Karamelas
Laboratoire Français de
Gemmologie, Paris, France

Lore Kiefert
Dr. Lore Kiefert Gemmology
Consulting, Heidelberg,
Germany

Hiroshi Kitawaki
Central Gem Laboratory,
Tokyo, Japan

Michael S. Krzemnicki
Swiss Gemmological
Institute SSEF, Basel

Shane F. McClure
Gemological Institute
of America, Carlsbad,
California

Jack M. Ogden
London

Federico Pezzotta
Natural History Museum
of Milan, Italy

Gérard Panczer
Claude Bernard University
Lyon 1, France

Jeffrey E. Post
Smithsonian Institution,
Washington DC, USA

George R. Rossman
California Institute of
Technology, Pasadena, USA

Karl Schmetzer
Petershausen, Germany

Dietmar Schwarz
Bellerophon Gemlab,
Bangkok, Thailand

Menahem Sevdemish
Gemwizard Ltd, Ramat
Gan, Israel

Andy H. Shen
China University of
Geosciences, Wuhan

Guanghai Shi
China University of
Geosciences, Beijing

James E. Shigley
Gemological Institute
of America, Carlsbad,
California

Christopher P. Smith
American Gemological
Laboratories Inc.,
New York, New York

Elisabeth Strack
Gemmologisches Institut
Hamburg, Germany

Tay Thye Sun
Far East Gemological
Laboratory, Singapore

Frederick 'Lin' Sutherland
Port Macquarie, New
South Wales, Australia

Pornsawat Wathanakul
Kasetsart University,
Bangkok, Thailand

Chris M. Welbourn
Reading, Berkshire

Bear Williams
Stone Group Laboratories
LLC, Jefferson City,
Missouri, USA

J. C. (Hanco) Zwaan
Naturalis Biodiversity
Center, Leiden,
The Netherlands



Gem-A
THE GEMMOLOGICAL ASSOCIATION
OF GREAT BRITAIN

21 Ely Place
London EC1N 6TD
UK

t: + 44 (0)20 7404 3334
f: + 44 (0)20 7404 8843
e: information@gem-a.com
w: <https://gem-a.com>

Registered Charity No. 1109555
A company limited by guarantee and
registered in England No. 1945780
Registered office: Palladium House,
1-4 Argyll Street, London W1F 7LD

PRESIDENT

Richard Drucker

VICE PRESIDENTS

David J. Callaghan
Alan T. Collins
Nigel Israel

HONORARY FELLOWS

Gaetano Cavalieri
Terrence S. Coldham
Richard Drucker
Emmanuel Fritsch

HONORARY DIAMOND MEMBER

Martin Rapaport

CHIEF EXECUTIVE OFFICER

Alan D. Hart

COUNCIL

Justine L. Carmody – Chair
Nevin Bayoumi-Stefanovic
Maggie Campbell Pedersen
Kate Flitcroft
Joanna Hardy
Philip Sadler
Pia Tonna

BRANCH CHAIRMEN

Midlands – Craig O'Donnell
North East – Mark W. Houghton
North West – Liz Bailey
South West – Rachael Boothroyd

COVERED BY THE FOLLOWING ABSTRACTING AND INDEXING SERVICES:

Clarivate Analytics' (formerly Thomson Reuters/ISI) Science Citation Index Expanded (in the Web of Science), Journal Citation Reports (Science Edition) and Current Contents (Physical, Chemical and Earth Sciences); Elsevier's Scopus; Australian Research Council's Excellence in Research for Australia (ERA) Journal List; China National Knowledge Infrastructure (CNKI Scholar); EBSCO's Academic Search Ultimate; ProQuest (Cambridge Scientific Abstracts); GeoRef; CrossRef; Chemical Abstracts (CA Plus); Mineralogical Abstracts; Index Copernicus ICI Journals Master List; Gale Academic OneFile; British Library Document Supply Service; and Copyright Clearance Center's RightFind application.



CONTENT SUBMISSION

The Editor-in-Chief is glad to consider original articles, news items, conference reports, announcements and calendar entries on subjects of gemmological interest for publication in *The Journal of Gemmology*. A guide to the various sections and the preparation of manuscripts is given at <https://gem-a.com/membership/journal-of-gemmology/submissions>, or contact the Editor-in-Chief.

SUBSCRIPTIONS

Gem-A members receive *The Journal* as part of their membership package, full details of which are given at <https://gem-a.com/membership>. Laboratories, libraries, museums and similar institutions may become direct subscribers to *The Journal*; download the form from *The Journal's* home page.

ADVERTISING

Enquiries about advertising in *The Journal* should be directed to advertising@gem-a.com. For more information, see <https://gem-a.com/component/edocman/media-kit>.

COPYRIGHT AND REPRINT PERMISSION

For full details of copyright and reprint permission contact the Editor-in-Chief. *The Journal of Gemmology* is published quarterly by Gem-A, The Gemmological Association of Great Britain. Any opinions expressed in *The Journal* are understood to be the views of the contributors and not necessarily of the publisher.

DESIGN & PRODUCTION

Zest Design, London. <http://www.zest-uk.com>

PRINTER

Park Communications Ltd, London.
<http://www.parkcom.co.uk>



© 2023 Gem-A (The Gemmological Association of Great Britain)
ISSN 1355-4565 (Print), ISSN 2632-1718 (Online)

What's New

INSTRUMENTATION

GemID Diamond Fingerprinting Instrument

DRC India (Gujarat, India) released its new diamond 'DNA' device in July 2022. It is designed to record the unique 'fingerprint' of a loose or solitaire-mounted diamond so that the stone can be re-identified later, even after mounting. The device works with all shapes of faceted diamonds, ranging from 0.3 ct to 22 mm in diameter, D to K colour and flawless to I₃ clarity. A scan is performed within 10 seconds, and the result is saved in an online database. The registry is useful to prevent or detect switching of stones, and could also be helpful for identifying stolen diamonds. The unit measures 13.5 × 14.7 × 34.3 cm and weighs 9.5 kg. Visit <https://drcindia.in/product/gem-id>.



NEWS AND PUBLICATIONS

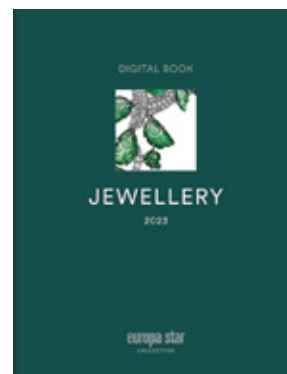
Carbon Footprint of Pandora Laboratory-grown Diamonds

As part of its stated intent to be a 'low-carbon business', in August 2022 Pandora Inc. (Copenhagen, Denmark) released a document titled *Carbon Footprint of Diamonds by Pandora Collection*, prepared by Denmark-based Ramboll Group. The report evaluates the carbon footprint of three Pandora rings, each set with a synthetic diamond (weighing 0.15, 1 and 1 ct) produced with 100% renewable electricity and set in recycled metal (silver or gold). The laboratory-grown diamonds were the primary contributors towards the carbon footprint, which suggests that the diamond growth process should be a main focus to reduce carbon impact. However, 'restricted access to the complete study and data' made it difficult for the report writers to identify specific areas that could be targeted to achieve this goal. Download the report at <https://pandoragroup.com/Diamonds-by-Pandora-carbon-footprint>.



Europa Star 'Digital Books'

Swiss publisher Europa Star is offering a series of free 'digital books', including seven volumes released so far in 2023, which include beautiful photos interspersed with articles. Most of these cover Europa Star's main focus—watches and watchmaking—but one titled *Jewellery* features interviews with leading designers, articles on vintage jewellery and profiles of several emerging designers. Other volumes include *Watchmaking & Sustainability*, *The State of Retail* and a collection of all their digital books from 2022. Read the books online at <https://www.europastar.com/books.html>.



Gemmes French Online Journal

Gemmes is a new biannual online journal of Gemmologie & Francophonie, a Geneva-based gemmological association. The articles are in French, with abstracts and figure captions in English. The first (Spring 2023) issue covers sustainability in business, growth of synthetic diamond with natural-like inclusions (to study natural diamond formation), photochromic zircon, hackmanite from Mogok and inclusions in aquamarine. It also includes a report on the Gemmologie & Francophonie roundtable at the November 2022 GemGenève show. Read or download *Gemmes* at <https://gemmologie-francophonie.com/index.php/la-revue-gemmes>.



Gemstone Supplier Conversations Guide



In May 2023, Ethical Metalsmiths—a USA-based, not-for-profit group dedicated to 'transparent, responsible and environmentally-sound practices' in the jewellery industry—released their Gemstone Supplier Conversations Guide online. The two-page 'condensed' guide provides tips and questions a buyer can use to discuss gem and mineral supply-chain issues with a supplier, 'to help assess the environmental, labor, and human rights practices of suppliers in the mining and gemstone space'. Tips include how to avoid becoming confrontational or critical, asking questions designed to elicit information (rather than just 'yes' or 'no') and navigating a trade-show environment. Download the guide at <https://ethicalmetalsmiths.org/em-member-guide-2023>.

JNA's Lab-Grown Diamond Special 2023

Released in May 2023, this issue covers (in English and Chinese) the growth in polished laboratory-grown diamonds exported from India, the increasing demand for synthetic diamonds, and GIA's detection and testing programme. The issue also focuses on companies that manufacture or polish laboratory-grown diamonds or feature them in jewellery, such as Smiling Rocks, Rockrush, GoGreen, Greenlab Diamonds, Diamsparckz and Bhanderi. The key theme is that the market for synthetic diamonds is growing rapidly. Read or download the issue at <https://news.jewellerynet.com/en/publications/supplements/LGD-Special-2023>.



Natural Diamond Council Report on Education in Retail Settings

In March 2023, NDC released a new study by CXG, a third-party marketing research group, which shows that educating consumers in retail settings is essential to the sales of natural diamond jewellery. Importantly, 93 % of consumers were more confident in buying diamonds when they felt educated. This includes informing customers about differences between natural and laboratory-grown diamonds. For details about how the study was conducted and what the findings suggest for in-store sales procedures, download the report at <https://www.naturaldiamonds.com/wp-content/uploads/2023/03/NDC-Report-Final-March-2023.pdf>. As a result of the study, NDC launched its Education Partner Program in April 2023 (see <https://www.naturaldiamonds.com/education-partner-program>).



Platinum Jewellery Business Review 2023

Platinum Guild International released its 46-page 2023 *Platinum Jewellery Business Review* in May, formatted as a presentation titled 'How Branded Collections are Reshaping the Platinum Jewellery Landscape'. It includes reviews by country (Japan, China, India and USA) of platinum jewellery shares, buyers and prices, as well as the impact of COVID-19, the importance of branded jewellery and strategies for marketing platinum jewellery. Projections for 2023 envision continued growth in some countries and a 'less negative' outlook in others. To download this review, as well as detailed quarterly reports for 2017–2022, visit <https://platinumguild.com/research-publications-platinum-jewellery-business-review>.



SSEF Facette Magazine

Issue no. 28 of Swiss Gemmological Institute SSEF's *Facette Magazine* was released in May 2023. The 74-page issue contains a wealth of information, including brief articles on the history of gems; testing tiny calibrated coloured stones; padparadscha-like pink sapphires with Fe hydroxides in fissures;



Ti-diffused sapphire cabochons; quality control of age dating with SSEF's GemTOF instrumentation; detection of low-temperature-heated corundum; value factors for cultured pearls; age dating and DNA fingerprinting of the Queen Mary pearl; pearl and diamond regalia; pearl and coral identification; emerald/green beryl terminology; impregnated and dyed jadeite; corundum irradiation; Zambian emeralds; the SSEF GemTrack Service; the ASDI-500 diamond screener; LED light boxes for grading coloured stones and diamonds; and more. Download PDFs of this and previous issues at <https://www.ssef.ch/ssef-facette>.

What's New provides announcements of new instruments/technology, publications, online resources and more. Inclusion in What's New does not imply recommendation or endorsement by Gem-A. Entries were prepared by Carol M. Stockton unless otherwise noted.

Gem Notes

COLOURED STONES

Benitoite Polished as Beads for Necklaces

Although the Benitoite Gem mine in California, USA, has been closed since 2005 (Laurs 2005), small quantities of faceted benitoite continue to be released into the market as rough stockpiles are cut. During mining activities from the mid-1960s until 2000, then-owners Elvis ‘Buzz’ Gray (the author’s father) and William ‘Bill’ Forrest set aside many kilograms of broken benitoite crystals that were collected from the washing plant to process at a later time. Most of this stockpile has been sorted to remove any facetable rough, leaving a considerable amount of fractured and translucent material.

Recently, a 2 kg sample consisting of some of the larger pieces of this leftover material was sent to a factory in Asia to investigate whether it would be suitable for cutting and polishing into beads. Due to its fractured nature and the relatively small quantity, it was not processed in the typical mechanised fashion. Instead, each bead was hand-shaped and polished. The factory cut a total of 640 beads, in sizes ranging from 3 to 6 mm in diameter. The yield after drilling was just over 3.5%. The beads were semi-transparent to (mostly) translucent, and displayed no readily apparent fractures. They ranged from white (obtained from the colourless core sections of the crystals) to dark blue, and have not been treated in any way.

Four necklaces were strung that each measured 40.6 cm (16 inches) long, and showed different combinations of colour intensities and sizes of the benitoite beads (e.g. Figure 1). They were strung on silk cords, with 18-carat gold clasps, and some contained small (2 mm) gold beads as spacers. All four of the necklaces sold in the first few minutes of the opening of the February 2023 GJX show in Tucson, Arizona, USA. As with the yearly supply of faceted benitoite offered to the trade, any new necklaces will be made available only at the annual GJX show.

Producers of gem materials are always looking for



Figure 1: This necklace contains benitoite beads ranging from 3 to 6 mm in diameter. On the left are some loose beads showing their appearance before being strung. The beads were recently cut and polished from translucent material that was obtained decades ago from the Benitoite Gem mine in California, USA. Photo by Orasa Weldon.

new ways to use everything that is mined. This is particularly the case for rare stones such as benitoite, which has not been sold previously as beads by the author’s family.

*Michael Gray (mgray@rarestone.com)
Coast to Coast Rare Stones
Mendocino, California,
USA*

Reference

- Laurs, B.M. 2005. Gem News International: Historic U.S. sapphire and benitoite mines close. *Gems & Gemology*, 41(3), 276.

Surface Structures on Beryl Crystals

The morphological features of minerals—especially their surface structures—reveal details of their formation and post-growth history. Crystal growth frequently occurs layer by layer, and new layers are piled up (stacked) in the direction of growth. Between such growth periods, the environment can change, and etching or dissolution of the as-grown surface (crystal face) may occur. Such etching periods can then be followed by subsequent growth steps. Examination of a crystal's surface by optical methods reveals the last step of the growth or post-growth history of such multi-step processes. In special cases, subsequent growth and dilution periods can create complex surface textures on emerald specimens, and the evaluation and interpretation of the observed patterns can be quite complicated (see Schmetzer & Martayan 2023).

Two examples from the author's collection showing interesting surface textures are briefly described here. The first one is an emerald crystal from Nigeria (Figure 2) that has a long, prismatic habit with large prism and basal faces and small hexagonal dipyramids $p\{10\bar{1}2\}$ and $s\{11\bar{2}2\}$. The crystal shows distinct colour zoning along the c -axis, ranging from bluish green to near-colourless. Viewed in immersion, regular growth layers can be seen parallel to the basal face and parallel to the hexagonal dipyramids (Figure 3a). These observations are consistent with the literature on gem-quality emerald from Nigeria (e.g. Lind *et al.* 1986; Schwarz *et al.* 1996).

However, some areas of the prism faces on this crystal show irregular grooves and/or indentations. These could be due to natural etching or result from inhibited growth

due to obstacles (e.g. mineral grains). Magnification (particularly in reflected light) further reveals surface patterns that appear similar to a stacked tile structure or to contour lines on a topographic map (Figure 3b).



Figure 2: This colour-zoned emerald crystal (20.0 × 9.9 × 7.0 mm) from Nigeria was found to display some unusual surface structures. Photo by K. Schmetzer.

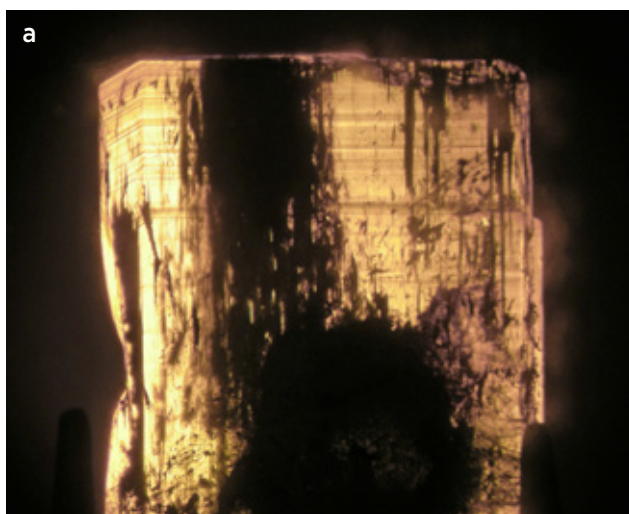


Figure 3: (a) Growth zoning in the Nigerian emerald (9.9 mm across) is visible in immersion in this view perpendicular to the c -axis, showing layers parallel to the basal pinacoid c and dipyramid p . (b) In reflected light, the prism faces of the crystal display grooves or surface indentations with a fine structure, as well as individual growth layers resembling contour lines on a topographic map (field of view 4.8 × 4.0 mm). Photomicrographs by K. Schmetzer.



Figure 4: Interesting surface features are also present on this slightly bluish (almost colourless) beryl crystal from Afghanistan, which measures 11.5 mm in the c-axis direction and 19.5 × 15.0 mm perpendicular to the c-axis. Photo by K. Schmetzer.

This structure represents the last period of the growth history of the crystal, perhaps subsequent to a natural etching phase.

The second sample is a slightly bluish, almost colourless beryl crystal from Afghanistan (Figure 4) that has a short prismatic habit with large prism and basal faces, as well as small hexagonal dipyrramids $s\{11\bar{2}2\}$. Irregular surface indentations or grooves between hillocks cover portions of the basal and prism faces (e.g. Figure 5a). Higher magnification with a Keyence VHX digital microscope reveals a distinct fine structure composed of stepped grooves and etched pyramids (Figure 5b). These pyramids show six larger and, frequently, six smaller faces with a densely striated surface formed by numerous micro-steps. The surface of these corrosion structures reflects the hexagonal symmetry of the basal face of beryl. Such dissolution features are commonly observed on various crystal faces of beryl (Kohlmann 1908; Kurumathoor & Franz 2018). The pattern observed on this beryl from

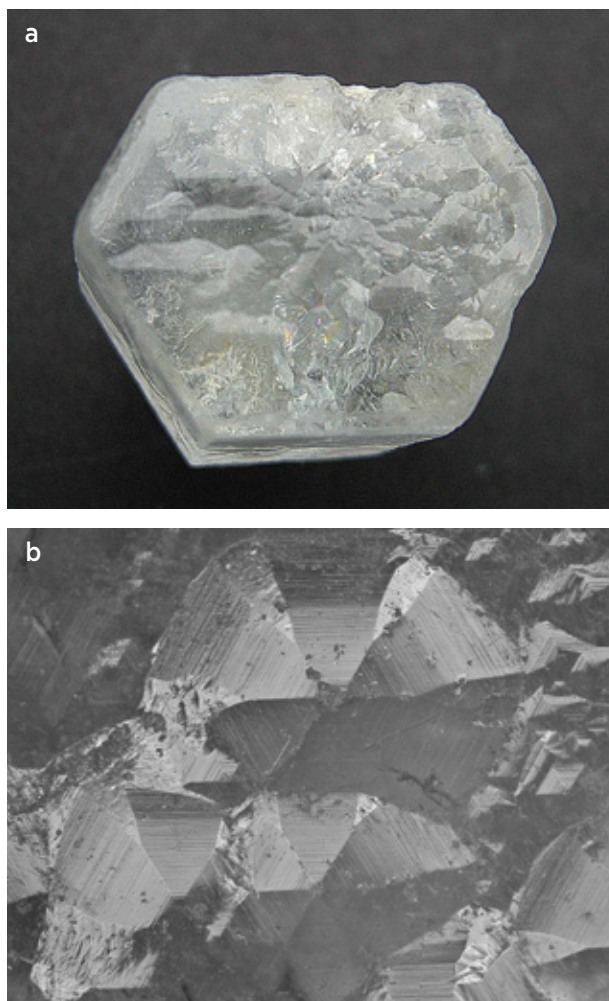


Figure 5: (a) The basal face of the Afghan beryl crystal shows surface indentations or grooves between hillocks. (b) A closer view of this face shows a fine structure consisting of hexagonally outlined hillocks with striated surfaces. Photo (a) by K. Schmetzer and photomicrograph (b) by H. A. Gilg.

Afghanistan thus indicates that the crystal has undergone etching by chemically aggressive fluids.

Dr Karl Schmetzer (SchmetzerKarl@hotmail.com)
Petershausen, Germany

References

- Kohlmann, H. 1908. Beiträge zur Kenntnis des brasilianischen Berylls. *Neues Jahrbuch für Mineralogie, Geologie und Paläontologie*, **25**, 135–181, <https://books.google.cd/books?id=9mxjAAAAIAAJ>.
- Kurumathoor, R. & Franz, G. 2018. Etch pits on beryl as indicators of dissolution behaviour. *European Journal of Mineralogy*, **30**(1), 107–124, <https://doi.org/10.1127/ejm/2018/0030-2703>.
- Lind, T., Schmetzer, K. & Bank, H. 1986. Blue and green beryls (aquamarines and emeralds) of gem quality from Nigeria. *Journal of Gemmology*, **20**(1), 40–48, <https://doi.org/10.15506/JoG.1986.20.1.40>.
- Schmetzer, K. & Martayan, G. 2023. Morphology of Colombian emerald: Some less-common cases and their growth and dissolution history. *Gems & Gemology*, **59**(1), 46–71, <https://doi.org/10.5741/gems.59.1.46>.
- Schwarz, D., Kanis, J. & Kinnaird, J. 1996. Emerald and green beryl from central Nigeria. *Journal of Gemmology*, **25**(2), 117–141, <https://doi.org/10.15506/JoG.1996.25.2.117>.

Morganite from Numbi, Democratic Republic of the Congo

For approximately the past decade, the Numbi area in the South Kivu region of the Democratic Republic of the Congo (DRC) has been a source of gem-quality tourmaline from alluvial, eluvial and possibly primary deposits (Laurs 2015). In addition, artisanal miners there have reportedly produced small amounts of gem-quality morganite (Laurs 2015). The tourmaline and morganite were probably derived from pegmatites mineralised with Sn, W, Nb and Ta that are related to granites which were recently determined to be 648 million years old (Villeneuve *et al.* 2022).

During the past several years, rough stone dealer Farooq Hashmi (Intimate Gems, Glen Cove, New York, USA) obtained three large gem-quality pieces of morganite that were mined in the Numbi area. He purchased one of them while visiting the mining area in April 2014, and obtained the other two on subsequent buying trips to Africa. The largest one was an etched crystal that weighed around 500 g. He provided the two smaller rough stones to Jeff White (J. L. White Fine Gemstones, Kingsport, Tennessee, USA), who cut one of them (67.6 g) into a nearly flawless brownish pink oval gemstone weighing 69.69 ct (Figure 6).

Hashmi indicated that during his visit to the Numbi area in April 2014, the miners thought the morganite was



Figure 6: These rough and cut specimens of morganite are from Numbi, DRC. The cut stone weighs 69.69 ct and measures 30.48 × 21.81 mm. Photo by Jeff White.

rose quartz, and therefore were not actively collecting it. Since then, small amounts of morganite have continued to be found there, and Hashmi estimates that perhaps several tens of kilograms have entered the market. It seems likely that additional morganite could be produced as a by-product of tourmaline mining in Numbi as the miners become more aware of it.

Brendan M. Laurs FGA

References

Laurs, B.M. 2015. Gem Notes: Tourmaline mining in the Democratic Republic of the Congo. *Journal of Gemmology*, **34**(6), 475–476.

Villeneuve, M., Wazi, N., Kalikone, C. & Gärtner, A. 2022. A review of the G4 “tin granites” and associated

mineral occurrences in the Kivu belt (eastern Democratic Republic of the Congo) and their relationships with the last Kibaran tectono-thermal events. *Minerals*, **12**(6), article 737, <https://doi.org/10.3390/min12060737>.

Colour-Change Garnet Showing Blue Colouration from Kamtonga, Kenya

Blue is the rarest of all garnet colours and is known from only a few localities worldwide. Gem-quality material consists of pyrope-spessartine (with minor almandine and grossular), and mainly comes from Embilipitiya and Ethiliwewa (or Athiliwewa) in Sri Lanka, Umba and Tunduru in Tanzania, and Bekily in Madagascar (Schmetzer & Bernhardt 1999). Rather than showing blue as the sole colour, such garnets typically display a colour change from (greenish) blue in daylight to red or reddish purple in incandescent light. However, in 2017, blue-green pyrope-spessartine without a colour change came from a deposit near the border of Tanzania and Kenya (Sun *et al.* 2017). In all cases, V has been found

to be the cause of the blue colour and the colour change (see also Krzemnicki *et al.* 2001; Qiu & Guo 2021).

During the February 2023 Tucson gem and mineral shows, the author obtained a 1.59 ct rectangle-cut garnet that reportedly came from a small new find at Kamtonga, Taita-Taveta County, Kenya (Jason Doubrava, pers. comm. 2023). In addition to its remarkably pure blue colouration in direct sunlight and daylight-equivalent illumination, the garnet showed a distinct colour change to purplish pink in incandescent light, and also appeared greyish bluish green in ‘cold’ LED illumination and intense blue under ‘warm’ LED illumination (Figure 7). By contrast, the colour of most of the material from



Figure 7: This 1.59 ct colour-change garnet from a new find at Kamtonga, Kenya, was characterised for this report. It exhibits different appearances under various types of illumination: (a) daylight-equivalent (6500 K) fluorescent, (b) incandescent, (c) 'cold' LED and (d) 'warm' LED. Photos by C. Schwarzingner.

this find was greyish green in daylight and purplish pink in incandescent light (Figure 8), and only a small amount showed a pure blue hue. These were available mostly as small pieces of rough, and only a few cut stones were seen in Tucson (the gem described here was the only one that exceeded 1 ct).

Standard gemmological testing of the garnet showed RI = 1.758 and hydrostatic SG = 3.64 (average of five

measurements), the latter being distinctly lower than the SG range of 3.83–3.88 reported by Sun *et al.* (2017). The only inclusions visible with a gemmological microscope were long needles (e.g. Figure 9) that were too thin for Raman analysis but appeared to be rutile.

Chemical analysis was performed by laser ablation inductively coupled plasma mass spectrometry (LA-ICP-MS), and the data were normalised to two Al atoms



Figure 8: Most of the recently produced garnets from Kamtonga lack blue colouration, and appear greyish green in daylight and purplish pink in incandescent light, as seen in this 1.94 ct example faceted by Tucson Todd's Gems. Photos by Todd Wacks.

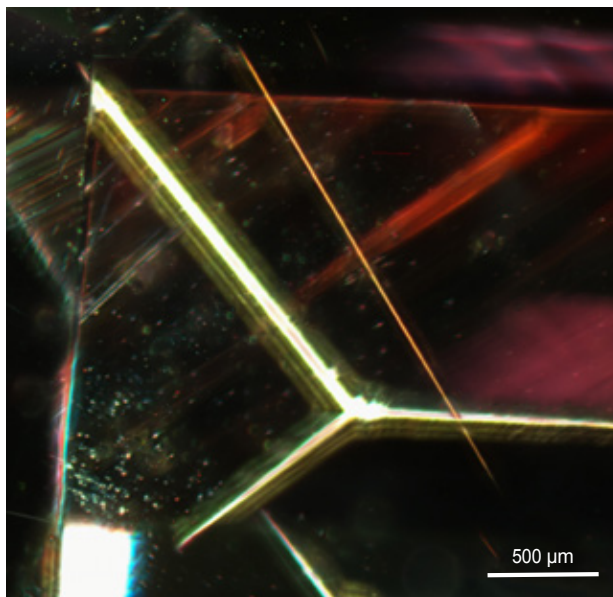


Figure 9: Long needles (probably rutile) such as this one are the only inclusions visible in the blue Kamtonga garnet. The thick bright lines are reflections from facet junctions and the minute bright spots are dust particles. Photomicrograph by C. Schwarzingner.

per formula unit. For comparison, a 0.4 g fragment of colour-change garnet from Tanzania (obtained from New Era Gems, Grass Valley, California, USA) was also analysed, which appeared pale greyish blue in daylight and purplish pink in incandescent light. The Kamtonga garnet had a composition of approximately 40 mol.% spessartine, 38 mol.% pyrope, 15 mol.% grossular and 7 mol.% almandine (Table I). This composition is similar to that of the blue-green material reported by Sun *et al.* (2017), except the latter had slightly more spessartine and less grossular. By contrast, the Tanzanian garnet analysed here for comparison contained significantly more spessartine, and less pyrope and grossular components (again, see Table I). The blue colour-change garnets from Madagascar are easily distinguishable, as they have higher pyrope contents (43–51 mol.%) and very low amounts of grossular (1.8–3.1 mol.%; Schmetzer & Bernhardt 1999).

Ultraviolet-visible-near infrared (UV-Vis-NIR) spectra (Figure 10) of both tested garnets were obtained with a Shimadzu UV-3600i Plus spectrometer with a micro-beam lens unit. The spectra of the two stones are essentially identical, although the face-up colour of the Kamtonga garnet is far more of a pure blue in daylight (thus demonstrating differences in how the human eye perceives colour as compared to a spectrometer). The spectra are dominated by absorptions associated with V^{3+} (a broad absorption centred at 575 nm and an additional band at 410 nm) and Mn^{2+} (410, 422 and 485 nm), with small

Table I: Chemical composition by LA-ICP-MS of the blue Kamtonga garnet compared to one from Tanzania.*

Mol.% end members	Kamtonga garnet	Tanzanian garnet
Pyrope	38.1	34.6
Spessartine	39.8	47.1
Almandine	7.2	6.8
Grossular	14.9	11.5
Trace elements (ppmw)		
Li	10	10
Ti	390	280
V	7700	6000
Cr	900	1300
Co	1500	2200
Ni	bdl	bdl
Cu	8	2
Zn	115	165
Ga	4	14
Ge	1	10
Sr	bdl	bdl
Y	140	850
Zr	29	26
La	<1	<1
Ce	<1	<1
Pr	<1	<1
Nd	<1	3
Sm	1	9
Eu	1	1
Gd	7	40
Tb	2	10
Dy	17	83
Ho	4	23
Er	13	80
Tm	2	13
Yb	13	85
Lu	2	13
Σ REE	60	350

* Average of three measurements. Abbreviation: bdl = below detection limit.

contributions from Fe^{2+} (459, 505 and 520 nm).

The pure blue daylight colouration of this Kamtonga garnet is notable, and this occurrence can now be added to the small number of localities for such material.

UV-Vis-NIR Spectra

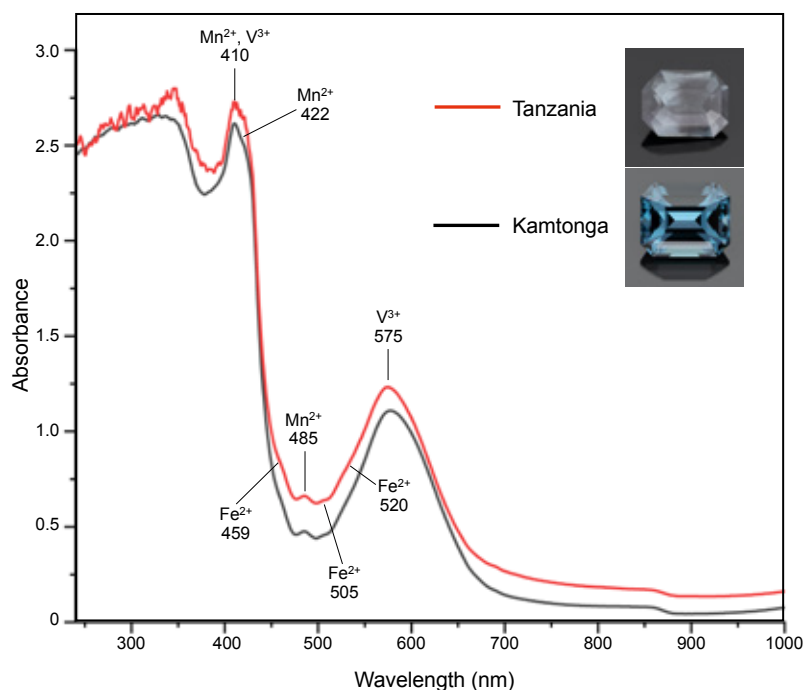


Figure 10: The UV-Vis-NIR spectra of the Kamtonga garnet and a comparison sample from Tanzania (shown here after being faceted into a 0.40 ct gemstone) are very similar, and display features typical of colour-change garnets from East Africa. The path length of the beam was approximately 4.3 mm for the Kamtonga garnet and 4 mm for the Tanzanian sample. Photos by C. Schwarzingner.

Dr Clemens Schwarzingner
(clemens.schwarzingner@jku.at)
Johannes Kepler University Linz
Austria

References

- Krzemnicki, M.S., Hänni, H.A. & Reusser, E. 2001. Colour-change garnets from Madagascar: Comparison of colorimetric with chemical data. *Journal of Gemmology*, **27**(7), 395–408, <https://doi.org/10.15506/JoG.2001.27.7.395>.
- Qiu, Y. & Guo, Y. 2021. Explaining colour change in pyrope-spessartine garnets. *Minerals*, **11**(8), article 865, <https://doi.org/10.3390/min11080865>.
- Schmetzer, K. & Bernhardt, H.-J. 1999. Garnets from Madagascar with a color change of blue-green to purple. *Gems & Gemology*, **35**(4), 196–201, <https://doi.org/10.5741/gems.35.4.196>.
- Sun, Z., Renfro, N.D. & Palke, A.C. 2017. Gem News International: Blue-green pyrope-spessartine garnet with high vanadium. *Gems & Gemology*, **53**(3), 373–375 (see data table at <https://www.gia.edu/gems-gemmology/fall-2017-gemnews-blue-green-pyrope-spessartine>).

A Remarkable Cr-bearing Red Musgravite

Recently, a red 1.59 ct cushion mixed-cut gemstone was submitted to the Central Gem Laboratory (CGL) in Tokyo, Japan, for identification (Figure 11). According to the client, the gem was obtained on the second-hand market, where it was sold as a ruby.

Although the overall appearance of the gem closely resembled ruby or red spinel, it had RIs of 1.715–1.721 (birefringence of 0.006 and uniaxial negative) and the hydrostatic SG was 3.60. These properties suggested

the possibility of taaffeite or musgravite. We observed pleochroic colours of purple-red (ordinary ray) and orange (extraordinary ray). Microscopic observation of the gem revealed fluid inclusions (Figure 12a) and fractures that appeared to contain iron oxide. We also noted a purple-red colour band in a direction parallel to the optic axis, and a near-colourless area was seen in other orientations when the stone was immersed in methylene iodide (Figure 12b, c).



Figure 11: This 1.59 ct gemstone was submitted to CGL for identification, and proved to be the first reported red musgravite. The irregular chipped outline is presumably due to wear while the stone was on the market for a long time before it was properly identified. Photo by Junichi Kubo.

Musgravite ($\text{BeMg}_2\text{Al}_6\text{O}_{12}$; in the trigonal system) is now recognised by the International Mineralogical Association as magnesiotaafeite-6 N 3S, but as a gemstone it is traditionally called musgravite. Since the physical and chemical properties of musgravite are similar to those of taafeite ($\text{BeMg}_3\text{Al}_6\text{O}_{16}$; in the hexagonal system and now called magnesiotaafeite-2 N 2S), distinguishing between taafeite and musgravite is challenging. Powder X-ray diffraction (XRD) has traditionally been used to separate these minerals, but non-destructive single-crystal XRD analysis, energy-dispersive X-ray fluorescence (EDXRF) and Raman spectroscopy have also been applied in previous studies (Kiefert & Schmetzer 1998; Okano *et al.* 2006; Abduriyim *et al.* 2008).

Table II: Semi-quantitative normalised EDXRF chemical data for the red musgravite.

Oxide	Mass fraction (wt.%)	Mole fraction (mol.%) ^a
BeO ^b	6.08	16.67
MgO	19.32	33.02
Al ₂ O ₃	73.06	49.37
K ₂ O	0.01	0.01
CaO	0.05	0.06
TiO ₂	0.02	0.02
V ₂ O ₃	0.03	0.02
Cr ₂ O ₃	0.51	0.23
FeO	0.09	0.09
ZnO	0.44	0.37
Ga ₂ O ₃	0.39	0.14
Sum	100.00	100.00

^a The mole fraction was calculated from the mass fraction.

^b BeO was calculated since Be is not detectable by EDXRF analysis.

Table II gives the results of EDXRF analysis of the 1.59 ct red stone. The ratio of $\Sigma_{\text{mol.}\%}(\text{XO}, \text{X} = \text{Mg}, \text{Ca}, \text{Mn}, \text{Fe}, \text{Zn})$ to $\Sigma_{\text{mol.}\%}(\text{X}_2\text{O}_3, \text{X} = \text{Al}, \text{V}, \text{Cr}, \text{Ga}) = 2:3$, suggesting that the specimen is musgravite rather than taafeite. However, the amounts of Cr, Zn and Ga are significantly higher, and Fe is lower, than reported previously for musgravite (Schmetzer *et al.* 2005). The high Cr content is similar to that of a purplish red taafeite analysed by Schmetzer *et al.* (2000).

Raman spectroscopy showed the most intense peaks around 489 and 409 cm^{-1} , a less intense peak around 711 cm^{-1} and weaker peaks at approximately 804, 662, 620, 574 and 441 cm^{-1} (Figure 13a). This pattern is closer to the Raman spectra of musgravite than taafeite in the RRUFF database (<https://rruff.info>).

The Fourier-transform infrared (FTIR) reflectance spectrum of the gem was compared to reference spectra collected from musgravite and taafeite (Figure 13b)

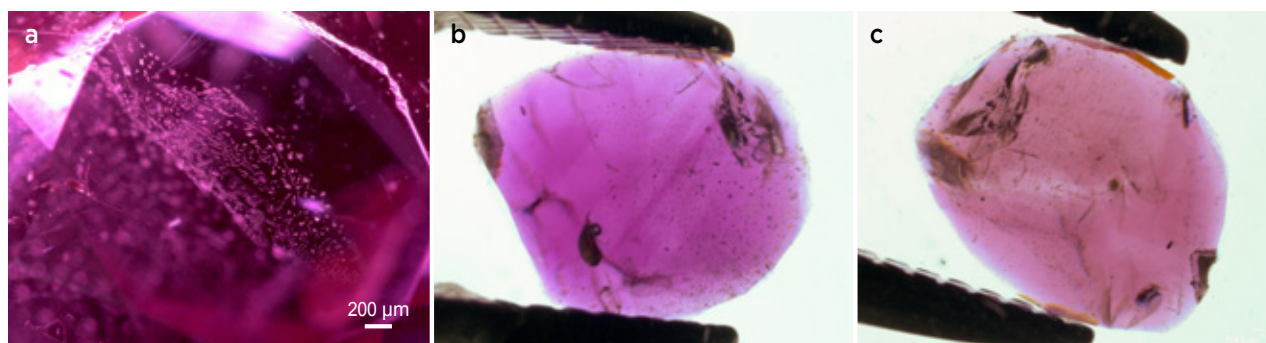


Figure 12: (a) The musgravite contains arrays of two-phase (liquid and gas) fluid inclusions. In addition, when viewed with immersion in methylene iodide, the 1.59 ct stone displays (b) a purple-red colour band in the optic-axis direction and (c) in other orientations, a near-colourless area (seen here in the centre of the stone). Photomicrographs by H. Kitawaki.

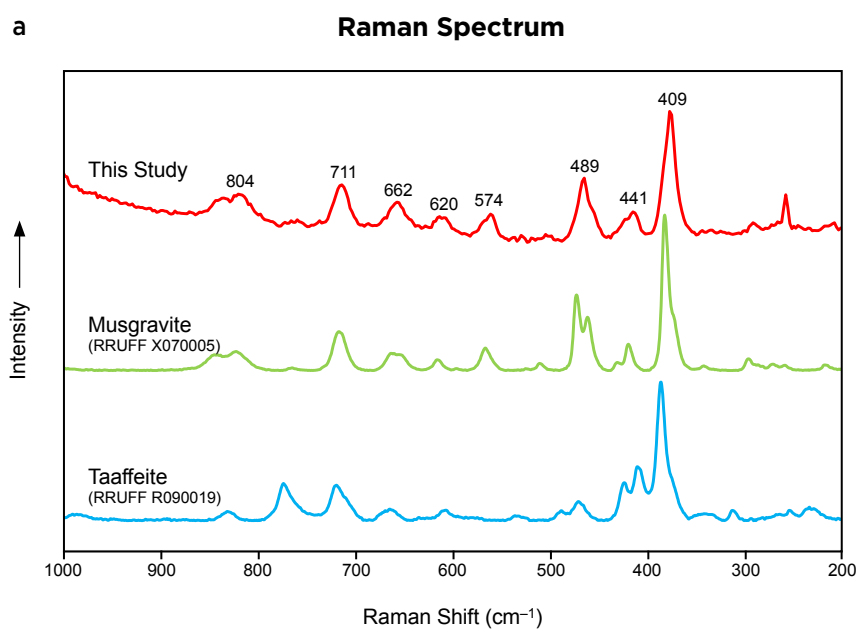
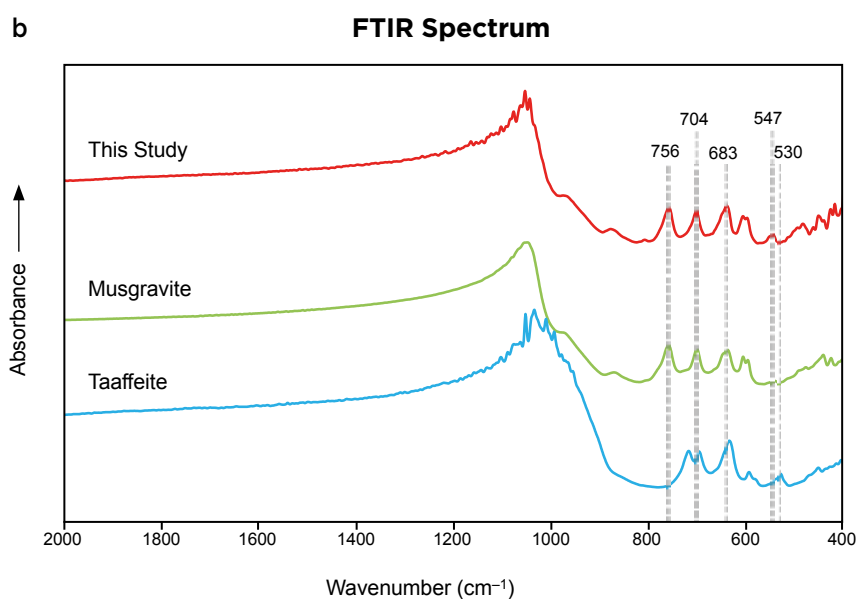


Figure 13: (a) The Raman spectrum of the red gem shows a closer resemblance to a reference spectrum of musgravite than of taaffeite in the RRUFF database. (b) The FTIR reflectance spectrum of the stone likewise exhibits greater similarities to the reference spectrum of musgravite than of taaffeite.



that were previously identified by Raman spectroscopy and powder XRD at CGL (Manaka & Ogata 2009). The presence of bands at 756 and 547 cm^{-1} , and the lack of any feature at 530 cm^{-1} , are consistent with musgravite but not taaffeite.

UV-Vis spectroscopy revealed a peak near 686 nm and broad, strong absorptions near 395 and 547 nm (Figure 14). These features are similar to those known for Cr-bearing gems such as ruby and red spinel, and

therefore are considered to represent absorption by Cr^{3+} .

The stone documented in this study was confirmed to be musgravite by a combination of EDXRF, Raman and FTIR spectroscopy. To our knowledge, musgravite with such a bright red colour has not been described previously in the gemmological literature. Although it remains an extreme rarity, gemmologists should be aware of the possibility of encountering red musgravite.

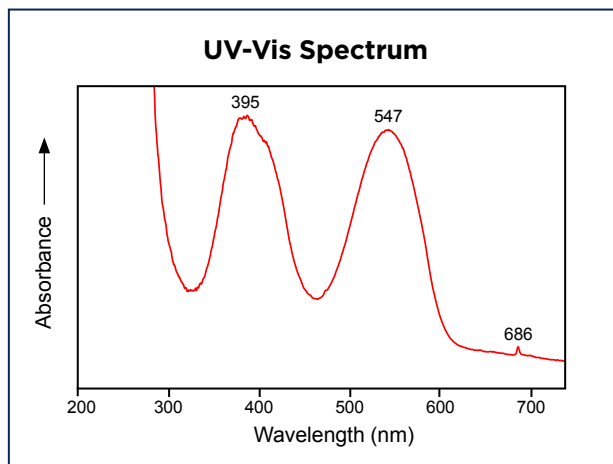


Figure 14: The UV-Vis spectrum of the red musgravite shows a small, sharp absorption peak near 686 and broad bands at about 395 and 547 nm; these features are attributable to Cr^{3+} .

Zhengkao Zhao (zhengkao@cgl.co.jp),
Dr Hiroshi Kitawaki FGA,
Kentaro Emori, Makoto Okano,
Yuji Manaka and
Satoshi Ebisubo
CGL, Tokyo, Japan

References

- Abduriyim, A., Kobayashi, T. & Fukuda, C. 2008. Identification of taaffeite and musgravite using a non-destructive single-crystal X-ray diffraction technique with an EDXRF instrument. *Journal of Gemmology*, **31**(1–2), 43–54, <https://doi.org/10.15506/JoG.2008.31.1.43>.
- Kiefert, L. & Schmetzer, K. 1998. Distinction of taaffeite and musgravite. *Journal of Gemmology*, **26**(3), 165–167, <https://doi.org/10.15506/JoG.1998.26.3.165>.
- Manaka, Y. & Ogata, T. 2009. About identification of rare stones encountered recently (Part 1). *Gemmy*, No. 151, 3–8, https://www.cgl.co.jp/latest_jewel/gemmy/151/77.html, accessed 18 April 2023 (in Japanese).
- Okano, M., Kitawaki, H. & Abduriyim, A. 2006. Taaffeite and musgravite < Gemstones in the latest topics > . https://grjapan.ddo.jp/gaaj_report/2006a/2006_10a-01en.html, 12 October, accessed 18 April 2023.
- Schmetzer, K., Kiefert, L. & Bernhardt, H.-J. 2000. Purple to purplish red chromium-bearing taaffeites. *Gems & Gemology*, **36**(1), 50–58, <https://doi.org/10.5741/gems.36.1.50>.
- Schmetzer, K., Kiefert, L., Bernhardt, H.-J. & Burford, M. 2005. Gem-quality musgravite from Sri Lanka. *Journal of Gemmology*, **29**(5–6), 281–289, <https://doi.org/10.15506/JoG.2005.29.5.281>.

Rhodonite from Italy and Indonesia

Rhodonite and pyroxmangite are polymorphs of MnSiO_3 —with varying amounts of Ca, Fe and Mg substituting for Mn—that are commonly found in association with one another, and even can be intergrown. They typically form massive polycrystalline aggregates, and advanced analytical techniques such as X-ray powder diffraction are needed to differentiate between them. In the gem trade, the material is commonly referred to simply as *rhodonite*.

During the February 2023 Tucson gem and mineral shows, this author encountered two new occurrences of rhodonite that were interesting for their mineral association (occurring with layers of spessartine) or locality (Indonesia). Both were exhibited by Rare Earth Mining Co. (Amherst, New Hampshire, USA).

The rhodonite associated with spessartine came from Piedmont, in the Alps of north-west Italy. According to Rare Earth's president Curtis Heher, his supplier indicated that the deposit is located on Monviso Mountain. Although gem-quality rhodonite has been previously reported from Piedmont (Alagna Valsesia

and Strona Valley; Diella *et al.* 2014)—and several localities for rhodonite in Piedmont are listed on Mindat (<https://www.mindat.org/min-3407.html>)—interestingly Monviso is not included among them. Heher obtained about 5 kg of the rough rhodonite that was mined in 2022, from which he had cut several dozen cabochons and polished tablets (about 100 matched pairs and 50 singles). Some of the stones displayed conspicuous orange bands (e.g. Figure 15, left pair), which Heher indicated had been identified as spessartine. In addition, they typically contained colourless layers (probably quartz). While spessartine is commonly associated with massive rhodonite, it usually occurs as fine-grained disseminations (Diella *et al.* 2014; Caucia *et al.* 2020) rather than discrete layers.

The Indonesian rhodonite also showed a layered appearance, but with black and pale yellow areas (e.g. Figure 15, right pair). It was notable since this was the first time this author has seen gem-quality rhodonite from Indonesia, and a literature search revealed no mention of such material from there. Heher obtained



Figure 15: These matched pairs are representative of new occurrences of massive rhodonite seen at the 2023 Tucson gem and mineral shows. The polished tablets on the left side contain rhodonite associated with orange spessartine from Piedmont, Italy (28 × 20 mm each), and those on the right side consist of a layered rhodonite assemblage from Sulawesi, Indonesia. Photo by Jeff Scovil.

3 kg of rough shortly before the 2023 Tucson shows, and cut about 200 matched pairs of cabochons and polished tablets. He was initially unsure of the exact locality, but later learned from his supplier that the rough came from Sulawesi, Indonesia. This origin was also indicated by Indonesian stone dealer Dace Irwan (CV Anugrah Alam, Sukabumi, West Java), who noted that similar material (Figure 16) was recently mined from near Uevololo village in Parigi Moutong Regency, Central Sulawesi Province.

Brendan M. Laurs FGA



Figure 16: These rhodonite slabs were cut from material recently mined in Sulawesi, Indonesia. Photo courtesy of Dace Irwan.

References

- Caucia, F., Marinoni, L., Riccardi, M.P., Bartoli, O. & Scacchetti, M. 2020. Rhodonite-pyroxmangite from Tanatz Alp, Switzerland. *Gems & Gemology*, **56**(1), 110–123, <https://doi.org/10.5741/gems.56.1.110>.
- Diella, V., Adamo, I. & Bocchio, R. 2014. Gem-quality rhodonite from Val Malenco (Central Alps, Italy). *Periodico di Mineralogia*, **83**, 207–221.

Three-Ray Asterism in Quartz: A Multi-Star Network

Phenomenal quartz is known from various localities. Commonly, six- or 12-rayed stars are encountered, but samples are also known that display multi-star networks consisting of four-, six-, eight-, ten- and/or 12-rayed stars (Schmetzer & Glas 2003). Another optical phenomenal pattern in quartz consists of light spots that can be observed on the surface of asteriated rose-quartz spheres (Schmetzer & Krzemnicki 2006).

Rarely mentioned in the gemmological literature is quartz showing three-rayed asterism. Recently, Schmetzer and Steinbach (2022) described such samples having not only a single three-rayed star, but also a network of interconnected asterism, in which two stars are linked by a common arm or branch. In contrast

to the ‘ordinary’ light bands of asteriated gemstones, the light bands of three-rayed stars do not cross one another, but only meet at one central point. Due to the unfavourable orientation of the *c*-axis in samples previously examined and/or the unfavourable shapes of those cabochons, the complete multi-star network of the samples (i.e. the theoretical number of stars that could be present and their orientation relative to the quartz crystal lattice) was not fully understood.

Further information is now available from the investigation of a complete quartz sphere showing a multi-star network of three-rayed stars (Figure 17). The sample weighs 380 g (65 mm in diameter) and was purchased by one of the authors (MPS) at the February 2023 Tucson

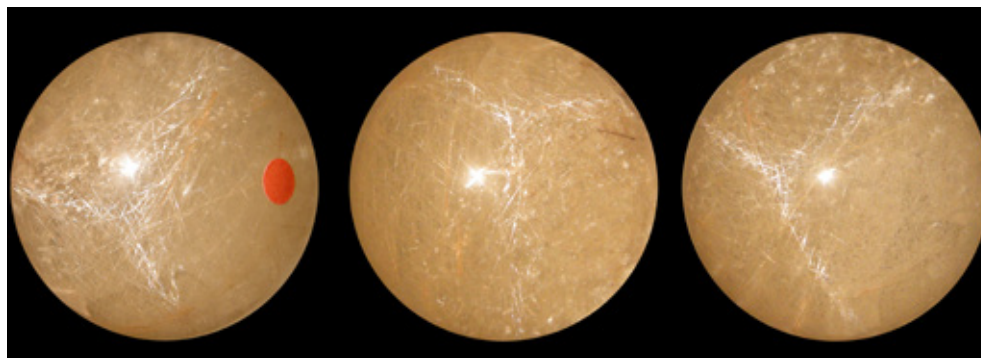


Figure 17: Three examples are shown of three-rayed stars visible on the surface of a quartz sphere (65 mm in diameter), reportedly from Brazil, that contains abundant fibrous inclusions. The sphere is shown in three different orientations; in the left photo, the position of the *c*-axis of the quartz is indicated by a red dot. Composite photo by K. Schmetzer.

gem and mineral shows. It reportedly originated from Brazil, but more detailed information about its origin was not provided by the vendor.

In a view parallel to the *c*-axis of the quartz, the sphere can be subdivided virtually into an upper and a lower half, which meet along an equatorial line. Following the arms of the three-rayed stars by rotating the sphere, the surface of the upper half reveals a pattern of diffuse light bands of six three-rayed stars forming the network shown schematically in Figure 18. Three of these six stars are depicted in Figure 17. Due to the fact that the curved light bands move across the surface of the sphere as it is rotated, each three-rayed star does not have a fixed centre. However, we can estimate an observed angle of approximately 60° between each of the six symmetrically equivalent stars, which is consistent with a six-fold rotation axis of the quartz lattice along the *c*-axis.

By following the arms of the stars, we observed that one branch of each of the three-rayed stars connects the network on the upper half of the sphere with an identical network of six three-rayed stars on the lower half of the sphere. These six arms intersect with one additional light band of low intensity running perpendicular to the *c*-axis (i.e. completely around the equatorial line of the sphere). In this way, six four-rayed stars of weak intensity, but clearly visible, are formed.

In summary, the complete multi-star network of the quartz sphere consists of 12 (2×6) three-rayed stars and six somewhat weaker four-rayed stars. Such a network is consistent with the symmetry of quartz, but the exact mechanism of its formation is still unknown.

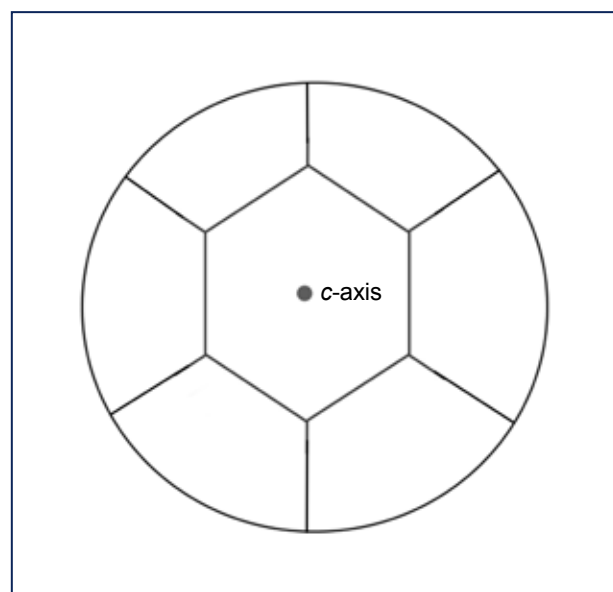


Figure 18: This schematic representation of the upper half of the asteriated quartz sphere, viewed parallel to the *c*-axis, shows a multi-star network of three-rayed stars. One branch of each star is connected with one of six three-rayed stars forming an identical network on the lower half of the sphere. Each of these connecting branches intersects with an additional light band running perpendicular to the *c*-axis (i.e. around the equatorial line of the sphere), thus forming six additional, four-rayed stars.

Dr Karl Schmetzer
(SchmetzerKarl@hotmail.com)
Petershausen, Germany

Martin P. Steinbach
Idar-Oberstein, Germany

References

- Schmetzer, K. & Glas, M. 2003. Multi-star quartzes from Sri Lanka. *Journal of Gemmology*, **28**(6), 321–332, <https://doi.org/10.15506/JoG.2003.28.6.321>.
- Schmetzer, K. & Krzemnicki, M. 2006. The orientation and symmetry of light spots and asterism in rose quartz

spheres from Madagascar. *Journal of Gemmology*, **30**(3–4), 183–191, <https://doi.org/10.15506/JoG.2006.30.3.183>.

- Schmetzer, K. & Steinbach, M.P. 2022. Gem News International: Three-rayed asterism in quartz. *Gems & Gemology*, **58**(2), 249–252.

Quartz with Kyanite Inclusions from Brazil

Attractive specimens composed of blades of kyanite in massive quartz have been known for many years from Brazil, mainly from Minas Gerais, Bahia and Goiás states (Laurs & Quinn 2005; Cook 2008). The kyanite typically ranges from bluish grey to blue to deep blue, and may attain large sizes (50+ cm long). Although facet-grade kyanite is sometimes found, most of the material is sold as mineral specimens.

At the February 2023 Tucson gem and mineral shows, attractive cabochons consisting of quartz with kyanite inclusions from Brazil were seen by this author for the first time (Figure 19). They were exhibited by Rare Earth Mining Co., and company president Curtis Heher said they purchased about 8 kg of rough material that was mined in Bahia State in 2020. Only 10% of the pieces contained kyanite that could be attractively displayed as inclusions in the quartz, so they obtained a rather low yield after cutting the cabochons (approximately 30 stones, including eight matched pairs). The kyanite shows pure blue colouration and is sometimes zoned from pale to intense blue. The quartz matrix is transparent with typical clouds and veils.

Although kyanite from Brazil is commonly hosted by massive quartz, it is unusual for the quartz to be transparent enough to cut into cabochons that display the kyanite inclusions.

Brendan M. Laurs FGA

References

Cook, R.B. 2008. Connoisseur's Choice: Kyanite—Minas Gerais, Brazil. *Rocks & Minerals*, **83**(6), 520–527, <https://doi.org/10.3200/RMIN.83.6.520-527>.



Figure 19: This cabochon of quartz with kyanite inclusions is from Bahia State, Brazil, and measures 34 × 21 mm. Photo by Jeff Scovil.

Laurs, B.M. & Quinn, E.P. 2005. Gem News International: Kyanite widely available. *Gems & Gemology*, **41**(1), 59–60.

Ruby from Central Madagascar

Madagascar is an important source of gem-quality ruby, which has been mined from several deposits on the island (Rakotondrazafy *et al.* 2008). At the February 2023 Tucson gem shows, rubies from a reportedly new deposit in central Madagascar were exhibited by Columbia Gem House Inc. (Vancouver, Washington, USA). According to president and CEO Eric Braunwart, the initial production took place in February 2022, and the rough is sourced from a small valley that is a rice- and apple-growing area where local people dig alluvial rubies when they are not farming. Braunwart initially received about 250 g

of rough, followed by another 250 g, and he had 50 g of it cut before the 2023 Tucson shows. The stones are not treated in any way, and they are being marketed as ‘Pomme’ ruby, since *pomme* means apple in French. The gems hold their colour to sizes as small as 1.5 mm and are mostly available as melee, with larger cut stones typically up to 0.5 ct and exceptionally up to 2 ct.

Braunwart kindly loaned three of the faceted rubies for examination (0.26–0.58 ct; Figure 20), and gemmological properties were collected by author NDR: RIs—1.759–1.769 (birefringence 0.008–0.009);



Figure 20: These three rubies from central Madagascar (0.26–0.58 ct) were examined for this report. Photo by Annie Haynes, © GIA.

hydrostatic SG—4.00; fluorescence—very weak to short-wave UV and moderate red to long-wave UV radiation; and a typical ruby spectrum was seen with a desk model spectroscope. The stones were selected specifically for the presence of inclusions, which consisted of dark brown protogenetic rutile crystals (identified visually by their classic appearance; Figure 21), as well as elongate needles oriented in three directions and



Figure 21: Blocky protogenetic crystals of dark brown rutile form conspicuous inclusions in this ruby from central Madagascar. Photomicrograph by N. D. Renfro, © GIA; image width 2.3 mm.

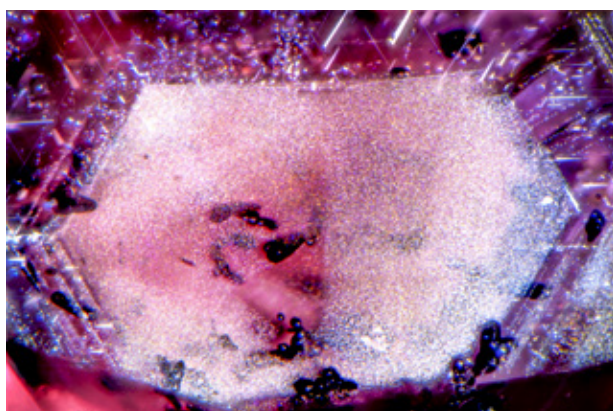


Figure 22: Internal features in this Madagascar ruby consist of oriented elongate needles and hexagonal growth zoning marked by minute reflective platelets. Both the needles and platelets probably consist of rutile. Photomicrograph by N. D. Renfro, © GIA; image width 2.4 mm.

Table III: LA-ICP-MS analyses of rubies from central Madagascar.

Element (ppmw)*	0.26 ct round	0.56 ct oval		0.58 ct oval	
		Spot 1	Spot 2	Spot 1	Spot 2
Mg	53.8	34.9	58.4	38.7	41.9
Ti	102	69.3	92.9	73	78.2
V	42.4	50.1	53.2	34.3	35.7
Cr	3510	1060	1380	599	678
Fe	2010	2430	2490	2350	2390
Ni	<0.441	0.48	0.45	<0.147	<0.148
Ga	38.5	33.7	35.2	45.7	46.1
Zr	0.007	0.012	<0.002	<0.002	<0.002
Nb	0.006	<0.001	<0.003	<0.001	<0.001
Sn	0.22	0.25	0.22	0.22	0.31
Ta	0.041	<0.001	<0.003	<0.001	<0.001
Pb	0.24	0.140	0.037	0.010	<0.009

* Be, Mn, Mo, Rh, La, Ce, Nd, Hf, W, Pt, Th and U were analysed but not detected.

hexagonal growth zoning marked by reflective platelets (both probably also consisting of rutile; Figure 22). Chemical analyses of the stones by LA-ICP-MS showed significant Cr and Fe, with traces of Ti, V, Mg, Ga and Sn, as well as various other trace elements (Table III).

The properties of the samples examined, and the location of the deposit in central Madagascar, are consistent with a basaltic source (cf. Rakotosamizany *et al.* 2014). Untreated ruby that holds its colour even at small sizes is a welcome addition to the market, although the future availability of the ‘Pomme’ ruby will depend on the production from the local diggers and the changing regulations for exporting gem material from Madagascar.

Brendan M. Laurs FGA

Nathan D. Renfro

Gemological Institute of America (GIA)
Carlsbad, California, USA

References

- Rakotondrazafy, A.F.M., Giuliani, G., Ohnenstetter, D., Fallick, A.E., Rakotosamizany, S., Andriamamonjy, A., Ralantoarison, T., Razanatseho, M. *et al.* 2008. Gem corundum deposits of Madagascar: A review. *Ore Geology Reviews*, **34**(1–2), 134–154, <https://doi.org/10.1016/j.oregeorev.2007.05.001>.
- Rakotosamizany, S., Giuliani, G., Ohnenstetter, D., Rakotondrazafy, A.F.M., Fallick, A.E., Paquette, J.-L. & Tiepolo, M. 2014. Chemical and oxygen isotopic compositions, age and origin of gem corundums in Madagascar alkali basalts. *Journal of African Earth Sciences*, **94**, 156–170, <https://doi.org/10.1016/j.jafrearsci.2013.06.003>.

Spessartine from Engare Naibor, Tanzania

Tanzania is an important source of several varieties of gem-quality garnet, including pyrope-spessartine (malaya and colour change), pyrope-almandine (rhodolite), green grossular (tsavorite) and pyrope. Spessartine is less commonly mined there, and is known from Loliondo (north-eastern Tanzania, near the Kenyan border; Chadwick *et al.* 2008) and the Iringa region in central Tanzania (Laurs 2002).

In mid- to late 2022, a new deposit of spessartine was discovered in north-eastern Tanzania near Engare Naibor (i.e. about 90 km south-east of Loliondo). Gem and mineral dealer Dudley Blauwet (Dudley Blauwet Gems, Louisville, Colorado, USA) obtained 2 kg of clean rough in early October 2022 that his supplier had selected from 20 kg of mostly included material. The pieces were small but of intense orange colour, and consisted of broken fragments and some dodecahedral crystals. So far he has cut about 50–100 carats—which he debuted at the February 2023 Tucson gem and mineral shows—that are mostly 2.0–2.5 mm with some 3.0 mm and a few 3.5 mm stones. Blauwet also reported that a 6 kg rough parcel of this spessartine recently sold by an East African dealer in Bangkok contained somewhat larger sizes and showed better clarity.

Blauwet loaned three rough (0.08–0.17 g) and two faceted stones (3.5 mm in diameter or 0.21 ct each) to authors BW and CW for examination (Figure 23). They were intense yellowish orange with a faint brown modifier. The RI was over the limit of a standard refractometer (>1.810). Hydrostatic SG values were not



Figure 23: A new deposit near Engare Naibor in north-eastern Tanzania is the source of these spessartine samples (0.08–0.17 g rough and 0.21 ct faceted stones). Photo by B. Williams.

obtained due to the small sizes of the stones. The garnets were strongly attracted to a rare-earth-element magnet (sticking to it). Under magnification, the only inclusions consisted of classic, lace-like, fluid-filled ‘fingerprints’ typical of spessartine. Raman spectroscopy with a Magilabs GemmoRaman-532SG unit provided a strong match to spessartine in the RRUFF database. Chemical analysis with an Amptek X123-SDD EDXRF spectrometer revealed the expected abundant amount of Mn, along with some Fe and Ca (Figure 24). UV-Vis spectroscopy with a Magilabs GemmoSphere unit showed strong absorptions due to Mn^{2+} and also the presence of Fe^{2+} (Figure 25).

EDXRF Spectrum

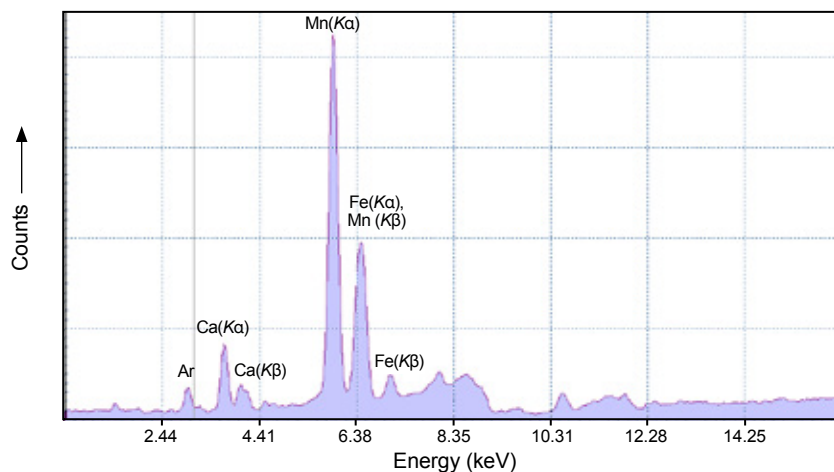


Figure 24: EDXRF spectroscopy of the spessartine shows intense Mn peaks, as well as some Fe and Ca. The Ar peak is due to the analysis taking place in air.

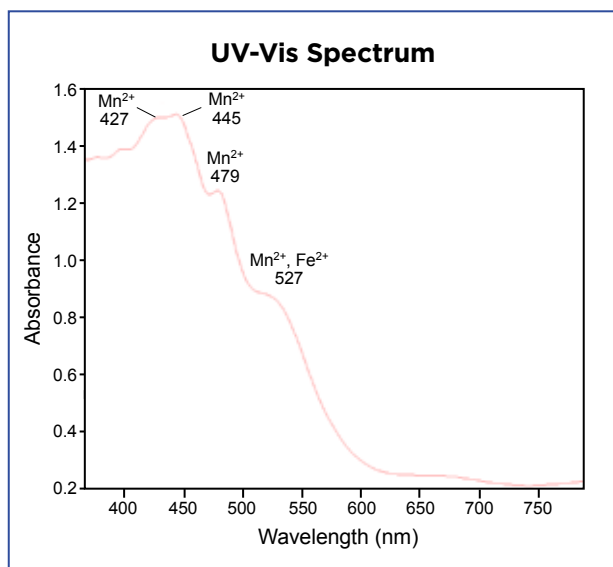


Figure 25: The UV-Vis spectrum of the spessartine is dominated by Mn²⁺-related absorptions. The path length of the beam was approximately 0.1 mm.

The highly saturated orange colour of this spessartine makes it an attractive gem material, even when cut into rather small sizes.

Bear Williams FGA and Cara Williams FGA
(info@stonegrouplabs.com)
Stone Group Laboratories
Jefferson City, Missouri, USA

Brendan M. Laurs FGA

References

- Chadwick, K.M., Koivula, J.I., Laurs, B.M., Attard, J., Simmons, W.B. & Falster, A.U. 2008. Gem News International: Spessartine from Loliondo, Tanzania. *Gems & Gemology*, **44**(1), 76–78.
- Laurs, B.M. (ed) 2002. Gem News International: Aquamarine and spessartine from Tanzania. *Gems & Gemology*, **38**(3), 259.

SYNTHETICS AND SIMULANTS

Update: Colourless HPHT-grown Synthetic Diamonds Testing as Synthetic Moissanite

Diamond is an electrical insulator when boron is absent from its structure, but when it contains sufficient levels of uncompensated boron it acts as a semi-conductor. Traces of uncompensated boron are commonly present in near-colourless, high-pressure, high-temperature (HPHT)-grown synthetic diamonds, and a previous study by the author documented that those showing a slight blue tinge may be misidentified as synthetic moissanite on diamond testers due to their electrical conductivity (Griffith & Dupuy 2021). HPHT synthetic diamonds with high colour grades can also contain uncompensated boron (Eaton-Magaña *et al.* 2017), so hypothetically they likewise could be conductive enough to be misidentified by diamond testers. Nevertheless, according to Griffith and Dupuy (2021, p. 575), 'There have been no reports of colourless HPHT synthetic diamonds equivalent to D–F colour grades exhibiting electrical conductivity'. This study explores whether electrical conductivity can be exhibited by such colourless HPHT-grown synthetics, thus causing incorrect readings from diamond multi-testers.

Seven HPHT-grown synthetic diamonds with colour grades equivalent to D–F were studied (Figure 26 and

Table IV). Four samples were equivalent to D colour, two were equivalent to E and one was equivalent to F. The HPHT growth method is stated on their accompanying IGI laboratory-grown diamond reports and was confirmed through a combination of gemmological tests, including screening (Dr. Watson by Yehuda), reactions to long- and short-wave UV radiation (Jewellery Inspector by Gemetrix), and a lack of strain between cross-polarised filters. The D-colour samples were chosen randomly from an online wholesaler, while the E- and F-colour synthetics were from the author's laboratory-grown diamond collection. The latter specimens showed anomalous behaviour on diamond testers, which aroused suspicion that some high-colour HPHT-grown synthetic diamonds could be electrically conductive.

The samples were first tested to determine whether they contained uncompensated boron impurities and thus display electrical conductivity. Room-temperature infrared (IR) absorption spectra were collected using a PerkinElmer Spectrum BX FTIR spectrometer, and all but one of them (E colour equivalent) showed an absorption at 2800 cm⁻¹ indicating the presence of uncompensated boron. Next, each specimen was

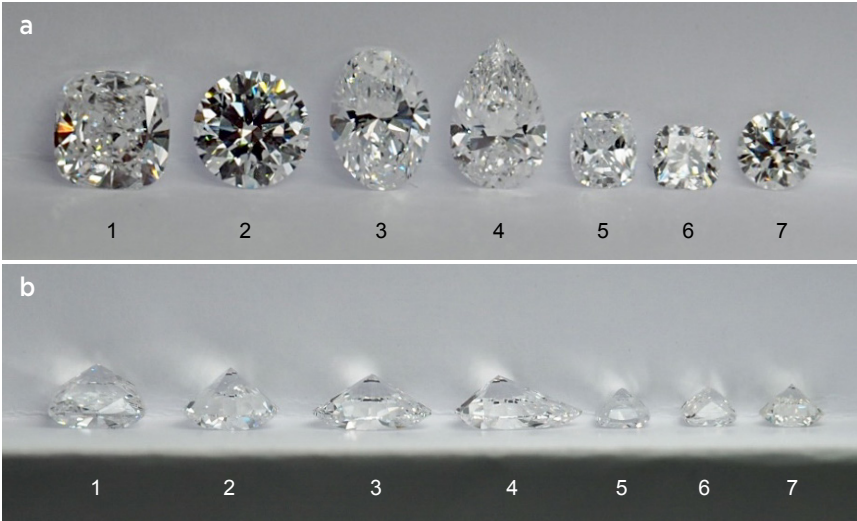


Figure 26: These seven colourless HPHT-grown synthetic diamonds (0.30-1.58 ct) with colour grades equivalent to D-F were examined for this report and are shown here (a) face-up and (b) table-down. Six of them tested as ‘moissanite’ with the two diamond testers used. Only sample 6—for which boron was not detected by IR spectroscopy—correctly and consistently tested as ‘diamond’. Photos by J. Griffith.

probed with two models of diamond multi-testers that employ both thermal and electrical conductivity: Multi Plus by GemTrue and Multi Tester III by Presidium. All six samples that showed uncompensated boron in their FTIR spectra consistently tested as ‘moissanite’ on both diamond multi-testers, indicating they are semi-conductors of electricity. However, the sample that did not reveal any uncompensated boron in its FTIR spectrum tested as ‘diamond’ on both of the devices.

A second round of experiments using both multi-testers

was then performed to check whether different areas of an individual sample varied in electrical conductivity. Several showed a mixture of ‘moissanite’ and ‘diamond’ results on both testers, depending on which part of the sample was tested (Table V). This is apparently due to the presence of growth zones containing different concentrations of uncompensated boron (cf. Eaton-Magaña *et al.* 2017). Conversely, the specimen that tested as ‘diamond’ gave consistent results regardless of the specific area that was targeted.

Table IV: HPHT-grown synthetic diamond samples tested for this study.

Sample no.	Weight (ct)	Shape	Equivalent colour	Equivalent clarity	Boron detected by IR	Semi-conductor of electricity
1	1.58	Cushion	D	I ₁	Yes	Yes
2	1.10	Round	D	VS ₂	Yes	Yes
3	1.04	Oval	D	VS ₁	Yes	Yes
4	1.00	Pear	D	VS ₂	Yes	Yes
5	0.34	Cushion	E	SI ₂	Yes	Yes
6	0.30	Cushion	E	SI ₁	No	No
7	0.35	Round	F	SI ₁	Yes	Yes

Table V: Results obtained with the diamond multi-testers.*

Instrument	Multi Plus by GemTrue					Multi Tester III by Presidium				
Test no.	1	2	3	4	5	1	2	3	4	5
Sample no.										
1	Moiss	Moiss	Moiss	Moiss	Dia	Moiss	Moiss	Moiss	Moiss	Dia
2	Moiss	Moiss	Moiss	Moiss	Dia	Moiss	Moiss	Moiss	Moiss	Dia
3	Moiss	Dia	Moiss	Dia	Moiss	Moiss	Dia	Moiss	Moiss	Moiss
4	Moiss	Moiss	Moiss	Moiss	Moiss	Moiss	Moiss	Moiss	Moiss	Moiss
5	Moiss	Moiss	Moiss	Moiss	Moiss	Moiss	Moiss	Moiss	Moiss	Moiss
6	Dia	Dia	Dia	Dia	Dia	Dia	Dia	Dia	Dia	Dia
7	Moiss	Moiss	Moiss	Dia	Moiss	Moiss	Moiss	Moiss	Dia	Moiss

* The samples were tested in a consistent pattern with each tester: (1) centre of table, (2) 12 o'clock position, (3) 9 o'clock position, (4) 6 o'clock position and (5) 3 o'clock position of the table. Abbreviations: Dia = 'Diamond', Moiss = 'Moissanite'.

Clearly, despite lacking any blue colour tinge, HPHT synthetic diamonds equivalent to D–F colour grades can contain uncompensated boron impurities that result in enough electrical conductivity for them to test as ‘moissanite’ on diamond multi-testers. This should be kept in mind by anyone using such probes to test their inventory. In addition, results may vary depending on the specific places on a sample that are tested, and therefore it is advisable to probe different areas of a stone. Electrical conductivity is not included on laboratory-grown diamond reports and must be tested for independently. As stated by Griffith and Dupuy (2021, pp. 576–577), it is important to emphasise the following: ‘To avoid misidentification, it is advisable to perform further tests and observations (such as checking for single vs double refraction and observing UV fluorescence and phosphorescence) on all samples that give a “moissanite” result with such testers.’

Acknowledgements: Thanks to Noam Lenzini and Pandora Maloney of the World Gemological Institute, Hatton Garden, London, for collecting the FTIR spectra.

Julia Griffith FGA DGA (julia@thegemac.com)

The Gem Academy
Online Education, UK

References

- Eaton-Magana, S., Shigley, J.E. & Breeding, C.M. 2017. Observations on HPHT-grown synthetic diamonds: A review. *Gems & Gemology*, **53**(3), 262–284, <https://doi.org/10.5741/gems.53.3.262>.
- Griffith, J. & Dupuy, H. 2021. Gem Notes: Near-colourless HPHT-grown synthetic diamonds that test as synthetic moissanite. *Journal of Gemmology*, **37**(6), 575–577, <https://doi.org/10.15506/JoG.2021.37.6.575>.

Polymer Carving Imitating Dickite

The authors recently encountered a yellow carving (Figure 27) resembling dickite or perhaps talc, such as documented for another piece from the same collection (Tay *et al.* 2023). However, this one turned out to be much different.

When handled, the 3,550.6 g carving seemed rather heavy for its size and had a plastic-like feel. When examined with a 10 × loupe, small rounded beads were visible along grooves in the carving (Figure 28), and some parts showed specks of white inclusions. The spot RI reading was 1.55, and unlike dickite, the carving fluoresced weak chalky blue to a long-wave UV lamp (although it was inert to short-wave UV radiation).

A small amount of powder was extracted from the base of the carving for further analysis. Some of the powder fragments formed elongated white fibres, while others were very light yellow in colour. Raman spectroscopy of the powder using a Bruker Senterra instrument equipped with a red direct-diode laser (785 nm) yielded a fluorescence peak at 110 cm⁻¹, which is typical for organic matter. Similar results were obtained with a green solid-state Nd-YAG laser (532 nm), so the sample was suspected to be of organic composition.

The powder was then analysed with a Perkin-Elmer Spectrum 100 attenuated total reflectance (ATR) FTIR spectrometer in the range of 4000–600 cm⁻¹ at the Department of Pharmacy, National University of Singapore. The spectrum showed main absorption bands



Figure 27: This yellow carving (297.82 × 134.36 × 81.78 mm) shows a group of children playing in a bamboo garden and depicts fruits of longevity with ancient Chinese coins, a wheel of fortune, a lantern, a gourd and scrolls of books. Photo by Tay Thye Sun.

at 3618, 3524, 3449, 2923, 1722, 1259, 1115, 1067, 1018, 740 and 700 cm^{-1} (Figure 29). The bands between 3621 and 3395 cm^{-1} and the sharp peaks at 3618 and 3524 cm^{-1} are attributed to stretching vibrations of O–H and N–H bonds (Fleming & Williams 2019; Pretsch *et al.* 2020). The intense band at 1722 cm^{-1} has been attributed to the characteristic stretching vibration of C=O bonds, the band at 2923 cm^{-1} is from aliphatic C–H stretching, and the peaks from 1259 to 1018 cm^{-1} have been assigned to the stretching frequency of C–O bonds (Pretsch *et al.* 2020). A search of the Fluka FTIR spectral library (supplied with the PerkinElmer Spectrum IR 10.6 software) yielded dibutyl phthalate and pivaloyl cyanide with search scores of 0.61 and 0.53, respectively (with 1 being a perfect match). However, dibutyl phthalate is an oil (Wypych 2013) and pivaloyl cyanide is a colourless liquid (Sperber & Fricano 2002), whereas the sample is solid. Hence, the identity of the carving remained inconclusive.

Next, a pressed pellet containing 1 mg of the powdered sample mixed with 100 mg of potassium bromide (KBr) was prepared and analysed with a Bruker Alpha FTIR spectrometer in the range of 4000–400 cm^{-1} (resolution 4 cm^{-1}). The results were similar to the ATR FTIR spectrum, with main absorption bands at 3621, 3526, 3465, 3395, 1727, 1119, 1075, 1022 and 609 cm^{-1} (Figure 30). An automated search of Bruker's Opus 7.2 spectral library yielded a single result of acrylic resin, but the hit quality of 177 was low (a hit score of 1,000 is a perfect match).

Based on the results of the FTIR analyses, the yellow carving consists of a mixture of organic components, including one or more polymers (e.g. dibutyl



Figure 28: Viewed with 10× magnification, small rounded beads are seen along grooves in the carving in Figure 27. Photo by Tay Thye Sun.

phthalate), but determination of the exact composition of the sample would require further analysis.

Acknowledgement: Many thanks to Bill Loh for allowing the sample to be analysed.

TAY Thye Sun ^{FGA}¹ (tay@gem.com.sg),

Prof. Dr Leander Franz²,

Prof. Dr Koh Hwee Ling³,

Eng Chun Heng³ and Loke Hui Ying ^{FGA}¹

¹Far East Gemological Laboratory, Singapore

²University of Basel, Switzerland

³National University of Singapore

References

- Fleming, I. & Williams, D. 2019. Infrared and Raman spectra. In: *Spectroscopic Methods in Organic Chemistry*. Springer Nature, Cham, Switzerland, 85–121, https://doi.org/10.1007/978-3-030-18252-6_3.

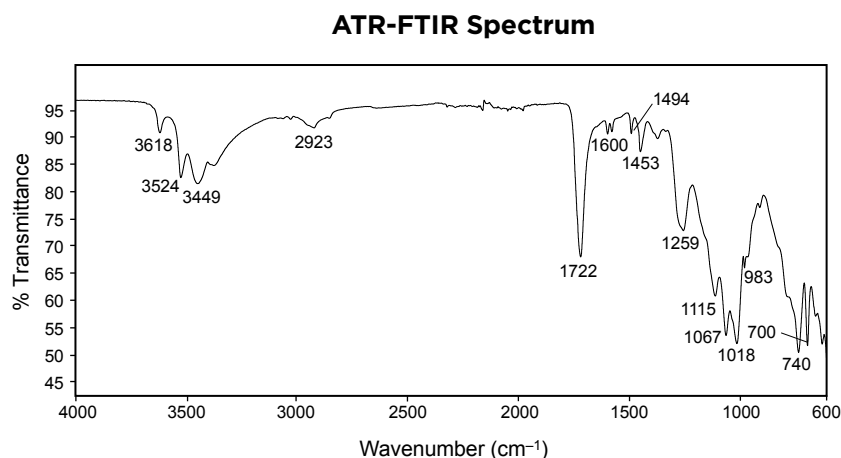


Figure 29: The ATR-FTIR spectrum of powder from the carving shows features associated with organic compounds.

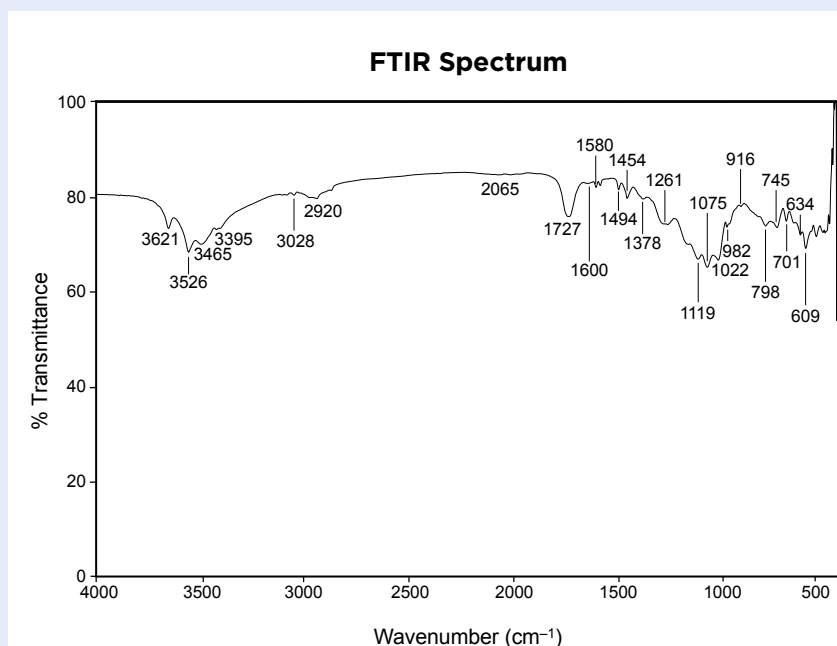


Figure 30: The FTIR spectrum of a KBr pressed pellet containing powder from the carving also shows features consistent with organic compounds.

Pretsch, E., Bühlmann, P. & Badertscher, M. 2020. IR spectroscopy. In: *Structure Determination of Organic Compounds*. Springer-Verlag, Berlin, Germany, 307–373, https://doi.org/10.1007/978-3-662-62439-5_7.

Sperber, N. & Fricano, R. 2002. The reaction of tributylacetyl chloride and anhydrous cuprous cyanide. *Journal of the American Chemical Society*, **72**(6), 2792–2793, <https://doi.org/10.1021/ja01162a531>.

Tay, T.S., Franz, L., Ling, K.H. & Li, J. 2023. Gem Notes: A Chinese seal stone consisting of yellow talc. *Journal of Gemmology*, **38**(5), 424–426, <https://doi.org/10.15506/jog.2023.38.5.424>.

Wypych, A. 2013. Phthalates. In: *Plasticizers Databook*. ChemTec Publishing, Toronto, Ontario, Canada, 387–510, <https://doi.org/10.1016/b978-1-895198-58-4.50026-2>.

Synthetic Ruby and Sapphire **Produced by the Kyropoulos Method**

The Kyropoulos method, proposed by scientist Dr Spyro Kyropoulos in Germany, was developed at the beginning of the 20th century to grow large single crystals for industrial use (Bliss 2004). In recent years, the Kyropoulos technique has evolved to yield single crystals of synthetic corundum weighing up to 200 kg. In addition, using this method it is possible to produce coloured synthetic corundum by doping with various transition elements. As an example, for use in a European research project (Nehari *et al.* 2011), the company RSA produced Ti^{3+} -doped, optical-quality reddish orange Kyropoulos synthetic sapphires weighing 5 kg, with a diameter of 100 mm, to use as a laser crystal. Also, BIEL Crystal of Shenzhen, China, currently produces Kyropoulos boules in pink, red, yellow, bright green and bright blue colours (<https://www.bielcrystal.com/en/business#materials>).

To produce synthetic corundum by the Kyropoulos technique, a melt-growth apparatus similar to that of the Czochralski method is used. Synthetic corundum fragments produced by the Verneuil method are used as a starting material. They are melted in a tungsten crucible, and a cooled seed crystal is lowered into the melt. Due to the high thermal conductivity of corundum, this causes spontaneous crystal growth. The growing crystal enlarges until it almost touches the crucible wall and then it is slowly pulled out of the melt. By pulling and turning the growing crystal, while slowly lowering the temperature of the melt, the boule grows towards the bottom without touching the crucible wall. Compared to the Czochralski technique, the Kyropoulos method uses a very low thermal gradient. The main advantage is that very large crystals can be produced at a low cost as compared to the



Figure 31: Five samples of synthetic corundum produced by the Kyropoulos method in Russia were examined for this study: four synthetic rubies (left) and a pink synthetic sapphire (top centre). For comparison, we also examined the two synthetic rubies on the right, which were produced in Idar-Oberstein by the Kyropoulos method in a modified Czochralski apparatus using natural rubies from East Africa (such as those at bottom right) as starting material. The faceted gems range from 1.52 to 18.69 ct. Photo by T. Stephan.

Verneuil method. Colourless Kyropoulos sapphires, for example, are offered for approximately USD60/kg on the Chinese market.

For the first time, in October 2022, the authors received faceted synthetic corundum grown by the Kyropoulos method. We investigated four synthetic rubies and one reportedly Ti^{3+} -doped synthetic pink sapphire that were produced in Russia. For comparison, we also examined two synthetic rubies produced in Idar-Oberstein, Germany, by the Kyropoulos method using a modified Czochralski apparatus. Natural rubies from East Africa were used as the starting material (Figure 31).

The gemmological properties of all the samples were in the known range for natural and synthetic corundum:

$n_e = 1.760\text{--}1.762$, $n_o = 1.768\text{--}1.770$ (birefringence = 0.008) and hydrostatic SG = 3.98–4.03. Microscopic examination of the Russian-grown Kyropoulos rubies revealed gas bubbles, commonly elongated into pear-like to torpedo-like shapes (Figure 32). Often, these bubbles occurred in clusters. However, the most diagnostic internal feature in the Russian Kyropoulos rubies were skeletal, dendritic structures that not only provide evidence of synthetic origin, but also indicate production by the Kyropoulos method. These structures are the result of rapid cooling and a brief crystallisation time. The overall abundance of inclusions is unusual for synthetic corundum produced by a flame-fusion technique. In the samples produced in Idar-Oberstein, the same types of inclusions were observed but were less abundant. In the Ti^{3+} -doped

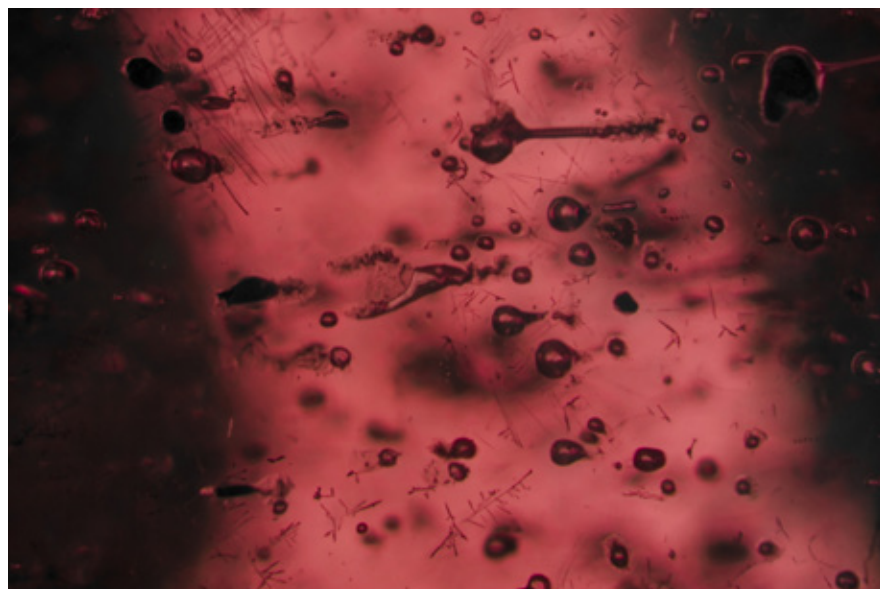


Figure 32: Microscopic characteristics of the Russian-grown Kyropoulos rubies include elongated gas bubbles, partly in clusters, and distinctive skeletal, dendritic structures. Photomicrograph by T. Stephan; magnified 20 \times .

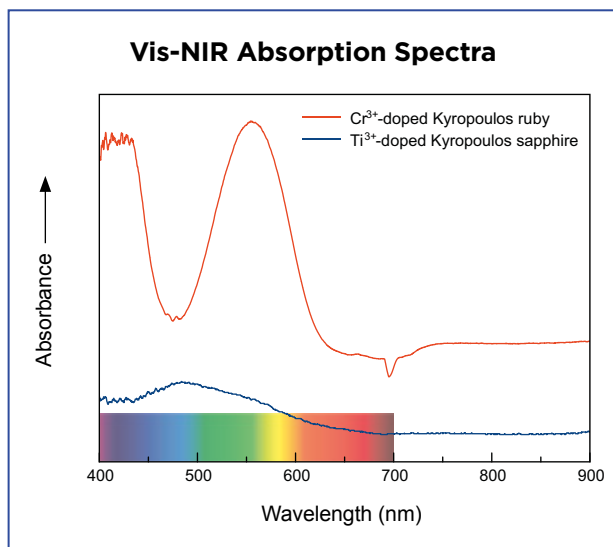


Figure 33: The Vis-NIR absorption spectrum of a Ti^{3+} -doped pink Kyropoulos sapphire is clearly different from that of a Cr^{3+} -doped Kyropoulos ruby. The spectral characteristics of Ti^{3+} provide diagnostic evidence of the material's synthetic origin, but not of the particular laboratory synthesis method.

synthetic sapphire, however, no inclusions were visible with a standard gemmological microscope at magnifications up to $115\times$. However, the material was easily identified as synthetic by its absorption and photoluminescence spectra (Figures 33 and 34, respectively), due to the presence of Ti^{3+} -related features. By contrast, the synthetic rubies we examined were coloured by Cr^{3+} , as is typical for ruby and pink sapphire. None of the samples contained the curved striae that are typically seen in melt-grown synthetic corundum.

Even though faceted Kyropoulos synthetic corundum has rarely been observed in the gem trade, the technical progress in crystal size and colouration is remarkable. Due to the low price of these products, it is possible that

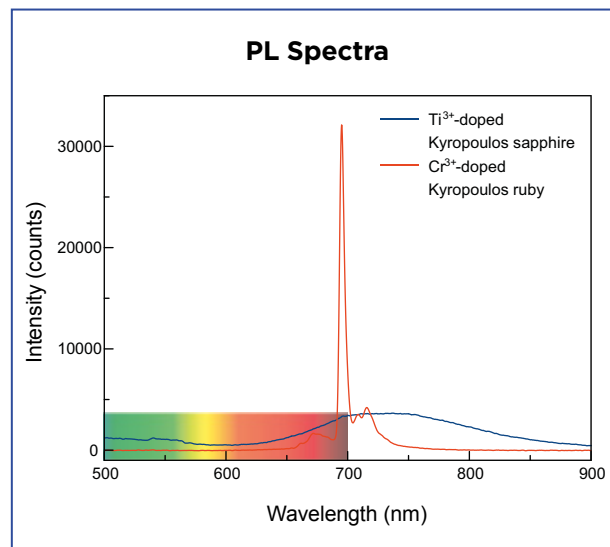


Figure 34: Comparison of the photoluminescence spectra for a Ti^{3+} -doped pink Kyropoulos sapphire and a Cr^{3+} -doped Kyropoulos ruby also reveals distinct differences. Again, the PL spectrum of the Ti^{3+} -doped pink sample provides diagnostic evidence for its synthetic origin, but not for the particular synthesis method.

they could become an alternative to Verneuil synthetic corundum in the gem trade. Our initial examination of the samples described here shows that it is possible to identify Kyropoulos synthetic corundum by standard gemmological testing even if, as for the Ti^{3+} -doped sapphire, a clear assignment to the production technique is not always possible.

Dr Tom Stephan (t.stephan@dgemg.com)
German Gemmological Association
Idar-Oberstein, Germany

Dr habil. Lothar Ackermann
Laser Crystal Consult
Idar-Oberstein, Germany

References

Bliss, D.F. 2004. Evolution and application of the Kyropoulos crystal growth method. In: Feigelson, R.S. (ed), *50 Years Progress in Crystal Growth: A Reprint Collection*. Elsevier, Amsterdam, The Netherlands, 29–34.

Nehari, A., Brenier, A., Panzer, G., Lebbou, K., Godfroy, J., Labor, S., Legal, H., Chériaux, G. *et al.* 2011. Ti-doped sapphire (Al_2O_3) single crystals grown by the Kyropoulos technique and optical characterizations. *Crystal Growth & Design*, **11**(2), 445–448, <https://doi.org/10.1021/cg101190q>.

Join us on social media to keep up-to-date with the latest news, events and offers from Gem-A



facebook.com/GemAofGB



@GemAofGB



linkd.in/1GisBTP



Instagram: @gemaofgb



WeChat: Scan the QR code to add us on WeChat



Characterisation and *In Situ* Age Determination of Zircon Inclusions in Sapphires from Muling, North-East China

Yimiao Liu, Ren Lu and Shaokui Pan

ABSTRACT: In recent decades, blue and fancy-colour sapphires have been gathered from secondary deposits derived from Tertiary basalts in the Muling area of north-eastern China. In this article, zircon inclusions in the blue sapphires were studied to characterise their morphology and structure, as well as to obtain the age of the host sapphires. The zircon inclusions in the studied samples were euhedral and transparent, and their dominant morphology was similar to that of typical zircon inclusions in sapphires associated with alkali basalts. Raman spectroscopy of the zircons showed only slight radiation damage, and cathodoluminescence images revealed two distinctive zoning patterns (in their cores and rims). LA-ICP-MS analyses of the zircon rims showed typical magmatic Th/U ratios. *In situ* U-Pb dating of the zircon rims yielded ages of 9 to 8 Ma—which is the inferred upper limit of the formation age of the host sapphires—while cores had much older ages that exceeded 110 Ma (i.e. an inherited age component). The 9–8 Ma sapphire age coincides with Late Miocene basaltic eruptions in the Dunhua-Mishan graben. Age dating of zircon inclusions in the Muling sapphires helps elucidate their geological origin and provides useful information for the provenance determination of gem corundum.

The Journal of Gemmology, 38(6), 2023, pp. 564–581, <https://doi.org/10.15506/JoG.2023.38.6.564>
© 2023 Gem-A (The Gemmological Association of Great Britain)

Muling is a small city located in the eastern part of Heilongjiang Province in north-eastern China, near the border with Russia. Secondary (alluvial) deposits in this area have produced fine gem-quality corundum (e.g. Figure 1) exhibiting a wide variety of colours and high transparency (Liu & Lu 2022). During the 1980s and 1990s, ruby and sapphire deposits throughout China were briefly documented by various researchers (Keller & Keller 1986; Keller & Wang 1986; Wang 1988; Guo *et al.* 1992; Galibert & Hughes 1995). The gem corundum deposits near Muling were noted during the same period (Su 1990), but research on them has been relatively limited. Their geological characteristics, as well as the mineralogical features of the gem corundum, were initially



Figure 1: A 0.5 ct blue sapphire from Muling, China, exemplifies some of the fine-quality gem material available from this locality. Photo by Y. Liu.



Figure 2: Rough gem corundum from Muling exhibits various colours and forms. Some of the material is subhedral to euhedral with hexagonal outlines, while other pieces have a more rounded appearance, indicating erosion and transport. Photo by Y. Liu.

studied by Jianxun Sun, who prepared a geological survey of Heilongjiang Province (Sun 1995; Sun *et al.* 2005). Besides corundum, other gem materials found in these deposits—including zircon, garnet and spinel—have been described by various researchers (Qiu *et al.* 2007; Chen *et al.* 2011, 2013; Hu *et al.* 2022).

Muling corundum displays the most diverse colour range of the known ruby and sapphire deposits in China (e.g. Figure 2), which is interesting for both scientific and commercial reasons. However, local environmental policy and the short working season have restricted most mining activities in this region. There has been no commercial production of gem materials in the Muling area for many years, and only sporadic digging has been carried out by local villagers. To the authors' knowledge, the rough rubies and sapphires from this area typically range from 0.2 to 0.6 g.

All the gem corundum from Muling has been found in secondary deposits, and the source rocks of the rubies and sapphires remain unknown. Several possibilities for the origin of the corundum have been proposed, including correlation with the Tertiary basaltic rocks in the area (Sun *et al.* 2005; Qiu *et al.* 2007; Chen *et al.* 2011). The present authors recently documented the gemmological characteristics of Muling corundum, including the inclusion assemblage, spectral features and chemical characteristics (Liu & Lu 2022), which indicate that the geological origins of the different colour varieties could be complex (i.e. both metasomatic and magmatic origins). More information is needed to unravel the genetic origin of this corundum.

Fortunately, zircon inclusions provide an opportunity for further investigation of the age and geological formation environment of the host sapphires. As a relatively reliable geochronometer, U-Pb age dating of zircon is widely used in geological studies (see Box A). With this method, it is possible to reliably date mineral and geological processes (Corfu 2003). In recent years, *in situ* U-Pb age dating of inclusions in rubies and sapphires has been employed in gemmology (Link 2015; Akinin *et al.* 2017; Elmaleh *et al.* 2019; Krzemnicki *et al.* 2019; Phyo *et al.* 2020; Xu & Krzemnicki 2021).

Zircon is present as a mineral inclusion in corundum of all geological types (Giuliani *et al.* 2014; Palke *et al.* 2019a, b). Encapsulation of zircon inclusions in the corundum host prevents compositional changes (e.g. Pb loss), thus enabling the determination of an accurate age for the upper limit of ruby and sapphire formation. Extensive geochronological information on worldwide corundum deposits has been provided by numerous geological and gemmological studies (see Appendix I in *The Journal's* online data depository). Thus, age data on gem corundum can be helpful for provenance determination by correlating with distinct formation eras (such as for 'Kashmir-like' sapphires from Madagascar; Bui *et al.* 2012; Palke *et al.* 2019a). Furthermore, events in the earth's evolutionary history can be correlated from a new gemmological perspective with the increased availability of geochronological data on gem materials.

In this article, zircon inclusions in blue sapphires from Muling are characterised in detail by optical microscopy and scanning electron microscopy, as well

BOX A: AGE DATING OF ZIRCON

Zircon (ZrSiO_4) is one of the best minerals for determining an accurate estimate of geological age (or geochronometer; Harley & Kelly 2007). Zircon has an affinity for attracting elements such as uranium into its crystal structure, while lead ions (Pb^{2+}) are not usually present at measureable concentrations during its formation (ideally below the detection limit of LA-ICP-MS; Link 2015). This is because the ionic radius of Zr^{4+} (0.80–0.92 Å) is relatively compatible with U^{4+} (1.03–1.09 Å), while the substitution of Pb^{2+} (1.33–1.37 Å) will cause serious lattice deformation. Other bonding properties such as coordination, electronegativity and cation exchange also restrain this substitution.

After zircon crystallises, two long-lived isotopes of uranium, ^{238}U and ^{235}U , naturally decay into the daughter elements ^{206}Pb and ^{207}Pb , respectively. Distortion of the zircon lattice increases with the accumulation of Pb, along with radioactive decay damage due to alpha particles, until the crystal structure becomes amorphous. The half-lives of the two radioactive decay chains $^{238}\text{U} \rightarrow ^{206}\text{Pb}$ and $^{235}\text{U} \rightarrow ^{207}\text{Pb}$ are constant at 4.468 and 0.704 billion years, respectively (Machado & Simonetti 2001). By measuring the U concentration and the radiogenic Pb concentration in zircon, one can precisely calculate two U-Pb ages: $^{206}\text{Pb}/^{238}\text{U}$ and $^{207}\text{Pb}/^{235}\text{U}$.

G. W. Wetherill developed the concordia diagram (see Figure A-1), so named because ‘Where these two ages are found to be equal to one another, the ages are said to be “concordant”. When they are unequal, they are said to be “discordant”’ (Wetherill 1956, p. 320). This provides valuable information for the plausibility of the calculated ages. The curved concordia line is the geometric locus of all points whose two U-Pb ages are concordant. In general, when both ages of a sample are deemed concordant, it represents a closed system, without loss or gain of U or Pb since the time of crystallisation. The age of a sample is shown as an ellipse, the shape and size of which are determined by the amount of its error (1σ or 2σ). Mean square weighted deviation (MSWD) is a statistical method which measures the amount of fit between the observed scatter of the ages and the expected scatter calculated from the assigned errors and correlations. If $\text{MSWD} > 1$, the systematic bias of at least one of the data points is greater than random

scatter (Villa & Hanchar 2017).

Some samples’ plotted ages may deviate from the concordia line; instead, they form a straight discordia line, which intersects the curved concordia line at two points (again, see Figure A-1). Causes of discordance are extensive. A zircon may yield discordant U-Pb ages due to its intrinsic features and geological history. It is well known that zircon is vulnerable to lead loss (i.e. episodic or continuous diffusion of Pb out of the system), which results in discordant $^{206}\text{Pb}/^{238}\text{U}$ and $^{207}\text{Pb}/^{235}\text{U}$ ages (Holmes 1954; Tollstrup *et al.* 2012; Villa & Hanchar 2017). The age of a zircon sample is related to the uncertainty in measured ages, excluding the possible influence of analytical procedures (Machado & Simonetti 2001).

For decades, laser ablation inductively coupled plasma mass spectrometry (LA-ICP-MS) has been a well-established method for measuring U and Pb isotopes (Scott & Gauthier 1996; Horn *et al.* 2000). In this study, LA-ICP-MS analyses were conducted *in situ* and created micro-sized ablation spots, which represent minimal damage to the samples. Although the zircon inclusions we analysed were difficult to date precisely due to their small size, the high spatial resolution of LA-ICP-MS can provide precise U-Pb dating, as well as the measurement of trace elements and rare-earth elements (REEs). During the

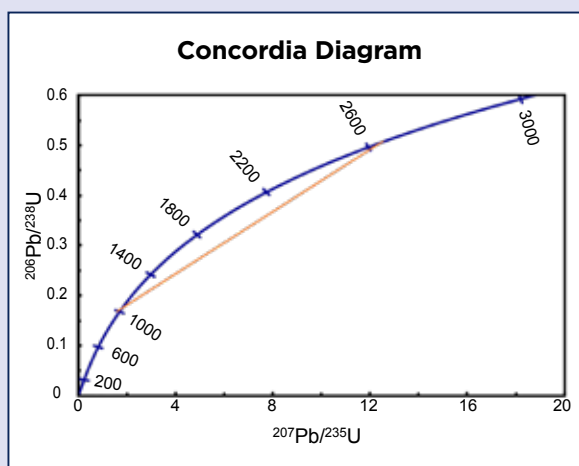


Figure A-1: In this concordia diagram (modified after Wetherill 1956), the dark blue curve with labelled ages (given in million years) is referred to as the concordia curve, along which the two ages acquired by $^{206}\text{Pb}/^{238}\text{U}$ and $^{207}\text{Pb}/^{235}\text{U}$ are in agreement. The red line is an example of discordia, which occurs when the two age determinations are unequal due to a sample's geological history, Pb loss or other factors.

past decade, LA-ICP-MS has been more commonly applied (Hirata & Nesbitt 1995; Günther *et al.* 1997; Horn *et al.* 2000; Jackson *et al.* 2004; Tollstrup *et al.* 2012; Villa & Hanchar 2017), and has evolved to yield $^{206}\text{Pb}/^{238}\text{U}$ and $^{207}\text{Pb}/^{235}\text{U}$ ages with a precision of 0.3–3% (Machado & Simonetti 2001). Laser-induced elemental fractionation is one of the fundamental limiting uncertainties in U-Pb geochronology. To eliminate the fractionation, the laser should be of a shorter wavelength and/or pulse width (Guillong *et al.* 2003; Horn 2008; Horstwood 2008).

There are other large instruments, such as the thermal ionisation mass spectrometer (TIMS), secondary ion mass spectrometer (SIMS), LA-multi-collector-ICP-MS and high resolution-ICP-MS, which can be powerful tools for U-Pb dating (Halliday *et al.* 1998; Machado & Simonetti 2001; Yuan *et al.* 2004;

Gerdes & Zeh 2006; Tollstrup *et al.* 2012; Sakata *et al.* 2014). These methods can yield highly precise data (Halliday *et al.* 1998; Yuan *et al.* 2004), but they show various disadvantages for the U-Pb age dating of gems. For example, these instruments are not easily accessible, and their operating costs are much higher than LA-ICP-MS. In addition, TIMS will destroy the sample. The acquisition volume of samples by the SIMS technique is so small that it may be affected by the interference of common Pb from the environment (Machado & Simonetti 2001; Yuan *et al.* 2004; Gerdes & Zeh 2006). LA-ICP-MS, however, is capable of dating zircons with relatively high accuracy, although it may be affected by spatial resolution. Based on this study, with the assistance of CL imaging, LA-ICP-MS was the technique of choice.

as by Raman spectroscopy. *In situ* U-Pb age dating was then performed on three surface-reaching inclusions to obtain the formation age of the host sapphires. Finally, these data are used to help unravel the geological origin of Muling gem corundum and elucidate its chronological position in the timeline of the world's ruby and sapphire deposits.

GEOLOGICAL SETTING

The Muling area is located along the northern section of the Dunhua-Mishan fault (Figure 3). This large thrust fault trends N50°E (Wang & Dou 1997), and juxtaposes the Jiamusi block on the north-west (where Muling is located) against the Khanka block on the south-east (Li *et al.* 2023). These blocks formed part of the southern margin of the Central Asian Orogenic Belt before drifting further south to their current location after about 500 Ma (Li *et al.* 2023). During the Palaeozoic, the tectonic evolution of this region was governed by the Paleo-Asian Ocean tectonic regime. Since early Mesozoic time, this area has been strongly overprinted by circum-Pacific tectonic events (Wang *et al.* 2014; Li *et al.* 2020). The eastern margin of the Jiamusi block experienced accretion processes caused by paleo-Pacific plate subduction in the Middle Jurassic to Early Cretaceous (approximately 165–128 Ma), forming the Raohe accretionary complex (Li *et al.* 2020). Subsequently, north-eastern China entered a period of magmatic dormancy until the widespread eruption of the Cenozoic basalts (Pan *et al.* 2015). Basaltic eruptions in the Dunhua-Mishan

graben began at about 44.9 Ma and ended 5,140 years ago (Wang *et al.* 2001; Pan *et al.* 2015). The most intense volcanic eruptions occurred in the Tertiary period (i.e. during the Miocene epoch, around 16–7 Ma; Shen 1987). Volcanic rocks in the Dunhua-Mishan rift are mainly tholeiites, alkaline olivine basalts and basanites (Wang *et al.* 2001; Xu *et al.* 2013).

Muling gem corundum shows a wide range of colouration—including blue, green, yellow and reddish hues (e.g. pink, orangey pink, purple and purplish red)—and therefore is not typical of a 'BGY' (blue, green and yellow) magmatic corundum suite (Liu & Lu 2022). The corundum-bearing layers lie beneath soft sandy-clay soil and fertile topsoil. The associated heavy-mineral suite includes zircon, black spinel, magnetite, ilmenite, augite, garnet (almandine and pyrope) and hematite. U-Pb dating of zircon megacrysts from Muling alluvial deposits yielded an age of 9.4 Ma (Chen *et al.* 2011). It is assumed that the gem-bearing placers are derived from the weathering of the Tertiary basalts in the area (Sun *et al.* 2005; Qiu *et al.* 2007), but the exact source and formation conditions of the gem corundum are unknown.

MATERIALS AND METHODS

Numerous sapphire samples were obtained during and after three field trips by the authors to Muling between 2014 and 2018. Some of the samples were collected by the authors from placer deposits, and others were donated by Aijun Yi—the former director of mineral resource



Figure 3: The distribution of Cenozoic (about 28–21 Ma) volcanic rocks in north-eastern China is shown on this map (adapted from Liu *et al.* 2001). The Muling gem-producing area is indicated by the red rectangle.

administration of the Muling government and a lifetime resident of the region—who purchased the sapphires from local farmers. The resulting corundum collection consisted of transparent pieces showing various colours and shapes (see Figure 2 and Liu & Lu 2022).

Zircon inclusions were found in only a few deep blue sapphire samples after thorough examinations with an optical microscope and Raman micro-spectroscopy. We used a Bruker Senterra confocal Raman microscope with a 532 nm laser at the Gem Laboratory of Chemical and Spectral Testing, Gemmological Institute of China University of Geosciences (Wuhan). The magnification of the objective lens was $20\times$. The laser power was 20 mW and the acquisition time was 10 s. The spectral resolution was $3\text{--}5\text{ cm}^{-1}$. A single-crystal silicon wafer was analysed to calibrate the Raman shift (521 cm^{-1}); three scans were collected and averaged.

From our examination of 88 deep-blue sapphire samples, three of them (samples nos. 28, 29 and 35) were found to contain zircon inclusions with good potential for reliable age dating. One zircon inclusion in each sample was selected that measured approximately 150 μm long and 50 μm wide and was entirely included

within the sapphire host without being located near any fractures (e.g. Figure 4), thus minimising any possible interaction with permeating fluids or other contamination. The three sapphires were sawn and polished to expose the largest cross-section of each zircon inclusion on the surface.

Growth zoning in the three zircon inclusions was revealed with a Hitachi TM4000 scanning electron microscope (SEM) at the Techcomp (China) Ltd Beijing laboratory. Backscattered electron (BSE) imaging was performed to locate the position of zircon inclusions, and their growth zoning was observed in cathodoluminescence (CL) mode. For CL imaging, the electron beam was emitted from a pre-centred cartridge using a tungsten filament with an accelerating voltage of 10 kV and a current of about 90 μ A. A high-sensitivity low-vacuum detector was utilised to avoid interference between secondary electrons. The sample was placed at a working distance of 10 mm from the detector.

To characterise heterogeneities in the zircon inclusions at micro-scale resolution, additional Raman analyses were performed after the CL imaging (and chemical analysis; see next page). The locations of the

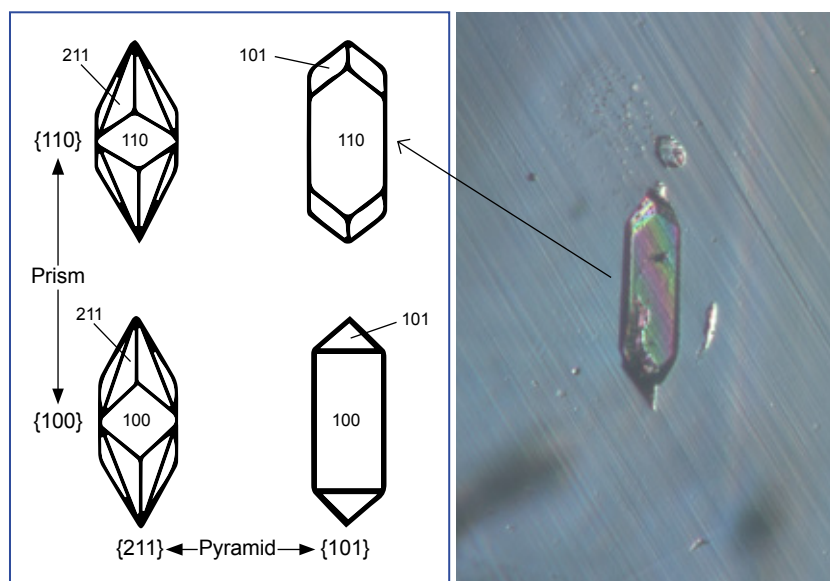


Figure 4: Zircon inclusions in blue sapphires from Muling, such as the example shown here in cross-polarised light, form euhedral crystals dominated by {110} prism and {101} pyramid forms. The accompanying drawings from Pupin (1980) illustrate the morphologies resulting from the prevalence of different prismatic and pyramidal forms. Photomicrograph by Y. Liu; image width 0.53 mm.

Raman analyses were chosen to avoid the spots from laser ablation and to sample the different growth zones within the three zircon inclusions. The analyses were performed with a Horiba LabRAM HR Evolution Raman spectrometer at the State Key Laboratory of Geological Processes and Mineral Resources of China University of Geosciences (Wuhan). The instrumentation included a 532 nm laser, a 100 \times objective and a holographic grating (1,800 grooves/mm). The lateral resolution was better than 1 μ m and met the requirement for the high spatial resolution needed for this study. The spectral range was 80–2000 cm^{-1} and the resolution was $\leq 0.65 \text{ cm}^{-1}$. The acquisition time was 10 s and three accumulations were obtained. To evaluate the degree of zircon metamictisation, the full width at half maximum (FWHM) of the Raman band at around 1010 cm^{-1} was quantitatively analysed, and the FWHM values were corrected for instrumental broadening using the empirical formula of Váczi (2014). The influence of the apparatus function on the spectra was considered (Nasdala *et al.* 2001). Band fitting was done after appropriate background correction, assuming Lorentzian–Gaussian band shapes.

For age dating, *in situ* U–Pb ages of different growth zones in the three zircon inclusions were acquired with LA-ICP-MS at the State Key Laboratory of Geological Processes and Mineral Resources, China University of Geosciences (Wuhan). This method of obtaining data for age dating is the best choice for gem labs due to its relatively low cost combined with high precision, accuracy, spatial resolution and efficiency, and is a well-established and frequently employed method for measuring elemental isotopes and their ratios (Machado & Simonetti 2001). Laser sampling was performed using a system equipped with a 193 nm ArF excimer laser.

An Agilent 7900a ICP-MS was employed to acquire ion-signal intensities. The ablation spot size was limited to 35 μ m. A low-pulse frequency of 5 Hz was used to keep time-dependent elemental fractionation at a relatively low level (Günther & Heinrich 1999). The laser energy density (fluence) was set to 10 J/cm². Each analysis incorporated approximately 20 s of background acquisition (gas blank) followed by 50 s of data acquisition from the sample. Agilent ChemStation software was used for the acquisition of each analysis. Counts for ²⁹Si, ⁴⁹Ti, ⁸⁹Y, ⁹¹Zr, ⁹³Nb, ¹³⁹La, ¹⁴⁰Ce, ¹⁴¹Pr, ¹⁴³Nb, ¹⁴⁷Sm, ¹⁵¹Eu, ¹⁵⁵Gd, ¹⁵⁹Tb, ¹⁶³Dy, ¹⁶⁵Ho, ¹⁶⁶Er, ¹⁶⁹Tm, ¹⁷³Yb, ¹⁷⁵Lu, ¹⁷⁹Hf, ¹⁸¹Ta, ²⁰²Hg, ²⁰⁴Pb, ²⁰⁶Pb, ²⁰⁷Pb, ²⁰⁸Pb, ²³²Th and ²³⁸U were collected in time-resolved, peak-hopping mode. The dwell time of key measured isotopes was: 10 ms for ²⁰²Hg; 15 ms for ²³²Th; 20 ms for ²⁰⁴Pb, ²⁰⁸Pb and ²³⁸U; and 25 ms for ²⁰⁶Pb and ²⁰⁷Pb. Off-line selection and integration of background and ablation signals, time-drift correction and quantitative calibration for U–Pb dating were performed using ICPMSDataCal software developed by Liu *et al.* (2010). Concordia diagrams were made using Isoplot3 macros for Microsoft Excel (Ludwig 2003).

To avoid contamination effects from the host corundum, the analysed signal was carefully monitored for any sudden change in indicative elements, such as Si. This element was particularly useful because zircon (ZrSiO₄) is a silicate mineral and thus has an abundance of Si, whereas corundum contains only low traces of Si. The collected data were used for analysis only when the area of real-time-monitored Si showed a flat plateau. The stable region of the isotopic ratios (e.g. ²⁰⁶Pb/²³⁸U) of each spot was selected for integration. Zircon GJ-1 reference material was used as the primary

standard ($^{206}\text{Pb}/^{238}\text{U}$ age of 609.7 ± 1.8 Ma; Jackson *et al.* 2004), and zircon 91500 was used as an external reference material for correcting mass discrimination ($^{206}\text{Pb}/^{238}\text{U}$ age of 1062.4 ± 0.4 Ma; Wiedenbeck *et al.* 1995). Common Pb is low in zircon inclusions, so no common-Pb correction was made.

It is worth noting that a couple of factors could affect the accuracy of measured ages. Except for Pb and U loss (or increase) in zircon, and instrumental problems, the inherent age of the sample will influence the age dating (Machado & Simonetti 2001). Since ^{207}Pb is generally considered to be the least abundant isotope of zircon, it is also the isotope that is most impacted by even minute amounts of common Pb (Garnier *et al.* 2005; Litvinenko *et al.* 2020). For young zircon, the small amount of radiogenic ^{207}Pb is difficult to measure (because the Pb content may be close to the detection limit), and the signal-to-noise ratio of ^{206}Pb and ^{207}Pb may be poor during laser ablation (Hirata & Nesbitt 1995; Iizuka & Hirata 2004; Sakata *et al.* 2014). As a result, the accuracy of $^{207}\text{Pb}/^{235}\text{U}$ ages of young zircon can be significantly impacted (Garnier *et al.* 2005). Therefore, the $^{206}\text{Pb}/^{238}\text{U}$ ages (reported with 1σ error) are preferred in this study.

RESULTS AND DISCUSSION

Morphology of the Zircon Inclusions

The zircon inclusions in the Muling sapphires were colourless and transparent, indicating a low amount of metamictisation (the process by which the crystal structure of zircon is destroyed during radioactive decay, which causes it to become amorphous and opaque; Nasdala *et al.* 1998, 2003).

The zircon inclusions formed euhedral doubly terminated prismatic crystals (e.g. Figure 4). The angular relationships of zircon crystal faces indicated that the main habits were the $\{110\}$ prism and $\{101\}$ pyramid (Figure 4; cf. Pupin 1980). The composition of the crystallisation medium is thought to be a key parameter in the development of zircon crystal morphology (Benisek & Finger 1993; Corfu 2003). The dominance of the $\{110\}$ prism and the $\{101\}$ pyramid is favoured by a high abundance of alkalis, and also by the presence of certain elements (e.g. U, Th and REEs; Kostov 1973; Benisek & Finger 1993). This morphology ($\{110\}$ -dominant form) is similar to zircon inclusions in basalt-associated sapphires from the Changle area of China and from Australia (Guo *et al.* 1996; Sutherland *et al.* 1998), and differs from those in Kashmir sapphires (Xu & Krzemnicki 2021).

The well-developed euhedral crystal shapes indicate a stable formation environment when the zircons

crystallised (Rubatto & Gebauer 2000). The lack of mechanical abrasion on their surfaces indicates they did not experience a subsequent stage of weathering after crystallisation and before being incorporated as protogenetic or syngenetic inclusions (as defined by Gübelin & Koivula 1986) in the host sapphires. Thus, the final stage of zircon crystallisation is inferred to be relatively close to the initial formation of the host sapphire, constraining the maximum possible sapphire crystallisation age.

Cathodoluminescence Imaging of the Zircon Inclusions

Growth zoning and associated heterogeneities are common characteristics of natural zircon (Corfu 2003; Zeug *et al.* 2017), and these were carefully evaluated in this study. CL imaging provides high-spatial-resolution images of the interior structures of zircon (Corfu 2003). Such imagery helps locate different domains of a zircon inclusion, and this is useful when choosing the positions of Raman spectroscopic and LA-ICP-MS analyses.

In this study, we used BSE imagery to quickly locate the zircon inclusions in the sapphire samples, due to the sharp intensity contrast resulting from zircon's overall greater atomic number than the sapphire matrix (Figures 5a, c and e). Next, CL images (Figures 5b, d and f) were captured of the same areas. The interior of the zircons exhibited a clear zoning pattern under CL, with bright cores and darker rims. In addition, the irregularly shaped cores exhibited complex zoning. Oscillatory zoning was present in the rim of the zircon in sample 29 (Figure 5d), while there was no visible zoning in the rim portions of the zircons in samples 28 and 35 (Figures 5b and f).

Various CL patterns can indicate different geological processes (e.g. magmatism, metamorphism and hydrothermal alteration; Rubatto & Gebauer 2000). For example, rims with oscillatory growth zoning provide evidence of later-stage magmatic events (Corfu 2003). The oscillatory zoning mainly reflects the compositional variation of trace elements (e.g. Y, REEs, U and Th; see Tables I and II), which may relate to the magmatic differentiation process (Hoskin 2000). The rims of the zircons in samples 28 and 35 were homogeneous and free of zoning, possibly because any luminescence was quenched by high U contents (Rubatto & Gebauer 2000). Another possibility is that they formed in a relatively stable magma body with a slow crystallisation rate.

The zircon cores showed much higher CL intensity than the rims (Figures 5b, d and f). A negative correlation exists between CL intensity and the contents of U and Y in zircon (Hanchar & Rudnick 1995; Rubatto

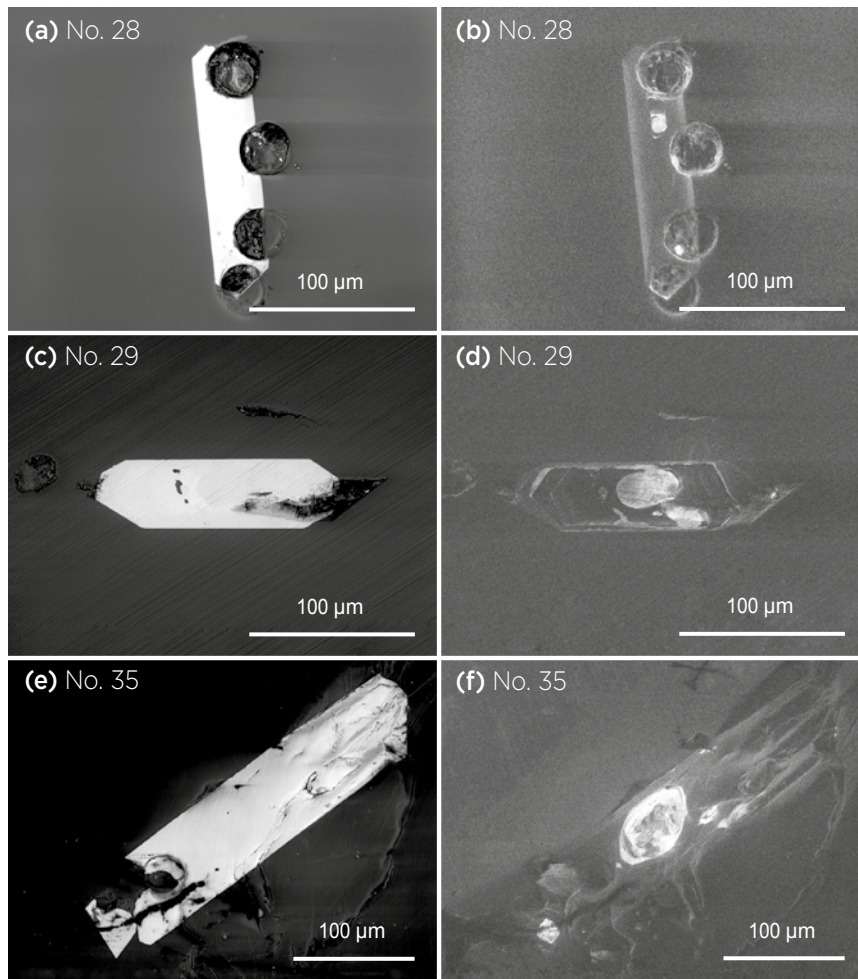


Figure 5: (a, c and e) BSE images of the three zircon inclusions analysed for this report exhibit distinct, bright patterns, while the dark background corresponds to the host sapphire. (b, d and e) Corresponding CL images reveal more structural details, including dark rims, bright cores (lower U and Y than the rims) and complex zoning in the cores. The images for sample 28 show some initial laser-ablation spots, which were not considered valid for the zircon inclusion. Images by Y. Liu; image widths are 250 μm (a–d) and 320 μm (e–f).

& Gebauer 2000). Chemical analyses (see Table II) confirmed that the bright cores in each sample exhibited lower U and Y contents than the dark rims.

Overall, the distinctive zonation of the zircon inclusions under CL indicates a possible discontinuous crystal-growth scenario.

Raman Spectral Features of the Zircon Inclusions

High-resolution Raman spectra across different regions of the zircon inclusions in samples 28, 29 and 35 are shown in Figures 6, 7 and 8, respectively. Both rim and core regions of the inclusions showed typical zircon peaks with Raman shifts of about 356 cm^{-1} (external lattice mode), 440 cm^{-1} (symmetric bending mode $\nu_2(\text{SiO}_4)$), 973 cm^{-1} (symmetric stretching mode $\nu_1(\text{SiO}_4)$) and 1010 cm^{-1} (anti-symmetric stretching mode $\nu_3(\text{SiO}_4)$; Nicola & Rutt 1974; Syme *et al.* 1977; Nasdala *et al.* 2003). The two regions (core and rim) had different characteristic peaks in the $500\text{--}900\text{ cm}^{-1}$ range, as well as significantly different peak widths of the $\nu_3(\text{SiO}_4)$ Raman band around 1010 cm^{-1} .

Table I: REE composition of zircon inclusions in three Muling sapphires.

Spot no.	28-2	29-2	29-3	35-1	35-2	35-3	35-4
Position	Rim	Core	Rim	Core	Core	Rim	Rim
Element (ppmw)							
La	0.03	bdl*	bdl	0.08	0.07	0.03	0.01
Ce	230	27	92	3	13	55	101
Pr	0.98	0.38	0.44	0.08	0.14	0.47	0.59
Nd	24	7	13	1	3	10	13
Sm	79	19	40	2	6	27	43
Eu	18.1	2.1	7.2	0.3	1.3	2.1	4.1
Gd	451	96	246	14	36	183	256
Tb	166	35	89	7	13	77	91
Dy	1893	397	1018	88	165	917	1016
Ho	627	147	350	28	58	327	337
Er	2405	660	1400	110	235	1362	1287
Tm	442	140	266	24	46	254	236
Yb	3523	1335	2240	227	410	2074	1841
Lu	542	275	384	50	81	350	302

* Abbreviation: bdl = below detection limit (i.e. 0.01 ppmw for La).

Table II: U-Pb isotopic age data from LA-ICP-MS analysis of zircon inclusions in Muling sapphires.

Spot no. ^a	Position	Y (ppmw)	Th (ppmw)	U (ppmw)	Th/U	Total Pb (ppmw)	²⁰⁷ Pb/ ²³⁵ U ($\pm 1\sigma$ error)	²⁰⁶ Pb/ ²³⁸ U ($\pm 1\sigma$ error)	²⁰⁷ Pb/ ²³⁵ U age (Ma)	²⁰⁶ Pb/ ²³⁸ U age (Ma)	Concordance ^b
28-1p	Rim	12759.6	11931.6	11912.4	1.00	24	0.0083 \pm 0.0005	0.00129 \pm 0.00003	8.4 \pm 0.5	8.4 \pm 0.2	99%
28-2	Rim	17003.6	15488.3	15401.3	1.01	28	0.0080 \pm 0.0004	0.00126 \pm 0.00001	8.2 \pm 0.4	8.1 \pm 0.1	99%
29-1	Rim	8533.7	3256.7	9407.5	0.35	15	0.0083 \pm 0.0004	0.00132 \pm 0.00002	8.4 \pm 0.4	8.5 \pm 0.1	99%
29-3	Rim	9806.8	5501.5	10482.0	0.52	18	0.0088 \pm 0.0004	0.00138 \pm 0.00002	8.9 \pm 0.4	8.9 \pm 0.1	99%
35-1p	Rim	8999.4	9419.3	11654.4	0.81	22	0.0086 \pm 0.0004	0.00134 \pm 0.00002	8.7 \pm 0.4	8.7 \pm 0.2	99%
35-2p	Rim	9630.1	7192.2	10025.0	0.72	19	0.0081 \pm 0.0005	0.00127 \pm 0.00003	8.2 \pm 0.5	8.2 \pm 0.2	99%
35-3	Rim	9242.7	2671.7	5249.9	0.51	10	0.0091 \pm 0.0007	0.00136 \pm 0.00004	9.2 \pm 0.7	8.8 \pm 0.2	95%
35-4	Rim	9511.5	9185.1	11772.1	0.78	23	0.0093 \pm 0.0004	0.00141 \pm 0.00002	9.4 \pm 0.4	9.1 \pm 0.1	96%
28-1	Core ^c	14739.5	4641.5	7517.0	0.62	13	0.0094 \pm 0.0008	0.00125 \pm 0.00004	9.5 \pm 0.8	8.1 \pm 0.2	83%
29-2	Core	4389.2	1389.7	2900.7	0.48	70	0.1438 \pm 0.0057	0.02119 \pm 0.00048	136 \pm 5	135 \pm 3	99%
35-1	Core	908.5	97.6	1813.3	0.05	35	0.1176 \pm 0.0039	0.01798 \pm 0.00024	113 \pm 4	115 \pm 2	98%
35-2	Core	1791.9	318.1	1571.5	0.20	34	0.1224 \pm 0.0046	0.01825 \pm 0.00027	117 \pm 4	117 \pm 2	99%

^a The positions of the analysis spots are shown in Figure 10.

^b Concordance is a measure of the fit between the age of the analysed spot and the curved concordia line (see Box A).

^c The analysis of spot 28-1 included both the rim and core, and the calculated data fell into the range for rims; see text for explanation.

In the spectral range of 500–900 cm⁻¹ Raman shift, a distinct set of multiple peaks was present in the Raman spectra of the rims, whereas these peaks were nearly absent from the spectra of the cores (Figures 6, 7 and 8). These emissions are from laser-induced photoluminescence caused by traces of REE³⁺ (Lenz *et al.* 2015). Therefore, the concentrations of REEs are consistently higher in the rims than in the cores, which is also shown by the LA-ICP-MS data (Table I).

The $\nu_3(\text{SiO}_4)$ Raman band around 1010 cm⁻¹ shows generally greater FWHM values for the rims than the cores. The FWHM obtained for the rims ranged from 6.3 to 14.0 cm⁻¹ (average of 9.6 cm⁻¹), while the cores varied from 2.9 to 5.7 cm⁻¹ (average of 3.9 cm⁻¹). The width of the $\nu_3(\text{SiO}_4)$ Raman band reflects the degree of metamictisation (Nasdala *et al.* 2001). Self-radiation damage of zircon is the main factor in the broadening of the $\nu_3(\text{SiO}_4)$ band (Zeug *et al.* 2017), and its FWHM can vary from < 3 cm⁻¹ for very well-ordered zircon to > 30 cm⁻¹ for metamict zircon (Nasdala *et al.* 1998). The FWHM values of this band can be used to estimate zircon age (Nasdala *et al.* 2001; Palenik *et al.* 2003; Váczi & Nasdala 2016; Härtel *et al.* 2021) and thus may be useful to infer the age of host sapphires (Xu &

Krzemnicki 2021). However, age determination based on the Raman band width alone needs to be done with caution, since both the heterogeneity and annealing history of zircon inclusions need to be considered (Zeug *et al.* 2017).

In this study, the older cores, which should have exhibited a broader $\nu_3(\text{SiO}_4)$ Raman peak due to the relatively greater accumulation of self-radiation, instead showed narrower FWHM values than the younger rims (again, see Figures 6, 7 and 8). This phenomenon could be attributed to a natural annealing history of the cores, which resulted in a sharpening of the peaks (Nasdala *et al.* 2001; Geisler *et al.* 2002). It could also be due to the high U content of the rims, resulting in greater FWHM values (Marsellos & Garver 2010).

U-Pb Age Dating

Consistent with the conclusions derived from the CL images, the age data for the three analysed zircon inclusions varied dramatically from core to rim (with the one exception of spot 28-1; see Table II). While the cores yielded ages in the Cretaceous era at 140–110 Ma (referred to as the ‘old age’ group; see Figure 9b), the rims crystallised in the Miocene era at 9–8 Ma (referred

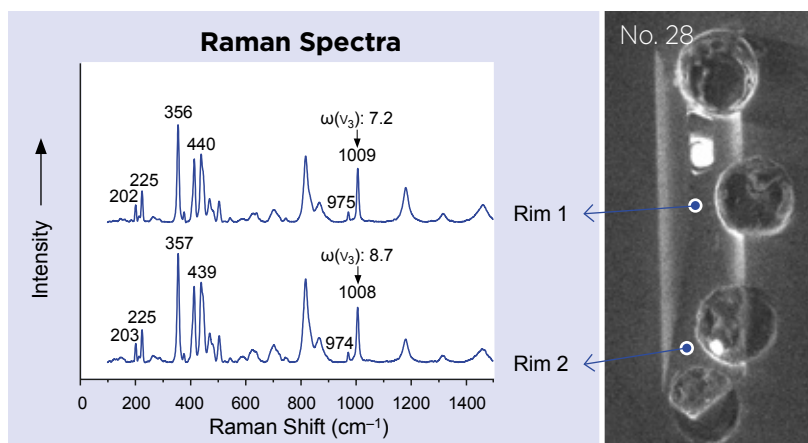


Figure 6: Raman spectra are shown for two different rim areas of the zircon inclusion in sapphire sample 28. The CL image (width 65 μm) shows the locations of these Raman analyses. The FWHM of the $v_3(\text{SiO}_4)$ Raman band at around 1010 cm^{-1} is indicated by the notation $\omega(v_3)$. Image by Y. Liu.

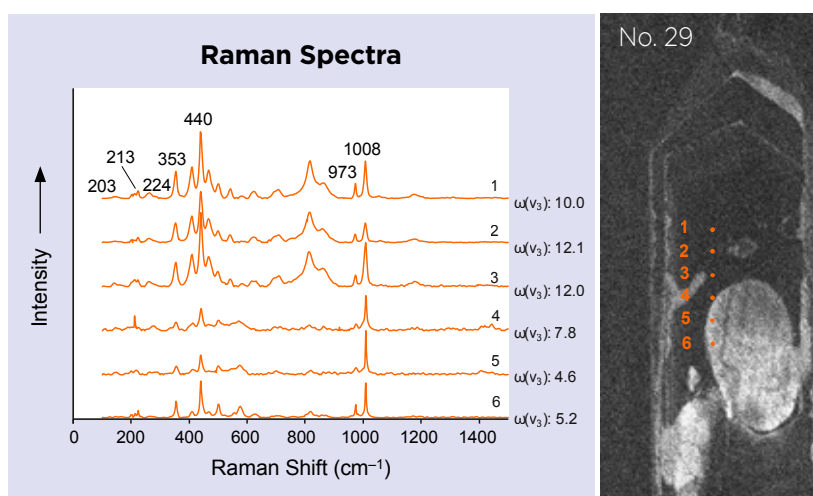


Figure 7: Raman spectra across the rim and core portions of the zircon inclusion in sapphire sample 29 show corresponding differences. The spectra from the rim include a distinct set of multiple peaks in the 500–900 cm^{-1} range due to REEs, which are nearly absent from the spectra of the core. The CL image (width 63 μm) shows the locations of these Raman analyses. The FWHM of the $v_3(\text{SiO}_4)$ Raman band at around 1010 cm^{-1} is significantly greater in the spectra of the rim (1–3) than in those of the core (4–6). Image by Y. Liu.

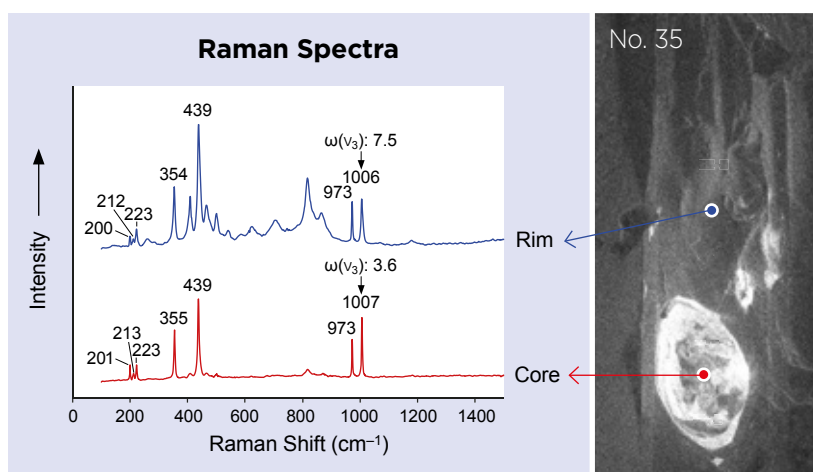


Figure 8: Raman spectra of the rim and core areas of the zircon inclusion in sapphire sample 35 display similar features as those noted in Figure 7. The CL image (width 94.6 μm) shows the locations of the Raman analyses. Image by Y. Liu.

to as the ‘young age’ group, see Figure 9a). Thus, the age difference between the core and the rim of an individual zircon inclusion can span over 100 million years. Many studies have reported the presence of older cores in younger zircons (e.g. Koschek 1993; Bowring & Schmitz 2003; Miller *et al.* 2003). These cores are thought to be inherited from older rock complexes (Bjerga *et al.* 2022), which may or may not have any relationship with subsequent geological events.

Within the ‘old age’ group, the cores in the three samples also exhibited a large age gap. The core of sample 29 (spot 29-2 in Figure 10b) yielded a $^{206}\text{Pb}/^{238}\text{U}$ age of 135 ± 3 Ma, which is 20 million years older than the core ages obtained from sample 35 (spots 35-1 and 35-2 in Figure 10c, with $^{206}\text{Pb}/^{238}\text{U}$ ages of 115 ± 2 Ma and 117 ± 2 Ma, respectively; see also Table II). The age variations between the cores could be due to different inherited histories of geological events during the long

period of the Late Cretaceous. Another possibility could be that, at the end of the LA-ICP-MS analysis, the laser penetrated the rim zone below the core, resulting in a slightly reduced ‘mixed age’. The rims, in contrast, yielded ages within a narrow range of 9–8 Ma (Figure 9a and Table II), indicating a relatively concentrated formation period in the later part of the Miocene epoch.

The dashed error ellipse in Figure 9c refers to the age data for the spot 28-1. Although the laser targeted a very small core area, it ablated both the rim and core of the zircon inclusion (see Figure 10a), and the calculated data fell in the range of the ‘young age’ group. Because the laser ablated a cylindrical volume of material, the core made up a low proportion of the ablated volume compared to the rim. The mixture of different-aged materials caused a low concordance of 83% for this spot. Therefore, the age data for spot 28-1 should not be considered valid.

Natural zircons are commonly heterogeneous in texture, and if the scale of the various domains is smaller than the analysed area, then the acquired data will contain mixed information. Data deviation always happens to a lesser or greater degree. The same circumstances occurred with the age data for two spots (35-3 and 35-4 in Figure 10c), whose corresponding isotope ratios have 95% and 96% concordance, respectively. Such deviations are still considered ‘concordant’ according to Corfu (2013), with their error ellipses both overlapping the concordia curve.

Geological Origin of Muling Blue Sapphires

The morphology of the zircon inclusions in the Muling sapphires showed {110}-dominant prism features, similar to those in basalt-associated sapphires from Changle, China, and from Australia (Guo *et al.* 1996; Sutherland *et al.* 1998). Their morphology differs from those in Kashmir sapphires, which have {100}-dominant prism features (Xu & Krzemnicki 2021). The internal zones of the zircon inclusions revealed by CL images indicate a typical magmatic environment for the rim portions, with oscillatory growth patterns (Corfu 2003).

The Th/U ratio of zircon has been used as a method to help distinguish its growth process (e.g. metamorphic vs magmatic; Williams & Claesson 1987). Magmatic zircon generally shows relatively high Th/U ratios exceeding 0.1 (Rubatto & Gebauer 2000). In this study, 10 of the 11 data points exhibited Th/U ratios greater than 0.1, with a single exception of spot 35-1 (core). All rim spots had elevated Th/U ratios (> 0.3) and correlate with a magmatic growth environment.

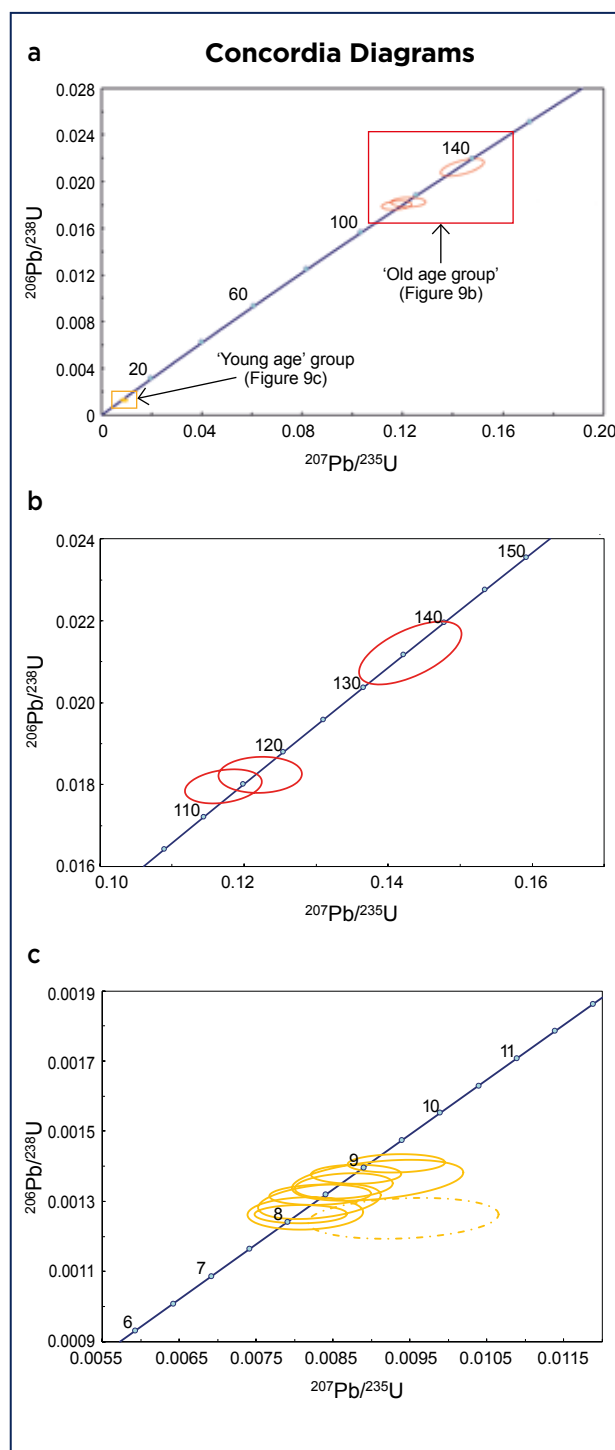


Figure 9: (a) This concordia diagram of the ratios $^{206}\text{Pb}/^{238}\text{U}$ vs $^{207}\text{Pb}/^{235}\text{U}$ shows all valid age data for the zircon inclusions analysed in this study. Numbers along the solid blue line (the concordia line) are ages in million years. Error ellipses (68.3% confidence) are shown for the ‘old age’ group in red and for the ‘young age’ group in yellow. (b) The section of the concordia diagram for the ‘old age’ group summarises data from the zircon cores, which yielded ages ranging from about 110 to 140 Ma. (c) The section of the concordia diagram for the ‘young age’ group shows data from the zircon rims, which yielded ages of 9–8 Ma. The dashed yellow error ellipse refers to the age data for spot 28-1, which incorporated both the rim and core and therefore yielded an unreliable age with low concordance.

The Raman spectra, CL images and isotopic analyses confirm that the zircon inclusions formed in two stages: (1) a much older stage at about 140–110 Ma, at which time the zircon formed with irregular shapes and chaotic internal zoning; and (2) a younger stage at 9–8 Ma,

corresponding to recrystallisation of the zircon in a magmatic environment with euhedral crystal shapes and typical oscillatory zoning. The stage most closely related to the host sapphires is the younger stage, which provides some hints about the formation conditions of the sapphires.

The age of the rims of the zircon inclusions provides the maximum formation age of Muling blue sapphires. Combined with the geological setting, the approximate age of 9–8 Ma constrains the potential genesis of the sapphires. The volcanic eruptions of the Dunhua-Mishan graben began around 44.9 Ma and ended about 5,140 years ago (Wang *et al.* 2001), which allows for numerous volcanic events to deliver the corundum as xenocrysts from the source to the earth's surface. A close relationship between the Muling gem corundum and the late Miocene basaltic rocks is quite reasonable (Sun 1995).

Relative Chronological Position of Muling Sapphires

Gem corundum deposits did not form continuously during the long history of Earth's evolution. Their formation times can be divided into four main periods (Figure 11a) that were accompanied by plate-tectonic processes of subduction and collision (Stern *et al.* 2013). The outlined sector in Figure 11a (expanded as Figure 11b) includes the formation periods of the most economically valuable corundum deposits (i.e. from the late Proterozoic to the Cenozoic era). The formation period of East African rubies and sapphires (i.e. Pan-African orogeny-related deposits) coincided with the so-called Cambrian explosion (about 540 Ma), an unparalleled stage in the evolutionary development of life on Earth. In Asia, gem corundum formed in the Cenozoic era (including Himalayan orogeny-related deposits and alkali basalt-related deposits), well after the dinosaurs had gone extinct. Sapphires from Muling are relatively young among worldwide gem corundum deposits (see Figure 11c), and formed at the time when Earth's primates started to emerge (Ciochon & Corruccini 1983; Wood & Harrison 2011).

Age data supply additional information for the provenance determination of gems. Muling sapphires exhibit various provenance characteristics, which might be similar in some aspects to sapphires from other deposits worldwide (such as those from Madagascar, Myanmar and Montana, USA; Liu & Lu 2022). Muling sapphires exhibit a variety of hues with a full range of saturations, similar to those from Madagascar. However, they are much younger than Madagascar sapphires (Figure 11), which are related to the Pan-African orogeny

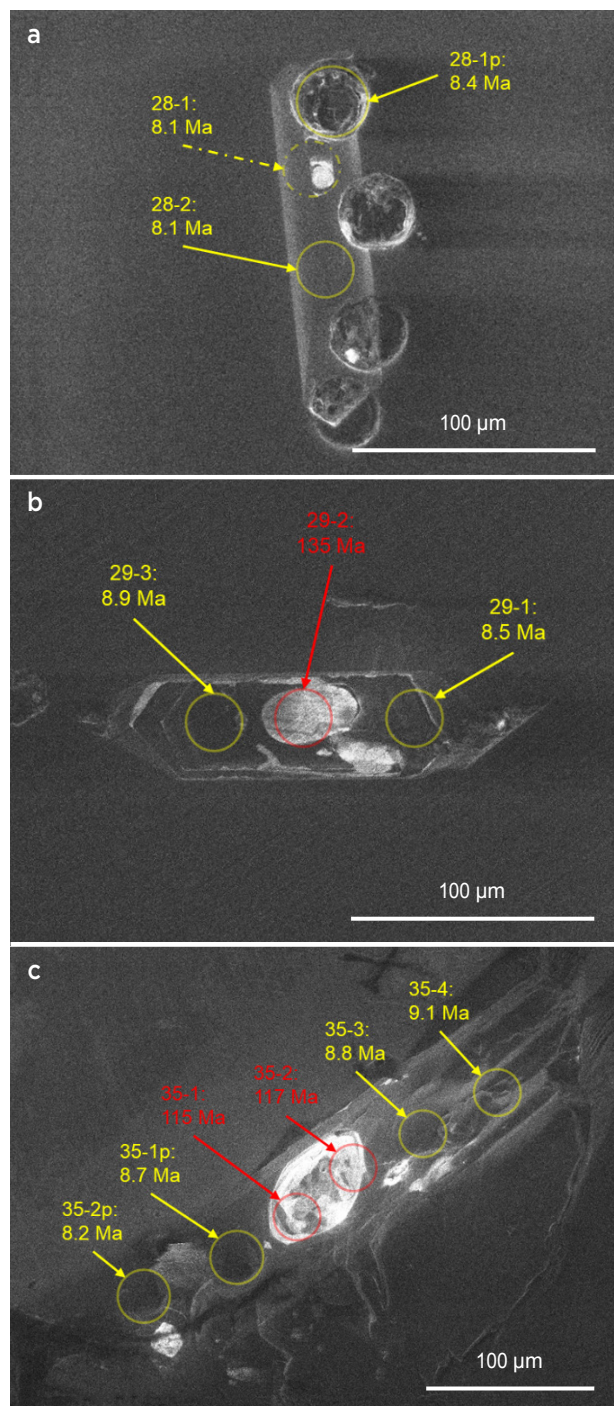
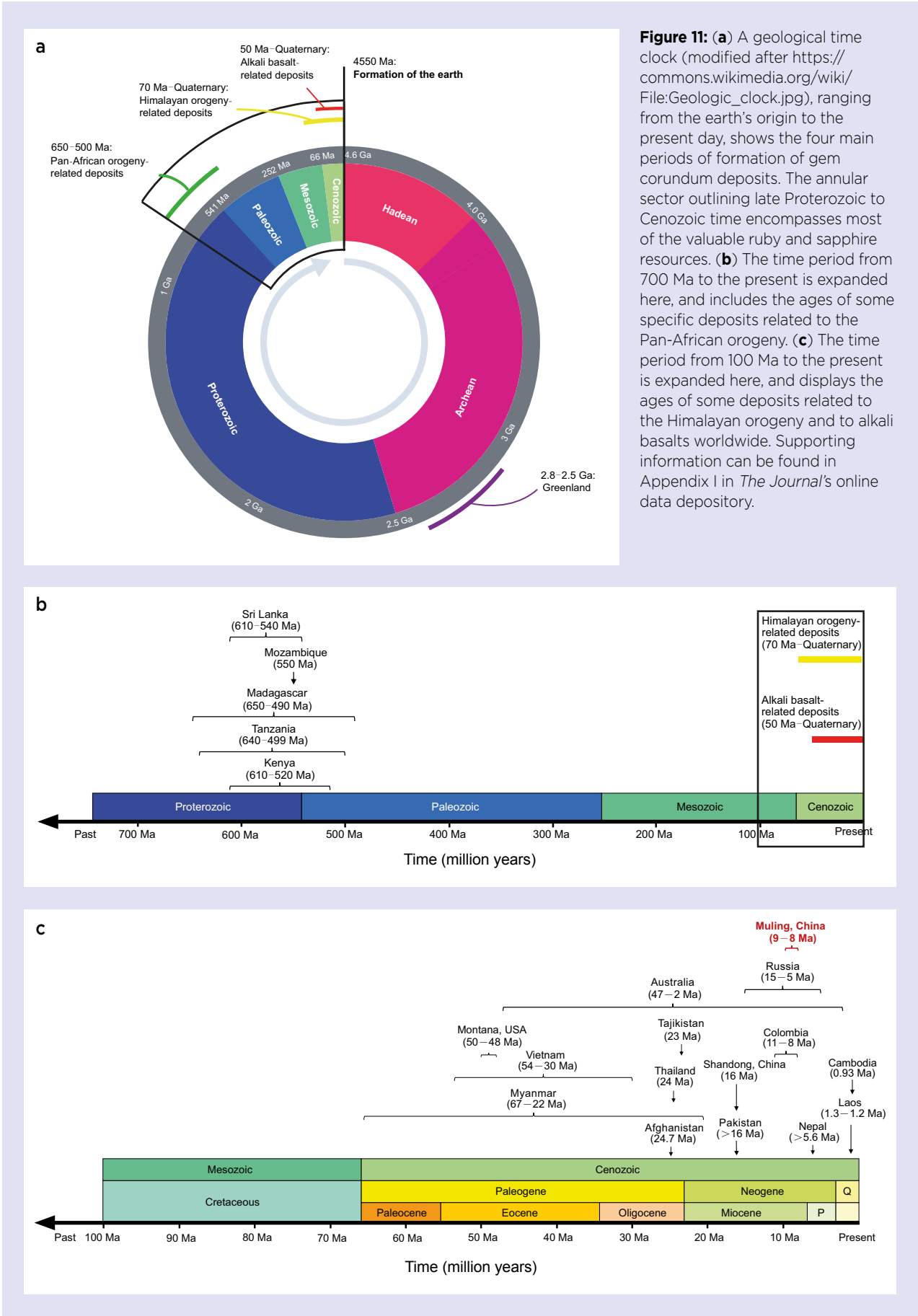


Figure 10: Laser-ablated spots and relevant $^{206}\text{Pb}/^{238}\text{U}$ ages are labelled on the CL images of the zircon inclusions in sapphire samples (a) 28, (b) 29 and (c) 35. Yellow circles refer to the 'young age' group and red circles indicate the 'old age' group. The dashed yellow circle for sample 28 refers to the low-concordance age data of spot 28-1. Images by Y. Liu.



(Rakotondrazafy *et al.* 2008). The sapphires from Muling and Montana also show similarities in their wide range of hues. However, Muling sapphires generally exhibit comparatively higher colour saturation. Furthermore, the plate-tectonic processes related to these deposits are different, and so are the formation times (Figure 11c; see Smith *et al.* 2014). Some Muling sapphires exhibit inclusion scenes similar to those of Burmese sapphires (Liu & Lu 2022), both of which formed in the Eurasian Plate, but at very different times (Figure 11c).

Both the age of formation (Figure 11c) and the geographical location of Muling sapphires closely correlate with Cenozoic magmatic events of the Western Pacific continental margins. A number of other alkali basalt-related sapphire deposits also formed along these margins during the Cenozoic era (e.g. Queensland, Australia; Chanthaburi, Thailand; Changle, China). The Muling area is chronologically and geologically consistent with these deposits in general, yet the colour range of Muling gem corundum is significantly wider than that of typical alkali-basaltic sapphires. The formation age of Muling sapphires determined in this study is a valuable addition to the history of gem corundum deposits of the Western Pacific continental margins.

CONCLUSIONS

Zircon inclusions in Muling blue sapphires were analysed in detail. CL imagery and Raman spectra revealed the heterogeneity of these inclusions. *In situ* U-Pb dating yielded ages of 9–8 Ma for the rims of the zircon

inclusions, while their cores showed much older ages that exceeded 110 Ma. The morphology of the zircon inclusions, mainly decided by the crystallisation of their outer rims, indicates a magmatic formation environment consistent with that of typical alkali-basaltic sapphires. Their magmatic origin is also supported by the oscillatory growth pattern of their rims under CL, and also their relatively high Th/U ratios (> 0.1). Therefore, it is quite likely that the formation environment of the host sapphires could be of a magmatic type. The oldest possible ages of the host sapphires are constrained by the youngest ages of the rim of the zircon inclusions (i.e. 9–8 Ma). This age is consistent with an active period of Miocene volcanic events in the Dunhua-Mishan graben.

By determining the position of Muling sapphires on the geological timeline, our understanding of this corundum resource becomes more complete. Combined with their specific geological background, the ages of these sapphires can also be utilised as supporting criteria for provenance determination. Once a comprehensive database of the time and space of global gem corundum resources has been established, then more complete knowledge of the world's sapphire origins (including those from Muling) will be possible.

To further understand the formation of Muling gem corundum, more research and exploration of the area are needed. The data in this study are related to deep blue sapphires, and in order to obtain further provenance information, additional corundum varieties from this deposit (such as pink, light blue, green and yellow sapphires) should be investigated.

REFERENCES

- Akinin, V.V., Vysotskiy, S.V., Coble, M. & Aseeva, A.V. 2017. U-Pb age and geochemistry of zircon inclusions in sapphire: Alkali basaltic source of gems in placers of Primorye. *Doklady Earth Sciences*, **476**(2), 1173–1176, <https://doi.org/10.1134/s1028334x17100129>.
- Benisek, A. & Finger, F. 1993. Factors controlling the development of prism faces in granite zircons: A microprobe study. *Contributions to Mineralogy and Petrology*, **114**(4), 441–451, <https://doi.org/10.1007/bf00321749>.
- Bjerga, A., Stubseid, H.H., Pedersen, L.E.R. & Pedersen, R.B. 2022. Radiation damage allows identification of truly inherited zircon. *Communications Earth & Environment*, **3**(1), article 37, <https://doi.org/10.1038/s43247-022-00372-2>.
- Bowring, S.A. & Schmitz, M.D. 2003. High-precision U-Pb zircon geochronology and the stratigraphic record. In: Hanchar, J.M. & Hoskin, P.W.O. (eds) *Zircon, Reviews in Mineralogy and Geochemistry*, **53**(1), 305–326, <https://doi.org/10.2113/0530305>.
- Bui, H.A.N., Fritsch, E. & Rondeau, B. 2012. Geographical origin: Branding or science? *InColor*, No. 19, 30–39.
- Chen, T., Ai, H., Yang, M., Zheng, S. & Liu, Y. 2011. Brownish red zircon from Muling, China. *Gems & Gemology*, **47**(1), 36–41, <https://doi.org/10.5741/gems.47.1.36>.
- Chen, T., Liu, Y., Yin, Z. & Liu, N. 2013. Gemology and spectra characterization of gem garnet from Muling City, Heilongjiang Province. *Spectroscopy and Spectral Analysis*, **33**(11), 2964–2967, <http://www.gpxygpfx.com/EN/Y2013/V33/I11/2964> (in Chinese with English abstract).
- Ciochon, R. & Corruccini, R.S. (eds) 1983. *New Interpretations of Ape and Human Ancestry*. Springer Science + Business Media, New York,

- New York, USA, xxiv + 888 pp., <https://doi.org/10.1007/978-1-4684-8854-8>.
- Corfu, F. 2003. Atlas of zircon textures. In: Hanchar, J.M. & Hoskin, P.W.O. (eds) *Zircon, Reviews in Mineralogy and Geochemistry*, **53**(1), 469–500, <https://doi.org/10.2113/0530469>.
- Corfu, F. 2013. A century of U-Pb geochronology: The long quest towards concordance. *Geological Society of America Bulletin*, **125**(1–2), 33–47, <https://doi.org/10.1130/b30698.1>.
- Elmaleh, E., Schmidt, S.T., Karampelas, S., Link, K., Kiefert, L., Sussenberger, A. & Paul, A. 2019. U-Pb ages of zircon inclusions in sapphires from Ratnapura and Balangoda (Sri Lanka) and implications for geographic origin. *Gems & Gemology*, **55**(1), 18–28, <https://doi.org/10.5741/gems.55.1.18>.
- Galibert, O. & Hughes, R.W. 1995. Chinese ruby and sapphire – A brief history. *Journal of Gemmology*, **24**(7), 467–473, <https://doi.org/10.15506/JoG.1995.24.7.467>.
- Garnier, V., Ohnenstetter, D., Giuliani, G., Fallick, A.E., Phan Trong, T., Hoàng Quang, V., Pham Van, L. & Schwarz, D. 2005. Basalt petrology, zircon ages and sapphire genesis from Dak Nong, southern Vietnam. *Mineralogical Magazine*, **69**(1), 21–38, <https://doi.org/10.1180/0026461056910233>.
- Geisler, T., Pidgeon, R.T., van Bronswijk, W. & Kurtz, R. 2002. Transport of uranium, thorium, and lead in metamict zircon under low-temperature hydrothermal conditions. *Chemical Geology*, **191**(1–3), 141–154, [https://doi.org/10.1016/s0009-2541\(02\)00153-5](https://doi.org/10.1016/s0009-2541(02)00153-5).
- Gerdes, A. & Zeh, A. 2006. Combined U-Pb and Hf isotope LA-(MC-)ICP-MS analyses of detrital zircons: Comparison with SHRIMP and new constraints for the provenance and age of an Armorican metasediment in central Germany. *Earth and Planetary Science Letters*, **249**(1–2), 47–61, <https://doi.org/10.1016/j.epsl.2006.06.039>.
- Giuliani, G., Ohnenstetter, D., Fallick, A.E., Groat, L.A. & Fagan, A.J. 2014. Chapter 2: The geology and genesis of gem corundum deposits. In: Groat, L.A. (ed) *Geology of Gems Deposits*, 2nd edn. Mineralogical Association of Canada, Québec, Canada, **44**, 29–112.
- Gübelin, E.J. & Koivula, J.I. 1986. *Photoatlas of Inclusions in Gemstones*, Opinio Verlag, Basel, Switzerland, 532 pp.
- Guillong, M., Horn, I. & Günther, D. 2003. A comparison of 266 nm, 213 nm and 193 nm produced from a single solid state Nd:YAG laser for laser ablation ICP-MS. *Journal of Analytical Atomic Spectrometry*, **18**(10), 1224–1230, <https://doi.org/10.1039/b305434a>.
- Günther, D. & Heinrich, C.A. 1999. Comparison of the ablation behaviour of 266 nm Nd:YAG and 193 nm ArF excimer lasers for LA-ICP-MS analysis. *Journal of Analytical Atomic Spectrometry*, **14**(9), 1369–1374, <https://doi.org/10.1039/a901649j>.
- Günther, D., Frischknecht, R., Heinrich, C.A. & Kahlert, H.-J. 1997. Capabilities of an argon fluoride 193 nm excimer laser for laser ablation inductively coupled plasma mass spectrometry microanalysis of geological materials. *Journal of Analytical Atomic Spectrometry*, **12**(9), 939–944, <https://doi.org/10.1039/a701423f>.
- Guo, J., Wang, F. & Yakoumelos, G. 1992. Sapphires from Changle in Shandong Province, China. *Gems & Gemology*, **28**(4), 255–260, <https://doi.org/10.5741/gems.28.4.255>.
- Guo, J., O'Reilly, S.Y. & Griffin, W.L. 1996. Corundum from basaltic terrains: A mineral inclusion approach to the enigma. *Contributions to Mineralogy and Petrology*, **122**(4), 368–386, <https://doi.org/10.1007/s004100050134>.
- Halliday, A.N., Lee, D.-C., Christensen, J.N., Rehkämper, M., Yi, W., Luo, X., Hall, C.M., Ballentine, C.J. *et al.* 1998. Applications of multiple collector-ICPMS to cosmochemistry, geochemistry, and paleoceanography. *Geochimica et Cosmochimica Acta*, **62**(6), 919–940, [https://doi.org/10.1016/s0016-7037\(98\)00057-x](https://doi.org/10.1016/s0016-7037(98)00057-x).
- Hanchar, J.M. & Rudnick, R.L. 1995. Revealing hidden structures: The application of cathodoluminescence and back-scattered electron imaging to dating zircons from lower crustal xenoliths. *Lithos*, **36**(3–4), 289–303, [https://doi.org/10.1016/0024-4937\(95\)00022-4](https://doi.org/10.1016/0024-4937(95)00022-4).
- Harley, S.L. & Kelly, N.M. 2007. Zircon: Tiny but timely. *Elements*, **3**(1), 13–18, <https://doi.org/10.2113/gselements.3.1.13>.
- Härtel, B., Jonckheere, R., Wauschkuhn, B., Hofmann, M., Frölich, S. & Ratschbacher, L. 2021. Zircon Raman dating: Age equation and calibration. *Chemical Geology*, **579**, article 120351, <https://doi.org/10.1016/j.chemgeo.2021.120351>.
- Hirata, T. & Nesbitt, R.W. 1995. U-Pb isotope geochronology of zircon: Evaluation of the laser probe-inductively coupled plasma mass spectrometry technique. *Geochimica et Cosmochimica Acta*, **59**(12), 2491–2500, [https://doi.org/10.1016/0016-7037\(95\)00144-1](https://doi.org/10.1016/0016-7037(95)00144-1).
- Holmes, A. 1954. The oldest dated minerals of the Rhodesian shield. *Nature*, **173**(4405), 612–614, <https://doi.org/10.1038/173612a0>.
- Horn, I. 2008. Comparison of femtosecond and nanosecond laser interactions with geologic matrices and their influence on accuracy and precision of LA-(MC)-ICPMS data. In: Sylvester, P. (ed) *Laser Ablation ICP-MS in the Earth Sciences: Current Practices and Outstanding Issues*. Mineralogical Association of Canada, Québec, Canada, **40**, 53–56.
- Horn, I., Rudnick, R.L. & McDonough, W.F. 2000. Precise elemental and isotope ratio determination by

- simultaneous solution nebulization and laser ablation-ICP-MS: Application to U–Pb geochronology. *Chemical Geology*, **164**(3–4), 281–301, [https://doi.org/10.1016/S0009-2541\(99\)00168-0](https://doi.org/10.1016/S0009-2541(99)00168-0).
- Horstwood, M.S.A. 2008. Data reduction strategies, uncertainty assessment and resolution of LA–(MC–) ICP–MS isotope data. In: Sylvester, P. (ed) *Laser Ablation–ICP–MS in the Earth Sciences: Current Practices and Outstanding Issues*. Mineralogical Association of Canada Short Course Series, **40**, 283–303.
- Hoskin, P.W.O. 2000. Patterns of chaos: Fractal statistics and the oscillatory chemistry of zircon. *Geochimica et Cosmochimica Acta*, **64**(11), 1905–1923, [https://doi.org/10.1016/S0016-7037\(00\)00330-6](https://doi.org/10.1016/S0016-7037(00)00330-6).
- Hu, L., Pan, S., Lu, R., Zheng, J., Dai, H., Guo, A., Yu, L. & Sun, H. 2022. Origin of gem-quality megacrysts in the Cenozoic alkali basalts from the Muling area, northeastern China. *Lithos*, **422–423**, article 106720, <https://doi.org/10.1016/j.lithos.2022.106720>.
- Iizuka, T. & Hirata, T. 2004. Simultaneous determinations of U–Pb age and REE abundances for zircons using ArF excimer laser ablation-ICPMS. *Geochemical Journal*, **38**(3), 229–241, <https://doi.org/10.2343/geochemj.38.229>.
- Jackson, S.E., Pearson, N.J., Griffin, W.L. & Belousova, E.A. 2004. The application of laser ablation-inductively coupled plasma-mass spectrometry to in situ U–Pb zircon geochronology. *Chemical Geology*, **211**(1–2), 47–69, <https://doi.org/10.1016/j.chemgeo.2004.06.017>.
- Keller, A.S. & Keller, P.C. 1986. The sapphires of Mingxi, Fujian Province, China. *Gems & Gemology*, **22**(1), 41–45, <https://doi.org/10.5741/gems.22.1.41>.
- Keller, P.C. & Wang, F. 1986. A survey of the gemstone resources of China. *Gems & Gemology*, **22**(1), 3–13, <https://doi.org/10.5741/gems.22.1.3>.
- Koschek, G. 1993. Origin and significance of the SEM cathodoluminescence from zircon. *Journal of Microscopy*, **171**(3), 223–232, <https://doi.org/10.1111/j.1365-2818.1993.tb03379.x>.
- Kostov, I. 1973. Zircon morphology as a crystallogenic indicator. *Kristall und Technik*, **8**(1–3), 11–19, <https://doi.org/10.1002/crat.19730080103>.
- Krzemnicki, M.S., Wang, H.A.O. & Phylo, M.M. 2019. Age dating applied as a testing procedure to gemstones and biogenic gem materials. *International Gemmological Conference*, Nantes, France, 27–31 August, 48–50.
- Lenz, C., Nasdala, L., Talla, D., Hauzenberger, C., Seitz, R. & Kolitsch, U. 2015. Laser-induced REE³⁺ photoluminescence of selected accessory minerals—An “advantageous artefact” in Raman spectroscopy. *Chemical Geology*, **415**, 1–16, <https://doi.org/10.1016/j.chemgeo.2015.09.001>.
- Li, G.Y., Zhou, J.B. & Li, L. 2023. The Jiamusi block: A hinge of the tectonic transition from the paleo-Asian Ocean to the paleo-Pacific Ocean regimes. *Earth-Science Reviews*, **236**, article 104279, <https://doi.org/10.1016/j.earscirev.2022.104279>.
- Li, W.M., Liu, Y.J., Zhao, Y.L., Feng, Z.Q., Zhou, J.P., Wen, Q.B., Liang, C.Y. & Zhang, D. 2020. Tectonic evolution of the Jiamusi block, NE China. *Acta Petrologica Sinica*, **36**(3), 665–684 (in Chinese with English abstract).
- Link, K. 2015. Age determination of zircon inclusions in faceted sapphires. *Journal of Gemmology*, **34**(8), 692–700, <https://doi.org/10.15506/JoG.2015.34.8.692>.
- Litvinenko, A.K., Sorokina, E.S., Häger, T., Kostitsyn, Y.A., Botcharnikov, R.E., Somsikova, A.V., Ludwig, T., Romashova, T.V. *et al.* 2020. Petrogenesis of the Snezhnoe ruby deposit, central Pamir. *Minerals*, **10**(5), article 478, <https://doi.org/10.3390/min10050478>.
- Liu, J., Han, J. & Fyfe, W.S. 2001. Cenozoic episodic volcanism and continental rifting in northeast China and possible link to Japan Sea development as revealed from K–Ar geochronology. *Tectonophysics*, **339**(3–4), 385–401, [https://doi.org/10.1016/S0040-1951\(01\)00132-9](https://doi.org/10.1016/S0040-1951(01)00132-9).
- Liu, Y., Gao, S., Hu, Z., Gao, C., Zong, K. & Wang, D. 2010. Continental and oceanic crust recycling-induced melt–peridotite interactions in the Trans-North China Orogen: U–Pb dating, Hf isotopes and trace elements in zircons from mantle xenoliths. *Journal of Petrology*, **51**(1–2), 537–571, <https://doi.org/10.1093/petrology/egp082>.
- Liu, Y. & Lu, R. 2022. Sapphire beneath the rich black soil of Muling, northeastern China. *Gems & Gemology*, **58**(3), 290–317, <https://doi.org/10.5741/gems.58.3.290>.
- Ludwig, K.R. 2003. *User's Manual for Isoplot 3.00: A Geochronological Toolkit for Microsoft Excel*. Berkeley Geochronology Centre, Berkeley, California, USA, 74 pp.
- Machado, N. & Simonetti, A. 2001. U–Pb dating and Hf isotopic composition of zircon by laser ablation-MC-ICP-MS. In: Sylvester, P. (ed) *Laser Ablation-ICPMS in the Earth Sciences: Principles and Applications*. Mineralogical Association of Canada, Québec, Canada, **29**, 121–146.
- Marsellos, A.E. & Garver, J.I. 2010. Radiation damage and uranium concentration in zircon as assessed by Raman spectroscopy and neutron irradiation. *American Mineralogist*, **95**(8–9), 1192–1201, <https://doi.org/10.2138/am.2010.3264>.
- Miller, C.F., McDowell, S.M. & Mapes, R.W. 2003. Hot and cold granites? Implications of zircon saturation temperatures and preservation of inheritance. *Geology*, **31**(6), 529–532, [https://doi.org/10.1130/0091-7613\(2003\)031%3C0529:HACGIO%3E2.0.CO;2](https://doi.org/10.1130/0091-7613(2003)031%3C0529:HACGIO%3E2.0.CO;2).

- Nasdala, L., Pidgeon, R.T., Wolf, D. & Irmer, G. 1998. Metamictization and U-Pb isotopic discordance in single zircons: A combined Raman microprobe and SHRIMP ion probe study. *Mineralogy and Petrology*, **62**(1–2), 1–27, <https://doi.org/10.1007/bf01173760>.
- Nasdala, L., Wenzel, M., Vavra, G., Irmer, G., Wenzel, T. & Kober, B. 2001. Metamictisation of natural zircon: Accumulation versus thermal annealing of radioactivity-induced damage. *Contributions to Mineralogy and Petrology*, **141**(2), 125–144, <https://doi.org/10.1007/s004100000235>.
- Nasdala, L., Zhang, M., Kempe, U., Panczer, G., Gaft, M., Andrut, M. & Plötze, M. 2003. Spectroscopic methods applied to zircon. In: Hanchar, J.M. & Hoskin, P.W.O. (eds) *Zircon, Reviews in Mineralogy and Geochemistry*, **53**(1), 427–467, <https://doi.org/10.2113/0530427>.
- Nicola, J.H. & Rutt, H.N. 1974. A comparative study of zircon (ZrSiO₄) and hafnon (HfSiO₄) Raman spectra. *Journal of Physics C: Solid State Physics*, **7**(7), 1381–1386, <https://doi.org/10.1088/0022-3719/7/7/029>.
- Palenik, C.S., Nasdala, L. & Ewing, R.C. 2003. Radiation damage in zircon. *American Mineralogist*, **88**(5–6), 770–781, <https://doi.org/10.2138/am-2003-5-606>.
- Palke, A.C., Saeseaw, S., Renfro, N.D., Sun, Z. & McClure, S.F. 2019a. Geographic origin determination of blue sapphire. *Gems & Gemology*, **55**(4), 536–579, <https://doi.org/10.5741/gems.55.4.536>.
- Palke, A.C., Saeseaw, S., Renfro, N.D., Sun, Z. & McClure, S.F. 2019b. Geographic origin determination of ruby. *Gems & Gemology*, **55**(4), 580–613, <https://doi.org/10.5741/gems.55.4.580>.
- Pan, S., Zheng, J., Griffin, W.L., Xu, Y. & Li, X. 2015. Nature and evolution of the lithospheric mantle beneath the eastern Central Asian Orogenic Belt: Constraints from peridotite xenoliths in the central part of the Great Xing'an Range, NE China. *Lithos*, **238**, 52–63, <https://doi.org/10.1016/j.lithos.2015.09.013>.
- Phyo, M.M., Wang, H.A.O., Guillong, M., Berger, A., Franz, L., Balmer, W.A. & Krzemnicki, M.S. 2020. U–Pb dating of zircon and zirconolite inclusions in marble-hosted gem-quality ruby and spinel from Mogok, Myanmar. *Minerals*, **10**(2), article 195, <https://doi.org/10.3390/min10020195>.
- Pupin, J.P. 1980. Zircon and granite petrology. *Contributions to Mineralogy and Petrology*, **73**(3), 207–220, <https://doi.org/10.1007/bf00381441>.
- Qiu, Z., Yang, J., Yang, Y., Yang, S., Li, C., Wang, Y., Lin, W. & Yang, X. 2007. Trace element and hafnium isotopes of Cenozoic basalt-related zircon megacrysts at Muling, Heilongjiang Province, northeast China. *Acta Petrologica Sinica*, **23**(2), 481–492 (in Chinese with English abstract).
- Rakotondrazafy, A.F.M., Giuliani, G., Ohnenstetter, D., Fallick, A.E., Rakotosamizanany, S., Andriamamonjy, A., Ralantoarison, T., Razanatsheho, M. *et al.* 2008. Gem corundum deposits of Madagascar: A review. *Ore Geology Reviews*, **34**(1–2), 134–154, <https://doi.org/10.1016/j.oregeorev.2007.05.001>.
- Rubatto, D. & Gebauer, D. 2000. Use of cathodoluminescence for U-Pb zircon dating by ion microprobe: Some examples from the western Alps. In: Pagel, M., Barbin, V., Blanc, P. & Ohnenstetter, D. (eds) *Cathodoluminescence in Geosciences*. Springer, Berlin, Heidelberg, Germany, 373–400, https://doi.org/10.1007/978-3-662-04086-7_15.
- Sakata, S., Hattori, K., Iwano, H., Yokoyama, T.D., Danhara, T. & Hirata, T. 2014. Determination of U-Pb ages for young zircons using laser ablation-ICP-mass spectrometry coupled with an ion detection attenuator device. *Geostandards and Geoanalytical Research*, **38**(4), 409–420, <https://doi.org/10.1111/j.1751-908X.2014.00320.x>.
- Scott, D.J. & Gauthier, G. 1996. Comparison of TIMS (U-Pb) and laser ablation microprobe ICP-MS (Pb) techniques for age determination of detrital zircons from Paleoproterozoic metasedimentary rocks from northeastern Laurentia, Canada, with tectonic implications. *Chemical Geology*, **131**(1–4), 127–142, [https://doi.org/10.1016/0009-2541\(96\)00030-7](https://doi.org/10.1016/0009-2541(96)00030-7).
- Shen, Y. 1987. A preliminary study on the Cenozoic volcanic rocks in Mudanjiang District. *Acta Petrologica Sinica*, **3**(3), 35–45 (in Chinese with English abstract).
- Smith, M.E., Carroll, A.R., Jicha, B.R., Cassel, E.J. & Scott, J.J. 2014. Paleogeographic record of Eocene Farallon slab rollback beneath western North America. *Geology*, **42**(12), 1039–1042, <https://doi.org/10.1130/g36025.1>.
- Stern, R.J., Tsujimori, T., Harlow, G. & Groat, L.A. 2013. Plate tectonic gemstones. *Geology*, **41**(7), 723–726, <https://doi.org/10.1130/g34204.1>.
- Su, L. 1990. Sapphire from eastern Heilongjiang Province. *China Non-Metallic Mining Industry Herald*, No. 2, 10–11 (in Chinese with English abstract).
- Sun, J. 1995. Basalt related to ruby and sapphire in eastern Heilongjiang and reconstruction of paleovolcanic mechanism. *Acta Petrologica et Mineralogica*, **14**(2), 126–132 (in Chinese with English abstract).
- Sun, J., Li, F., Dang, Y., Cui, G. & Zhou, X. 2005. Mineralogical features of ruby and sapphire from Heilongjiang Province. *Acta Petrologica et Mineralogica*, **24**(1), 62–66 (in Chinese with English abstract).
- Sutherland, F.L., Hoskin, P.W.O., Fanning, C.M. & Coenraads, R.R. 1998. Models of corundum origin from alkali basaltic terrains: A reappraisal. *Contributions to Mineralogy and Petrology*, **133**(4), 356–372, <https://doi.org/10.1007/s004100050458>.
- Syme, R.W.G., Lockwood, D.J. & Kerr, H.J. 1977. Raman spectrum of synthetic zircon (ZrSiO₄) and thorite (ThSiO₄).

- Journal of Physics C: Solid State Physics*, **10**(8), 1335–1348, <https://doi.org/10.1088/0022-3719/10/8/036>.
- Tollstrup, D.L., Xie, L.W., Wimpenny, J.B., Chin, E., Lee, C.T. & Yin, Q.Z. 2012. A trio of laser ablation in concert with two ICP-MSs: Simultaneous, pulse-by-pulse determination of U-Pb discordant ages and a single spot Hf isotope ratio analysis in complex zircons from petrographic thin sections. *Geochemistry, Geophysics, Geosystems*, **13**(3), article 4027, <https://doi.org/10.1029/2011gc004027>.
- Váczi, T. 2014. A new, simple approximation for the deconvolution of instrumental broadening in spectroscopic band profiles. *Applied Spectroscopy*, **68**(11), 1274–1278, <https://doi.org/10.1366/13-07275>.
- Váczi, T. & Nasdala, L. 2016. Electron-beam-induced annealing of natural zircon: A Raman spectroscopic study. *Physics and Chemistry of Minerals*, **44**(6), 389–401, <https://doi.org/10.1007/s00269-016-0866-x>.
- Villa, I.M. & Hanchar, J.M. 2017. Age discordance and mineralogy. *American Mineralogist*, **102**(12), 2422–2439, <https://doi.org/10.2138/am-2017-6084>.
- Wang, F. 1988. The sapphires of Penglai, Hainan Island, China. *Gems & Gemology*, **24**(3), 155–159, <https://doi.org/10.5741/gems.24.3.155>.
- Wang, W., Li, Y. & Guo, S. 2014. The northeast China block group and its tectonic evolution. *Geology and Resources*, **23**(1), 4–24, <https://doi.org/10.13686/j.cnki.dzyzy.2014.01.002> (in Chinese with English abstract).
- Wang, X., Qiu, S., Song, C., Kulakov, A., Tashchi, S. & Myasnikov, E. 2001. Cenozoic volcanism and geothermal resources in northeast China. *Chinese Geographical Science*, **11**(2), 150–154, <https://doi.org/10.1007/s11769-001-0035-z>.
- Wang, Y. & Dou, L. 1997. Formation time and dynamic characteristics of the northern part of the Tanlu fault zone in east China. *Seismology and Geology*, **19**(2), 185–192 (in Chinese with English abstract).
- Wetherill, G.W. 1956. Discordant uranium-lead ages, I. *Eos, Transactions of the American Geophysical Union*, **37**(3), 320–326, <https://doi.org/10.1029/TR037i003p00320>.
- Wiedenbeck, M., Allé, P., Corfu, F., Griffin, W.L., Meier, M., Oberli, F., Quadt, A.V., Roddick, J.C. *et al.* 1995. Three natural zircon standards for U-Th-Pb, Lu-Hf, trace element and REE analyses. *Geostandards and Geoanalytical Research*, **19**(1), 1–23, <https://doi.org/10.1111/j.1751-908X.1995.tb00147.x>.
- Williams, I.S. & Claesson, S. 1987. Isotopic evidence for the Precambrian provenance and Caledonian metamorphism of high grade paragneisses from the Seve Nappes, Scandinavian Caledonides. *Contributions to Mineralogy and Petrology*, **97**(2), 205–217, <https://doi.org/10.1007/bf00371240>.
- Wood, B. & Harrison, T. 2011. The evolutionary context of the first hominins. *Nature*, **470**(7334), 347–352, <https://doi.org/10.1038/nature09709>.
- Xu, W. & Krzemnicki, M.S. 2021. Raman spectroscopic investigation of zircon in gem-quality sapphire: Application in origin determination. *Journal of Raman Spectroscopy*, **52**(5), 1011–1021, <https://doi.org/10.1002/jrs.6092>.
- Xu, W.L., Pei, F.P., Wang, F., Meng, E., Ji, W.Q., Yang, D.B. & Wang, W. 2013. Spatial-temporal relationships of Mesozoic volcanic rocks in NE China: Constraints on tectonic overprinting and transformations between multiple tectonic regimes. *Journal of Asian Earth Sciences*, **74**, 167–193, <https://doi.org/10.1016/j.jseaes.2013.04.003>.
- Yuan, H., Gao, S., Liu, X., Li, H., Günther, D. & Wu, F. 2004. Accurate U-Pb age and trace element determinations of zircon by laser ablation-inductively coupled plasma-mass spectrometry. *Geostandards and Geoanalytical Research*, **28**(3), 353–370, <https://doi.org/10.1111/j.1751-908X.2004.tb00755.x>.
- Zeug, M., Rodríguez Vargas, A.I. & Nasdala, L. 2017. Spectroscopic study of inclusions in gem corundum from Mercaderes, Cauca, Colombia. *Physics and Chemistry of Minerals*, **44**(3), 221–233, <https://doi.org/10.1007/s00269-016-0851-4>.

The Authors

Dr Yimiao Liu, Dr Ren Lu* and Dr Shaokui Pan

Gemmological Institute, China University of Geosciences, No. 388 Lumo Road, 430074 Wuhan, China

*Email: renlu.cc@gmail.com

Acknowledgements

The authors thank Aijun Yi for his generous help during fieldwork and sample collection. We also thank Dr Tao Luo for his helpful advice on geochronological experiments, and Dr Qishen Zhou for field support in Muling. Anonymous peer reviewers are also thanked for providing constructive comments and suggestions.

Comparison of Emeralds from the Chitral District, Pakistan, with other Pakistani and Afghan Emeralds

Carina S. Hanser, Tom Stephan, Bilal Gul, Tobias Häger and Roman Botcharnikov

ABSTRACT: Emeralds from various deposits in Pakistan (Chitral, Swat and Khaltaro) and Afghanistan (Panjshir and Laghman) were examined and compared. In addition, we compared the lighter-coloured Chitral emeralds from our previous study to newly acquired, more deeply coloured samples from Chitral. The specimens were characterised by Raman, FTIR and UV-Vis-NIR spectroscopy. Chemical analyses by EPMA and LA-ICP-MS also were performed on the samples from Chitral and Khaltaro. Distinguishing features of our Chitral emeralds include a lack of three-phase inclusions, a strong Fe^{2+} -related absorption at about 830 nm in the UV-Vis-NIR spectra, and elevated Cs and Li contents. These characteristics may provide clues for geographic origin determination.

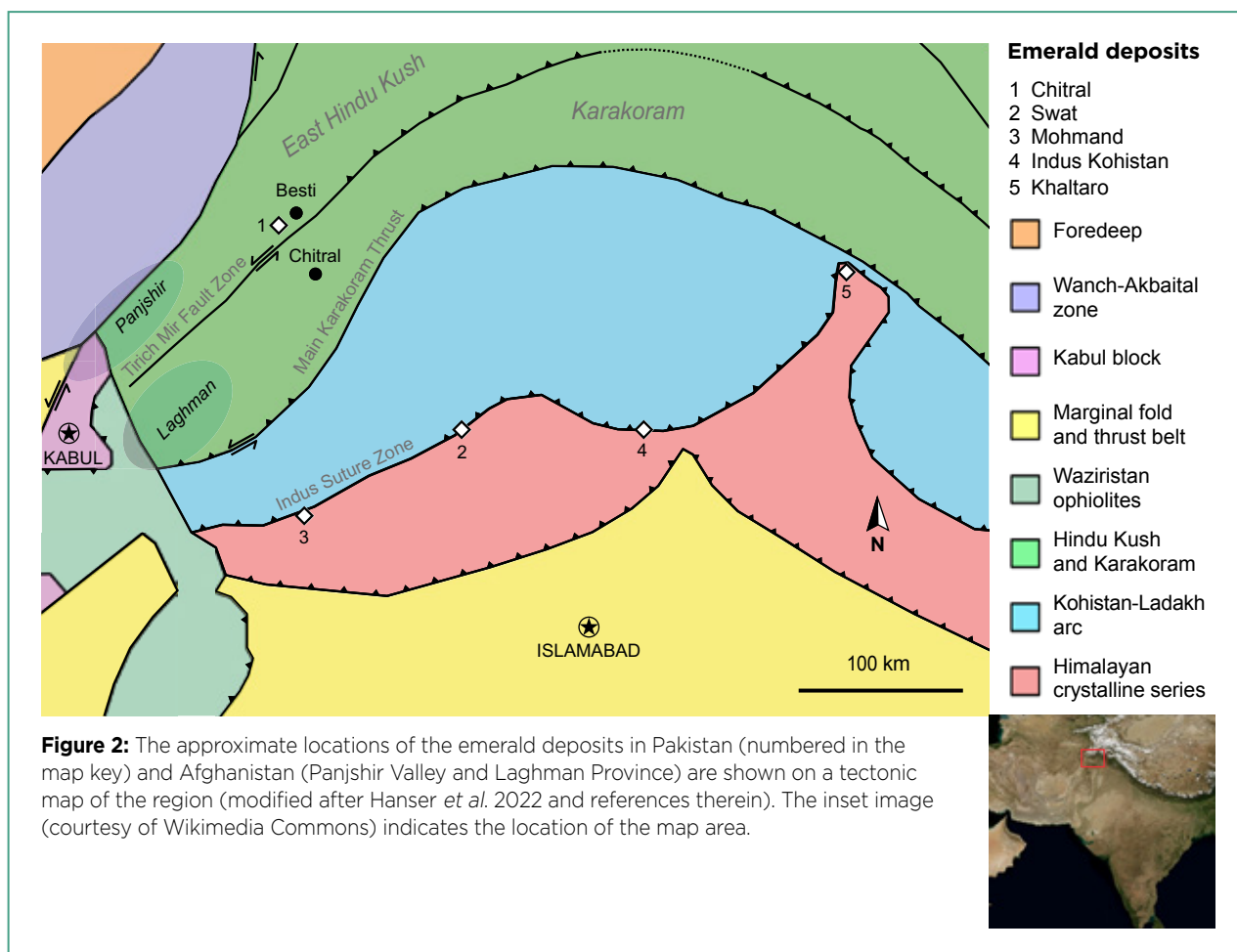
The Journal of Gemmology, 38(6), 2023, pp. 582–599, <https://doi.org/10.15506/JoG.2023.38.6.582>
© 2023 Gem-A (The Gemmological Association of Great Britain)

Emeralds from Pakistan and Afghanistan have most likely been known for thousands of years. It is widely recognised today that the so-called Bactrian emeralds from old Hindu treasures (around 1000 CE) may have originated from mines in Afghanistan and Pakistan (Schwarz & Curti 2021). Giuliani *et al.* (2000) determined the oxygen isotopic composition of an emerald set in a Gallo-Roman earring, which exhibited an isotopic signature known only from emeralds of the Swat Valley in Pakistan. This discovery is seen as proof that mining in this region has taken place since antiquity. Yet, new deposits continue to be found there, including the recent discovery in 2021 of emeralds in the Chitral District of north-western Pakistan (Hanser *et al.* 2022; see, e.g., Figure 1 and the cover of this issue).

During the late 1950s to mid-1960s, emeralds were rediscovered in the Swat and Mohmand districts of Pakistan (Kazmi & Snee 1989; Lawrence *et al.* 1989).



Figure 1: Gem-quality emeralds were recently discovered in the Chitral District of north-western Pakistan. This specimen of Chitral emerald crystals on a mica matrix weighs approximately 1.25 kg. Photo by Waqar Ahmed.



These deposits are limited to a narrow tectonic zone—the Indus suture zone (Figure 2), often also referred to as the ‘emerald belt’ (Lawrence *et al.* 1989)—in which melanges of various oceanic rocks provided the necessary Cr and V for the genesis of emeralds (Kazmi 1989; Lawrence *et al.* 1989; Snee *et al.* 1989). The later discovery (in 1985) of emeralds near Khaltaro in the Haramosh mountains—where pegmatites and hydrothermal veins intruded amphibolite—represent the first Pakistani findings outside the ‘emerald belt’ (Laurs *et al.* 1996). According to previous work, Pakistani emeralds from Swat, Mohmand and Khaltaro show differences in their chemical compositions, possibly serving as fingerprints for these localities (Snee *et al.* 1989). Further detailed studies of emeralds from Afghanistan and Pakistan have been published in recent years (e.g. Krzemnicki *et al.* 2021; Hanser *et al.* 2022). These studies include the tectonic-metasomatic deposits of the Panjshir Valley and the likely metabasite-related Laghman emeralds, both in Afghanistan (Giuliani *et al.* 2019; Krzemnicki *et al.* 2021).

Emeralds from the new deposit near Chitral in Pakistan occur in veins within quartz- and mica-rich

host rocks of the Hindu Kush mountains (Hanser *et al.* 2022). The majority of this region consists of the metapelites of the Arkari Formation, which was intruded by dykes and plutons of pegmatitic leucogranite (Khan 1986; Zahid *et al.* 2016). The remoteness and altitude of the deposit only allow limited access to the mining area by a narrow road. In 2022 this road, which previously ended several hundred metres from the mine, was extended to the mining site itself. This enabled the transport of machines to the emerald workings. Despite the strongest monsoon season in a decade, production increased from 130 kg of loose emerald in 2021 to over 300 kg in 2022.

The previous study by Hanser *et al.* (2022) mainly focused on comparing Chitral emeralds to those from the most important global localities, but some similarities of light-coloured Chitral samples to emeralds from other deposits in Afghanistan and Pakistan were established. However, the Chitral deposit also produces emeralds of more intense colour (Figure 3). This follow-up study characterises these more deeply coloured Chitral emeralds and compares them to those of other Pakistani and Afghan deposits. The main goal



Figure 3: Chitral produces emeralds with sufficiently saturated colour, such as this 11.25 ct cushion-cut stone, to make it a potentially important source for the gem market. Photo by Anne Fulton; courtesy of Dudley Blauwet Gems.

is to differentiate emeralds from these occurrences based on their physical, chemical and microscopic characteristics in order to identify features that are helpful for origin determination.

MATERIALS AND METHODS

Samples

For this study, a total of 32 emeralds were examined (Table I and Figure 4). They consisted of 22 Pakistani samples (six from Chitral, two from Khaltaro and 14 from the Swat District), and ten specimens from Afghanistan (two from Laghman Province and eight from the Panjshir Valley). The emeralds from the various mining areas in the Swat District—including two from Charbagh, four from Gujar Killi, three from Makhad and five of unspecified origin—proved to show insignificant differences, so these samples are lumped together under ‘Swat’ in this study. The samples from Swat, Laghman and Panjshir came from the reference collection of the German Gemmological Association. The Khaltaro specimens used in this study were obtained from old stock, since mining of this locality has ceased almost entirely. The Chitral emeralds were supplied by mine owner Imran Khan.

Small slices from each of the Chitral and Khaltaro emeralds were cut and polished with their faces oriented parallel to the *c*-axis, as described by Hanser *et al.* (2022). The Swat samples had been previously polished into plates with two surfaces parallel to the *c*-axis. One of the Panjshir samples consisted of a crystal which contained

some parallel faces, while the other seven Panjshir samples—and the two from Laghman—were faceted with the *c*-axis oriented parallel to the table facet.

Analyses of Chitral and Khaltaro Emeralds

The Chitral and Khaltaro emeralds were analysed at Johannes Gutenberg-University (Mainz, Germany). Refractive indices were measured with a standard refractometer and SG was determined hydrostatically. A Leica microscope was used to examine internal features. The optical path was vertical and photos were taken with an attachable camera unit.

For ultraviolet-visible-near infrared (UV-Vis-NIR), Fourier-transform infrared (FTIR) and Raman spectroscopy, polarised spectra were recorded in two directions, with the electric field vector *E* of the incident light being perpendicular (*E*⊥*c*) and parallel (*E*||*c*) to the *c*-axis. While all of the Chitral emeralds were analysed with the various spectroscopic methods, only one Khaltaro sample was transparent enough to allow UV-Vis-NIR and FTIR analyses to be performed. Details of the analysis parameters for the different techniques and instruments can be found in Hanser *et al.* (2022). However, for UV-Vis-NIR spectroscopy the acquisition times for the UV and NIR ranges were increased to 222 ms and 250 ms, respectively, to compensate for the decreasing output of an ageing light source.

The Chitral and Khaltaro emeralds were chemically analysed at Johannes Gutenberg-University by electron probe micro-analysis (EPMA; six spots per sample) and laser ablation inductively coupled plasma mass spectrometry (LA-ICP-MS; five spots per sample). Details on the instruments and their operating conditions are provided by Hanser *et al.* (2022). The trace elements Cs and Rb were determined only with LA-ICP-MS. For EPMA, the samples were embedded in acrylic using ClaroCit (powder and liquid hardener). EPMA analyses of surface-reaching inclusions utilised different standards than the beryl analyses: calibrations on pollucite and metallic vanadium were not performed; wollastonite was used for Ca and Si, and α-Al₂O₃ was used for Al (rather than diopside and aluminosilicate, respectively).

Analyses of Swat, Laghman and Panjshir Emeralds

The Swat, Laghman and Panjshir emeralds were analysed in the laboratories of the German Gemmological Association and the DSEF German Gem Lab in Idar-Oberstein, Germany. Refractive indices were measured with a standard refractometer using a contact liquid with

Table I: Emerald samples examined for this study.

Sample*	Colour	Diaphaneity	Dimensions (mm)	Weight (ct)
Chi8	Medium green	Transparent	9.06 × 11.95 × 3.17	2.959
Chi9	Dark green	Transparent (except for mica cluster)	5.42 × 9.44 × 4.09	2.272
Chi10	Medium green	Transparent	9.65 × 6.49 × 3.08	1.533
Chi11	Medium green	Transparent	10.03 × 6.54 × 3.51	1.775
Chi12	Medium green	Transparent	8.62 × 7.97 × 3.79	2.777
Chi13	Light green	Transparent	8.61 × 9.55 × 5.35	4.429
Kha1	Pale green	Translucent	6.95 × 6.81 × 2.98	1.177
Kha2	Pale green	Slightly translucent, almost opaque	9.14 × 8.02 × 2.64	1.433
Lag1	Intense green	Semi-transparent	10.59 × 10.55 × 3.98	3.546
Lag2	Dark green	Semi-transparent	11.28 × 9.03 × 3.92	2.991
Pan1	Green	Transparent	6.59 × 6.46 × 5.50	1.935
Pan2	Green	Transparent	3.07 × 3.03 × 1.91	0.122
Pan3	Green	Transparent	3.14 × 3.12 × 1.89	0.133
Pan4	Green	Transparent	4.22 × 2.74 × 1.68	0.148
Pan5	Green	Transparent	3.24 × 3.21 × 1.93	0.155
Pan6	Light green	Transparent	4.47 × 2.99 × 1.73	0.186
Pan7	Green	Transparent	3.53 × 3.52 × 2.20	0.204
Pan8	Green	Transparent	5.70 × 3.33 × 2.29	0.361
Swat1	Intense green	Transparent	3.50 × 2.58 × 1.05	0.087
Swat2	Intense green	Transparent	3.35 × 2.95 × 1.28	0.107
Swat3	Intense green	Translucent	4.03 × 2.75 × 1.58	0.138
Swat4	Intense green	Transparent	3.20 × 2.27 × 1.20	0.089
Swat5	Intense green	Transparent	2.90 × 2.64 × 1.55	0.111
Swat6	Pale green	Transparent (except for clusters of dark inclusions)	5.15 × 3.61 × 1.40	0.208
Swat7	Pale green	Transparent	3.32 × 2.90 × 1.55	0.128
Swat8	Pale green	Transparent	3.20 × 3.04 × 1.22	0.094
Swat9	Pale green	Translucent	3.07 × 2.55 × 2.01	0.170
Swat10	Green	Translucent	2.61 × 1.98 × 1.28	0.060
Swat11	Intense green	Transparent	2.86 × 2.39 × 1.80	0.105
Swat12	Intense green	Transparent	2.21 × 2.08 × 1.36	0.061
Swat13	Intense green	Translucent	2.43 × 1.97 × 1.59	0.069
Swat14	Intense green	Transparent	2.36 × 2.23 × 1.16	0.047

* Chi = Chitral, Pakistan; Kha = Khaltaro, Pakistan; Lag = Laghman, Afghanistan; Pan = Panjshir Valley, Afghanistan; Swat = Swat District, Pakistan.

$n = 1.780$. Specific gravity was determined hydrostatically. Internal features were examined using a Schneider gemmological microscope with Zeiss Stemi2000 optics.

Optical absorption spectra were collected in both E||c and E⊥c directions with a PerkinElmer Lambda 950S UV-Vis-NIR spectrometer in the 200–2500 nm range, with a spectral resolution of 1 nm. Deuterium and tungsten halogen lamps were used as light sources. A detector change took place at 810 nm; longer wavelengths were recorded with an InGaAs detector, and shorter wavelengths with a photomultiplier tube.

In the 200–810 nm range the slit width was fixed at 4 nm, and for 810–2500 nm it was variable (2–4 nm). The device was equipped with an integration sphere to collect scattered light.

Infrared spectra were collected with a Magilabs GemmoFtir diffuse reflectance infrared Fourier transform (DRIFT) spectrometer. Polarisation is not possible with this device, so unpolarised spectra were recorded. Each sample was measured in the 400–7500 cm^{-1} range with 64 accumulations.

Raman spectroscopy of the emeralds was performed

using a Renishaw InVia Raman spectrometer with excitation in both E_Lc and E_{||}c directions. The device was equipped with a 514 nm laser, a CCD detector and a grating with 1,200 lines/mm. The acquisition time was 10 s for each interval, and two accumulations were measured for each sample. The confocal analysis spot was focused slightly into the sample to avoid surface effects. Selected inclusions were identified with the same instrumentation using 514 and 785 nm lasers (and a grating with 1,800 lines/mm for the latter laser).

RESULTS

Sample Description

As with the previous Chitral emerald study (Hanser *et al.* 2022), the six Chitral samples examined here consisted of fragments of larger crystals, although some crystal faces were recognisable. In contrast to the previous study, the present Chitral samples were of higher quality, with a more saturated green colour and/or fewer inclusions (Figure 4a). Five of the emeralds were medium to dark green and only one sample (Chi13) was light green. Apart from a large mica cluster inclusion in Chi9, all six Chitral samples were transparent. However, the two Khaltaro samples were translucent to almost opaque (i.e. heavily included

and fractured; again, see Figure 4a). Although several pieces were sawn from the original rough sample Kha2, none were suitable for UV-Vis-NIR and FTIR analyses because the lack of diaphaneity did not allow enough light to be transmitted.

The samples from Panjshir, Laghman and Swat are shown in Figure 4b. All of the Panjshir samples were transparent. The crystal fragment (Pan1) was heavily included, but the faceted stones (Pan2–8) were quite clean. The Panjshir emeralds were mostly of a saturated green colour (some slightly yellowish). By contrast, the two faceted samples from Laghman were deeper green, semi-transparent and quite fractured. The Swat samples consisted of smaller, transparent to translucent fragments showing pale to intense green colouration (some slightly bluish). Some of the fragments were heavily included, particularly with eye-visible dark inclusions. One Swat sample (Swat5) was twinned.

Gemmological Properties and Inclusions

A summary of the gemmological properties and internal features in the study samples is provided in Table II. A variety of inclusions were present and some of them—such as partially healed fissures, hollow tubes, two-phase inclusions, carbonates and micas—were found to occur in samples from almost all of the localities.



Figure 4: The samples examined for this study consisted of: (a) six Chitral and two Khaltaro emeralds; and (b) reference emerald samples from the collection of the German Gemmological Association that originated from Laghman (two faceted stones), Panjshir (one crystal fragment and seven faceted stones) and the Swat District (14 polished fragments from various mining localities there). See Table I for the dimensions and weights of the stones. Photos by (a) C. S. Hanser and (b) T. Stephan.

Chitral. Two-phase inclusions in the Chitral samples were of a more-or-less rectangular to irregular shape (Figure 5a–d). The gas bubbles therein were mostly round, but some fluid inclusions contained more gas, which took up the majority of the space in these inclusions, thus causing the bubbles to become elongated (Figure 5d). Hollow tubes sometimes contained yellowish precipitates (Figure 5e, f). Although these solids could not be identified by Raman spectroscopy or EPMA, they may be iron hydroxides. One Chitral sample also contained a colourless rod-like crystal that reached the surface (Figure 5g), but it could not be analysed since it was on the side of the specimen that was mounted in acrylic. Fissures showing iridescent reflections were also seen (Figure 5h).

EPMA analyses of surface-reaching inclusions in the Chitral emeralds (Figure 6 and Table III) revealed that white, irregular crystal aggregates consisted of several mineral phases, including calcite, K-feldspar, plagioclase and quartz. The composition of plagioclase corresponded to oligoclase and andesine (cf. Deer *et al.* 2001), with CaO contents of approximately 3–8 wt.%. Darker inclusions were identified as phlogopite (Figure 6f, g). Only one mica inclusion analysed was consistent with the composition of muscovite (cf. Fleet 2003). Apart from phlogopite, no other dark mineral inclusions were present in the samples from Chitral.

Khaltaro. The Khaltaro samples contained many, mostly light-coloured, inclusions. White crystals typically consisted of calcite and albite (with less than 0.5 wt.% CaO; see Table III and Figure 7a). Mica was also present, with compositions corresponding to muscovite (Table III and Figure 7a; cf. Laurs *et al.* 1996). In addition, the

Khaltaro samples contained altered, partly dissolved elongate crystal inclusions, some of which exhibited recognisable crystal faces (Figure 7b). Their appearance suggested an amphibole, but Raman spectroscopy and EPMA analyses identified them as muscovite.

Panjshir. The most common internal features in the Panjshir samples were fluid inclusions, which were present as partially healed fractures, isolated negative crystals (i.e. three-phase inclusions; Figure 8a, b) and hollow tubes (Figure 8c). The tubes were observed in all samples, always elongated parallel to the *c*-axis. The surface-reaching ones were sometimes filled with a yellowish brown substance (most likely iron hydroxides). The fluid inclusions in the Panjshir specimens contained two or three phases. In the larger ones especially, we observed the typical combination of a liquid, a gas and a solid (cubic) phase, as is also known to occur in Colombian emeralds. According to Bowersox *et al.* (1991), the three-phase inclusions in Panjshir emeralds contain up to eight daughter crystals, an H₂O-dominated liquid and CO₂ as the gaseous phase. The solid inclusions are most commonly halite (NaCl), but sometimes sylvite (KCl). Often, the three-phase inclusions were oriented along the *c*-axis and had rectangular shapes, but in other orientations they showed irregular shapes with jagged outlines.

The solid inclusions in our Panjshir emeralds consisted of irregular-shaped to well-formed rhombohedral carbonate inclusions (most likely calcite and/or dolomite), as well as colourless crystals, mostly in irregular shapes. Some were identified as quartz, others as feldspar. In addition, sample Pan1 hosted dark, opaque inclusions with a metallic lustre (Figure 8d). These were

Table II: Summary of the standard gemmological properties of the emeralds examined for this study.

Locality	SG	RIs	Birefringence	Inclusions
Chitral, Pakistan	2.71–2.74	1.580–1.582 1.589–1.590	0.008–0.009	Quartz, calcite, plagioclase (andesine, oligoclase), K-feldspar, phlogopite, muscovite (minor amounts), two-phase inclusions, partially healed fissures, hollow tubes
Khaltaro, Pakistan	2.65–2.73	1.581–1.590	0.009	Calcite, plagioclase (almost pure albite), muscovite
Laghman, Afghanistan	2.77	1.584–1.592	0.008	Two- and three-phase inclusions, partially healed fissures, hollow tubes, mica (biotite), growth structures parallel to the <i>c</i> -axis
Panjshir, Afghanistan	2.70–2.78	1.578–1.586 1.585–1.593	0.008–0.009	Two- and three-phase inclusions (with serrated rims), partially healed fissures, hollow tubes, carbonates (probably calcite or dolomite), opaque cubes (probably pyrite), colourless crystals (quartz and feldspar), strong growth structures (both parallel and perpendicular to the <i>c</i> -axis)
Swat, Pakistan	2.73–2.78	1.582–1.593 1.590–1.602	0.008–0.009	Micas (probably biotite/phlogopite and muscovite), carbonates (probably calcite or dolomite), talc(?), two-phase (rarely three-phase) inclusions, liquid thin films, partially healed fissures, hollow tubes, colour zoning, black opaque minerals (probably spinel and/or pyrite)

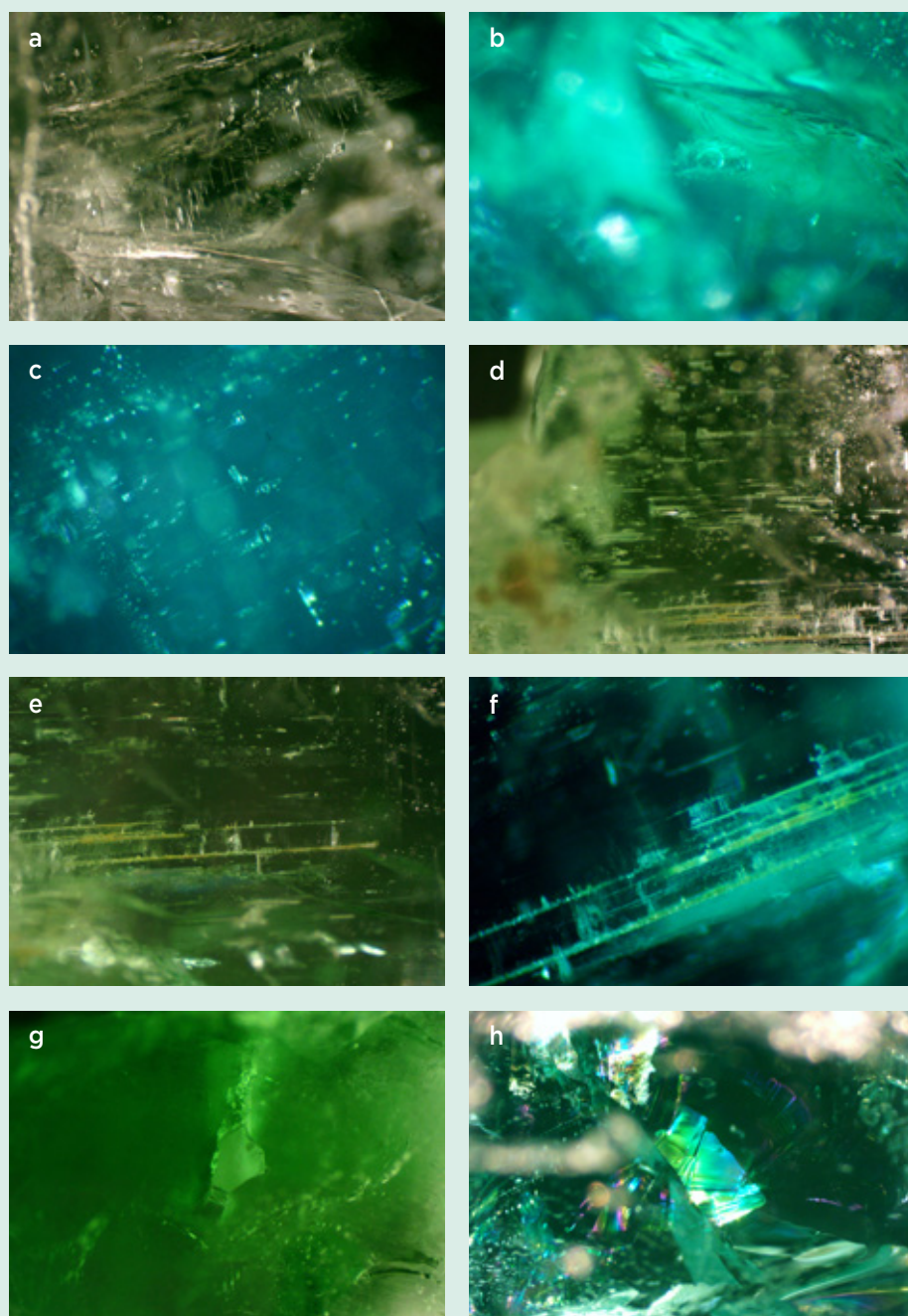


Figure 5: Inclusions found in the Chitral emeralds of this study include (a) partially healed fissures composed of two-phase fluid inclusions (sample Chi12; magnified 30×); (b) irregular two-phase fluid inclusions (Chi8; 100×); (c) rectangular two-phase fluid inclusions (Chi13; 100×); (d) thin, needle-like two-phase fluid inclusions with elongated gas bubbles and growth tubes (Chi13; 30×); (e) growth tubes (Chi13; 30×); (f) hollow tubes, partially filled with yellow precipitates, which may be iron hydroxides (Chi13; 100×); (g) a surface-reaching, rod-like, colourless crystal (Chi11; 30×); and (h) fissures showing bright iridescent reflections (Chi8; 30×). Photomicrographs by C. S. Hanser.

mostly irregularly shaped to rounded, and some had a subhedral cubic shape. They could not be identified by Raman spectroscopy because of a weak signal, but most likely consisted of pyrite (Bowersox *et al.* 1991; Schwarz & Pardieu 2009; Schwarz & Curti 2021).

Other internal features in the Panjshir samples included prominent growth structures parallel and perpendicular to the *c*-axis, often with typical ‘sawtooth’ structures.

Overall, our observations of the Panjshir emeralds are consistent with the literature (Bowersox *et al.* 1991; Moroz & Eliezri 1999; Sabot *et al.* 2001; Schwarz & Pardieu 2009; Schwarz & Curti 2021). However, these

authors additionally mentioned limonite, beryl, tourmaline and graphite inclusions.

Laghman. The two faceted Laghman emeralds possessed low transparency, particularly due to many cracks and fissures, as well as tiny liquid inclusions (Figure 9a). These same samples were also studied previously by Henn and Schmitz (2014), who identified flake-like doubly refractive mineral inclusions as micas in both stones (Figure 9b). EPMA analysis by Henn and Schmitz (2014) of one such surface-reaching inclusion identified it as biotite. Henn and Schmitz (2014) also reported

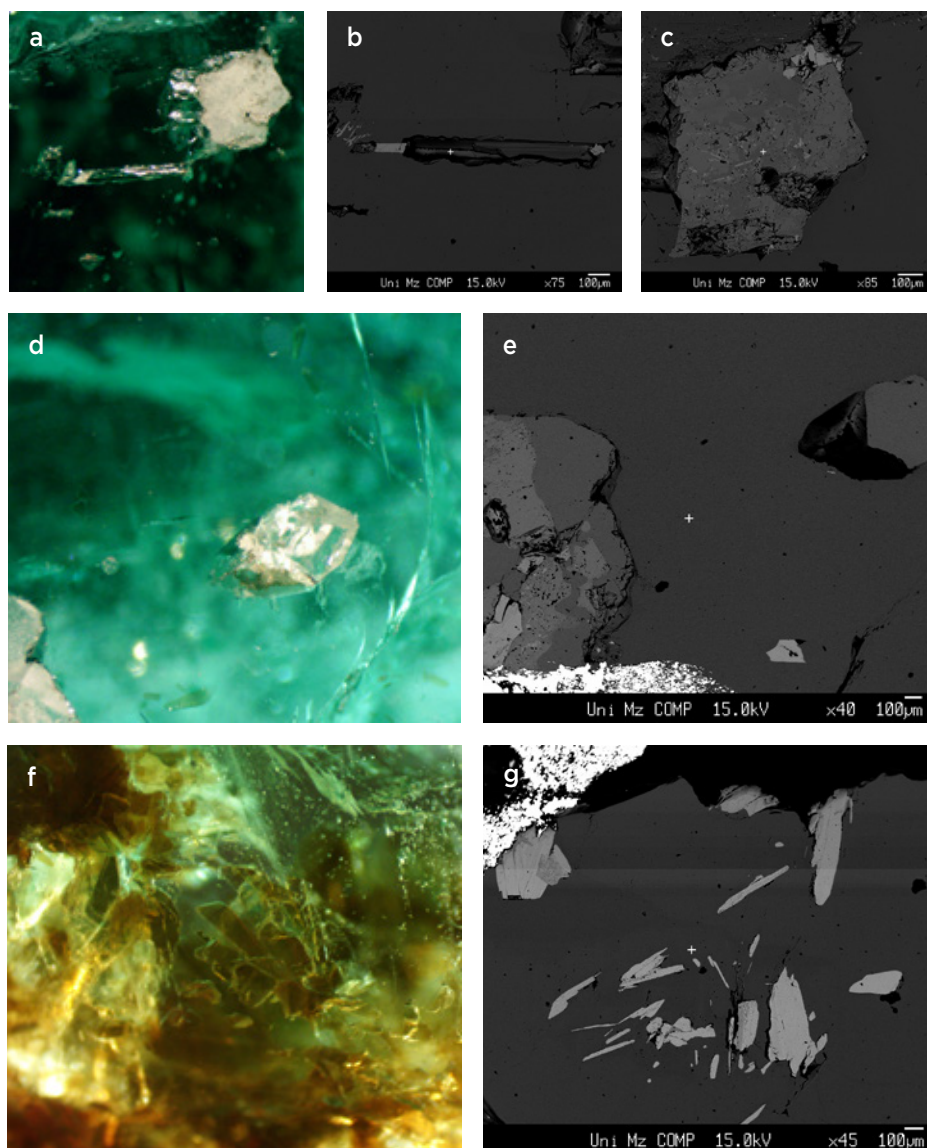


Figure 6: A number of surface-reaching inclusions were analysed by EPMA in the Chitral emeralds. (a) A rod-like crystal and a white, irregular inclusion were present in sample Chi8 (30×). Back-scattered electron (BSE) images obtained during EPMA analysis show (b) the rod-like crystal and (c) the irregular inclusion. The various grey tones seen in the irregular inclusion are due to differences in overall atomic weight corresponding to different mineral phases (identified as calcite, andesine, oligoclase and K-feldspar). (d) The colourless, partly euhedral crystal inclusion in the centre of this image of sample Chi8 was identified as quartz, while a cluster of inclusions at the lower left consists of quartz, andesine and K-feldspar (30×). (e) A BSE image is shown for a portion of the same area. The dark feature in the quartz crystal indicates where part of the crystal was plucked out during the cutting process. (f) A cluster of brown mica flakes is seen in Chi9 (30×). (g) A BSE image shows a similar cluster of mica (primarily phlogopite) in the same sample. Photomicrographs by C. S. Hanser and BSE images by N. Groschopf.

Table III: Representative EPMA analyses of inclusions in emeralds from Chitral and Khaltaro, Pakistan.^a

Mineral	Oligoclase	Andesine	K-feldspar	Quartz	Calcite	Phlogopite	Muscovite	Albite	Muscovite
Sample no.	Chi8					Chi9		Kha2	
Oxide (wt.%)									
SiO ₂	64.19	58.18	64.78	99.75	0.08	39.79	48.64	67.75	47.26
TiO ₂	nd	nd	0.03	nd	0.04	0.64	0.12	nd	0.03
Al ₂ O ₃	21.73	25.85	18.11	0.04	nd	14.33	28.24	19.48	29.95
Cr ₂ O ₃	0.01	0.02	0.01	0.01	0.01	0.25	0.40	0.05	0.17
FeO	0.02	0.03	0.02	nd	0.11	9.83	0.66	0.04	1.76
MnO	0.01	0.02	nd	nd	nd	0.10	0.01	nd	0.31
MgO	0.01	nd	0.02	nd	0.05	18.00	2.86	nd	2.49
CaO	3.07	8.08	nd	nd	60.78	nd	nd	0.27	nd
Na ₂ O	9.98	7.33	0.05	nd	nd	0.32	0.27	11.66	0.30
K ₂ O	0.05	0.05	15.96	0.02	0.02	8.90	10.61	0.09	10.77
Total	99.07	99.57	98.99	99.83	61.10 ^b	92.16 ^b	91.81 ^b	99.34	93.04 ^b

^a Abbreviation: nd = not detected.

^b Total oxide content is low because CO₂, H₂O and possibly F cannot be determined by EPMA.

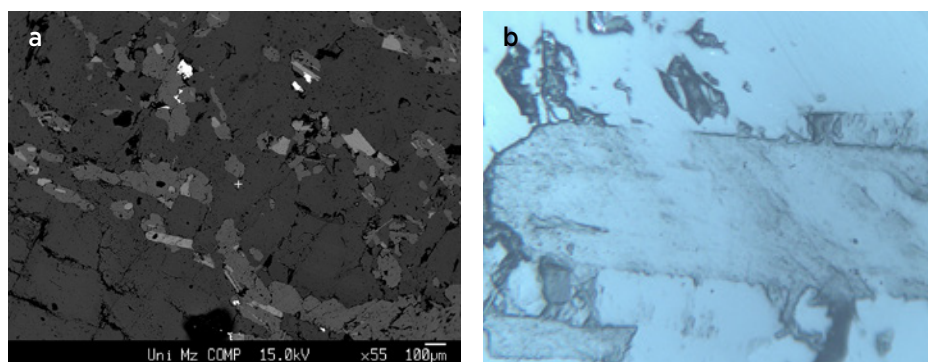


Figure 7: Various inclusions were analysed by EPMA in the Khaltaro emeralds. (a) This BSE image of Kha2 contains inclusions of mica, albite and calcite. (b) An elongated inclusion in Kha2 has an appearance that resembles an amphibole, but it was identified as muscovite (500 \times). Photomicrograph by C. S. Hanser and BSE image by N. Groschopf.

hollow tubes, rectangular two-phase negative crystals oriented parallel to the *c*-axis (Figure 9a) and partially healed fractures composed of tiny liquid droplets. In addition, Krzemnicki *et al.* (2021) mentioned amphibole (tremolite), mica (especially phlogopite) and graphite inclusions in Laghman emeralds.

In the present study, we identified no additional solid or liquid inclusions, except for yellowish brown substances in surface-reaching fissures and hollow tubes, again most likely iron hydroxides. The samples also showed prominent growth structures parallel to the *c*-axis.

Swat. The study samples from the Swat Valley were quite included, and all of them contained partially healed fractures composed of small liquid droplets which, in the larger ones, also contained a gas bubble. In addition, three-phase inclusions have been reported in Swat emeralds (Guo *et al.* 2020). Besides these fluid inclusions, larger

isolated two-phase negative crystals were also common in our samples, mainly with rectangular shapes parallel to the *c*-axis, but also showing irregular forms in other orientations. In addition, hollow tubes were observed.

The most common solid inclusions in the Swat emeralds were black opaque minerals (Figure 10), usually irregular in shape and with moderate-to-strong metallic lustre. They typically formed groups or were present as clouds. It was not possible to identify these inclusions with Raman spectroscopy due to their weak signal, but according to the literature they are most likely spinel and/or pyrite (Schwarz & Curti 2021). Flake-like mineral inclusions with strong double refraction were identified as mica. The colourless transparent ones were most likely muscovite, while the darker, brownish ones were probably biotite or phlogopite.

Irregularly shaped to partly rhombohedral transparent mineral inclusions were identified by Raman

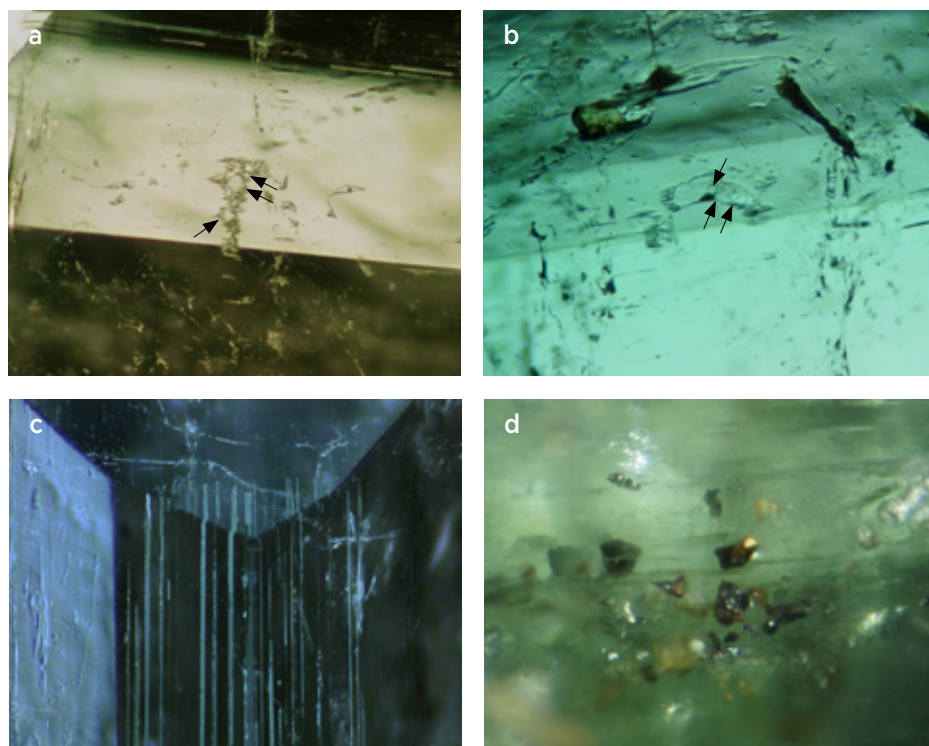


Figure 8: The Panjshir emeralds of this study exhibit both fluid and solid inclusions. (a, b) Sample Pan7 contains three-phase inclusions that each hosts three daughter crystals, which are marked by arrows (both 50 \times). (c) Hollow tubes are present in specimen Pan8 (40 \times). (d) Metallic inclusions, probably pyrite, are seen in sample Pan1 (50 \times). Photomicrographs by T. Stephan.

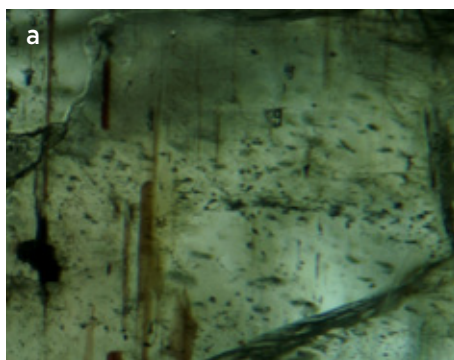


Figure 9: (a) Laghman emerald Lag2 contains abundant two-phase inclusions and brownish flakes that are most likely biotite (50×). (b) A mica inclusion is seen in Laghman sample Lag1 (40×); a similar inclusion was identified as biotite by Henn and Schmitz (2014). Photomicrographs by T. Stephan.

spectroscopy as carbonates, most likely calcite and/or dolomite (cf. Gübelin 1982). Furthermore, some colourless to slightly greenish mineral inclusions were present, often as scaly to flaky crystals, and sometimes also irregularly distributed along fissures (Figure 10b). Owing to their small size and irregular distribution in fissures, these inclusions could not be identified by Raman spectroscopy, but they are most likely talc (cf. Gübelin & Koivula 2008; Schwarz & Curti 2021).

Growth lines were rarely observed in our Swat samples, but all showed weak-to-strong colour zoning, which was most obvious along the *c*-axis. Growth lines were previously described in Swat emeralds by Gübelin (1982) and by Schwarz and Curti (2021).

Our observations are consistent with the literature for Swat emeralds (Gübelin 1982; Gübelin & Koivula 2008; Schwarz & Curti 2021). Additional mineral inclusions documented by these other authors include actinolite, albite, magnesite, chlorite, chromite, enstatite, fuchsite, gersdorffite, plagioclase, pyrrhotite and quartz.

UV-Vis-NIR Spectroscopy

Figure 11 displays representative UV-Vis-NIR spectra (for the E_Lc direction) for emeralds from the various localities. (Spectra for the E_{||}c direction are not shown since they are not as helpful for origin determination.) While all the samples exhibit V- and Cr-related absorptions, Fe-related features were noticeably stronger in some of them, especially those from Chitral and Laghman. The

broad Fe²⁺ absorption around 830 nm is only weakly visible to absent in the emeralds from Panjshir and Swat (for the latter, regardless of the specific mine locality). Weaker absorption due to Fe²⁺ than to Cr³⁺ and V³⁺ is reported in the literature for emeralds from both Panjshir and Swat (Guo *et al.* 2020; Krzemnicki *et al.* 2021). By contrast, the Laghman emeralds showed similar to higher absorption intensities for Fe²⁺ compared to Cr³⁺ and V³⁺, consistent with the literature (Krzemnicki *et al.* 2021). In the Chitral emeralds, the Fe²⁺ absorption was always stronger than the Cr³⁺ and V³⁺ features, which is consistent with previous findings (Hanser *et al.* 2022; see also the spectrum for sample PK1 in Figure 11).

Near-Infrared Spectroscopy

Representative near-infrared spectra of the Chitral and Khaltaro emeralds are shown in Figure 12. Several H₂O overtone peaks (Wood & Nassau 1967; Schmetzer & Kiefert 1990; Qiao *et al.* 2019; Hu & Lu 2020; Wang *et al.* 2022) are present in both the E_{||}c and E_Lc spectra in the 6800–7300 cm⁻¹ region (with fewer peaks in the E_Lc direction). In general, the patterns of these spectra agree with those of the lighter-coloured Chitral emeralds examined by Hanser *et al.* (2022), as can be seen by comparison with sample PK2 in Figure 12.

The same features were observed for the samples from Panjshir, Laghman and Swat, but those spectra were unpolarised and therefore are not shown for comparison.

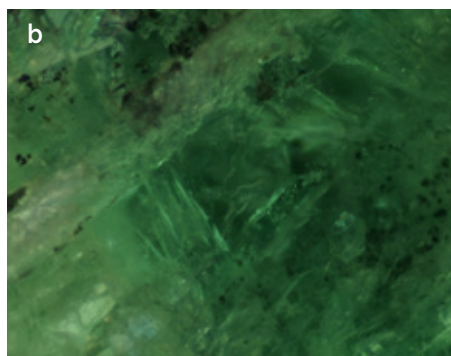
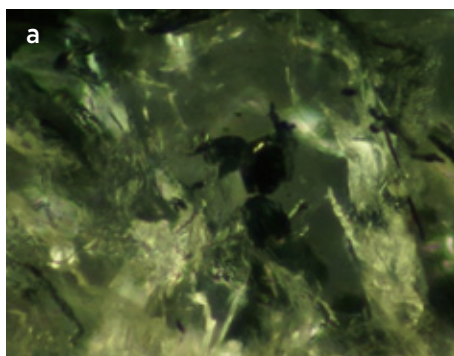


Figure 10: (a) Black and metallic inclusions, probably spinel and pyrite, respectively, are present in Swat emerald sample Swat5 (50×). (b) Emerald Swat12 contains a whitish vein (probably talc) and dark-appearing metallic inclusions (40×). Photomicrographs by T. Stephan.

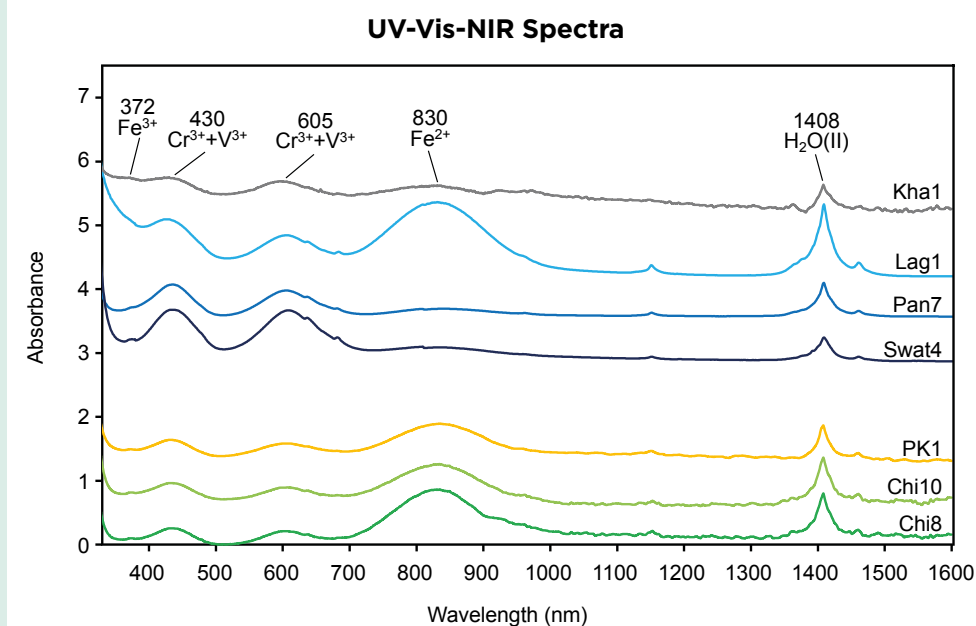


Figure 11: Representative UV-Vis-NIR spectra (for E_{Lc}) for emeralds of this study are shown along with the spectrum of a Chitral sample (PK1) that was documented previously by Hanser *et al.* (2022). The spectra are offset vertically for clarity.

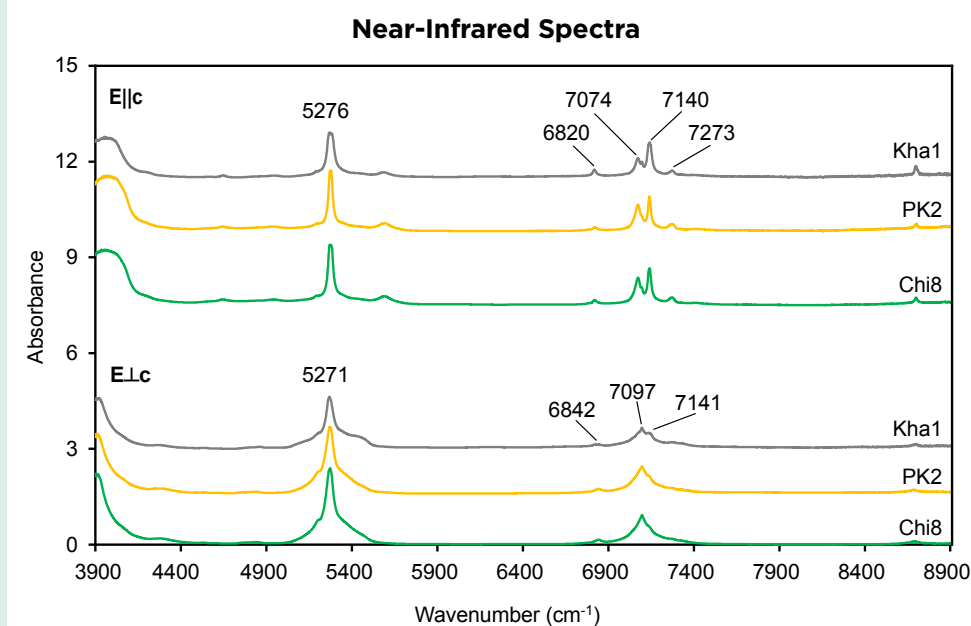
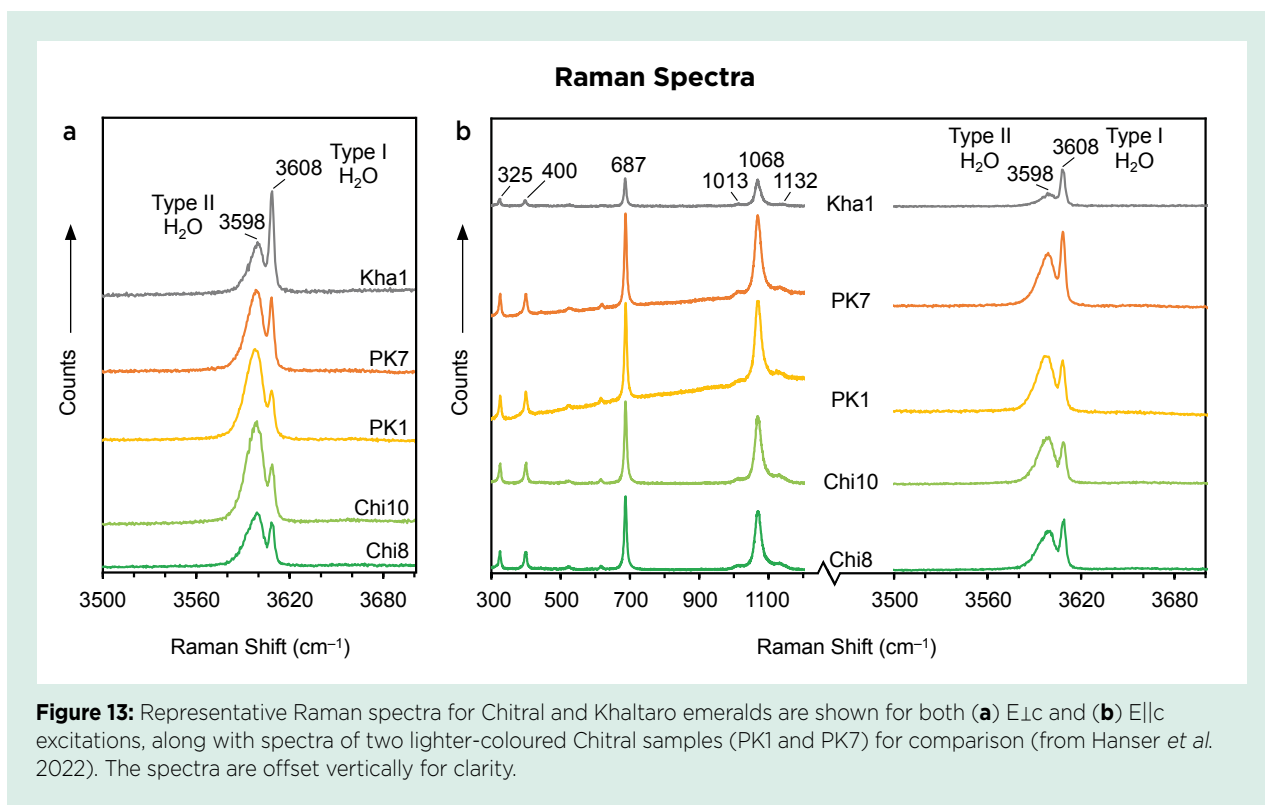


Figure 12: Representative near-infrared spectra of emeralds from Chitral (Chi8) and Khaltaro (Kha1) are shown for both the E_{||c} and E_{⊥c} directions. A representative spectrum of a lighter-coloured Chitral emerald (PK2) is provided for comparison (from Hanser *et al.* 2022). The spectra are offset vertically for clarity.

Raman Spectroscopy

For the E_{⊥c} excitation direction (Figure 13a), in all the Chitral emerald samples the type I H₂O peak at a Raman shift of approximately 3608 cm⁻¹ (Huong *et al.* 2010; Karampelas *et al.* 2019) was weaker than the type II H₂O peak at about 3598 cm⁻¹ (Hagemann *et al.* 1990; Huong *et al.* 2010; Karampelas *et al.* 2019). This is consistent with our previous observations for lighter-coloured Chitral emeralds (see samples PK1 and PK7 in Figure 13a).

While the strength of these features was reversed in some Chitral samples for the E_{||c} direction (Figure 13b), the type I H₂O peak was stronger in both our Khaltaro samples, independent of the excitation direction. The Swat, Laghman and Panjshir emeralds also displayed strong type II water peaks (not shown here). This is in accordance with previous findings by Krzemnicki *et al.* (2021), who reported stronger type II water peaks for Laghman and some Panjshir emeralds.



Chemical Composition

Chemical analyses of the Chitral and Khaltaro emeralds by EPMA and LA-ICP-MS are summarised in Tables IV and V, respectively. In addition, *The Journal's* online data depository contains all of the EPMA and LA-ICP-MS data obtained for this study (Tables DD-1 and DD-2, respectively), as well as all of the LA-ICP-MS analyses done by Hanser *et al.* (2022) on the previously examined Chitral emeralds (Table DD-3). Chemical plots from the EPMA and LA-ICP-MS data obtained for the present study, which also include analyses from the literature, are shown in Figures 14 and 15. For both analytical techniques, the chemical data for the Chitral emeralds in the present study are mostly in agreement with previous analyses reported by Hanser *et al.* (2022).

The contents of MgO and Na₂O show a positive correlation overall (Figure 14a). In general, lower concentrations of these elements are seen in Panjshir emeralds compared to those from Chitral, but they are enriched in Swat emeralds (Hammarstrom 1989; Aurisicchio *et al.* 2018). The contents of Mg and Na in the Laghman emeralds overlap those of Chitral (cf. Krzemnicki *et al.* 2021), and both of these elements were less abundant in the Khaltaro samples (Figure 14a and Table IV). In addition, some other common elements found in emerald—including Fe, Ca and V—were higher in the samples from Chitral than in

those from Khaltaro. Concentrations of other elements—such as Li, K, Sc, Ti, Cr, Ga and Rb—overlapped between both localities, whereas Mn and Zn were at least twice as high in the Khaltaro emeralds. Concentrations of Fe overlap among emeralds from all the localities represented in this study (Figure 14b; see also Hammarstrom 1989 and Aurisicchio *et al.* 2018), except for the higher Fe values reported in Swat emeralds by Aurisicchio *et al.* (2018).

The Li contents of the Chitral samples were generally higher than in emeralds from all of the other Pakistani and Afghan localities except, in some cases, Khaltaro (Figure 15a; Guo *et al.* 2020; Krzemnicki *et al.* 2021; Chen *et al.* 2022). In addition, the Chitral emeralds showed notable Cs enrichment, generally exceeding the contents found in stones from the other localities considered in this study (except for Khaltaro in some cases; Figure 15b). Panjshir and Swat emeralds have low Cs values (Guo *et al.* 2020; Chen *et al.* 2022), but higher Cs contents are found in emeralds from Laghman (Krzemnicki *et al.* 2021). Similar trends apply to Rb (again, see Figure 15b; Guo *et al.* 2020; Krzemnicki *et al.* 2021; Chen *et al.* 2022). Overall, Cs shows a positive correlation with Rb for the analysed emeralds from Chitral, although not necessarily for the other localities.

The chromophores Cr and V also exhibited a positive correlation for the analysed stones from Chitral, but

Table IV: Average EPMA analyses of emeralds from Chitral and Khaltaro, Pakistan.^a

Sample no.	Chi8	Chi9	Chi10	Chi11	Chi12	Chi13	Kha1	Kha2
Locality	Chitral						Khaltaro	
Oxide (wt.%)								
SiO ₂	63.80	63.63	63.62	63.70	63.95	64.41	64.86	64.93
TiO ₂	0.01	nd	nd	nd	nd	nd	nd	0.01
Al ₂ O ₃	15.90	15.75	15.47	15.58	15.26	16.11	17.35	16.96
Cr ₂ O ₃	0.12	0.17	0.11	0.12	0.10	0.09	0.08	0.23
V ₂ O ₃	0.05	0.07	0.05	0.05	0.06	0.04	0.02	0.01
Fe ₂ O ₃	0.57	0.54	0.59	0.63	0.54	0.50	0.27	0.41
BeO ^b	13.60	13.60	13.60	13.60	13.60	13.60	13.60	13.60
MgO	1.60	1.70	1.81	1.74	1.93	1.61	0.81	0.98
CaO	0.03	0.04	0.05	0.05	0.05	0.03	nd	nd
Na ₂ O	1.54	1.58	1.54	1.46	1.52	1.47	1.04	1.01
K ₂ O	0.04	0.04	0.06	0.05	0.06	0.03	0.03	0.04
H ₂ O ^b	0.85	0.85	0.85	0.85	0.85	0.85	0.85	0.85
Total	98.11	97.97	97.75	97.83	97.92	98.74	98.91	99.03
FeO ^c	0.51	0.48	0.53	0.57	0.49	0.45	0.24	0.37

^a Averages are of six spots per sample. See *The Journals* online data depository for complete data. Abbreviation: nd = not detected.

^b H₂O and BeO contents are fixed values, as commonly reported for beryl.

^c The standard format for reporting Fe content in beryl by our instrument is Fe₂O₃, which is here recalculated to FeO.

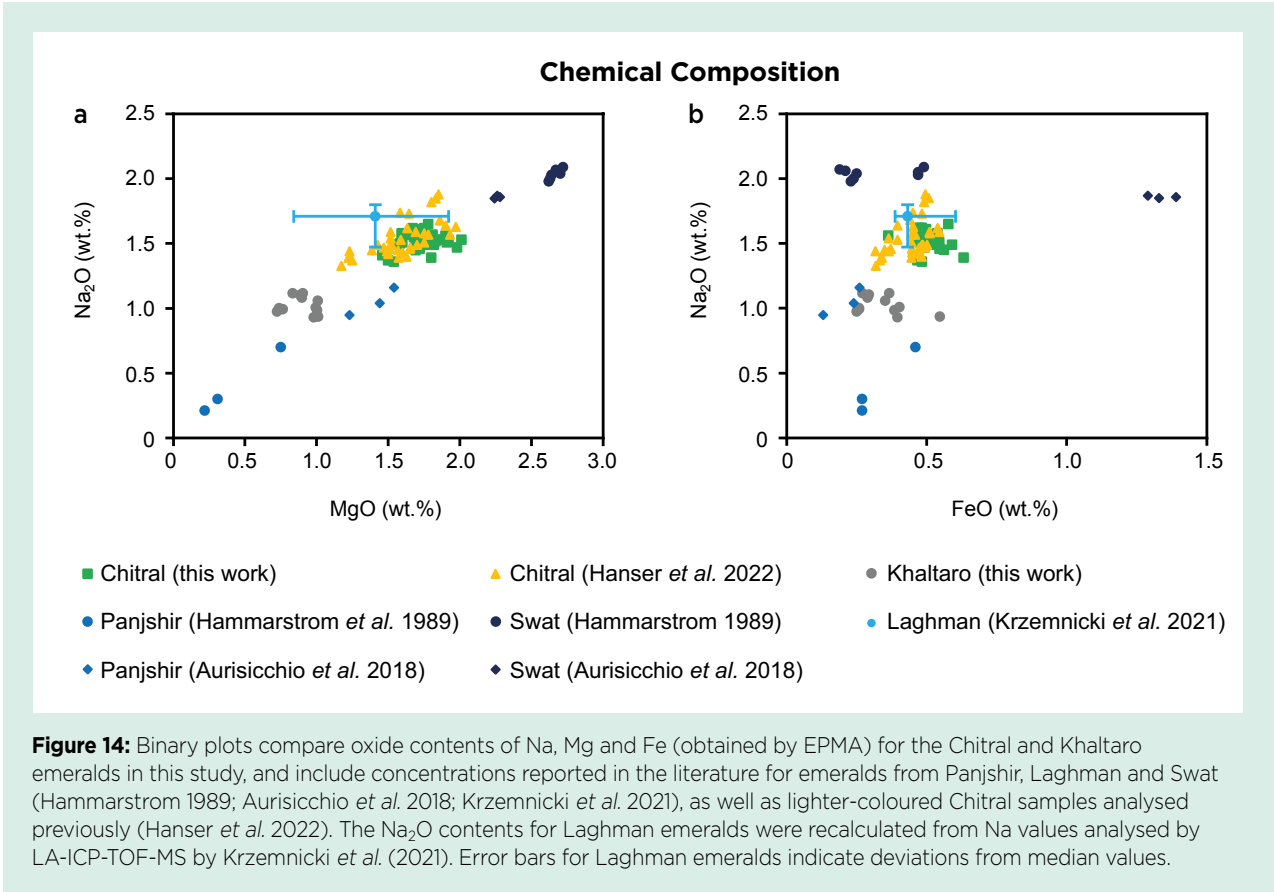


Table V: Average LA-ICP-MS analyses of emeralds from Chitral and Khaltaro, Pakistan.*

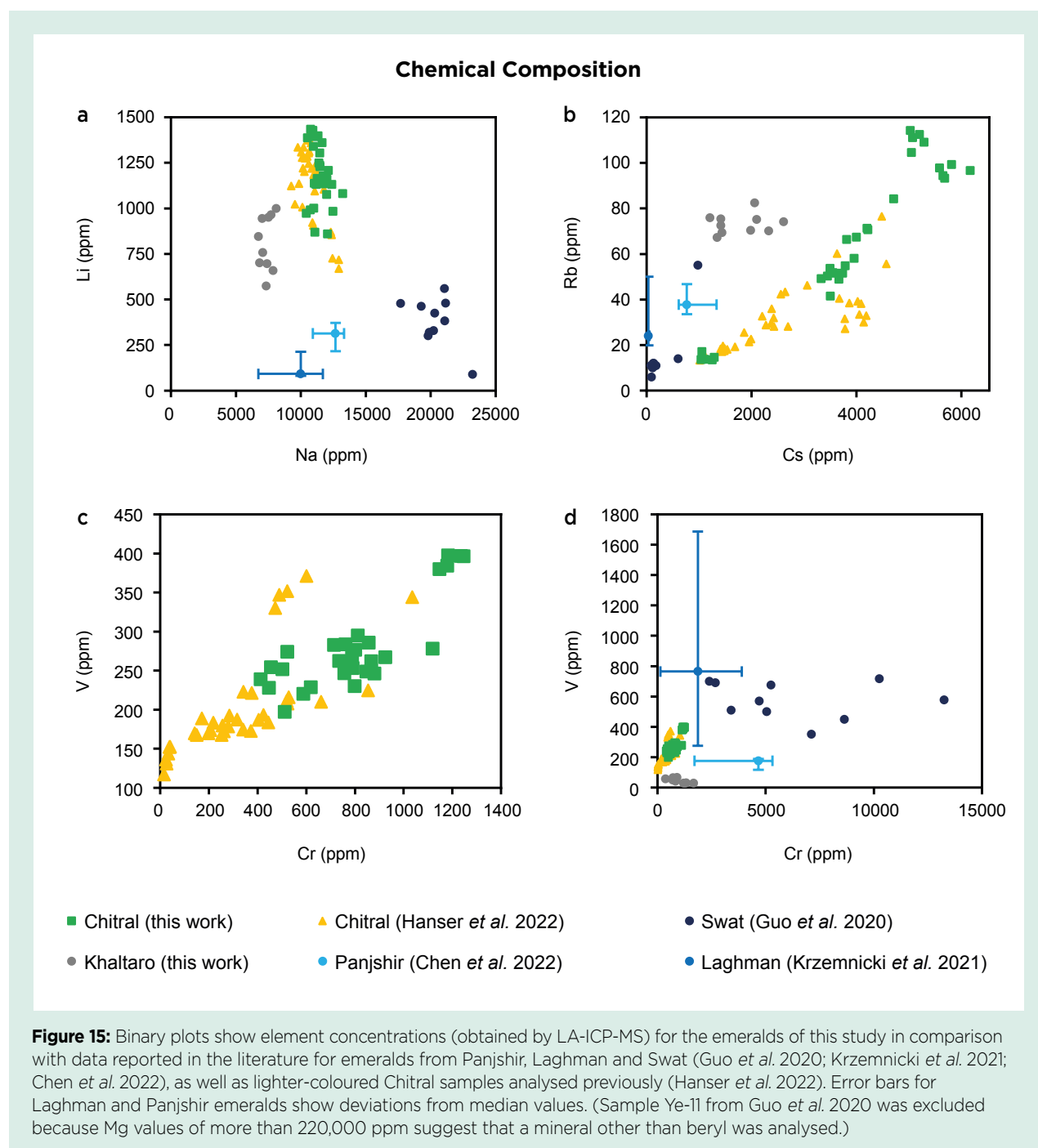
Sample no.	Chi8	Chi9	Chi10	Chi11	Chi12	Chi13	Kha1	Kha2
Locality	Chitral						Khaltaro	
Element (ppm)								
Li	1133 (96.12)	1136 (37.49)	1231 (138.5)	1359 (80.70)	1309 (106.7)	938.7 (68.66)	940.7 (57.31)	677.6 (67.53)
Be	48080 (1567)	48330 (568.2)	47850 (871.2)	47350 (892.3)	46800 (568.8)	47500 (577.2)	47540 (1435)	48630 (710.2)
B	nd	1.56 (0.20)	2.16 (0.64)	nd	1.72 (0.28)	nd	nd	nd
Na	11490 (576.6)	11790 (197.6)	12040 (878.3)	10940 (359.8)	11530 (345.2)	11070 (617.5)	7434 (542.9)	7315 (386.4)
Mg	9188 (435.5)	9794 (184.3)	10640 (370.7)	10030 (566.9)	11140 (513.2)	9182 (602.8)	4407 (367.1)	5285 (809.0)
K	262.8 (20.32)	302.0 (4.89)	459.6 (43.76)	375.2 (23.75)	476.5 (25.19)	199.6 (15.64)	196.9 (30.69)	278.2 (612.50)
Ca	304.7 (67.74)	266.9 (61.05)	506.4 (38.32)	395.9 (104.3)	467.0 (67.66)	306.1 (55.21)	nd	nd
Sc	95.19 (3.95)	118.7 (4.35)	54.12 (3.47)	95.36 (3.50)	68.36 (3.54)	66.16 (15.14)	75.29 (13.14)	43.37 (25.12)
Ti	12.59 (3.21)	11.52 (1.54)	11.59 (0.77)	11.42 (1.47)	18.62 (1.61)	14.13 (1.82)	11.37 (5.48)	17.57 (6.53)
V	251.0 (14.54)	391.1 (8.21)	265.1 (14.24)	271.6 (17.55)	269.4 (15.46)	222.7 (15.65)	48.69 (13.10)	36.80 (16.82)
Cr	862.9 (46.34)	1197 (41.63)	779.0 (46.96)	858.4 (145.7)	590.3 (136.8)	514.9 (88.40)	659.7 (199.4)	1279 (276.5)
Mn	22.67 (2.83)	17.86 (0.72)	22.63 (1.59)	26.60 (1.37)	18.78 (1.52)	15.85 (1.82)	52.52 (3.26)	59.74 (28.32)
Fe	3876 (216.2)	3695 (135.1)	3965 (163.7)	4164 (213.0)	3659 (143.1)	3413 (301.5)	1789 (20.82)	2673 (107.5)
Co	1.83 (0.23)	1.79 (0.08)	1.76 (0.07)	1.73 (0.10)	1.52 (0.10)	1.54 (0.28)	nd	1.05 (0.18)
Ni	3.84 (1.50)	nd	2.49 (1.22)	nd	2.44 (0.61)	3.38 (1.78)	nd	13.21 (2.22)
Cu	nd	0.16 (0.03)	nd	0.12 (0.05)	nd	nd	nd	nd
Zn	18.47 (2.75)	12.95 (1.95)	14.65 (1.43)	15.15 (3.35)	13.20 (2.63)	17.78 (5.75)	45.41 (34.54)	32.13 (9.60)
Ga	15.80 (0.76)	13.06 (0.40)	8.65 (0.37)	11.44 (0.42)	6.79 (0.35)	12.49 (0.89)	10.53 (2.19)	9.51 (1.83)
Ge	nd	0.80 (0.19)	0.80 (0.22)	0.59 (0.08)	nd	nd	nd	nd
Rb	50.97 (6.29)	51.30 (1.74)	110.3 (3.71)	71.98 (7.16)	96.25 (2.43)	14.50 (1.54)	74.45 (5.01)	72.09 (3.74)
Y	nd	nd	nd	0.01 (0.01)	nd	nd	nd	nd
Zr	0.04 (0.01)	0.11 (0.18)	0.02 (0.02)	0.02 (0.004)	0.02 (0.02)	nd	nd	0.06 (0.04)
Sn	2.08 (1.36)	1.04 (0.38)	1.35 (0.37)	2.00 (0.55)	3.80 (0.46)	1.35 (0.43)	nd	0.81 (0.35)
Cs	3731 (167.3)	3486 (105.2)	5130 (113.4)	4190 (336.3)	5782 (233.5)	1151 (114.7)	2218 (254.21)	1366 (93.07)
Ba	nd	0.04 (0.01)	nd	nd	nd	nd	0.85 (0.67)	nd
Hf	nd	nd	nd	nd	0.01 (0.004)	nd	nd	nd
Tl	0.20 (0.08)	0.23 (0.05)	0.50 (0.07)	0.29 (0.04)	0.40 (0.05)	nd	0.95 (0.56)	0.40 (0.12)
U	0.01 (0.0004)	nd	nd	nd	nd	nd	nd	nd

* Averages are of five spots per sample, with corresponding standard deviations in parentheses. See *The Journal's* online data depository for complete data. Abbreviation: nd = not detected.

this trend was not seen in the data for all of the other localities. (Figure 15c, d). The lighter Chitral emeralds have tended to have slightly lower concentrations of Cr and V, and the darkest sample of the previous study (PK1) showed similar contents of these elements as the Chitral emeralds analysed here. The Chitral samples showed higher V and overlapping Cr with those from Khaltaro, less Cr than emeralds from Laghman and Swat, and typically less V than those from Panjshir (Figure 15d; Guo *et al.* 2020; Krzemnicki *et al.* 2021; Chen *et al.* 2022).

DISCUSSION

The occurrence of quartz and mica inclusions in the Chitral emeralds is consistent with their geological setting in quartz- and mica-rich host rocks. Furthermore, the presence of inclusions of phlogopite as the main mica phase is consistent with the composition of the matrix rock (e.g. Figure 1 and the cover of this issue). By contrast, muscovite is the main mica inclusion in the Khaltaro samples. The plagioclase inclusions in the Chitral emeralds contain higher



amounts of Ca (corresponding to andesine and oligoclase) than the albite in the samples from Khaltaro. The presence of muscovite and albite in the Khaltaro samples is consistent with their occurrence in hydrothermal veins rich in these minerals (Lauris *et al.* 1996). The general light green colour of the Khaltaro emeralds and their abundant inclusions, which also caused low transparency in our samples, have been noted in the literature (Lawrence *et al.* 1989). These characteristics limit their potential use as gemstones, although some clearer samples have been reported (Lawrence *et al.* 1989).

While usually of deep green colour, Swat emeralds are generally small and often included (Lawrence *et al.* 1989). This was also true for our Swat samples. The numerous dark inclusions may represent a variety of different minerals, and this contrasts with what we observed in our Chitral emeralds, in which phlogopite is the only dark inclusion present. Similarly, the biotite inclusions in Laghman emeralds differ from the phlogopite in Chitral emeralds.

Although two-phase inclusions were found in almost all the samples in this study, three-phase inclusions were absent from our Chitral emeralds. This is in contrast to our observations and the literature data on emeralds from Swat, Panjshir and Laghman, which all can contain three-phase inclusions. Nevertheless, it is possible that three-phase inclusions could rarely be encountered in Chitral emeralds in the future. The rectangular elongated and irregular shapes of the two-phase inclusions in Chitral emeralds resemble those of schist-hosted emeralds (Saeseaw *et al.* 2019).

The strong Fe^{2+} absorption at 830 nm in the UV-Vis-NIR spectra of our Chitral samples also identifies them as schist-hosted emeralds (Saeseaw *et al.* 2019), and thus distinguishes them from Swat and Panjshir emeralds, in which this feature is less pronounced or missing.

Raman spectroscopy in the E_{Lc} excitation showed a stronger type II H₂O peak than type I H₂O peak in samples from most localities examined for this study. The only exceptions were the specimens from Khaltaro, in which type I water was more pronounced regardless of the excitation direction. Since the presence of type II water correlates with alkalis in beryl (Wood & Nassau 1967; Aines & Rossman 1984; Mashkovtsev & Lebedev 1993; Fukuda & Shinoda 2008; Fukuda 2012), this indicates that the Chitral emeralds are alkali-rich (cf. Łodziński *et al.* 2005; Qiao *et al.* 2019) and contain more alkalis than those from Khaltaro. This was confirmed by

chemical analyses, which showed less Na in the Khaltaro samples.

Chemical analyses revealed further differences among emeralds from the various localities. Compared to emeralds from Chitral, those from Swat have greater Mg, Na, Fe, Cr and Sc, but less Li and Cs. Thus, concentrations of these elements further distinguish these two localities, in addition to their differing UV-Vis-NIR spectra. Similarly, concentrations of Li, Na, Mg and Cs are lower in Panjshir emeralds than in our Chitral samples and can, therefore, help to differentiate between them.

More compositional overlap is seen among Khaltaro, Laghman and Chitral emeralds. Apart from lower Na and Mg contents, the lower V in Khaltaro emeralds may help distinguish them from Chitral emeralds. While Li is lower in Laghman emeralds than in those from Chitral, Cr is higher. Both elements may thus help distinguish Chitral from Laghman emeralds.

CONCLUSION

This follow-up study on deeper-coloured emeralds from Chitral in north-western Pakistan is largely in accordance with earlier observations of lower-quality stones from this deposit. In general, both the lighter- and darker-coloured samples exhibited similar spectra and chemical compositions, whereas some significant differences were found for emeralds from other localities in Pakistan and Afghanistan. This study confirms that the Chitral samples are alkali-rich, schist-hosted emeralds, which can thus be separated from Swat and Panjshir emeralds by their UV-Vis-NIR spectra and from Khaltaro emeralds also by their Raman spectra with E_{Lc} excitation.

Separation of Chitral from Laghman emeralds is less straightforward, since there can be considerable similarities in their spectra. Therefore, chemical analyses and inclusion observations are needed for their potential origin determination.

With the recent increase in emerald production from the Chitral region, distinguishing these emeralds from those of similar geological settings could become even more relevant and important in the near future.

REFERENCES

- Aines, R.D. & Rossman, G.R. 1984. The high temperature behavior of water and carbon dioxide in cordierite and beryl. *American Mineralogist*, **69**(3–4), 319–327.

- Aurischio, C., Conte, A.M., Medeghini, L., Ottolini, L. & De Vito, C. 2018. Major and trace element geochemistry of emerald from several deposits: Implications for genetic models and classification schemes. *Ore Geology Reviews*, **94**, 351–366, <https://doi.org/10.1016/j.oregeorev.2018.02.001>.
- Bowersox, G., Snee, L.W., Foord, E.E. & Seal, R.R. 1991. Emeralds of the Panjshir Valley, Afghanistan. *Gems & Gemology*, **27**(1), 26–39, <https://doi.org/10.5741/gems.27.1.26>.
- Chen, Q., Bao, P., Li, Y., Shen, A.H., Gao, R., Bai, Y., Gong, X. & Liu, X. 2022. A research of emeralds from Panjshir Valley, Afghanistan. *Minerals*, **13**(1), article 63, <https://doi.org/10.3390/min13010063>.
- Deer, W.A., Howie, R.A. & Zussman, J. 2001. *Rock-Forming Minerals—Framework Silicates: Feldspars*, Vol. 4A, 2nd edn. The Geological Society, London, xii + 972 pp.
- Fleet, M.E. 2003. *Rock-Forming Minerals—Sheet Silicates: Micas*, Vol. 3A, 2nd edn. The Geological Society, London, xxii + 758 pp.
- Fukuda, J. 2012. Water in rocks and minerals – Species, distributions, and temperature dependences. In: Theophanides, T. (ed) *Infrared Spectroscopy – Materials Science, Engineering and Technology*. IntechOpen, London, 77–96, <https://doi.org/10.5772/35668>.
- Fukuda, J. & Shinoda, K. 2008. Coordination of water molecules with Na⁺ cations in a beryl channel as determined by polarized IR spectroscopy. *Physics and Chemistry of Minerals*, **35**(6), 347–357, <https://doi.org/10.1007/s00269-008-0228-4>.
- Giuliani, G., Groat, L.A., Marshall, D., Fallick, A.E. & Branquet, Y. 2019. Emerald deposits: A review and enhanced classification. *Minerals*, **9**(2), article 105, <https://doi.org/10.3390/min9020105>.
- Giuliani, G., Chaussidon, M., Schubnel, H.-J., Piat, D.H., Rollion-Bard, C., France-Lanord, C., Giard, D., de Narvaez, D. et al. 2000. Oxygen isotopes and emerald trade routes since antiquity. *Science*, **287**(5453), 631–633, <https://doi.org/10.1126/science.287.5453.631>.
- Gübelin, E.J. 1982. Gemstones of Pakistan: Emerald, ruby, and spinel. *Gems & Gemology*, **18**(3), 123–139, <https://doi.org/10.5741/gems.18.3.123>.
- Gübelin, E.J. & Koivula, J.I. 2008. *Photoatlas of Inclusions in Gemstones*, Vol. 3. Opinio Publishers, Basel, Switzerland, 672 pp.
- Guo, H., Yu, X., Zheng, Y., Sun, Z. & Ng, M.F. 2020. Inclusion and trace element characteristics of emeralds from Swat Valley, Pakistan. *Gems & Gemology*, **56**(3), 336–355, <https://doi.org/10.5741/gems.56.3.336>.
- Hagemann, H., Lucken, A., Bill, H., Gysler-Sanz, J. & Stalder, H.A. 1990. Polarized Raman spectra of beryl and bazzite. *Physics and Chemistry of Minerals*, **17**(5), 395–401, <https://doi.org/10.1007/bf00212207>.
- Hammarstrom, J.M. 1989. Mineral chemistry of emeralds and some associated minerals from Pakistan and Afghanistan: An electron microprobe study. In: Kazmi, A.H. & Snee, L.W. (eds) *Emeralds of Pakistan*. Van Nostrand Reinhold, New York, New York, USA, 125–150.
- Hanser, C.S., Häger, T., Botcharnikov, R. & Gul, B. 2022. Emerald from the Chitral region, Pakistan: A new deposit. *Journal of Gemmology*, **38**(3), 234–252, <https://doi.org/10.15506/JoG.2022.38.3.234>.
- Henn, U. & Schmitz, F. 2014. Smaragde aus der Provinz Laghman, Afghanistan: Ein Vergleich mit Smaragden aus dem Panjshir-Tal. *Gemmologie: Zeitschrift der Deutschen Gemmologischen Gesellschaft*, **63**, 101–106.
- Hu, Y. & Lu, R. 2020. Color characteristics of blue to yellow beryl from multiple origins. *Gems & Gemology*, **56**(1), 54–65, <https://doi.org/10.5741/gems.56.1.54>.
- Huong, L.T., Häger, T. & Hofmeister, W. 2010. Confocal micro-Raman spectroscopy: A powerful tool to identify natural and synthetic emeralds. *Gems & Gemology*, **46**(1), 36–41, <https://doi.org/10.5741/gems.46.1.36>.
- Karampelas, S., Al-Shaybani, B., Mohamed, F., Sangsawong, S. & Al-Alawi, A. 2019. Emeralds from the most important occurrences: Chemical and spectroscopic data. *Minerals*, **9**(9), article 561, <https://doi.org/10.3390/min9090561>.
- Kazmi, A.H. 1989. A brief overview of the geology and metallogenic provinces of Pakistan. In: Kazmi, A.H. & Snee, L.W. (eds) *Emeralds of Pakistan*. Van Nostrand Reinhold, New York, New York, USA, 1–11.
- Kazmi, A.H. & Snee, L.W. (eds) 1989. *Emeralds of Pakistan*. Van Nostrand Reinhold, New York, New York, USA, xii + 269 pp.
- Khan, T. 1986. *Geology of the Pegmatite Belt in Chitral, Northwest Frontier Province, Pakistan*. Geological Survey of Pakistan Information Release 266, Quetta, Pakistan, 16 pp. + 5 maps.
- Krzemnicki, M.S., Wang, H.A.O. & Büche, S. 2021. A new type of emerald from Afghanistan's Panjshir Valley. *Journal of Gemmology*, **37**(5), 474–495, <https://doi.org/10.15506/JoG.2021.37.5.474>.
- Laurs, B.M., Dilles, J.H. & Snee, L.W. 1996. Emerald mineralization and metasomatism of amphibolite, Khaltaro granitic pegmatite-hydrothermal vein system, Haramosh Mountains, northern Pakistan. *Canadian Mineralogist*, **34**(6), 1253–1286.

- Lawrence, R.D., Kazmi, A.H. & Snee, L.W. 1989. Geological setting of the emerald deposits. In: Kazmi, A.H. & Snee, L.W. (eds) *Emeralds of Pakistan*. Van Nostrand Reinhold, New York, New York, USA, 13–38.
- Łodziński, M., Sitarz, M., Stec, K., Kozanecki, M., Fojud, Z. & Jurga, S. 2005. ICP, IR, Raman, NMR investigations of beryls from pegmatites of the Sudety Mts. *Journal of Molecular Structure*, **744–747**, 1005–1015, <https://doi.org/10.1016/j.molstruc.2004.12.042>.
- Mashkovtsev, R.I. & Lebedev, A.S. 1993. Infrared spectroscopy of water in beryl. *Journal of Structural Chemistry*, **33**(6), 930–933, <https://doi.org/10.1007/bf00745616>.
- Moroz, I.I. & Eliezri, I.Z. 1999. Mineral inclusions in emeralds from different sources. *Journal of Gemmology*, **26**(6), 357–363, <https://doi.org/10.15506/JoG.1999.26.6.357>.
- Qiao, X., Zhou, Z., Schwarz, D.T., Qi, L., Gao, J., Nong, P., Lai, M., Guo, K. *et al.* 2019. Study of the differences in infrared spectra of emerald from different mining areas and the controlling factors. *Canadian Mineralogist*, **57**(1), 65–79, <https://doi.org/10.3749/canmin.1800042>.
- Sabot, B., Cheilletz, A., de Donato, P., Banks, D., Levresse, G. & Barrès, O. 2001. The Panjsher-Afghanistan emerald deposit: New field and geochemical evidence for Colombian style mineralisation. *European Union Geoscience XI*, Strasbourg, France, 8–13 April, 548.
- Saeseaw, S., Renfro, N.D., Palke, A.C., Sun, Z. & McClure, S.F. 2019. Geographic origin determination of emerald. *Gems & Gemmology*, **55**(4), 614–646, <https://doi.org/10.5741/gems.55.4.614>.
- Schmetzer, K. & Kiefert, L. 1990. Water in beryl – A contribution to the separability of natural and synthetic emeralds by infrared spectroscopy. *Journal of Gemmology*, **22**(4), 215–223, <https://doi.org/10.15506/JoG.1990.22.4.215>.
- Schwarz, D. & Pardieu, V. 2009. Emeralds from the Silk Road countries – A comparison with emeralds from Colombia. *InColor*, No. 12, 38–43, <http://www.incolormagazine.com/books/rxf/#p=39>.
- Schwarz, D. & Curti, M. 2021. *Emerald – Modern Gemmology*. Bellerophon Gemlab, Bangkok, Thailand, 481 pp.
- Snee, L.W., Foord, E.E., Hill, B. & Carter, S.J. 1989. Regional chemical differences among emeralds and host rocks of Pakistan and Afghanistan: Implications for the origin of emerald. In: Kazmi, A.H. & Snee, L.W. (eds) *Emeralds of Pakistan*. Van Nostrand Reinhold, New York, New York, USA, 93–123.
- Wang, H., Shu, T., Chen, J. & Guo, Y. 2022. Characteristics of channel-water in blue-green beryl and its influence on colour. *Crystals*, **12**(3), article 435, <https://doi.org/10.3390/cryst12030435>.
- Wood, D.L. & Nassau, K. 1967. Infrared spectra of foreign molecules in beryl. *Journal of Chemical Physics*, **47**(7), 2220–2228, <https://doi.org/10.1063/1.1703295>.
- Zahid, M., Jan, M.Q. & Moon, C.J. 2016. Geochemistry of stratabound scheelite mineralisation and associated calc-silicate rocks from Chitral, NE Hindu Kush, Pakistan. *Arabian Journal of Geosciences*, **9**(13), article 620, <https://doi.org/10.1007/s12517-016-2637-x>.


The Authors

Carina S. Hanser FGA DGA*, **Dr Tobias Häger**
and **Prof. Dr Roman Botcharnikov**

Institute of Geosciences, Johannes Gutenberg
University Mainz, J.-J.-Becher-Weg 21,
55099 Mainz, Germany
and

Institute of Gemstone Research, Prof.-Schlossmacher-
Straße 1, 55743 Idar-Oberstein, Germany

*Email: chanser@uni-mainz.de

 <https://orcid.org/0000-0001-5504-8739>

Dr Tom Stephan

German Gemmological Association,
Prof.-Schlossmacher-Straße 1, 55743 Idar-Oberstein,
Germany

Bilal Gul

Department of Geology, University of Tartu,
Ravila 14a, 50411 Tartu, Estonia

Acknowledgements

This study was partly funded through collaboration between Johannes Gutenberg-University of Mainz, Germany, and Idar-Oberstein, Germany. The authors thank mine owner Imran Khan for the Chitral emerald samples. Thank you to Waqar Ahmad and Shehzad Hussain for help in selecting and shipping several of the specimens used in this study. Furthermore, we thank Regina Mertz, Mareike Leiter and Jana David (for LA-ICP-MS), and Nora Groschopf (for EPMA) at Johannes Gutenberg-University for their help with the chemical analyses. Thanks also to Stefan Müller of the DSEF German Gem Lab for collecting Raman spectra of the emerald samples from Panjshir, Laghman and Swat. In addition, we thank Dudley Blauwet, Federico Picciani and Waqar Ahmed for supplying photos of gem-quality Chitral emeralds.

Mineralogical and Gemmological Characteristics of Gem-quality Forsterite-Serpentine from North-eastern China

Bijie Peng, Mingyue He, Mei Yang, Xi Liu and Xinhao Sui

ABSTRACT: Gem-quality forsterite-serpentine is a translucent-to-opaque gem material from north-eastern China that entered the market in 2019 and was not well characterised until now. It ranges from greenish yellow to dark green to black, has a compact texture and exhibits good carving performance. It is mainly composed of forsterite (Fo), serpentine and brucite, and exhibits a metasomatic relict mesh texture in petrographic thin sections. The forsterite shows extremely high MgO contents, with Fo contents of 98.28–99.65 % (i.e. nearly end-member forsterite), and it has been partially serpentinised into lizardite and chrysotile. Infrared spectra of the material show a mixture of serpentine and forsterite. Based on Raman spectra, the black forsterite-serpentine rock contains more spinel, magnetite and phlogopite than the greenish yellow material. The mineral composition and geochemical characteristics, coupled with the geological setting, suggest that the forsterite-serpentine is dolomite-related in origin and represents a unique type of serpentine-bearing gem material.

The Journal of Gemmology, 38(6), 2023, pp. 600–614, <https://doi.org/10.15506/JoG.2023.38.6.600>
© 2023 Gem-A (The Gemmological Association of Great Britain)

Gem-quality serpentine is mainly composed of serpentine-group minerals, and has been used in ceremonial and decorative carvings since ancient times. In the gem trade, serpentine is a common imitation of jadeite and nephrite. It has widespread distribution, with many global sources, including China (Wang & Dong 2011; Wang & Ye 2014), the United States (Sonzogni *et al.* 2017), Italy (Adamo *et al.* 2016), New Zealand (Adams *et al.* 2007) and South Korea (Kim *et al.* 2011). Major sources in China include Liaoning Province (Wang & Dong 2011; Wang & Gan 2012a; Wang & Ye 2014), Guangdong Province (Guan & Chen 2005), Guangxi Province (Wang & Gan 2012b), Shanxi Province (Wang *et al.* 2012; Yang *et al.* 2021),

Xinjiang Province (Yu *et al.* 2017), Gansu Province (Ge *et al.* 2011), Shandong Province (Chen *et al.* 2011) and others (see also Yu *et al.* 2021).

Recently, a new type of forsterite-serpentine gem material has appeared on the market from Ji'an County, Jilin Province, north-eastern China. This rock, which was referred to as *jianite* by Wang *et al.* (2020), has a massive, very fine-grained texture and ranges from greenish yellow to dark green to black (e.g. Figure 1). The deposit was discovered around 2000 and later mined in an open pit by a local company in 2009. The deposit covers an area of 4,455 m² (Peng *et al.* 2022a), and its current production and reserves are unknown. Since 2019, the material has been fashioned into various items

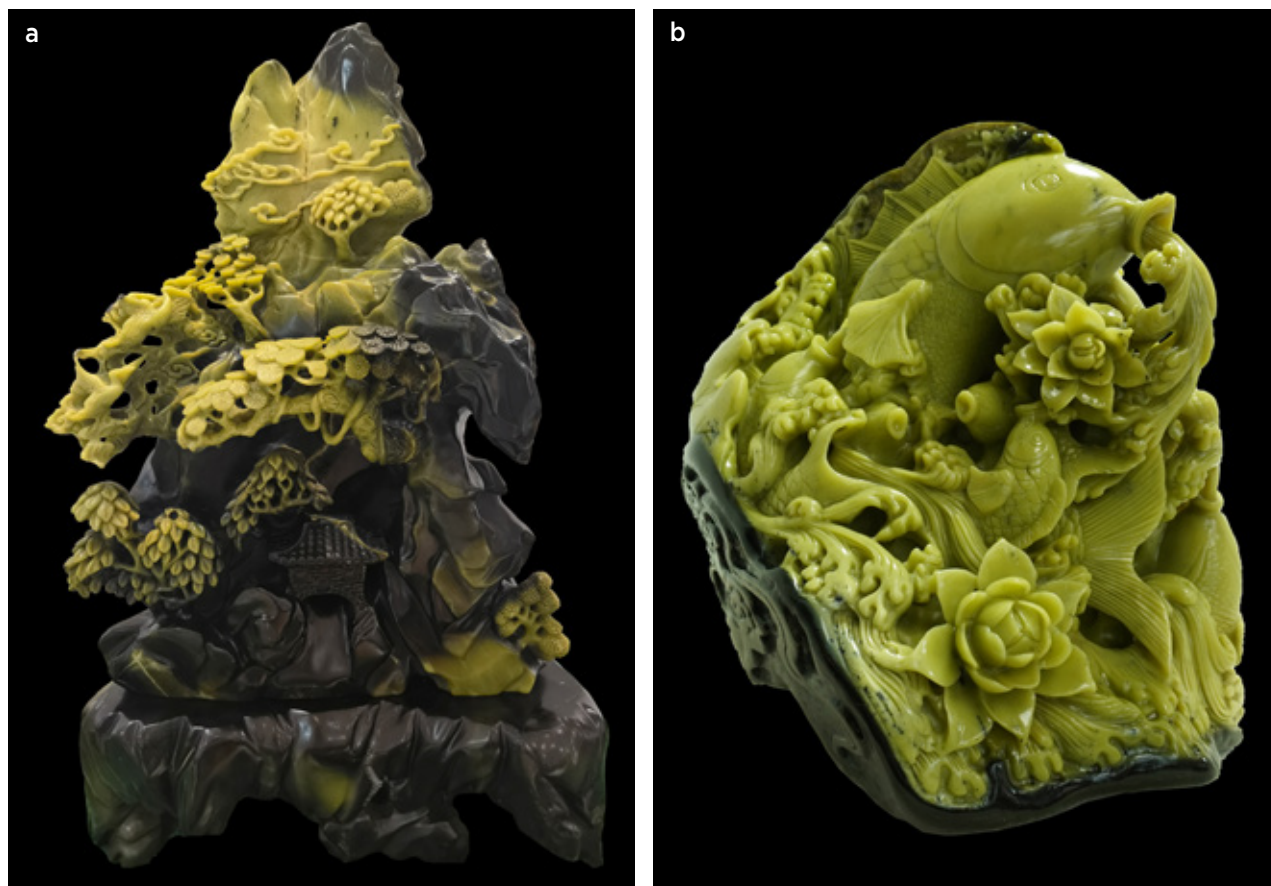


Figure 1: These ornate carvings of greenish yellow to black forsterite-serpentine depict (a) trees on a mountainside (45 × 20 × 73 cm) and (b) carp in a waterfall with flowers (30 × 15 × 40 cm). Photos by Mingyue He.

such as decorative carvings, bangles and beads.

Different from common gem-quality serpentine, its main mineral constituents are a combination of olivine and serpentine. The olivine has extremely high Mg contents, with forsterite (Fo) values up to 99.8%; such a near end-member composition is quite rare in terrestrial rocks (Blondes *et al.* 2012; Plechov *et al.* 2018). Wang *et al.* (2020) investigated the mineralogy, petrography and infrared spectral characteristics of the forsterite-serpentine rock. Peng *et al.* (2022a) studied the chemical and oxygen isotope composition of the forsterite, and Peng *et al.* (2022b) examined the crystal structure and spectroscopic characteristics of boron-rich forsterite in this material. Despite this research, questions remain about its geological origin, and gemmological data are lacking.

This study describes the mineralogical and gemmological characteristics of the forsterite-serpentine rock. We present the results of standard gemmological testing, polarised microscopy, Raman spectroscopy, electron microprobe analysis, scanning electron microscopy and infrared spectroscopy of 12 samples. Based on our mineralogical and gemmological data, we then discuss the formation and serpentinisation processes of this unusual material.

GEOLOGICAL SETTING

The study area is located in the Jiao-Liao-Ji Belt in the eastern part of the Eastern block of the North China craton. The Palaeoproterozoic Jiao-Liao-Ji Belt is located between the Archaean Nangrim block (to the south) and the Archaean Longgang block (to the north; Lu *et al.* 2006). In southern Jilin Province, the Jiao-Liao-Ji Belt includes the Ji'an and Liaoning groups (Figure 2a). The forsterite-serpentine rock occurs in the Mayihe Formation of the Palaeoproterozoic Ji'an Group (Figure 2b), which consists of metamorphosed (amphibolite facies) volcanic and sedimentary rocks (Lu *et al.* 2006; Zhang *et al.* 2018). The Mayihe Formation belongs to the lowest layer of the Ji'an Group and was deposited along an active continental margin. It is characterised by various altered felsitic and gneissic rocks, dolomitic marble, serpentinised olivine-bearing marble, boron- and iron-bearing serpentinite, amphibolite, and some other mafic volcanic and metamorphic rocks (Meng *et al.* 2017a; Zhang *et al.* 2018). The Mayihe Formation formed 2.18 billion years ago (Ga) and underwent metamorphic events at 1.90 and 1.85 Ga (Meng *et al.* 2017b).

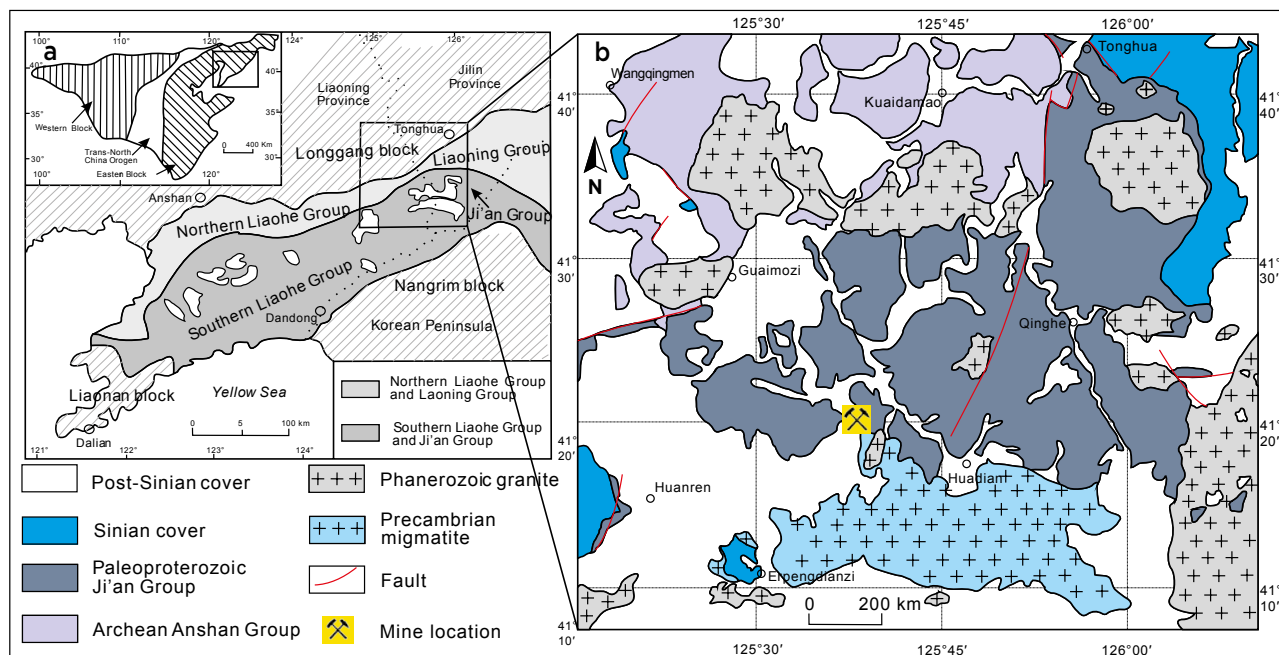


Figure 2: (a) Tectonic sub-divisions of the North China craton are shown after Lu *et al.* (2006). The forsterite-serpentine deposit is hosted by the Ji'an Group in the Jiao-Liao-Ji Belt. This belt is also comprised of the Liaoning, Northern Liaohe and Southern Liaohe groups in this region. (b) This map shows the geological context and location of the forsterite-serpentine deposit (after Peng *et al.* 2022a).

The forsterite-serpentine orebodies are hosted by forsterite marble of the Ji'an Group. The main surrounding rock is migmatitic gneiss (Peng *et al.* 2022a). The forsterite-serpentine observed during the authors' field investigations was mainly greenish yellow and had a strongly weathered layer on the surface. The middle of the deposit was cross-cut by pegmatites (composed of feldspar, diopside and biotite) and by phlogopite veins (Figure 3). Adjacent to these veins the forsterite-serpentine rock was dark coloured, and dark green areas occurred between the black and greenish yellow forsterite-serpentine.

MATERIALS AND METHODS

For this study, we examined 12 specimens of forsterite-serpentine (numbered JAY01–JAY12) that represent the colour range of the material (Figure 4). These include uniform greenish yellow (JAY01–JAY04), green to dark green with a yellowish hue (JAY05–JAY08 and JAY11–JAY12) and black (JAY09 and JAY10).

Standard gemmological properties of all the samples were collected at the School of Gemmology, China University of Geosciences (Beijing). Their colour, lustre and diaphaneity were observed in daylight. Refractive indices were obtained with a refractometer and SG was measured hydrostatically. The Vickers hardness of all samples was measured with a TH763

digital microhardness tester. Short-wave (254 nm) and long-wave (365 nm) lamps were used to test UV fluorescence.

The mineralogy and texture of the samples were studied in petrographic thin sections that were cut and polished from all 12 samples at the National Infrastructure of Mineral, Rock and Fossil Resources, China University of Geosciences (Beijing). A petrographic microscope with a camera attachment was used to take photomicrographs of the thin sections in plane-polarised and cross-polarised light.

To identify the minerals and inclusions present in the forsterite-serpentine rock, Raman spectra were acquired on all 12 thin sections at the School of Gemmology, China University of Geosciences (Beijing). A Horiba LabRAM HR Evolution Raman spectrometer coupled with an Ar-ion laser (532 nm) was used to collect the spectra, using an entrance slit of 100 μm and a grating with 1,200 grooves/mm. The scanning range was 4000–100 cm^{-1} , with a resolution of 1 cm^{-1} and a scan time of 10 s. The RRUFF spectral database was used to identify the phases.

The chemical composition of the major and minor mineral constituents of the forsterite-serpentine were measured on all 12 polished thin sections at the Electron Probe Laboratory, China University of Geosciences (Beijing), using a Shimadzu EPMA-1720 electron probe micro-analyser (EPMA). An accelerating voltage of 15 kV

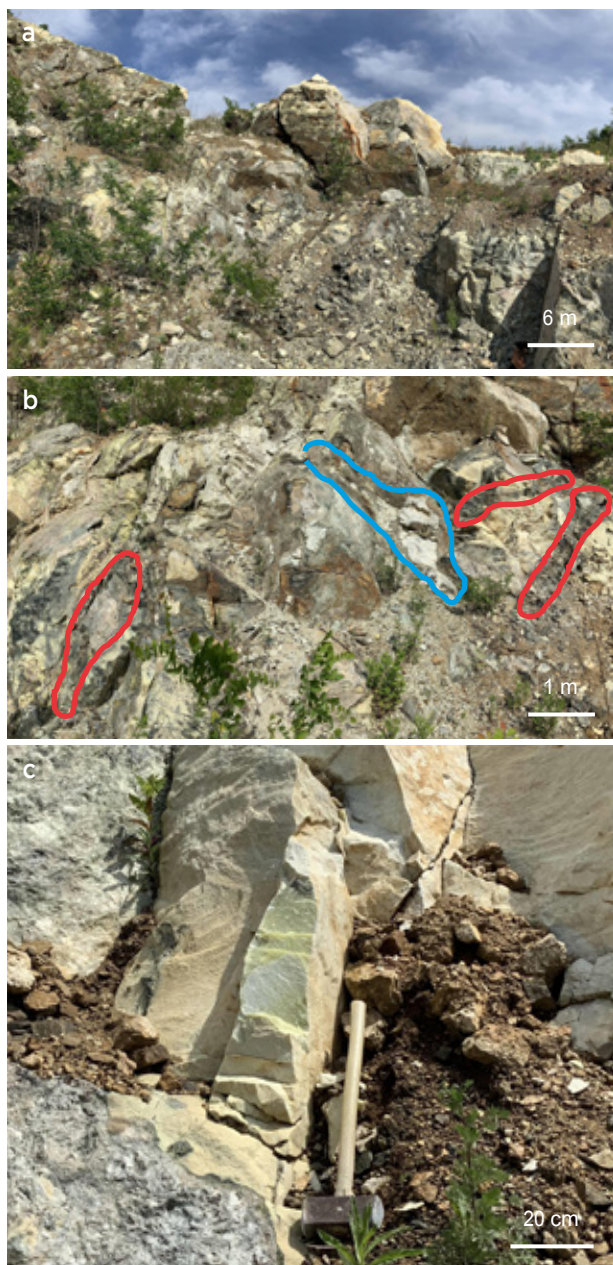


Figure 3: These photos of the forsterite-serpentine deposit consist of: (a) an overall view of some of the rock outcrops, (b) a closer view showing phlogopite veins (outlined by red lines) and a pegmatite body (outlined by blue lines) penetrating the forsterite-serpentine rock, and (c) a freshly broken surface of forsterite-serpentine. Photos by Bijie Peng.

and a beam current of 10 nA were used, and the beam diameter was 5 μm . The following standards were employed: diopside (Si), rutile (Ti), chlorite (Al), chromite (Fe and Cr), rhodonite (Mn), diopside (Ca), forsterite (Mg), pentlandite (Ni), willemite (Zn), albite (Na) and sanidine (K).

The microstructural properties of two samples of the forsterite-serpentine rock (JAY01 and JAY11) were documented with a scanning electron microscope (SEM),

using a Phenom XL G2 instrument with an accelerating voltage of 15 kV, a beam current of 10 nA and a working distance of 10 mm. The specimens were fractured and carbon-coated for analysis. Both secondary-electron and backscattered electron images were captured.

Infrared spectra of four samples of the forsterite-serpentine rock (JAY03, JAY05, JAY09 and JAY11) were obtained at the School of Gemmology, China University of Geosciences (Beijing). A Bruker Tensor 27 Fourier transform infrared (FTIR) spectrometer was used to collect spectra in transmission mode. The samples were powdered (particle size of $<2.5\ \mu\text{m}$) and about 0.5 mg of the powder was mixed with about 150 mg potassium bromide and pressed into a pellet for analysis. The scanning range was $4000\text{--}400\ \text{cm}^{-1}$, with a resolution of $4\ \text{cm}^{-1}$ and an accumulation of 64 scans.

RESULTS

Gemmological Properties

The forsterite-serpentine samples generally had a uniform colour, and were greenish yellow (Figure 4a–d) to dark green (Figure 4e–h) to black (Figure 4i, j), and sometimes showed white and black areas (Figure 4k, l). The specimens were translucent to opaque, with a greasy to vitreous lustre on polished surfaces. All samples had aphanitic texture and massive structure.

Spot RIs were approximately 1.55–1.56 and SG values ranged from 2.52 to 2.82 (Table I), which reflect variations in forsterite content. In general, the more forsterite in a sample (as noted in thin sections; see the Petrography section below), the higher the SG value. Most of the microhardness values ranged from 848 to 974 (due to forsterite) and from 135 to 183 (due to serpentine), corresponding to an overall Mohs hardness of 3–6½. All samples were inert to long- and short-wave UV radiation.

Petrography

Examination of the petrographic thin sections of the forsterite-serpentine rock showed a metasomatic relict texture that was manifested by a mesh texture (Figure 5). The main mineral constituents were forsterite, serpentine and brucite, with minor magnesite, phlogopite and magnetite.

Forsterite made up 10–60% of the rock and had a grain size of 0.2–2 mm. The forsterite appeared colourless in plane-polarised light and showed second- to third-order (bluish green) interference colours in cross-polarised light (Figure 5a–d). Serpentine constituted about 30–90% of the rock, and formed pseudomorphs after forsterite in the pervasively serpentinised samples

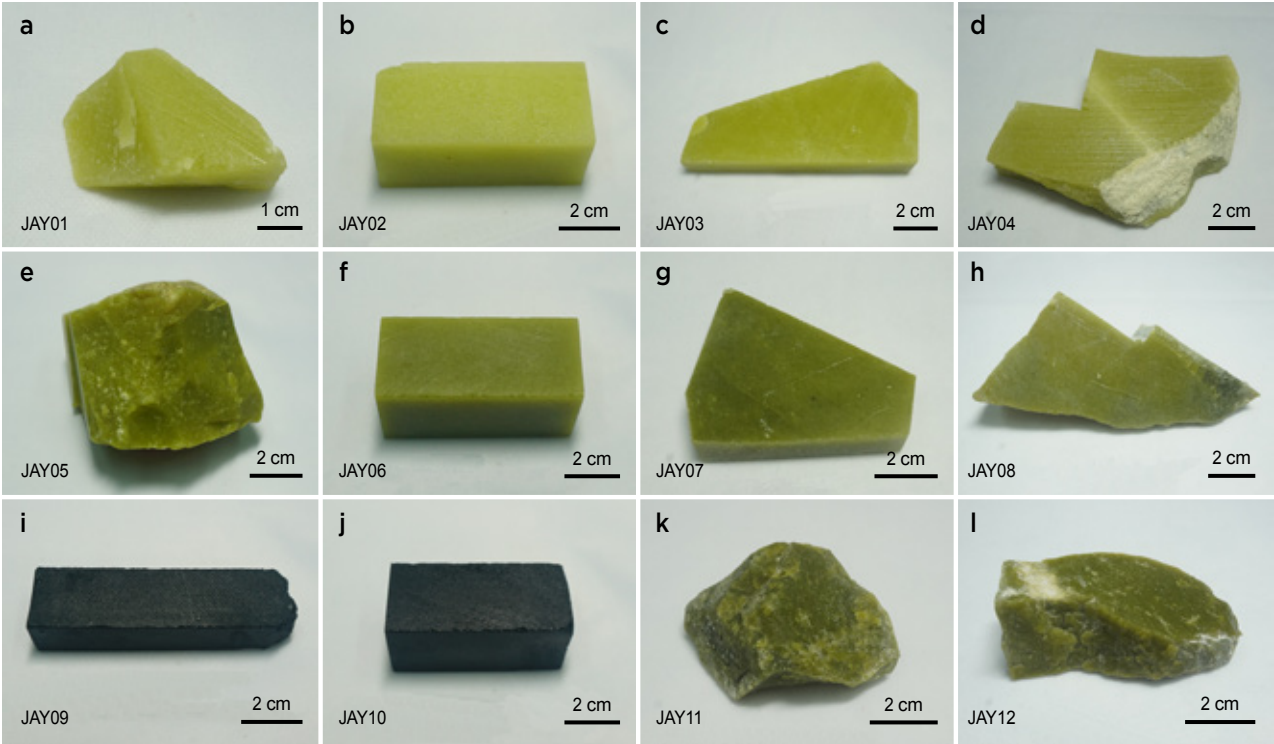


Figure 4: The 12 specimens of gem-quality forsterite-serpentine used for this study display four colours: (a–d) greenish yellow, (e–h) dark green, (i, j) black and (k, l) green, the last being pervasively serpentinised. Photos by Bijie Peng.

(Figure 5e, f). The serpentine appeared colourless to light yellow in plane-polarised light, and showed first-order grey-to-yellow interference colours in cross-polarised light. Brucite was present as colourless veins in the serpentine and made up about 10% of the rock.

Table I: Gemmological properties of forsterite-serpentine.^a

Sample no.	Colour	Diaphaneity	RI	SG	Microhardness (kg/mm ²) ^b
JAY01	Greenish yellow	Translucent	1.56	2.61	963/157
JAY02	Greenish yellow	Translucent	1.56	2.82	968/173
JAY03	Greenish yellow	Translucent	1.56	2.70	974/157
JAY04	Greenish yellow	Translucent	1.56	2.79	952/166
JAY05	Dark green	Translucent	1.56	2.68	952/183
JAY06	Dark green	Translucent	1.56	2.73	957/140
JAY07	Dark green	Translucent	1.56	2.68	952/135
JAY08	Dark green	Translucent	1.56	2.66	963/145
JAY09	Black	Opaque	1.55	2.71	848/168
JAY10	Black	Opaque	1.55	2.76	876/152
JAY11	Green	Translucent	1.55	2.52	364
JAY12	Green	Translucent	1.55	2.53	295

^a All samples showed a greasy to vitreous lustre.
^b The first value is due to forsterite and the second value is due to serpentine. Only one overall value was obtained for JAY11 and JAY12 due to their intense serpentinisation.

Minor phlogopite and magnetite were present in the black samples (JAY09 and JAY10), which contained less forsterite than the greenish yellow to dark green samples. In addition, green samples JAY11 and JAY12 were highly serpentinised, with black solid inclusions.

Raman Spectroscopy

Raman spectroscopy of the forsterite-serpentine samples showed that the main mineral constituents were forsterite (Figure 6a), serpentine (Figure 6b) and brucite. Additional minerals identified by Raman spectroscopy were magnesite (Figure 7a), pyrite (Figure 7b), talc (Figure 7c), dolomite, magnetite, phlogopite, spinel and warwickite. Representative Raman spectra of those minerals that are not shown in this article can be found in *The Journal’s* online data depository.

Forsterite. The characteristic Raman bands of forsterite (Mg₂SiO₄) occur at approximately 226, 304, 434, 544, 586, 609, 824, 857, 882, 920 and 966 cm⁻¹ (Figure 6a). The strongest bands, at 824 and 857 cm⁻¹, are characteristic peaks of forsterite (Chopelas 1991; Kuebler *et al.* 2006; Breitenfeld *et al.* 2018).

The forsterite hosted various inclusions with dimensions of 2–10 µm (e.g. Figure 7). They could be divided into two types: solid inclusions and secondary fluid inclusions. The most abundant solid inclusions were

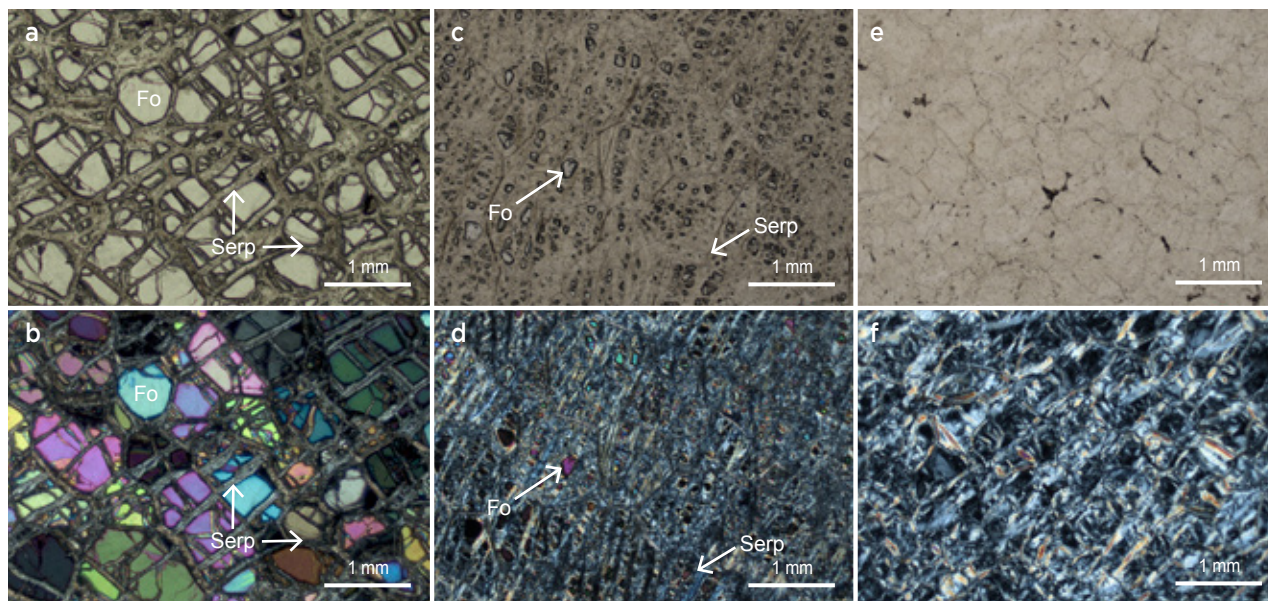


Figure 5: Photomicrographs of petrographic thin sections of the forsterite-serpentine are shown in plane-polarised light (top row) and with crossed polarisers (bottom row). The images depict examples of: **(a, b)** partially serpentinised forsterite with a relict mesh texture (sample JAY02); **(c, d)** forsterite with extensive serpentinisation (sample JAY06); and **(e, f)** forsterite with pervasive serpentinisation (sample JAY11). Abbreviations: Fo = forsterite and Serp = serpentine. Photomicrographs by Bijie Peng.

carbonates and hydrous silicates. Raman spectroscopy identified magnesite as the most common phase, followed by serpentine, talc and pyrite. The secondary fluid inclusions were usually found along partially healed fissures in the forsterite. These could be observed with $50\times$ magnification, but their constituents could not be positively identified with Raman spectroscopy. It is possible that they consisted of negative crystals containing methane or carbon dioxide, as seen previously in olivine (Raič *et al.* 2019).

Serpentine. Raman spectra of the serpentine phases showed characteristics typical of lizardite and chrysotile (both $\text{Mg}_3\text{Si}_2\text{O}_5(\text{OH})_4$). Low-wavenumber Raman spectra of these two serpentine polymorphs include features at approximately 129, 229, 345, 382, 461, 622, 690 and 1100 cm^{-1} for chrysotile, and 129, 229, 347, 382, 469, 620, 689 and 1089 cm^{-1} for lizardite (Figure 6b; Rinaudo *et al.* 2003; Trittschack *et al.* 2012; Schwartz *et al.* 2013; Petriglieri *et al.* 2015; Tarling *et al.* 2018). None of our Raman analyses contained a peak at 1044 cm^{-1} ,

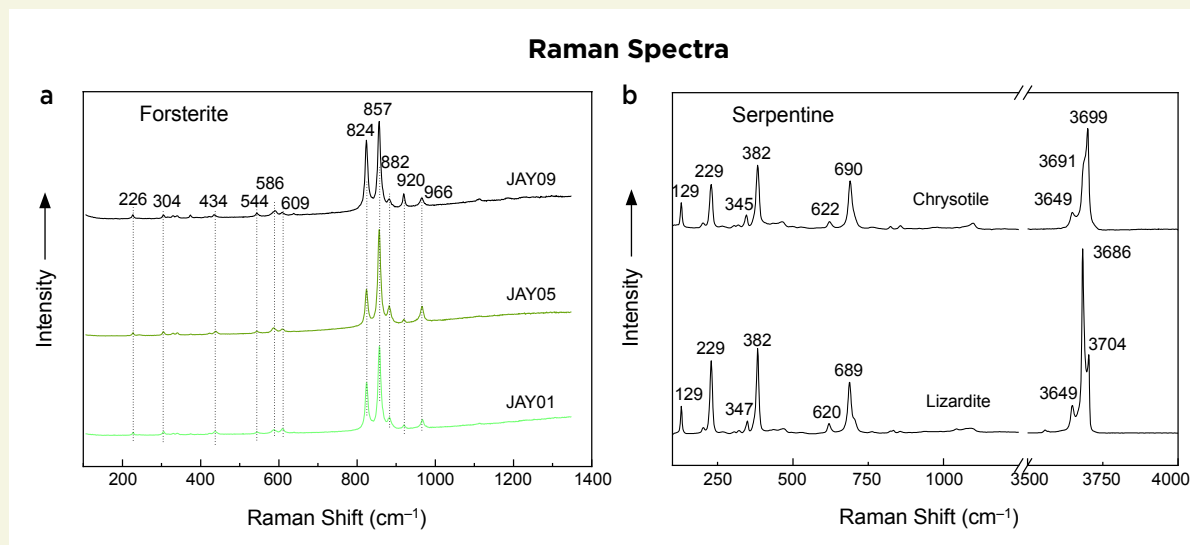


Figure 6: Raman spectra of the main mineral constituents in the forsterite-serpentine are shown for **(a)** forsterite and **(b)** the two serpentine minerals, chrysotile and lizardite. Spectra are offset vertically for clarity.

which is characteristic of antigorite. Experiments have shown that Raman spectral features of serpentine-group minerals in the high-wavenumber region ($3550\text{--}3850\text{ cm}^{-1}$) could be attributed to the stretching vibrations of OH groups, and are more reliable for identifying the serpentine-group minerals (Petriglieri *et al.* 2015; Tarling *et al.* 2018). The Raman spectra of lizardite in this study showed two bands at 3686 and 3704 cm^{-1} , while chrysotile displayed a main band at 3699 cm^{-1} with a shoulder at 3691 cm^{-1} . Differences in the Raman spectra of these two serpentine minerals are due to cell size, symmetry and cation substitutions (Petriglieri *et al.* 2015).

Brucite. Raman spectra of brucite ($\text{Mg}(\text{OH})_2$) showed the three expected Raman-active modes at 278 , 444 and 3650 cm^{-1} , in agreement with those reported in the literature (Klein *et al.* 2020). The strongest band was the O–H vibration mode at 3650 cm^{-1} .

Dolomite and Magnesite. Dolomite and magnesite were associated with forsterite and showed xenomorphic morphology. Magnesite was more common than dolomite and had a grain size of $0.1\text{--}0.2\text{ mm}$ (Figure 7a). Raman spectroscopy is useful to identify the carbonate-group minerals: magnesite (MgCO_3) has typical bands at approximately 213 , 330 , 738 , 1094 , 1445 and 1763 cm^{-1} , while dolomite ($\text{CaMg}(\text{CO}_3)_2$) has characteristic bands at approximately 176 , 258 , 299 , 1019 , 1069 , 1098 and 1393 cm^{-1} ; the difference is attributed to structural differences between the two minerals (Sun *et al.* 2014; Dufresne *et al.* 2018).

Magnetite. Grains of magnetite (Fe_3O_4) occurred sporadically in association with serpentine. The Raman spectrum of magnetite shows bands at approximately 316 , 542 and 671 cm^{-1} . The strongest band, at 671 cm^{-1} , has been attributed to symmetric stretching of Fe–O bonds, and the band at 542 cm^{-1} has been assigned to antisymmetric stretching of Fe–O bonds (Wang *et al.* 2013).

Phlogopite. Platelets of phlogopite ($\text{KMg}_3(\text{OH})_2\text{AlSi}_3\text{O}_{10}$) typically exhibited distinct cleavages. The Raman spectrum of phlogopite has peaks at approximately 191 , 278 , 354 , 429 , 457 , 679 , 815 , 1034 , 1076 and 1109 cm^{-1} . The bands between 800 and 1200 cm^{-1} have been attributed to the stretching vibrations of tetrahedral non-bridging oxygen, and bands between 550 and 800 cm^{-1} are related to the stretching vibrations of tetrahedral bridging oxygen (McKeown *et al.* 2015).

Pyrite. Pyrite (FeS_2) was rarely present as an inclusion in forsterite (Figure 7b). It exhibits two primary Raman bands at approximately 342 and 377 cm^{-1} , along with

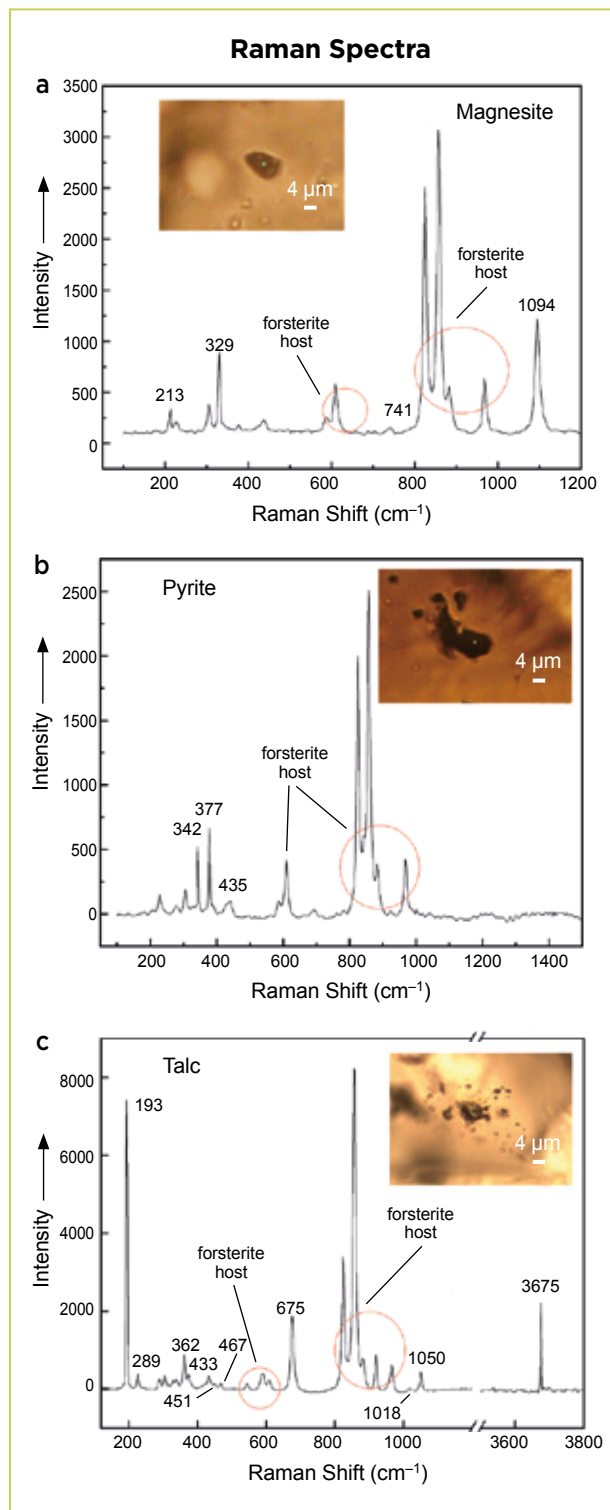


Figure 7: Various inclusions in the forsterite were identified by Raman spectroscopy, including (a) magnesite, (b) pyrite and (c) talc. Due to the minute size of these inclusions, the Raman spectra also contain features related to the forsterite host. Photomicrographs by Bijie Peng.

a minor band at around 435 cm^{-1} , which are attributed to the A_g , E_g and $T_g(3)$ vibrational modes, respectively (White *et al.* 2009).

Spinel. Spinel was commonly associated with phlogopite and showed a xenomorphic morphology. The most intense Raman peak for spinel is the E_g mode at 405 cm^{-1} , which has been assigned to the asymmetric bending motion of oxygen atoms (D'Ippolito *et al.* 2015). A small $F_{2g}(3)$ peak was also observed at 663 cm^{-1} , as well as an additional A_{1g} peak at 764 cm^{-1} due to Mg–O stretching vibrations. The $F_{2g}(1)$ mode at 309 cm^{-1} was weak and often hard to recognise. These features are in agreement with the characteristic Raman spectrum of end-member spinel (MgAl_2O_4 ; D'Ippolito *et al.* 2015).

Talc. Talc ($\text{Mg}_3(\text{Si}_4\text{O}_{10})(\text{OH})_2$) formed inclusions in forsterite (Figure 7c). Talc shows typical Raman bands at approximately 193, 289, 362, 433, 451, 467, 675, 1018, 1050 and 3675 cm^{-1} ; the strongest band at 193 cm^{-1} is assigned to lattice modes and is a characteristic peak of talc (Šontevska *et al.* 2017). The weak band at 1050 cm^{-1} is assigned as stretching vibrations of non-bridging oxygen in Si–O–Si groups. The band at 675 cm^{-1} is assigned to the symmetric Si–O–Si stretching mode. The lower-frequency bands are attributed to stretching Mg–O vibrations.

Warwickite. Warwickite, $(\text{Mg,Ti,Fe,Al})_2\text{O}(\text{BO}_3)$, occurred as isolated reddish brown grains. The Raman spectrum of warwickite yielded main bands at 180, 535 and 751 cm^{-1} .

Mineral Chemistry

The results of EPMA analysis of minerals in the forsterite-serpentine rock are presented in Tables II and III. All of the analysed olivine grains (Table II) had extremely high Mg contents that corresponded to 98.28–99.65% forsterite. The Fe content of the forsterite in the black samples JAY09 and JAY10 (1.37 and 1.75 wt. % FeO, respectively) was slightly higher than that in the greenish yellow samples JAY01 and JAY02 (0.35 wt. % FeO).

Serpentine was characterised by enriched Mg (Table III). The Fe content of the serpentine increased as the colour of the samples darkened from greenish yellow to dark green to black. The brucite contained traces of Si and Fe. The Mg-rich composition of the forsterite-serpentine rock is also reflected in the chemical compositions of phlogopite and magnesite, and even the magnetite contained some Mg (Table III).

Table II: Representative EPMA analyses of forsterite in the forsterite-serpentine rock.

Sample no.	JAY01	JAY02	JAY05	JAY06	JAY09	JAY10
Sample colour	Greenish yellow		Dark green		Black	
Oxides (wt.%)						
SiO ₂	43.34	42.28	41.09	41.07	42.32	42.10
TiO ₂	nd*	0.09	0.01	0.03	0.01	0.02
Al ₂ O ₃	nd	0.03	0.02	nd	0.01	nd
FeO	0.35	0.35	0.60	0.59	1.37	1.75
Cr ₂ O ₃	nd	0.05	nd	nd	nd	nd
MnO	0.03	0.02	0.04	0.05	0.08	0.06
CaO	0.02	0.03	0.02	0.02	nd	0.02
MgO	56.01	55.98	56.67	57.22	56.18	55.91
NiO	0.03	0.01	0.02	nd	0.08	0.06
ZnO	nd	0.06	nd	nd	nd	0.02
Na ₂ O	0.04	0.02	0.01	0.01	nd	0.03
K ₂ O	nd	nd	0.01	nd	nd	nd
Total	99.82	98.91	98.50	98.99	100.06	99.97
% Fo	99.65	99.65	99.41	99.42	98.65	98.28

* Abbreviation: nd = not detected.

Scanning Electron Microscopy

SEM imagery of the forsterite-serpentine revealed a metasomatic relict texture (Figure 8a, b). Forsterite grains showed irregular morphology and ranged from 100 to $300\text{ }\mu\text{m}$ in size. The forsterite in the greenish yellow samples had a larger grain size than in the dark green samples. Serpentine mainly displayed sheet-like (Figure 8c) and scaly (Figure 8d) structures that varied in size from 1 to $100\text{ }\mu\text{m}$ with a thickness up to $1\text{ }\mu\text{m}$. Serpentinisation was evident along fractures or cleavages in the forsterite.

Infrared Spectroscopy

The FTIR spectra showed similar absorption characteristics for the different-coloured samples, and displayed mixed characteristics of serpentine and forsterite (Figure 9). The pervasively serpentinised sample JAY11 was dominated by the characteristic absorptions of serpentine. No absorption bands for minor mineral phases such as magnesite and magnetite were observed. Bands near 3691 , 3649 , 1083 , 953 , 611 , 562 and 445 cm^{-1} are related to serpentine, while those characteristic of forsterite were recorded at approximately 882 , 840 , 760 , 611 , 507 , 466 and 410 cm^{-1} (cf. Yang *et al.* 2021; Peng *et al.* 2022b). The forsterite content of the samples positively correlated with the absorption intensity of the characteristic IR bands of forsterite.

The IR absorption spectrum of serpentine mainly

Table III: Representative EPMA analyses of serpentine, brucite, phlogopite, magnetite and magnesite in the forsterite-serpentine rock.

Mineral	Serpentine						Brucite	Phlogopite	Magnetite	Magnesite
Sample no.	JAY01	JAY02	JAY05	JAY06	JAY09	JAY10	JAY02	JAY09	JAY09	JAY03
Sample colour	Greenish yellow		Dark green		Black		Greenish yellow	Black	Black	Greenish yellow
Oxides (wt.%)										
SiO ₂	41.00	41.47	40.90	37.70	36.75	37.69	0.58	43.85	0.31	0.06
TiO ₂	nd*	0.01	0.03	nd	nd	0.15	0.01	0.53	nd	nd
Al ₂ O ₃	0.03	0.02	nd	nd	0.03	0.09	nd	12.35	nd	nd
FeO	0.23	0.26	0.52	0.51	1.66	1.73	0.18	0.43	98.25	0.14
Cr ₂ O ₃	nd	0.01	0.02	nd	nd	nd	0.02	0.03	0.02	nd
MnO	0.01	nd	0.02	0.01	nd	0.04	0.06	0.01	0.24	0.04
CaO	0.05	0.02	nd	0.01	0.03	0.04	0.03	nd	nd	0.35
MgO	42.51	41.97	43.04	45.41	45.53	45.24	77.65	27.10	1.10	48.01
NiO	0.02	0.06	nd	nd	0.09	nd	0.02	0.04	nd	nd
ZnO	0.01	nd	nd	nd	0.07	0.11	nd	nd	nd	nd
Na ₂ O	0.18	0.07	0.01	nd	0.02	0.14	0.04	0.38	0.04	nd
K ₂ O	0.03	0.02	nd	nd	0.04	0.11	0.01	9.51	nd	nd
Total	84.07	83.91	84.54	83.64	84.22	85.34	78.59	94.22	99.95	48.61

* Abbreviation: nd = not detected.

shows features in three characteristic regions of 3700–3600, 1100–950 and 600–400 cm⁻¹. According to Balan *et al.* (2002) and Yang *et al.* (2021), the strong absorption bands at 3691 and 3649 cm⁻¹ are related to inner-OH stretching vibrations and the two degenerate out-of-phase stretching modes of the inner-surface OH groups, respectively. The bands at 1083 and 953 cm⁻¹ are attributed to the symmetric stretching vibrations of Si–O. The bands at 611 and 562 cm⁻¹ are caused by in-plane bending vibrations of OH–Mg–OH, whereas the feature at 445 cm⁻¹ belongs to in-plane Mg–OH vibrations. The band at 3584 cm⁻¹ that is attributed to a small amount

of Fe was not observed. This is consistent with the low Fe content of the serpentine, as revealed by EPMA.

DISCUSSION

In a previous study of this forsterite-serpentine rock by Wang *et al.* (2020), the serpentine was identified as antigorite based on a prominent Raman peak at about 230 cm⁻¹, and lizardite and chrysotile were ruled out due to the low-wavenumber characteristics of their Raman spectra. However, Petriglieri *et al.* (2015) demonstrated that the characteristic Raman peak of antigorite is at

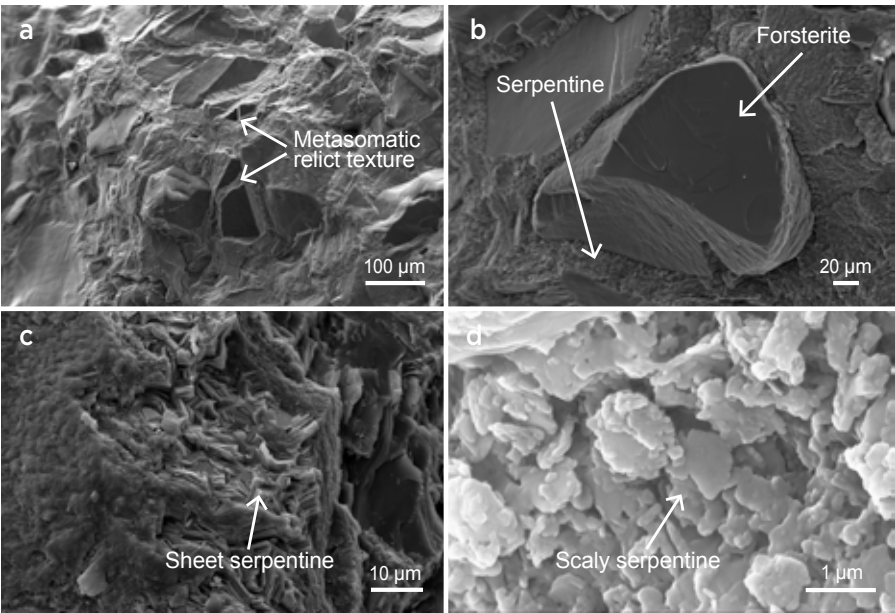


Figure 8: SEM images of broken surfaces of the forsterite-serpentine rock show different microstructural elements, including (a) a metasomatic relict texture (JAY01), (b) embayed relict grains of forsterite in serpentine (JAY01), (c) aggregates of sheet-like serpentine (JAY11) and (d) aggregates of scaly serpentine (JAY11).

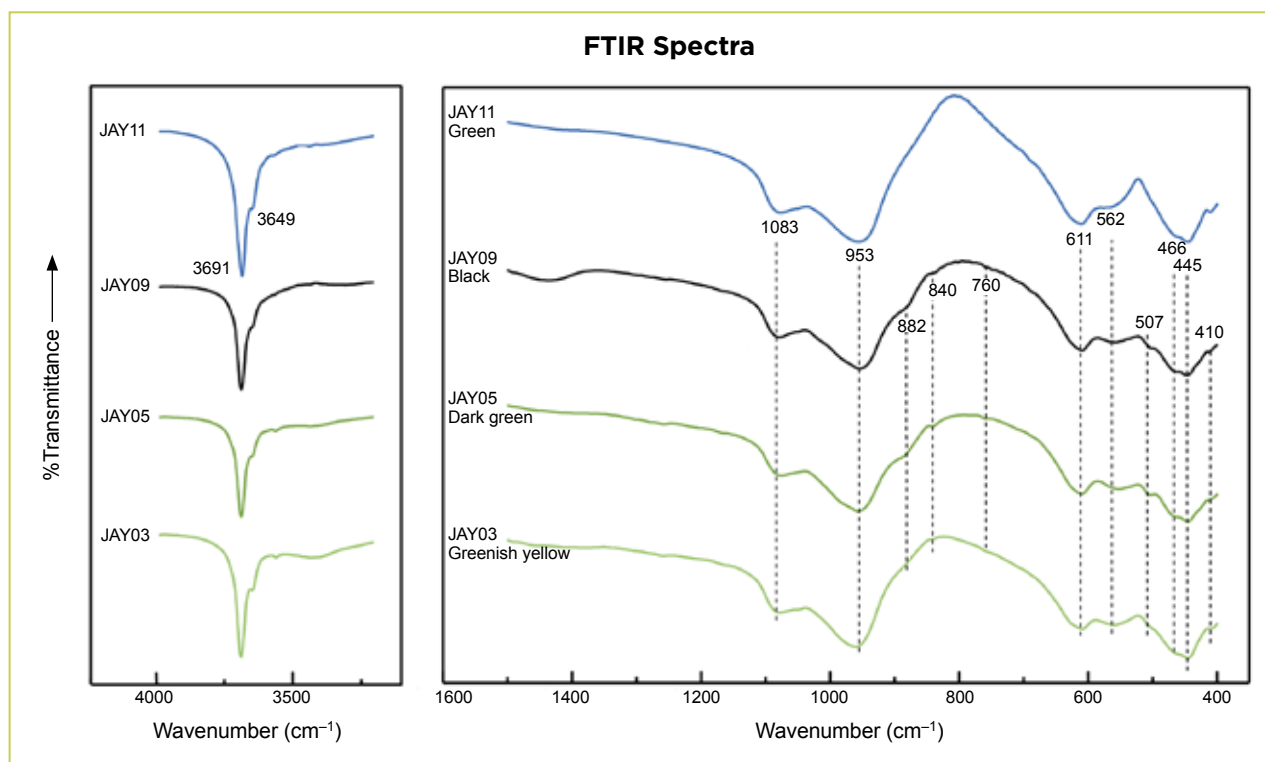


Figure 9: Representative FTIR spectra are shown for the different colours of forsterite-serpentine, including three samples with partial serpentinisation (JAY03, JAY05 and JAY09) and one with pervasive serpentinisation (JAY11). The three partially serpentinised specimens display mixed features of serpentine and forsterite. However, the pervasively serpentinised sample only shows features related to serpentine. Spectra are offset vertically for clarity.

1044 cm⁻¹, which was not found in the spectra obtained by Wang *et al.* (2020). Additionally, Raman spectral features in the high-wavenumber region have been shown to be more reliable for identifying the serpentine-group minerals (Petriglieri *et al.* 2015; Tarling *et al.* 2018). In the present study, our Raman spectra of serpentine displayed two peaks at 3686 and 3704 cm⁻¹ consistent with lizardite, or a main peak at 3699 cm⁻¹ with a shoulder at 3691 cm⁻¹ indicative of chrysotile (cf. Petriglieri *et al.* 2015). Therefore, our data indicate that the serpentine in the forsterite-serpentine rock consists of lizardite and chrysotile, rather than antigorite.

Serpentinisation

Serpentinisation plays a crucial role in the formation of island arcs, the occurrence of earthquakes, the behaviour of hydrothermal vent fluids, and the origin and evolution of life (Guillot & Hattori 2013; Klein & Le Roux 2020). Gem-quality serpentine—showing a compact structure and attractive colour (Wang *et al.* 2013; Adamo *et al.* 2016; Zucali *et al.* 2018)—is formed by the serpentinisation of Mg-rich carbonate or ultramafic rocks. The forsterite-serpentine rock described here is the result of the serpentinisation of forsterite during extensive water-rock interaction.

Several of the accompanying minerals in the forsterite-serpentine rock (e.g. brucite, magnetite, magnesite and talc) are also closely related to the serpentinisation process. In the water-rock reaction process, brucite can form by three mechanisms: (1) serpentinisation of olivine (Frost *et al.* 2013; Klein *et al.* 2013), (2) desilification of serpentine (Ayati & Mackizadeh 2017) and (3) hydration of periclase in marble (Wenzel 2002; Ayati & Mackizadeh 2017). Examination of the thin sections showed that brucite often formed veins within serpentine and was not in contact with forsterite. The association of brucite with serpentine indicates that brucite formed by the serpentinisation of forsterite. When the fluid is rich in H₂O and CO₂, magnesite and talc can also be formed, which is shown by abundant hydrous silicate and carbonate inclusions in the forsterite (Raič *et al.* 2019; Peng *et al.* 2022a).

Magnetite is also an important product of serpentinisation, although the formation mechanism has been widely debated (Bach *et al.* 2006; Evans 2008; Beard *et al.* 2009). Frost *et al.* (2013) suggested that magnetite is generated from the decomposition of early-formed Fe-rich serpentine and ferrous brucite. In this study, magnetite was only found in the black forsterite-serpentine rock, and almost no magnetite was present in

Table IV: Comparison of forsterite-serpentine rock with gem-quality serpentine from different locations in China.

Material, province	Association	Colouration	Diaphaneity	Mohs hardness	Lustre	RI	SG	Major minerals	Minor minerals	Reference
Forsterite-serpentine, Jilin	Marble	Greenish yellow, green to dark green, black	Translucent to opaque	3-6½	Greasy to vitreous	1.55-1.56	2.52-2.82	Forsterite, serpentine (lizardite, chrysotile), brucite	Phlogopite, magnetite, spinel, magnesite, dolomite, talc, pyrite, warwickite	This study
Xiuyan serpentine, Liaoning	Marble	Green, yellow-green, yellow, etc.	Translucent to transparent	—	Waxy to vitreous	1.56	2.79	Serpentine (antigorite, lizardite)	Olivine, talc, brucite, magnesite, dolomite, calcite, magnetite, pyrite, pyrrhotite, ludwigite	Wang & Ye (2014)
Xinyi serpentine, Guangdong	Marble	Yellow-green, dark green, black, etc.	Translucent	4-5	Waxy to silky	1.57	—	Serpentine (antigorite, lizardite, chrysotile)	Phlogopite, talc, calcite, tremolite, chlorite, epidote	Guan & Chen (2005)
Lantian serpentine, Shanxi	Marble	Yellow, green, grey, white, etc.	Translucent	3½-7	Waxy	1.57	2.60-2.90	Serpentine, calcite	Talc, calcite, chlorite, dolomite, diopside, tremolite	Wang <i>et al.</i> (2012)
Hanzhong serpentine, Shanxi	Marble	Dark green, green, light green, yellow-green, yellow-brown, etc.	Translucent to opaque	2-6½	Waxy to vitreous	1.56-1.57	2.51	Serpentine (lizardite)	Hornblende, calcite, dolomite, talc	Yang <i>et al.</i> (2021)
Luchuan serpentine, Guangxi	Marble	Green to dark green, bluish white to white	Translucent	—	Waxy to vitreous	—	—	Serpentine (antigorite, lizardite)	Calcite, dolomite	Wang & Gan (2012b)
Taishan serpentine, Shandong	Ultramafic rock	Dark green, grey-green, black, etc.	Translucent to opaque	5-6½	Waxy to greasy	1.56	2.50-2.66	Serpentine	Carbonate, magnetite, pyrite, limonite, talc, chlorite, illite, kaolinite, mica	Chen <i>et al.</i> (2011)
Yuanyang serpentine, Gansu	Ultramafic rock	Yellow-green, light green, 'emerald' green, grey-green, etc.	Translucent	4-5	Waxy to vitreous	1.55-1.57	2.61-2.72	Serpentine (antigorite, lizardite)	Tremolite, talc, dolomite, magnetite, limonite, 'hydronickel'	Ge <i>et al.</i> (2011)

the greenish yellow samples. Notably, the Fe contents of the forsterite and serpentine in the black material were higher than in the greenish yellow and dark green specimens. We infer that the presence of a small amount of magnetite is the decomposition product of Fe-rich serpentine. Furthermore, the presence of magnetite may be the main reason for the black colour of those samples.

Comparison with Gem-quality Serpentine

In general, gem-quality serpentine is associated with either marble or ultramafic rock. Marble-type serpentine

is mainly formed by contact metasomatism of Mg-rich carbonate rocks during the intrusion of intermediate-to-felsic magmas. Ultramafic-type serpentine is generally formed by the metamorphism of ultramafic rocks (mainly dunite and peridotite) under hydrothermal activity at low-to-moderate temperature. The marble vs ultramafic origin of gem-quality serpentine can be identified from the associated mineral constituents (Table IV) and the trace elements that are present. Marble-type serpentine is associated with Mg-skarn minerals (e.g. forsterite, dolomite and diopside). In addition, the contents of Cr, Co and Ni are significantly

higher in ultramafic-type serpentine than in Mg-rich marble-type serpentine (Wang *et al.* 2007; Ge *et al.* 2011; Wang & Gan 2012b).

Considering the geological setting, chemical features and microscopic characteristics of the minerals in the forsterite-serpentine, the deposit formed by contact metasomatism of Mg-rich carbonate rock (Peng *et al.* 2022a). The origin of the forsterite-serpentine deposit is therefore similar to marble-type serpentine. However, forsterite is typically rare in marble-type serpentine deposits. In addition, marble-type gem serpentine is formed by the direct serpentinisation of dolomite. However, the formation of the forsterite-serpentine rock appears to have involved a more complicated process in which forsterite first formed by the reaction between dolomite and Si-rich hydrothermal fluid, and subsequently underwent serpentinisation during infiltration of B-rich hydrothermal fluid (Peng *et al.* 2022a). The presence of B- and Mg-enriched forsterite is a distinctive feature of the forsterite-serpentine rock.

It can be challenging for a gemmologist to separate the forsterite-serpentine rock from gem-quality serpentine. Both materials have overlapping gemmological properties and bulk-chemical compositions (except for elevated B in the forsterite-serpentine, as mentioned above). Nevertheless, Raman and IR spectroscopy are useful for indicating the presence of forsterite. As the degree of serpentinisation increases, the forsterite content decreases (to just 10% or less of the rock) and thus the material can merge into gem-quality serpentine.

CONCLUSIONS

Expanding on prior investigations (Wang *et al.* 2020; Peng *et al.* 2022a, b), this article provides a comprehensive description of the gemmological characteristics of forsterite-serpentine from north-eastern China and also compares this material to gem-quality serpentine. The forsterite-serpentine rock has an appealing appearance—ranging from greenish yellow to dark green to black—and a compact microstructure that make it well suited for carving and fashioning into jewellery items (e.g. Figure 10). It is mainly composed of forsterite, serpentine and brucite. Minor phases include spinel, magnesite, magnetite and phlogopite, which more commonly occur in the black material.

We ascribe the formation of this forsterite-serpentine to contact metasomatism of Mg-rich carbonate rock. The presence of B- and Mg-rich forsterite is distinctive when compared to other serpentine gem materials.



Figure 10: These forsterite-serpentine jewellery items include (a) beaded necklaces and (b) a set of bangles. The diameter of the spherical forsterite-serpentine beads in the necklaces (which also contain turquoise, garnet and agate) is 1.0 cm, and the bangles are 8 cm in diameter. Photos by Bijie Peng.

REFERENCES

- Adamo, I., Diella, V., Bocchio, R., Rinaudo, C. & Marinoni, N. 2016. Gem-quality serpentine from Val Malenco, Central Alps, Italy. *Gems & Gemology*, **52**(1), 38–49, <https://doi.org/10.5741/gems.52.1.38>.
- Adams, C.J., Beck, R.J. & Campbell, H.J. 2007. Characterisation and origin of New Zealand nephrite jade using its strontium isotopic signature. *Lithos*, **97**(3–4), 307–322, <https://doi.org/10.1016/j.lithos.2007.01.001>.
- Ayati, F. & Mackizadeh, M.A. 2017. Petrogenesis of polygenic marbles, Baqi-Abad region, Yazd, central Iran. *Journal of African Earth Sciences*, **125**, 191–201, <https://doi.org/10.1016/j.jafrearsci.2016.11.013>.
- Bach, W., Paulick, H., Garrido, C.J., Ildefonse, B., Meurer, W.P. & Humphris, S.E. 2006. Unraveling the sequence of serpentinization reactions: Petrography, mineral chemistry, and petrophysics of serpentinites from MAR 15°N (ODP Leg 209, Site 1274). *Geophysical Research Letters*, **33**(13), article L13306, <https://doi.org/10.1029/2006gl025681>.
- Balan, E., Saitta, A.M., Mauri, F., Lemaire, C. & Guyot, F. 2002. First-principles calculation of the infrared spectrum of lizardite. *American Mineralogist*, **87**(10), 1286–1290, <https://doi.org/10.2138/am-2002-1003>.
- Beard, J.S., Frost, B.R., Fryer, P., McCaig, A., Searle, R., Ildefonse, B., Zinin, P. & Sharma, S.K. 2009. Onset and progression of serpentinization and magnetite formation in olivine-rich troctolite from IODP hole U1309D. *Journal of Petrology*, **50**(3), 387–403, <https://doi.org/10.1093/petrology/egp004>.
- Blondes, M.S., Brandon, M.T., Reiners, P.W., Page, F.Z. & Kita, N.T. 2012. Generation of forsteritic olivine (Fo_{99.8}) by subsolidus oxidation in basaltic flows. *Journal of Petrology*, **53**(5), 971–984, <https://doi.org/10.1093/petrology/egs006>.
- Breitenfeld, L.B., Dyar, M.D., Carey, C.J., Tague, T.J., Wang, P., Mullen, T. & Parente, M. 2018. Predicting olivine composition using Raman spectroscopy through band shift and multivariate analyses. *American Mineralogist*, **103**(11), 1827–1836, <https://doi.org/10.2138/am-2018-6291>.
- Bucher, K. & Grapes, R. 2011. *Petrogenesis of Metamorphic Rocks*. Springer-Verlag, Berlin, Germany, xii + 428 pp., <https://doi.org/10.1007/978-3-540-74169-5>.
- Chen, Y., Li, J., Fan, C. & Zhang, Z. 2011. Gemmological characteristics of “Taishan” jade. *Journal of Gems & Gemmology*, **13**(1), 29–32 (in Chinese with English abstract).
- Chopelas, A. 1991. Single crystal Raman spectra of forsterite, fayalite, and monticellite. *American Mineralogist*, **76**(7–8), 1101–1109.
- D’Ippolito, V., Andreozzi, G.B., Bersani, D. & Lottici, P.P. 2015. Raman fingerprint of chromate, aluminate and ferrite spinels. *Journal of Raman Spectroscopy*, **46**(12), 1255–1264, <https://doi.org/10.1002/jrs.4764>.
- Dufresne, W.J.B., Ruffledt, C.J. & Marshall, C.P. 2018. Raman spectroscopy of the eight natural carbonate minerals of calcite structure. *Journal of Raman Spectroscopy*, **49**(12), 1999–2007, <https://doi.org/10.1002/jrs.5481>.
- Evans, B.W. 2004. The serpentinite multisystem revisited: Chrysotile is metastable. *International Geology Review*, **46**(6), 479–506, <https://doi.org/10.2747/0020-6814.46.6.479>.
- Evans, B.W. 2008. Control of the products of serpentinization by the Fe²⁺ Mg⁻¹ exchange potential of olivine and orthopyroxene. *Journal of Petrology*, **49**(10), 1873–1887, <https://doi.org/10.1093/petrology/egn050>.
- Evans, B.W. 2010. Lizardite versus antigorite serpentinite: Magnetite, hydrogen, and life(?). *Geology*, **38**(10), 879–882, <https://doi.org/10.1130/g31158.1>.
- Frost, B.R., Evans, K.A., Swapp, S.M., Beard, J.S. & Mothersole, F.E. 2013. The process of serpentinization in dunite from New Caledonia. *Lithos*, **178**, 24–39, <https://doi.org/10.1016/j.lithos.2013.02.002>.
- Ge, Y., Wang, S., Yu, G., Guo, J., Wu, T., Fan, G., Liu, Y. & He, L. 2011. Geochemical and gemmological characteristics of Yuanyang jade from Wushan County, Gansu Province. *Acta Petrologica et Mineralogica*, **30**(Z1), 151–161 (in Chinese with English abstract).
- Guan, C. & Chen, Y. 2005. Geological characteristics of the southern jade ore deposit in Xinyi City, Guangdong Province. *West-China Exploration Engineering*, **17**(12), 152–153 (in Chinese).
- Guillot, S. & Hattori, K. 2013. Serpentinites: Essential roles in geodynamics, arc volcanism, sustainable development, and the origin of life. *Elements*, **9**(2), 95–98, <https://doi.org/10.2113/gselements.9.2.95>.
- Hemley, J.J., Montoya, J.W., Christ, C.L. & Hostetler, P.B. 1977. Mineral equilibria in the MgO-SiO₂-H₂O system; I, Talc-chrysotile-forsterite-brucite stability relations. *American Journal of Science*, **277**(3), 322–351, <https://doi.org/10.2475/ajs.277.3.322>.
- Kim, S.W., Santosh, M., Park, N. & Kwon, S. 2011. Forearc serpentinite mélange from the Hongseong suture, South Korea. *Gondwana Research*, **20**(4), 852–864, <https://doi.org/10.1016/j.gr.2011.01.012>.
- Klein, F. & Le Roux, V. 2020. Quantifying the volume increase and chemical exchange during serpentinization. *Geology*, **48**(6), 552–556, <https://doi.org/10.1130/g47289.1>.

- Klein, F., Bach, W. & McCollom, T.M. 2013. Compositional controls on hydrogen generation during serpentinization of ultramafic rocks. *Lithos*, **178**, 55–69, <https://doi.org/10.1016/j.lithos.2013.03.008>.
- Klein, F., Humphris, S.E. & Bach, W. 2020. Brucite formation and dissolution in oceanic serpentinite. *Geochemical Perspectives Letters*, **16**, 1–5, <https://doi.org/10.7185/geochemlet.2035>.
- Kuebler, K.E., Jolliff, B.L., Wang, A. & Haskin, L.A. 2006. Extracting olivine (Fo–Fa) compositions from Raman spectral peak positions. *Geochimica et Cosmochimica Acta*, **70**(24), 6201–6222, <https://doi.org/10.1016/j.gca.2006.07.035>.
- Lu, X.P., Wu, F.Y., Guo, J.H., Wilde, S.A., Yang, J.H., Liu, X.M. & Zhang, X.O. 2006. Zircon U–Pb geochronological constraints on the Paleoproterozoic crustal evolution of the Eastern block in the North China craton. *Precambrian Research*, **146**(3–4), 138–164, <https://doi.org/10.1016/j.precamres.2006.01.009>.
- McKeown, D.A., Bell, M.I. & Etz, E.S. 1999. Raman spectra and vibrational analysis of the trioctahedral mica phlogopite. *American Mineralogist*, **84**(5–6), 970–976, <https://doi.org/10.2138/am-1999-5-633>.
- Meng, E., Wang, C.Y., Yang, H., Cai, J., Ji, L. & Li, Y.G. 2017a. Paleoproterozoic metavolcanic rocks in the Ji'an Group and constraints on the formation and evolution of the northern segment of the Jiao-Liao-Ji Belt, China. *Precambrian Research*, **294**, 133–150, <https://doi.org/10.1016/j.precamres.2017.03.019>.
- Meng, E., Wang, C.-Y., Li, Z., Li, Y.-G., Yang, H., Cai, J., Ji, L. & Jin, M.-Q. 2017b. Palaeoproterozoic metasedimentary rocks of the Ji'an Group and their significance for the tectonic evolution of the northern segment of the Jiao–Liao–Ji Belt, North China craton. *Geological Magazine*, **155**(1), 149–173, <https://doi.org/10.1017/s0016756817000632>.
- Peng, B., He, M., Yang, M., Liu, X., Sui, X., Sun, K. & Wu, S. 2022a. Petrogenesis of Jian forsterite jade solely composed of end-member forsterite (Fo 99.8): Constrained by trace element and oxygen isotope. *Ore Geology Reviews*, **150**, article 105167, <https://doi.org/10.1016/j.oregeorev.2022.105167>.
- Peng, B., He, M., Yang, M., Wu, S. & Fan, J. 2022b. Natural forsterite strongly enriched in boron: Crystal structure and spectroscopy. *Crystals*, **12**(7), article 975, <https://doi.org/10.3390/cryst12070975>.
- Petriglieri, J.R., Salvioli-Mariani, E., Mantovani, L., Tribaudino, M., Lottici, P.P., Laporte-Magoni, C. & Bersani, D. 2015. Micro-Raman mapping of the polymorphs of serpentine. *Journal of Raman Spectroscopy*, **46**(10), 953–958, <https://doi.org/10.1002/jrs.4695>.
- Plechov, P.Y., Shcherbakov, V.D. & Nekrylov, N.A. 2018. Extremely magnesian olivine in igneous rocks. *Russian Geology and Geophysics*, **59**(12), 1702–1717, <https://doi.org/10.1016/j.rgg.2018.12.012>.
- Raič, S., Krenn, K. & Mogessie, A. 2019. Possible sources for CH₄-rich fluid inclusions in olivine from troctolitic rocks of the Bathtub intrusion, Duluth Complex, U.S.A. *Precambrian Research*, **331**, article 105376, <https://doi.org/10.1016/j.precamres.2019.105376>.
- Rinaudo, C., Gastaldi, D. & Belluso, E. 2003. Characterization of chrysotile, antigorite and lizardite by FT-Raman spectroscopy. *Canadian Mineralogist*, **41**(4), 883–890, <https://doi.org/10.2113/gscanmin.41.4.883>.
- Schwartz, S., Guillot, S., Reynard, B., Lafay, R., Debret, B., Nicollet, C., Lanari, P. & Auzende, A.L. 2013. Pressure–temperature estimates of the lizardite/antigorite transition in high pressure serpentinites. *Lithos*, **178**, 197–210, <https://doi.org/10.1016/j.lithos.2012.11.023>.
- Šontevska, V., Jovanovski, G. & Makreski, P. 2007. Minerals from Macedonia. Part XIX. Vibrational spectroscopy as identificational tool for some sheet silicate minerals. *Journal of Molecular Structure*, **834–836**, 318–327, <https://doi.org/10.1016/j.molstruc.2006.10.026>.
- Sonzogni, Y., Treiman, A.H. & Schwenzer, S.P. 2017. Serpentine with and without brucite: A reaction pathway analysis of a natural serpentinite in the Josephine ophiolite, California. *Journal of Mineralogical and Petrological Sciences*, **112**(2), 59–76, <https://doi.org/10.2465/jmps.160509>.
- Sun, J., Wu, Z., Cheng, H., Zhang, Z. & Frost, R.L. 2014. A Raman spectroscopic comparison of calcite and dolomite. *Spectrochimica Acta Part A: Molecular and Biomolecular Spectroscopy*, **117**, 158–162, <https://doi.org/10.1016/j.saa.2013.08.014>.
- Tarling, M.S., Rooney, J.S., Viti, C., Smith, S.A.F. & Gordon, K.C. 2018. Distinguishing the Raman spectrum of polygonal serpentine. *Journal of Raman Spectroscopy*, **49**(12), 1978–1984, <https://doi.org/10.1002/jrs.5475>.
- Trittschack, R., Grobety, B. & Koch-Muller, M. 2012. In situ high-temperature Raman and FTIR spectroscopy of the phase transformation of lizardite. *American Mineralogist*, **97**(11–12), 1965–1976, <https://doi.org/10.2138/am.2012.4162>.
- Wang, S. & Dong, P. 2011. Classification, geologic characteristics and origin of the jade from Xiuyan, Liaoning Province, China. *Geology and Resources*, **20**(5), 321–331 (in Chinese with English abstract).
- Wang, Y.Y. & Gan, F.X. 2012a. Coloration mechanism and chromaticity of Xiuyan jade of China. *Spectroscopy and Spectral Analysis*, **32**(9), 2305–2310 (in Chinese with English abstract).

- Wang, Y.Y. & Gan, F.X. 2012b. Mineral structure and mineralization mechanism of serpentine jade from Luchuan, Guangxi Province. *Rock and Mineral Analysis*, **31**(5), 788–793 (in Chinese with English abstract).
- Wang, C. & Ye, L. 2014. A genetic analysis of the Yingkou serpentine jade deposit in Liaoning Province. *Acta Petrologica et Mineralogica*, **33**(2), 397–406 (in Chinese with English abstract).
- Wang, S., Yun, X. & Li, S. 2007. Gemmological characteristics and developing prospect of Fe-rich serpentine jade from Liaoning Province. *Journal of Gems & Gemmology*, **9**(4), 1–6 (in Chinese with English abstract).
- Wang, Y.Y., Gan, F.X. & Zhao, H.X. 2012. Nondestructive analysis of Lantian jade from Shaanxi Province, China. *Applied Clay Science*, **70**, 79–83, <https://doi.org/10.1016/j.clay.2012.09.012>.
- Wang, Y.Y., Gan, F.X. & Zhao, H.X. 2013. Inclusions of black-green serpentine jade determined by Raman spectroscopy. *Vibrational Spectroscopy*, **66**, 19–23, <https://doi.org/10.1016/j.vibspec.2013.01.008>.
- Wang, Y., He, M., Yan, W., Yang, M. & Liu, X. 2020. Jianite: Massive dunite solely made of virtually pure forsterite from Ji'an County, Jilin Province, northeast China. *Minerals*, **10**(3), article 220, <https://doi.org/10.3390/min10030220>.
- Wenzel, T. 2002. Partial melting and assimilation of dolomitic xenoliths by mafic magma: The Ioko-Dovyren intrusion (North Baikal region, Russia). *Journal of Petrology*, **43**(11), 2049–2074, <https://doi.org/10.1093/petrology/43.11.2049>.
- White, S. 2009. Laser Raman spectroscopy as a technique for identification of seafloor hydrothermal and cold seep minerals. *Chemical Geology*, **259**(3–4), 240–252, <https://doi.org/10.1016/j.chemgeo.2008.11.008>.
- Yang, M., He, M., Wang, F., Wu, S., Li, Q. & Zhang, B. 2021. Mineralogical and spectral studies on the serpentine jade in Hanzhong, Shaanxi Province. *Northwestern Geology*, **54**(4), 142–155, <https://doi.org/10.19751/j.cnki.61-1149/p.2021.04.011> (in Chinese with English abstract).
- Yu, Q. & Li, S. 2017. *China Tremolite Jade and Serpentine Jade*. China University of Geosciences Press, Wuhan, China (see pp. 234–240; in Chinese).
- Yu, X.-Y., Long, Z.-Y., Zhang, Y., Qin, L.-J., Zhang, C., Xie, Z.-R., Wu, Y.-R., Yan, Y. *et al.* 2021. Overview of gemstone resources in China. *Crystals*, **11**, article 1189, <https://doi.org/10.3390/cryst11101189>.
- Zhang, W., Liu, F., Cai, J., Liu, C., Liu, J., Liu, P., Liu, L., Wang, F. *et al.* 2018. Geochemistry, zircon U-Pb dating and tectonic implications of the Palaeoproterozoic Ji'an and Laoling groups, northeastern Jiao-Liao-Ji Belt, North China craton. *Precambrian Research*, **314**, 264–287, <https://doi.org/10.1016/j.precamres.2018.06.010>.
- Zucali, M., Marinoni, N., Diella, V., Croce, A., Rinaudo, C. & Fontana, E. 2018. Deciphering the tectonic-geodynamic context of the gem-quality “noble serpentine” deposit formation combining microstructural, chemical and micro-Raman analyses in Palaeozoic olivine-bearing marbles and serpentine-hosting rocks (Pizzo Tremogge, Margna unit – Austroalpine, Val Malenco – Central Alps, Italy). *Ore Geology Reviews*, **92**, 257–270, <https://doi.org/10.1016/j.oregeorev.2017.11.020>.

The Authors

Dr Bijie Peng^{1,2}, Prof. Mingyue He^{1,2*}, Mei Yang², Prof. Xi Liu^{3,4} and Dr Xinhao Sui^{3,4}

¹ School of Gemmology, China University of Geosciences, No. 29 Xueyuan Road, Haidian District, Beijing 100083, China

² The National Mineral Rock and Fossil Specimens Resource Center, China University of Geosciences, No. 29 Xueyuan Road, Haidian District, Beijing 100083, China

³ School of Earth and Space Sciences, Peking University, No. 5 Yiheyuan Road, Haidian District, Beijing 100871, China

⁴ Key Laboratory of Orogenic Belts and Crustal Evolution, Ministry of Education of China, No. 5 Yiheyuan Road, Haidian District, Beijing 100871, China

* Email: hemy@cugb.edu.cn

Acknowledgements

This work was supported by the National Mineral Rock and Fossil Specimens Resource Center and the Strategic Priority Research Program (B) of the Chinese Academy of Sciences (grant no. XDB42000000).

Gem-A Members and Gem-A registered students receive 5% discount on books and 10% discount on instruments from Gem-A Instruments

Contact instruments@gem-a.com or visit our website for a catalogue



PERIDOT

The Gift of Hope



FULI GEMSTONES

fuligemstones.com



Late Nineteenth-Century Portraits Engraved on Diamond

Erik Schoonhoven

ABSTRACT: Engraved diamonds are a rare art form, and those depicting portraits are an even greater rarity. This article highlights three extant engraved portrait diamonds from the second half of the nineteenth century, when a revival of this art form took place. The author suggests a re-attribution of the engraver of one of these diamonds (J. J. Dreese rather than M. C. de Vries) and proposes that another one, known as the ‘Queen Frederica diamond’, instead shows the UK’s Queen Victoria.

The Journal of Gemmology, 38(6), 2023, pp. 616–620, <https://doi.org/10.15506/JoG.2023.38.6.616>
© 2023 Gem-A (The Gemmological Association of Great Britain)



Figure 1: This engraved diamond portrait of King William III of the Netherlands (15.7 × 15.2 × 2.6 mm) was made by M. C. de Vries Jr in 1878. Photo courtesy of the Koninklijke Verzamelingen/Joods Historisch Museum, Amsterdam.

Engraved diamonds are very rare, and may feature various subjects such as crowns, monograms, coats of arms, inscriptions, etc. This author is aware of just 75 of them, of which only 18 from before the nineteenth century are known to still exist. Moreover, it is necessary to go back to 1754 to find good, published information on them. Engraved portraits in diamond are even rarer (e.g. Figure 1).

One of the most important known gem engravers, Laurentius (Lorenz) Natter (1705–1763), wrote in his 1754 treatise, ‘The extreme Hardness of the Stones is a great Obstacle in the Working, because the Tools are sooner blunted and worn out, notwithstanding the Diamond-powder, which must be constantly applied’ (Natter 1754, p. xiii). He went on to say the following about diamond engraving (Natter 1754, pp. xv):

...I am persuaded that I could engrave a Portrait on one, equally well; but not without great Patience, and as much Labour as a Dozen of Oriental Stones should require. But such a Work would amount to so high a Price, that no Artist will undertake it from mere Curiosity, and without an express Order from some Nobleman.

Perhaps it was Natter’s treatise that inspired Moses Cohen de Vries Jr (1807–1883) to start working on such a Herculean task. He was a stone and stamp engraver, as well as a medallist and draughtsman. He received his education at the State Academy of Visual Arts in

Amsterdam, the Netherlands, and in 1837 he became a member of its Koninklijke Academie (Royal Academy; RKD 1994/2023).

With Amsterdam being a major diamond-cutting centre at the time, the industry invested much in the international exhibitions of the nineteenth century. Martin Coster, founder of Royal Coster Diamonds, had a replica of his Amsterdam diamond-cutting factory built at the 1867 Exposition Universelle in Paris, France. It received a lot of media attention, in part because a diamond intaglio portrait by de Vries of Napoleon Bonaparte was exhibited there (*Le Constitutionnel: Journal Politique, Littéraire, Universel*, 3 May 1867, p. 14). It was set in a pin made by Oscar Massin, surrounded by a gold laurel wreath ‘sprinkled’ with small diamonds (*Le Pays, Journal de l'Empire*, 26 April 1867, p. 2; Massin 1890). No image of this diamond intaglio is known, and it is unclear whether the diamond still exists. According to the *Journal des Débats Politiques et Littéraires* (27 June 1867, p. 2):

In the exhibition of M. Coster there still is a curiosity so extraordinary that one can confirm with certitude that it is unique in the world; I want to talk about an engraved diamond representing a portrait. It is not, like the famous bee which belongs to the Queen of England, a simple line; it is a true intaglio produced with the help of the reel and the rivet tool; the hollows and reliefs are observed with an unthinkable precision; the form is executed meticulously, and the resemblance is striking at first glance. He must have used diamond points to arrive at this result, which until now appeared to be outside the scope of human abilities. It is a feat of patience and skill.... This work, absolutely special and without precedence in the history of glyptics, is due to M. C.-M. de Vriés.¹

A TALE OF TWO ENGRAVED DIAMONDS

A portrait of King William III of the Netherlands was engraved on diamond by de Vries in 1878, and it is now in the Dutch Royal Collection (again, see Figure 1). Based on the king's profile used on coins (e.g. Figure 2),

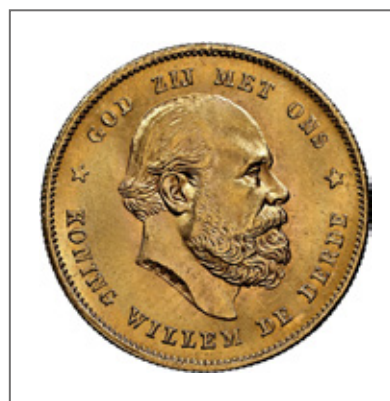


Figure 2: The portrait of King William III on this 1875 Netherlands 10 Gulden gold coin (22.5 mm in diameter) shows a close resemblance to the engraving on the diamond in Figure 1. Photo courtesy of Numismatic Guaranty Co.

the portrait is accurate, and the quality of the intaglio is so high that even individual beard hairs are visible. It weighs about 15 ct and was exhibited in the Dutch diamond pavilion at the 1878 Exposition Universelle in Paris (*Algemeen Handelsblad*, 8 May 1883, p. 1). Afterwards, the Dutch Consul-General in Paris, Martin Coster, had the diamond set in a medallion by Massin, which he gave to the king in 1879 for his wedding with Princess Emma of Waldeck-Pyrmont, who wore it during the ceremony (Anonymous n.d.).

Interestingly, the Field Museum in Chicago, Illinois, USA, also owns an engraved diamond portrait of King William III (Figure 3), which was listed in the museum's catalogue as having been made by 'De Vrees of Amsterdam' (Field Columbian Museum 1894, p. 79). The approximately 10 ct stone was displayed at the same Exposition Universelle of 1878. It was subsequently bought by Tiffany & Co., and exhibited by them at the 1893 World's Columbian Exhibition in Chicago, with the description: 'Portrait of William II. [sic], late King of Holland. Engraved on Diamond by the late DeVrees [sic] of Amsterdam. Exhibited at Paris Exposition of 1878' (Tiffany & Co. 1893, p. 107). Harlow N. Higinbotham (1838–1919), president of the Columbian Exhibition, head of the board of trustees and, later, president of the Field Museum, purchased Tiffany & Co.'s entire exhibit collection and donated it to the Field Museum in 1894. The original Field Museum catalogue listed it as '718. Diamond in scarf pin', followed by the description from

¹ Il est encore, dans l'exposition de M. Coster, une curiosité tellement extraordinaire, qu'on peut affirmer avec certitude qu'elle est unique au monde, je veux parler d'un diamant gravé représentant un portrait. Ce n'est point, comme la célèbre abeille appartenant à la reine d'Angleterre, un simple trait ; c'est une véritable intaille qu'on dirait obtenue à l'aide du touret et de la bouterolle; le creux et les reliefs sont observés avec une précision inconcevable; le modelé est exécuté avec minutie, et la ressemblance frappe dès le premier coup d'oeil. Il a fallu user bien des pointes de diamans pour arriver à ce résultat, qui jusqu'à présent paraissait hors de la portée des facultés humaines. C'est un chef-d'œuvre de patience et d'adresse. Par quel procédé l'artiste est-il arrivé à vaincre tant de difficultés qu'on croyait insurmontables? c'est ce que j'ignore. Ce travail, absolument particulier et sans précédent dans l'histoire de la glyptique, est dû à M. C.-M. de Vriés. (Available at <https://gallica.bnf.fr/ark:/12148/bpt6k4565532/f1.image>.)



Figure 3: A portrait of King William III of the Netherlands is also shown on this diamond (about 16 × 9 × 2 mm), which is mounted in a scarf pin. The stone was likely engraved by J. J. Dreeze in 1878. Photo courtesy of the Field Museum, GEO86518 3688Ad.

It is unlikely that de Vries made two diamond portraits of William III. The engravings are somewhat dissimilar, and are based on different portraits of the king, which suggests the two diamonds had different engravers. Fortunately, the Dutch news magazine *Nieuw Israelietisch Weekblad* (7 June 1878, p. 2) offers clarity:

At the Parisian exhibition, amongst the gemstones, sent by the local [Amsterdam] gentlemen A.E. Daniels and Son, and H. van der Linger in Paris, a diamond commands special attention, because in it is engraved the very well resembling portrait of our king. Engraving on diamond is an art form that was said to have been known up until three centuries ago, but which is lost today. Our fellow citizen, the engraver M. C. de Vries Jr, however, has revived that art form, according to the aforementioned diamond.

At the said exhibition there are more rare diamonds from here; amongst others, three attract attention

because of their fine treatment and pretty shapes, namely a brilliant cut and mounted like a lantern, a brilliant shaped as a heart and a portrait stone featuring the bust of our king. They were created by the local Mr. J. Dreeze [sic].²

Juda Joel Dreeze (1821–1906) was a famous diamond cutter (*Algemeen Handelsblad*, 29 October 1906, p. 14) who received no other artistic training. This could explain the different qualities of the two engraved portraits, and suggests that this second diamond portrait should be attributed to Dreeze.

THE ‘QUEEN FREDERICA DIAMOND’

A third late-nineteenth-century engraved portrait diamond reportedly depicts Queen Frederica (or Frederika) of the Netherlands (Figure 4; Copeland 1960; Crowningshield 1961; Dickinson 1965; Diamond Information Center 1971). It supposedly was exhibited at a Brussels Universal Exhibition after being acquired by the New York jeweller Max Fine & Sons around 1920 (*Schenectady Gazette*, 11 April 1967; JCK 1970), and on 23 December 1997 it was offered to the Museum of the City of New York.

However, it seems oral history went wrong here: There is no Dutch queen who was widely known as ‘Queen Frederica’. Instead, Frederica Louisa Wilhelmina (1774–1837), wife of King William I, was referred to as ‘Queen Wilhelmina’. Also, evidence for its presence at a Brussels exhibition is lacking. Further, the portrait does not show any resemblance to Queen Wilhelmina. However, it does look like the profile of Queen Victoria of the United Kingdom (1819–1901), as known from many stamps and coins (e.g. Figure 5). In fact, a portrait of Queen Victoria engraved on diamond by de Vries was exhibited at the 1883 International Colonial and Export Exhibition in Amsterdam, as reported in newspapers at the time (e.g. *De Tijd*, 23 April 1883, p. 2):

Amongst the gems of the Exhibition will probably be a beautifully worked gold medallion, within it a diamond of more than usual size and of the purest

² *Op de Parijsche tentoonstelling trekt onder de edelgesteenten, door de heeren A. E. Daniels en Zoon alhier, en H. van der Linger te Parijs ingezonden, een diamant de bijzondere aandacht, omdat daarin het welgelijkend portret van onzen koning is gegraveerd. Het graveeren op diamant is namelijk een kunst, die men voor drie eeuwen schijnt gekend te hebben, doch die sedert verloren is gegaan. Onze stadgenoot, de graveur M. C. de Vries Jr., heeft echter, blijkens de genoemde diamant, die kunst weder in het leven geroepen.*

Op genoemde tentoonstelling bevinden zich nog meer zeldzame diamanten van hier; o. a. drie, die door schoone bewerking en fraaie vormen de aandacht trekken, namelijk een brillant als lantaarn geslepen en gemonteerd, een brillant als hart en een als portretsteen bewerkt, met het borstbeeld van onzen koning. Zij zijn door den heer J. Dreeze alhier bewerkt. (Available at <https://resolver.kb.nl/resolve?urn=ddd:010871962:mpeg21:p002>.)



Figure 4: The engraved diamond portrait known as the ‘Queen Frederica diamond’ (10 × 8 × 2 mm; 1.88 ct) instead probably shows Queen Victoria of the United Kingdom. It was likely engraved by M. C. de Vries Jr in 1883. Private collection, courtesy of Hadrien Rambach; photo by Jeremy Zenou.

water, on which the portrait of H. M. Victoria, Queen of England, is engraved.

We learned that the engraving of this stone was the last labor of the recently deceased well known engraver M. C. De Vries, the only one here who worked in this artistic genre.³

What are the odds the ‘Queen Frederica diamond’ actually depicts the presumed Queen Victoria? We know the diamond does not well resemble ‘Queen Frederica’. We also know engraved diamond portraits are incredibly rare, and that one of Queen Victoria has been recorded, and the portrait does look a lot like her. Although the diamond in Figure 4 is wafer-thin, it has a considerable surface size. The unengraved plane has not been well polished (scratches are visible), which indicates it was not completely finished. With de Vries’ death shortly before the exhibition, this seems to coincide.

CONCLUSION

Within the already small niche of engraved diamonds, engraved portrait diamonds represent a very small minority. This is the first article on this



Figure 5: For most of her long reign, the profile of a young Queen Victoria was in circulation on coins. This so-called Young Head coinage was in use from 1838 to 1887, and her profile resembles the portrait on the diamond in Figure 4. The Young Head profile is the widest known portrait of the queen, and is shown here on an 1857 gold sovereign coin (22 mm in diameter). Courtesy of Heritage Auctions, HA.com.

subject—demonstrating the lack of academic study—and describes the only three extant late nineteenth-century examples. The author proposes the re-attribution of the engraver in one case (J. J. Dreese rather than M. C. de Vries) and a re-identification of the subject in another (Queen Victoria rather than ‘Queen Frederica’).

REFERENCES

- Anonymous n.d. *Diamanten Hanger Van Emma*. Koninklijke Verzamelingen, <https://tinyurl.com/yju7srjc>, accessed 22 February 2023.
- Diamond Information Center 1971. *Notable Diamonds of the World*. N.W. Ayer & Son, New York, New York, USA, 56 pp. (see p. 36).
- Copeland, L.L. (ed) 1960. *The Diamond Dictionary*. Literary Licensing LLC, Los Angeles, California, USA, 328 pp. (see p. 221).
- Crowningshield, R. 1961. Developments and Highlights at the Gem Trade Lab in New York: Carved diamond. *Gems & Gemology*, 10(7), 223, https://www.gia.edu/doc/fall_1961.pdf.

³ *Onder de klemoodiën op de Tentoonstelling zal vermoedelijk ook te vinden zijn een prachtig bewerkt gouden medaillon, waarin een diamant van meer dan gewone grootte en van het zuiverste water, op welken het portret van H. M. Victoria, koningin van Engeland, is gegraveerd. Wij vernemen dat het graveeren van dezen steen de laatste arbeid was van den onlangs overleden bekenden graveur M. C. DeVries, de eenige die hier dit kunstgenre beoefende.* (Available at <https://www.delpher.nl/nl/kranten/view?coll=ddd&identificer=ddd:010267549:mpeg21:p001>.)

Dickinson, J.Y. 1965. *The Book of Diamonds*. Bonanza, New York, New York, USA, 239 pp. (see p. 218).

Field Columbian Museum 1894. *An Historical and Descriptive Account of the Field Columbian Museum*. Field Columbian Museum, Chicago, Illinois, USA, 102 pp. (see p. 179), <https://archive.org/details/historicaldescri00fiel/page/78/mode/2up>.

Field Museum n.d. *Original Catalog Collection of Gems & Semi Precious Stones Bought off Tiffany & Co., Field Museum, Chicago*. Field Museum, Chicago, Illinois, USA (see p. 34).

JCK 1970. Directory: George & Arthur Fine. *Jewelers' Circular-Keystone*, **140**(7), 195.

Massin, O. 1890. Étude et Rapport Techniques sur la Joaillerie: De la taille du diamant. In: Jacta, G., Massin, O., Hénin, A. & Plichon (eds) *Études et Rapports Techniques sur la Bijouterie, la Joaillerie, l'Orfèvrerie et la Bijouterie en Or Doublé a l'Exposition Universelle de Paris, 1889 et Rapport de la Commission Administrative*. Chambre Syndicale de la Bijouterie, de la Joaillerie, de l'Orfèvrerie et des Industries qui s'y Rattachent, Paris, France, 69–79 (see p. 76), <https://archive.org/details/eytudesetrappor00expo/page/76/mode/2up>.

Natter, L. 1754. *A Treatise on the Ancient Method of Engraving on Precious Stones, Compared with the Modern*. Printed for the author, London, xxxvi + 182 pp., <https://arachne.dainst.org/entity/15836>.

RKD—Netherlands Institute for Art History 1994/2023. Moses de Vries. <https://rkd.nl/en/explore/artists/82142>, accessed 22 February 2023.

Tiffany & Co. 1893. *Catalogue of Tiffany & Co's Exhibit: Manufactures and Liberal Arts Building, World's Columbian Exposition, Chicago, 1893*. Tiffany & Co., New York, New York, USA, 120 pp., <https://archive.org/details/cataloguetiffan00tiff>.

The Author

Erik Schoonhoven

Cultural and literary historian,
Spadinalaan 682, 1031KB Amsterdam,
The Netherlands
Email: info@erikschoonhoven.com

Acknowledgements

The author would like to thank Hadrien Rambach, who inspired me to write this article and who has shown himself to be a great friend, for which I am eternally grateful. Many thanks to René Brus, who studied both diamond portraits of King William III, for providing estimates of the carat weights of those stones.



Gem-A
THE GEMMOLOGICAL ASSOCIATION
OF GREAT BRITAIN

Study gemmology online!

- Online class groups
- Virtual learning
- Interactive quizzes
- Start your journey to FGA Membership with online learning by leading provider, Gem-A



Contact education@gem-a.com for more information

Conferences

GEM-A MIDLANDS CONFERENCE

Founded on 30 September 1952, Gem-A's Midlands branch is the only one to have been in continual existence for over 70 years. As a celebration of their 70th anniversary (slightly delayed due to COVID restrictions), they held a conference in Birmingham on Saturday 25 February 2023.

Following a welcome and introduction by branch chair **Craig O'Donnell**, delegates were treated to talks by six speakers (Figure 1) during the course of the day, on a varied range of subjects.

Rosamond Clayton (independent jewellery valuer with the London Diamond Bourse) spoke first, giving an entertaining presentation titled 'Pearls: Incidents and Miscellany', in which she recounted many amusing anecdotes of auctions and valuations from her career in Hong Kong. She highlighted the popularity of natural pearls in France and England in the early 1900s, discussed how Japanese akoya cultured pearls overtook the market, and explained how freshwater cultured pearls from Lake Biwa in Japan were originally very pretty and expensive, but later their quality declined when they became mass produced. She went on to recount how Chinese freshwater cultured pearls then flooded the market until they waned in popularity in the 2010s, and how natural pearls again became

sought after. She finished with the history and mystery of Manchurian freshwater pearls from Northeast Asia, once highly prized by Qing rulers but which today have practically disappeared, leaving the question: Where are all of those pearl rosaries and jewellery items now?

Dr Colin McGuinness (De Beers Ignite, Maidenhead, Berkshire) discussed synthetic diamonds and the development of instruments for their detection. He emphasised that consumer confidence depends on disclosure, which usually necessitates identifying stones with a variety of instruments. As synthetic diamonds improve in quality and appearance, testing becomes more crucial and specific to detect their different characteristics. The HPHT- and CVD-grown products on the market today have different identifying features created by their production processes, and need to be tested by different methods. This is not a problem with larger stones, but more and more synthetics are being mixed with natural diamond melee, which has necessitated finding methods to screen large quantities rapidly. Dr McGuinness talked impartially about various instruments, including those produced by De Beers, and the capabilities, pros and cons of each.

Rebecca Tucker (W Hamond, Whitby) is an expert on jet, having worked with and studied it for many years. Her



Figure 1: The 2023 Gem-A Midlands conference speakers (left to right) consisted of Rebecca Tucker, Joanna Hardy, Rosamond Clayton, Stephen Whittaker, Maggie Campbell Pedersen and Colin McGuinness. Photo courtesy of Paul Phillips.

talk, 'The History of Whitby Jet', covered old methods of finding and extracting jet, the techniques used to cut and polish it, and life in Whitby at the heyday of this fascinating natural material. She went on to describe some of the myths surrounding jet and its amuletic uses, such as wearing it to guard against elves or enchantments. Due to the stringent rules of mourning observed in Victorian times, jet was the perfect material from which to make jewellery, as it is very black and could be polished to a dull sheen or a high lustre, depending on the period of mourning when it was worn. The various designs used also had great symbolism. For example, depictions of acorns symbolised truth. Her talk finished with photographs of modern jet jewellery, which has enjoyed a renaissance in recent years.

This author gave a presentation on tortoiseshell. The three species of marine turtle from which tortoiseshell is derived—mainly hawksbill, but also green and loggerhead—were introduced, and the characteristics and formation of tortoiseshell were reviewed. The uses of tortoiseshell through the ages, and throughout the world, were described, from the beautiful veneered furniture produced in Holland in the sixteenth century to the small items such as card cases and dressing-table sets of the twentieth century, and from the simple, tortoiseshell-adorned jewellery worn by Pacific islanders to the intricate craftsmanship of Japanese *beko* work. Although commonly utilised in countries where turtles could be found, tortoiseshell was also a valuable trading commodity as far back as Roman times which led, in the twentieth century, to turtles being at risk of extinction; today all marine turtles are listed in CITES Appendix 1.

Joanna Hardy (independent fine jewellery consultant, London) gave a presentation titled 'Sapphire – A Celebration of Colour', in which she covered this gem material through the ages from antiquity to the modern day. Colour was of great importance in times past—not least blue, which is the colour of the heavens.

In the fifteenth century, sapphires were used in ecclesiastical rings for the clergy as they represented truth and piety, and they were set in crowns or tiaras because the head is the part of the body closest to the sky. They were once believed to guard against epilepsy (which was regarded as possession by the devil), though in Hindu faith they were thought to encourage ills and were thus usually avoided. Hardy also talked about collections of sapphire jewellery and the craftsmanship involved in its production. She has travelled widely in her research, and finished by discussing sapphire mines in Myanmar, Sri Lanka and Australia, with a warning that we should never underestimate the power of gemstones!

The day's final speaker was **Steven Whittaker** (Fellows Auctioneers, Birmingham), whose talk was titled 'What Will Our Auctions Look Like in 2025?' He started with auctions in years past and continued to present trends. The days of the old-fashioned auction house are gone. It is more common to bid online now than in person or by commission. Many of the auction houses are also branching into other online markets, such as specialty shops. He discussed the large auction houses, and how in recent years they have been bought and sold by larger companies, with their worth based more on their client lists than on the value of their property, inventory and goodwill. The large companies increase in size by buying many smaller ones, though these companies are far from small themselves. As an example, the online auction house 'The Saleroom' is just one of the many companies owned by a larger entity, which in turn was recently acquired by a firm which publishes a well-known trade magazine. All this may be the death knell for small, independent auction houses, which do not have the possibility of making the investments needed to keep up.

*Maggie Campbell Pedersen FGA
(maggiecp@btinternet.com)
London*

NINETEENTH ANNUAL SINKANKAS SYMPOSIUM: SAN DIEGO COUNTY GEMS AND MINERALS

On 22 April 2023, the Nineteenth Annual Sinkankas Symposium was held at the Gemological Institute of America (GIA) in Carlsbad, California, USA, and was co-hosted by the Geo-Literary Society. The theme of this year's event was 'San Diego County Gems and Minerals', and 160 people attended the sold-out event and heard presentations by 12 speakers (Figure 2). There was also an impressive display of gems, minerals and jewellery

that was assembled for the event. Each participant received a colourful proceedings volume, and a free PDF version of that book will be available for download later in 2023 at <https://independent.academia.edu/SinkankasSymposium>.

The symposium was introduced and moderated by **Robert Weldon** (GIA, Carlsbad), who indicated that the focus for this and future Sinkankas symposia has



Figure 2: Speakers and organisers of the Nineteenth Annual Sinkankas Symposium gather for a group photo. From left to right: Nathan Renfro, Robert Weldon, Stuart Overlin, Caroline Nelms, Dr Aaron Palke, Orasa Weldon, Bill Larson, Dr George Rossman, Dr Skip Simmons, Cal Graeber, Meg Berry, Dr Aaron Celestian, Will Larson, Dona Dirlam, Brendan Laurs and Dr Raquel Alonso-Perez. Photo by Judy Colbert, © GIA.

been shifted from gem varieties to famous localities for gems and minerals.

Dr Raquel Alonso-Perez (Mineralogical & Geological Museum, Harvard University, Cambridge, Massachusetts, USA) kicked off the presentations by describing the geology, history and production of the Pala Chief mine in the Pala District. The deposit was discovered in 1903 and is particularly famous for yielding beautiful kunzite and large deep-pink tourmaline crystals. Two of the latter in Harvard's collection measure an impressive 17 cm and 30 cm tall.

Bill Larson (Pala International, Fallbrook, California) reviewed important tourmaline localities of the Pala District, including the Stewart Lithia, Pala Chief, Tourmaline Queen and Tourmaline King mines (all of which he has mined personally). The Stewart Lithia was the first gem mine in Pala, and has produced some of the best-colour 'hot pink' tourmaline in the district. The largest gem-bearing cavity found at the Pala Chief mine, known as the Treasure Pocket, measured approximately 3 × 6 m and contained bicoloured pink-green pencils as well as the large crystals mentioned above. The Tourmaline Queen mine is famous for its 'blue-cap' tourmaline crystals, and the Tourmaline King recently began producing gem- and specimen-quality tourmaline after nearly a century of little to no activity.

Will Larson (Pala International) reviewed the history and mineral wealth of the Himalaya mine in Mesa Grande, California, which was one of the largest producers of gem- and specimen-quality tourmaline in North America during much of the twentieth century. It was discovered in 1898 and initially worked in an open cut that produced literally tonnes of pink and

green tourmaline. Most of the pink material was shipped to China for carving and/or cutting until the death of Empress Dowager Cixi in 1908. Organised mining activities were resumed in the 1950s by Ralph Potter, resulting in the production of many famous mineral specimens. From 1977 to 1998 the mine was operated by Pala International, which recovered more fine crystals and gem rough.

This author (Gem-A, Encinitas, California) reviewed the geology of San Diego County pegmatites. Numerous pegmatite districts are hosted by the Peninsular Ranges batholith, including Aguanga Mountain, Chihuahua Valley/Warner Springs, Jacumba/Tule Mountain, Mesa Grande, Pala, Ramona and Rincon. Each district hosts a particular suite of gem minerals, which include different combinations of beryl (aquamarine and morganite), quartz (smoky and citrine), spessartine, spodumene (kunzite), topaz and tourmaline. The pegmatites were emplaced approximately 90–100 million years ago, typically as groups of subparallel dikes and sills that are mostly hosted by gabbroic rocks. Although hundreds are known, only a few of the pegmatites have the distinction of being economically important sources of gems and mineral specimens.

Nathan Renfro (GIA, Carlsbad) described inclusions in gem minerals from San Diego County pegmatites, such as spodumene, quartz, beryl and tourmaline. Quartz has the largest diversity of inclusions, encompassing 'cleavelandite' (albite) feldspar, lepidolite, pääkkönenite, pyrochlore, spessartine, stibiotantalite and tourmaline.

Dr William B. 'Skip' Simmons (Maine Mineral & Gem Museum, Bethel, Maine, USA) reviewed the



Figure 3: Dr Aaron Celestian discusses the processes he uses to design museum exhibits encompassing gems, minerals and jewellery. Photo by B. M. Laurs.

crystallography of tourmaline. The most common crystal faces are the pedion, trigonal pyramid and ditrigonal prism, the last of which commonly shows striations parallel to the *c*-axis. Tourmaline crystals commonly exhibit forms that are typical for specific localities. For example, those from San Diego County usually display ditrigonal prism and pedion faces, and less commonly show trigonal pyramids.

Cal Graeber (Cal Graeber Minerals, Fallbrook) described notable minerals and mines of San Diego County pegmatites. Of particular importance are: tourmaline from the Himalaya, Stewart Lithia, Tourmaline Queen, Pala Chief and Tourmaline King mines; kunzite from the Pala Chief mine; morganite from the Stewart Lithia and White Queen mines; and unusual zoned crystals of ‘aqua-morganite’ from the Oceanview mine.

Meg Berry (Megagem, Fallbrook) recounted her extensive experience with cutting and carving gems from the San Diego County pegmatites. Bicoloured tourmaline can be quite susceptible to cracking during the cutting of elongate emerald cuts, and to avoid this she positions the long axis of the crystal parallel to the direction the wheel is turning. She employs several steps for her carvings (e.g. tourmaline roses), including selecting the rough, orienting, shaping, designing, detailing and finishing.

Paula Crevoshay (Crevoshay, Albuquerque, New Mexico, USA) gave a pre-recorded lecture in which she described the jewels she has made using gems from San Diego County and elsewhere. She is particularly fond of tourmaline from the Stewart Lithia mine,

which she has incorporated into colourful pendants and mosaic bracelets. In addition, she has used kunzite from Pala in her orchid necklaces.

Dr Aaron Celestian (Natural History Museums of Los Angeles County, California; Figure 3) discussed how he uses gems to illuminate art and science in the museum exhibits he designs. When planning exhibits, his main goals are (1) to tell the narrative of what is happening in the world, (2) ensure a desirable fit with the interests of his audience and (3) work with local partners to build community trust. He also embraces technology to engage his audience, such as using augmented-reality gaming and learning. He showed various examples of exhibits containing items originating from San Diego County pegmatites.

The day ended with a joint presentation by **Dr George R. Rossman** (California Institute of Technology, Pasadena, California) and **Dr Aaron Palke** (GIA, Carlsbad) on the causes of colour in San Diego County gem minerals. They started by explaining that most of the elements composing pegmatites are not chromophores, and the most common ones—Fe, Ti and Mn—are typically present in only minor or trace amounts. Then they reviewed the causes of colour in spodumene, apatite, beryl, quartz (rose and smoky), topaz and tourmaline.

The theme of next year’s Sinkankas Symposium will be gems and minerals of Mogok, Myanmar.

Brendan M. Laurs FGA

Learning Opportunities

CONFERENCES AND SEMINARS

Goldschmidt 2023

9–14 July 2023

Lyon, France, and online

<https://conf.goldschmidt.info/goldschmidt/2023/meetingapp.cgi>

Session of interest: The Awesome Foursome: Volatiles, Intraplate Magmatism, Mantle Metasomatism and Diamonds

Initiatives in Art and Culture's 13th Annual International Gold and Diamond Conference

17–19 July 2023

New York, New York, USA

<https://artinitiatives.com/2023-gold-diamond-conference-maintaining-purpose>

Turquoise United 2023

10–12 August 2023

Albuquerque, New Mexico, USA

www.turquoiseunited.com

Note: Includes a seminar programme

7th Annual Chicago Responsible Jewelry Conference

11–12 August 2023

Rosemont, Illinois, USA

<https://chiresponsiblejewelryconference.com/2023-conference>

Note: An accompanying 'Responsible Gem Boutique' will take place on 13 August.

Kimberley International Diamond Symposium

23–27 August 2023

Kimberley, South Africa

<https://sadpo.co.za/symposium>

Note: Field trips and mine visits in the Northern Cape to be announced.

International Conference on the Application of Raman Spectroscopy in Art and Archaeology

6–9 September 2023

Athens, Greece

<https://www.raa2023.ugent.be>

Note: A pre-conference Raman Spectroscopy Training School will take place on 4–5 September and will include a session titled 'Application on Gemstones and Data Processing'.

68th Bangkok Gems & Jewelry Fair

6–10 September 2023

Bangkok, Thailand

<https://www.bkkgems.com>

Note: Includes a seminar programme

Maine Pegmatite Workshop

6–10 September 2023

Bethel, Maine, USA

<http://www.maine-pegmatite-workshop.com>

JVA Registered Valuer Conference

8–10 September 2023

Loughborough, Leicestershire

<https://thejva.org/jewellery-watch-valuer-conference>

33rd International Conference on Diamond and Carbon Materials

10–14 September 2023

Palma, Mallorca, Spain

<https://www.elsevier.com/events/conferences/international-conference-on-diamond-and-carbon-materials>

HardRock Summit 2023

15–18 September 2023

Denver, Colorado, USA

<https://hardrocksummit.com>

Note: Includes a seminar programme

Jewellery & Gem World Hong Kong

18–24 September 2023

Hong Kong

<https://jgw.exhibitions.jewellerynet.com>

Note: Includes a seminar programme

20th Rendez-Vous Gemmologiques de Paris

September 2023 (date TBA)

Paris, France

<https://www.afgems-paris.com/rdv-gemmologique>**86th Annual American Society of Appraisers (ASA) International Conference**

1–3 October 2023

New Orleans, Louisiana, USA, and online

<https://www.appraisers.org/asa-international-conference>**CIBJO Congress 2023**

3–5 October 2023

Jaipur, India

<https://www.cibjo.org/congress2023>**17th International Conference on Applied Mineralogy and Minerals (ICAMM 2023)**

9–10 October 2023

New York, New York, USA

<https://waset.org/applied-mineralogy-and-minerals-conference-in-october-2023-in-new-york>*Theme of interest:* Industrial Minerals, Gems, Ores, and Mineral Exploration**Geological Society of America Annual Meeting (GSA Connects 2023)**

15–18 October 2023

Pittsburgh, Pennsylvania, USA

<https://community.geosociety.org/gsa2023/home>*Session of interest:* Gemmological Research in the 21st Century—Gem Minerals and Localities**65th Anniversary Canadian Gemmological Association (CGA) Gem Conference**

20–22 October 2023

Vancouver, Canada

<https://canadiangemmological.com>**37th International Gemmological Conference**

23–27 October 2023

Tokyo, Japan

<https://www.igc-gemmology.org/igc-2023>**The Munich Show**

27–29 October 2023

Munich, Germany

<https://munichshow.de/en/home-en/?lang=en>*Note:* Includes a seminar programme**Gem-A Conference**

5 November 2023

London

<https://gem-a.com/event/conference-2023>*Note:* Workshops and field trips (and a graduation ceremony for Gem-A students) will take place on 6 November.**GemGenève**

2–5 November 2023

Geneva, Switzerland

<https://gemgeneve.com>*Note:* Includes a seminar programme**24th Federation for European Education in Gemmology (FEEG) Symposium**

13 January 2024

Barcelona, Spain

<http://www.feeg-education.com/symposium>**AGTA Gemfair Tucson**

30 January–4 February 2024

Tucson, Arizona, USA

<https://agta.org/agta-gem-fair-tucson>*Note:* Includes a seminar programme**Tucson Gem and Mineral Show**

8–11 February 2024

Tucson, Arizona, USA

<https://www.tgms.org/show>*Note:* Includes a seminar programme**Inhorgenta Munich**

16–19 February 2024

Munich, Germany

<https://inhorgenta.com/en>*Note:* Includes a seminar programme**Hong Kong International Jewellery Show**

27 February–11 March 2024

Hong Kong

<https://www.hktdc.com/event/hkjewellery/en/intelligence-hub>**7th Mediterranean Gem and Jewellery Conference**

7–11 May 2024

Cavalese, Italy and Piran, Slovenia

<https://www.gemconference.com>*Notes:* Workshops will take place 7–9 May in Italy and the conference will occur on 11 May in Slovenia.

12th International Kimberlite Conference

8–12 July 2024

Yellowknife, Northwest Territories,
Canada<https://12ikc.ca>**25th Federation for European Education in
Gemmology (FEEG) Symposium**

19 October 2024

Brussels, Belgium

<http://www.feeg-education.com/symposium>**OTHER EDUCATIONAL
OPPORTUNITIES****Gem-A Workshops and Courses**

Gem-A, London

<https://gem-a.com/education>**Gemstone Safari to Tanzania**

5–22 July 2023, 10–27 January 2024 and 3–20 July 2024

<https://www.free-form.ch/tanzania/gemstonesafari.html>**Lectures with The Society of Jewellery Historians**

Society of Antiquaries of London, Burlington House

[https://www.societyofjewelleryhistorians.ac.uk/
current_lectures](https://www.societyofjewelleryhistorians.ac.uk/current_lectures)

- Natasha Awais-Dean—Jewels Captured in Perpetuity: The Jewellery Book of Anne of Bavaria
27 June 2023
- Sébastien Aubry—Greek and Latin Inscriptions on Antique Engraved Gems and Rings
26 September 2023
- Cordelia Donohue—New Research on Tuareg Jewellery; and Kathleen Walker-Meikle—Pet Bling: Jewelled Animal Accessories in the Late Medieval and Early Modern Period
24 October 2023
- John Benjamin—Jewellery from Anglesey Abbey
28 November 2023

Gem-A: over **110** years of experience in gemmology education

Our FGA and DGA Members are located around the world –
join them by studying with Gem-A

**STUDY
IN ONE
OF THREE
WAYS**

At Gem-A HQ
London



Worldwide at one
of our ATC's



Online with
practical lab classes
in your area



Find out more by contacting: education@gem-a.com

Creating gemmologists since 1908



New Media



All the Queen's Jewels, 1445–1548: Power, Majesty and Display

By Nicola Tallis, 2022. Routledge, New York, New York, USA, 360 pages, illus., ISBN 978-1032065014 (hardcover), ISBN 978-1032065021 (softcover) or e-ISBN 978-1003202592, <https://doi.org/10.4324/9781003202592>. USD144.00 hardcover or USD29.65 softcover or eBook.

This book is a well-researched study of the jewellery owned by the ten women who were married to English kings from 1445 to 1548—from Margaret of Anjou, who married Henry VI, to Kateryn Parr, the last of Henry VIII's six wives. It is primarily based on the surviving documents, inventories and wills which the author, a renowned historian, collates and discusses, with copious references and an extensive bibliography. This may make the book sound dry, but it is not just a listing of the jewellery; it is about queenship and status, gifting and celebration, and the symbolism and importance of jewellery in royal circles during that period. It is a useful addition to the literature on fifteenth- and sixteenth-century English jewellery, a sadly neglected topic.

After an introduction, the chapters cover in turn the jewellery listed in the Queens' wills, the surviving inventories of the jewellery of Jane Seymour, Katherine Howard and Kateryn Parr, the jewellery shown in portraits of the queens, the goldsmiths and the commissioning of jewels, jewels as gifts, and the crown jewels. The appendix compares entries for the same jewellery in the inventories of Katherine Howard and Kateryn Parr. The different spelling the author uses for the latter—Kateryn—is

because, as she explains, it is how Kateryn Parr spelled it herself. Similarly, the author uses Anna of Cleves rather than the more usual Anne because that is how she signed her name.

This brings us to the first of two quibbles that this reviewer has about the book. The first is not the author's fault. The cover of the book features what the caption says is a portrait of 'Catherine Parr', the sixth wife of Henry VIII, contradicting the author's well-reasoned decision to refer to her as Kateryn Parr throughout. This may seem a minor error, but this cover image (which is neither repeated nor discussed in the text) is the only colour image in the book. There are only ten images in the book, all black-and-white. Nine are portraits of the various queens in which the jewellery is hard to see in any detail. There is not a single close-up of the jewellery in any of these portraits and no images of any actual jewellery of the period. This is inexcusable in a book that retails for USD144.00 in hardback. Plenty of books on equally erudite jewellery subjects are published with a plethora of colour plates, on better paper and often at a far cheaper price for the hardcover versions. As examples, there are Timothy Schroder's 2020 *'A Marvel to Behold': Gold and Silver at the Court of Henry VIII* (124 colour plates, GBP45.00 hardcover, Boydell Press) and the present reviewer's 2018 *Diamonds: An Early History of the King of Gems* (142 colour plates, GBP37.50 hardcover, Yale University Press). Colour printing, with the decent paper it needs, is not expensive in the twenty-first century. Most of the images in the book are stock photos from the Alamy photo library. One that is not is the portrait of Anna of Cleves now in the Louvre, Paris. The story behind this portrait is interesting. In the days before social media and dating apps, the best Henry VIII could do to see what his potential bride Anna looked like was to send the artist Hans Holbein off to the Duchy of Cleves to paint her. Good colour images of this flattering portrait are readily available, but the image used in the book is a black-and-white photo taken of it in the 1860s. An odd choice, but presumably selected because this old photo is in the J. Paul Getty Museum and is available for use royalty-free. The publisher should be ashamed. In their miserly approach to illustrations they have done a huge disservice to the author, the book and its audience.

The second quibble is most relevant to the likely readers of this review. One might playfully suggest that the title of this book should have placed the apostrophe differently—*All the Queens' Jewels*—but more seriously the word 'jewellery' might have been more appropriate than 'jewels'. Readers of this journal will be particularly interested in the gems. The fourteenth and fifteenth

centuries were arguably the most significant in the history of gem use in Europe, with the opening up of the trade with both India and the East, and the New World across the Atlantic. In England there was also the other great ‘gem mine’, the vast treasures liberated from cathedrals and other religious houses in Henry VIII’s dissolution of the monasteries in the final few years of the period covered by the book. Then there were the major advances in gem cutting, particularly diamond cutting, during this period, developments that had a major impact on how jewellery looked. But sadly, once again, we are faced with a book about gem and jewellery history written by an art historian who has neither gained a working knowledge of gems nor thought to ask a gemmologist to cast their eyes over their text prior to publication. We might not expect deep gemmological knowledge, but a basic familiarity with gems would have made this a much more useful contribution to the field.

Approaches to reviewing a book vary. This reviewer starts with a quick perusal of the contents, index, bibliography and any additional materials such as glossaries and appendices. These usually give a pretty good idea of the extent of the writer’s research and their scholarly approach. On opening the book, the glossary was the first surprise and disappointment. It has just 24 entries which include the names of two gem types. *Agate* is defined remarkably succinctly as ‘A mineral of the Quartz family’, which seems an odd and rather cursory way to describe it. Nothing is said about colour or colour banding, which should be a fundamental property to note. Then there is ‘Ballas ruby’. This, as is well known, is an old term for red spinel, but here the glossary gives an equally unsatisfactory definition: ‘A mineral often associated with rubies in their source rock’. That is it. Nothing about it being spinel or even that it is red and transparent. Neither *spinel* nor *balas ruby* is listed in the index, and when we compare the inventories with the author’s collated lists of the gems mentioned in them, it is clear that she has lumped rubies and balas rubies together under the single heading ‘rubies’. The compilers of the inventories took care to distinguish between these gems as best they could, so it is bewildering that the author did not do the same.

As this might indicate, the author’s discussion of the gems is very limited despite some of the tantalising descriptions in the inventories. Diamonds are variously described as ‘squared’, ‘pointed’, ‘table’, ‘lozenge’ and so on in the inventories, but there is no attempt to elaborate on these or to see if these descriptions varied at all with date. The reviewer has argued elsewhere that originally *lozenge*, in reference to a diamond, might have equated with the diamonds set on their side presenting

the lozenge shape that we see in some fourteenth and fifteenth century jewellery. The term seems to be used a bit too early to apply to a specific type of faceting, although this may have been its meaning later. More discussion would have been useful in the book, not least because Katherine Howard had an ornament described as set with a ‘lozenged’ emerald (although this inventory entry is not specifically mentioned by the author). We also find mention of a ‘round diamond’ in Katherine Howard’s inventory. This elicits no comment from the author, although it is intriguing, as this reviewer cannot recall encountering this term elsewhere.

Unfamiliarity with gem cutting and, thus, avoidance of any meaningful discussion of it, is a disadvantage when dealing with a period where jewellery history is almost defined by the advances in cutting technology. Thus, the author falls into the trap of not distinguishing between natural pointed octahedral diamond crystals, which were still occasionally set in jewellery at that time, and point-cut diamonds. So, the glossary just defines a ‘pointed diamond’ as ‘A diamond cut in a pyramid shape’. We may not need to be pedantic and explain that neither is technically a pyramid (they are octahedra), but we might expect more detail when the author does venture into mention of cutting. She justifies saying that there were those in England who could cut diamonds by 1500, citing a payment in 1499 for ‘setting and polishing of stones’. The reference she gives is to an exchequer record in the National Archives, which this reviewer has not checked, but it is unfortunate that she did not quote the excerpt in full. Were these stones really diamonds rather than other gem types where cutting and polishing were a very different matter? In this reviewer’s research on medieval diamond cutting, an English jeweller’s bill from around 1520 for polishing the diamonds in a ruby-and-diamond brooch was noted, but the conclusion was that the stones may have been sent abroad for this because, when rough diamonds were offered for sale in London around 1523, they were unsold due to, it was said, the fact there was nobody in London who could cut them. Clear evidence for diamond cutting in London back then would have been wonderful.

The author notes that ‘South American emeralds were generally favoured during the first half of the sixteenth century’. This is the only emerald source she lists, but she then goes on to quote an ornament ‘of gold anticke work set with ten emerales’ in Jane Seymour’s inventory of 1527. This can hardly have been very ‘anticke’ if the gems had come from South America. Practically no emeralds came from South America to Europe before the 1520s. Of

course, emeralds occur in far earlier inventories, and there were other sources. This all cries out for more comment, but there is none.

There are several descriptions of ‘rock rubies’ quoted in the book, but again, no discussion about this term. We often find ‘rock rubies’ listed in sixteenth and seventeenth century inventories, and it is tempting to assume that this term refers to uncut—rough—rubies. These gems, however, are almost invariably set in jewellery, including major pieces. For example, the upper border of the Imperial State Crown was described as set with ‘eight rocke rubies’ in the time of James I. So, one might assume that the term meant polished but uncut and of uneven form. Most of the rubies in the documents quoted in the book are simply described as ‘rubies’, and possibly these were faceted in contrast to the ‘rock rubies’. But then how do we explain the mention of ‘table rubies’ as well as just ‘rubies’ in the inventory of Katherine Howard?

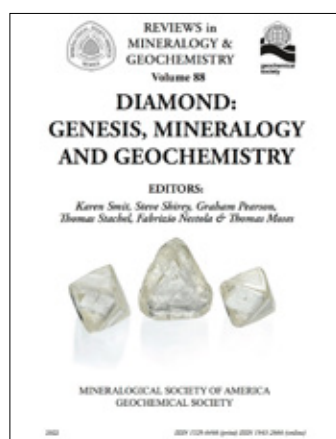
The range of gems listed in the inventories is fairly limited, but we find ‘beades of blewe stones called Lapis Lazarus’, which is amusing because today ‘lazarus’ is sadly not an uncommon misspelling of lazuli. (The reviewer recently saw an advertisement for a Cartier ‘gold and lapis lazarus bracelet’.) There are also those all-too-human cases where the inventory writers were unsure what a gem was and so, for example, we find beads of ‘blewe stones’, ‘red stones’ and ‘purple stones’ in Katherine Howard’s

inventory. It is important to note that the number and variety of gems listed in an old inventory can reflect the gemmological abilities of the compiler almost as much as the actual diversity of the collection.

The publisher’s blurb says that ‘This book is perfect for anyone interested in medieval and Tudor history, queenship, jewellery and the history of material culture’. Perhaps, but although it is a scholarly and readable study, it can be frustrating and in some cases misleading for those who would like to learn about gem history, a major component of that jewellery. We cannot blame the author for not delving more into the terminology, meaning, significance and chronology of the gems mentioned in the inventories because that was neither her intention nor speciality. But from her in-depth study of the relevant texts, it would have been easy to include the full descriptions of the gems as given in those texts in her tables of gem use. That would have been a small step for the author, but it would have been a huge leap in the usefulness of her work for future scholars.

All in all, this book is a useful addition to the jewellery historian’s library, but it suffers from the author’s meagre grasp of gem knowledge and the publisher’s dismal approach to illustration.

Dr Jack M. Ogden FGA
London



Diamond: Genesis, Mineralogy and Geochemistry

Ed. by Karen Smit, Steve Shirey, Graham Pearson, Thomas Stachel, Fabrizio Nestola and Thomas Moses, 2022. *Reviews in Mineralogy and Geochemistry*, Vol. 88, Mineralogical Society of America, Chantilly, Virginia, USA, xvi + 876 pages, illus., ISBN 978-1946850102, <https://doi.org/10.2138/rmg.2022.88.00>. USD65.00 softcover or free PDF.

When I embarked on a career in the diamond industry over 30 years ago as a non-Earth scientist, I managed for a few years to keep the complexities of geology at arm’s length. Ultimately, however, I was forced to engage with a completely new and hostile environment expressed in a very strange language. Fortunately, this novice geologist was assisted by some excellent introductory reviews (e.g. the Kirkley *et al.* article in the Spring 1991 issue of *Gems & Gemology*) in getting to grips with diamond as a geological material.

After over half a century of activity, *Reviews in Mineralogy and Geochemistry* now provides a full volume of articles devoted to laying down the current state of Earth science research into diamond. The book contains comprehensive reviews of the many branches of work that have evolved to address fundamental questions around diamond formation (conditions, chemistry and timing), what these studies tell us about the earth’s complex interior and the transfer of carbon between the earth’s surface and depths, and how this information is used to

guide and inform the industry that takes this remarkable mineral and turns it into the most precious of gems. This was an ambitious project, particularly in fulfilling the stated intention to 'leave little out' (page v), but it has been largely achieved through the grouping of authors for each of the 15 chapters who combine extensive experience with active research at the forefronts of their fields.

The comprehensive nature of the chapters means that this volume extends well beyond a simple introductory review, and a full reading of the whole issue is not for the faint-hearted. The intended audience is not, however, the general reader, although the articles are written so that 'any scientist could reach for this volume to obtain as much basic diamond knowledge as necessary' (page v). Referencing is very thorough, which does have the effect of making some parts difficult to read. One extremely valuable contribution of this work is the accompanying online database (<https://dataverse.scholarsportal.info/dataverse/diamond>). In it are compiled the analysis results from many of the techniques covered, and it will provide a firm foundation for future studies seeking to answer the questions posed at the ends of a number of the chapters.

One of the highlights is the opening chapter by Kjarsgaard *et al.*, 'A Review of the Geology of Global Diamond Mines and Deposits'. This update includes recent advances in the understanding of the mantle materials that transport diamonds from their regions of growth and emplace them in crustal deposits. It also clearly describes the re-classification of these rocks into three categories: the already familiar kimberlite and lamproite (olivine lamproite), along with carbonate-rich olivine lamproite. This re-classification has enabled a better interpretation of the inclusion-composition data and their application to commercially important indicator minerals.

Inclusion studies are featured in most of the book's chapters, heavily highlighting their importance in enabling scientists to study the environmental conditions deep within the earth's mantle where diamonds grow. The detailed descriptions of these analyses, and how their interpretation has evolved to understand deep-Earth processes, show how initial models have had to be modified to take into account new findings, better analytical techniques and improved understanding of actual rather than modelled environments. The tension is evident between 'destructive' inclusion studies, where minerals are liberated from their host diamond, and *in situ* analyses, where information linking the inclusion to its host is preserved (in

particular the interface between the inclusion and the diamond). However, this volume shows that within the research community there is constant dialogue to ensure that the best data are obtained from the very rare instances of suitably included diamonds available for study.

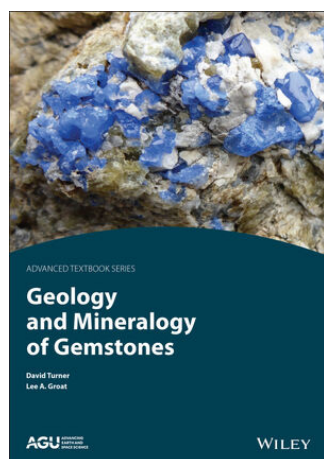
A chapter on fluid inclusions details the current understanding of the involvement of high-density fluids in the growth of fibrous diamonds, and explores the degree to which such fluids could be more generally involved in the growth of non-fibrous monocrystalline diamonds. This theme of growth environment is also picked up in a chapter on experimental petrology, which provides a summary of the extensive work investigating the crystallisation of diamond from a range of rocks and fluids under mantle pressure and temperature conditions. Incorporation of major impurities (nitrogen and boron) and inclusion formation are also considered in this chapter. The authors have made excellent use of tables to summarise the current situation, resulting in a very readable chapter.

Analyses of diamonds themselves are presented in detail, including a comprehensive review of our understanding of carbon and nitrogen isotope studies from the past 70 years. Such research helps determine the origin of the carbon from which diamonds grow, but interpretation of the isotope data is made difficult by the complex fractionation processes that modify the isotope ratios measured in the resulting diamond. A useful summary of the main point-defect-related spectroscopic features of importance to the Earth scientist is presented in a subsequent chapter, and this is followed by another chapter that offers insights into diamond growth provided by experiments in the laboratory synthesis of diamond. Chapters on crystallographic techniques (specifically X-ray crystallography) and on Raman spectroscopy offer clear guidance on methodologies to be followed in order to obtain consistent data that will allow determination of both the chemical and physical characteristics of the growth environment.

The authors and editors of this volume have provided an excellent resource to establish what is already known about the Earth-science aspects of diamond and to lay firm foundations for the future. I look forward to the next review, 'Should anyone take on the task up [*sic*] up-dating this volume, in perhaps another 50 years...' (page v)!

Dr David Fisher

De Beers Group Ignite
Maidenhead, Berkshire



Geology and Mineralogy of Gemstones

By David Turner and Lee A. Groat, 2022. AGU Advanced Textbook Series, American Geophysical Union, Washington DC, USA, and John Wiley and Sons Inc., Hoboken, New Jersey, USA, <https://www.wiley.com/en-us/Geology+and+Mineralogy+of+Gemstones-p-9781119299851>, 268 pages, illus., ISBN 978-1119299851 or e-ISBN 978-1119299875. USD109.95 softcover or USD88.00 eBook.

The study of precious and base metals is well established in university curricula and research departments worldwide, and there is growing interest by such institutions in the geological study of gem materials. Recognising this trend, and the need to support it, the authors have produced a well-thought-out textbook for introductory courses on the topic. Both authors are researchers and educators within this field, and their experience is apparent throughout this work.

The textbook is logically organised into two main parts. Part I, titled 'Developing Base Knowledge', provides a scientific overview of geology and mineralogy as applied to gemmology. Introduced quite rapidly, subjects are brief and cover so much in short order that the text feels rather 'bulleted' at times. However, Part I is meant to be a simple introduction or review, and it achieves that goal. Basic chemistry, geology, crystallography, light optics, and gemmological tools and testing are covered. Students with a general science background should be able to grasp the concepts addressed. Those already with deeper training will appreciate the refresher, as I did.

Part II, 'Gemstones and Their Origins' dives into an extensive list of individual gem materials and gem groups, including their gemmological properties

and geological modes of origin, treatments and even market valuation essentials. Specific chapters cover 'Diamond', 'Corundum' (ruby and sapphire), 'Beryl' (all gem varieties), 'Pegmatites' (including tourmaline, spodumene and topaz), 'Chrysoberyl', 'Spinel', 'Tanzanite', 'The Garnet Group', 'Jade: Jadeite and Nephrite', 'Quartz and Silica Gems' (including amethyst, agate and opal), 'Other Gems' (peridot, turquoise, lapis lazuli and zircon) and 'Organic Gems' (amber and ammolite). At first, the chapter on pegmatites seemed a little out of place, as the other chapters in Part II focus on specific gem materials, whereas this one concentrates on a geologic environment. Nevertheless, the three gem types that it covers are reviewed just like the others in the book.

The authors provide relatively more discussion of diamond, corundum and beryl, but their reviews of the other gems are thorough and not left as afterthoughts. It is refreshing to see such an equal treatment of smaller-market gem materials, such as ammolite and peridot, with more established gems such as tourmaline and topaz, making this textbook a standout. A notable exception is the single-page discussion dedicated to amber, which does not yield much to the reader. Unlike the other gems reviewed, there is no information presented on gemmological properties, geological processes and valuation. Only in passing are amber simulants mentioned.

Similar to Part I, the topics are short and concise but thorough. In this way, the authors have managed to consolidate a massive amount of information in a short volume. Each chapter ends with a list of references. Including the index, the entire textbook is only 268 pages.

In general, the quality of some of the photographs is not what you would typically expect for a book covering gem materials. However, this is an introductory textbook, so from that perspective the photography is adequate. Its purpose is to whet the appetite for further study, but I found many illustrations could have used better subjects for their photographs. Figures 6.3 and 6.4 in the chapter on corundum, for example, may not be the best photos to illustrate rough ruby and sapphire to students unfamiliar with those gem materials. These particular figures also illustrate the authors' tendency to include gem specimens from their own research in Canada and Greenland. Although understandable, better photographic examples are available to illustrate the subjects discussed.

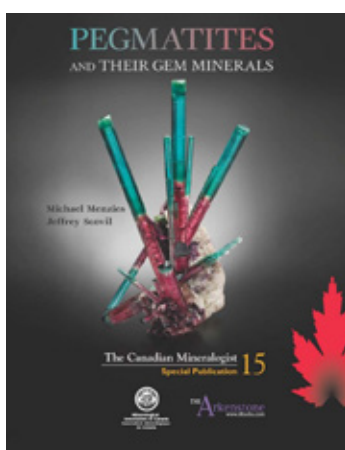
I did find a variety of errors scattered throughout the text. These include grammatical problems (resulting in

a garbled sentence on page 118) and factual issues (the Inca, not the Aztecs, used emeralds in Colombia [page 131], and the Victor diamond mine, Ontario, Canada is not active [page 93], but actually closed in 2019). A citation of ‘Emmett *et al.* 2017’ on page 106 is not listed in the references, and I humbly note that ‘Mychaluck *et al.* (2001)’ is misspelled on page 254. This was an ambitious project, so problems such as these may not be surprising for a first edition.

This is a solid, first-edition textbook that doubles as a reference guide for those who are more experienced. I particularly enjoyed the sections discussing gem materials outside of the ‘big four’, which is an important distinction from similar works. Chapter 8,

‘Pegmatites’, was my favourite though, for condensing such a challenging array of information and presenting it in a simple-to-understand format. The small number of errors, average photography quality and atypical specimens used to illustrate some subjects do allow room for improvement in future editions. On the whole though, I really enjoyed this book and feel it serves a vital educational role. *Geology and Mineralogy of Gemstones* can aid in teaching students from many diverse disciplines related to gemmology and may inspire others to focus further on any of the numerous topics introduced.

Keith Mychaluk, P.Geo.
Calgary, Alberta, Canada



Pegmatites and Their Gem Minerals

By Michael Menzies and Jeff Scovil, 2022. The Canadian Mineralogist Special Publication 15, Mineralogical Association of Canada, Québec City, Québec, Canada, <https://mac-amc.mysopify.com/products/copy-of-understanding-the-gem-minerals-a-practical-guide-1>, 602 pages, illus., ISBN 978-0921294665. CAN125.00 hardcover.

This is a monumental book in both size and scope. The first author, Michael Menzies, has a doctoral degree in geology and has been an avid mineral collector since the 1980s, concentrating especially on specimens from granitic pegmatites. The second author, Jeff Scovil, is a world-renowned gem and mineral photographer. Together they have produced a massive and well-illustrated compendium on what pegmatites are, where they are found, what is found in them (especially but not exclusively gem minerals) and the mechanisms of gem pegmatite formation.

So what is a pegmatite? On page 10 of the book, we learn that René-Just Haüy, the eighteenth-century ‘father of crystallography’, invented the term to refer to a rock known as graphic granite. Even now, graphic intergrowths of quartz and K-feldspar (or quartz and schorl tourmaline, or quartz and apatite, etc.) are a common feature of most pegmatites. But the word has a broader usage: A pegmatite is the large-scale expression of late-stage melts and fluids from solidifying (typically granitic) plutons. Such silicic melts eventually evolve into hydrothermal fluids and concentrate elements (e.g. B, Be, Li, Nb, Zr, REEs, etc.) that are not consumed by the rock-forming minerals which previously crystallised. Most important to gem and mineral aficionados are the crystal-lined cavities that form at the end stages of some pegmatites under certain conditions.

The book has seven chapters, a copious list of references and two appendices. The first three chapters provide an introduction, a historical overview and some geological concepts and terminology. Chapter 4 describes and classifies pegmatites relevant to gem minerals. Chapter 5—the heart of the book—provides armchair field trips to pegmatite localities around the world. Chapter 6 discusses pegmatite minerals and gems sorted by pegmatite ‘family’ (described below) and, for granitic deposits, by significant element present (Li, Be, etc.). Chapter 7 covers pegmatite formation. The appendices consist of a short glossary and a large table that lists gem-bearing pegmatite localities worldwide, including many that are not covered in Chapter 5. One strength of this book is that it is extremely up-to-date for a work of this size, in its locality descriptions, scientific explanations and

29-page reference list. Much of the work discussed was published in the past two decades, and I noticed at least one reference to a 2022 publication.

After the helpful reference information presented in chapters 1–3, in Chapter 4 we learn about the classification used to describe different families of pegmatites, summarising previous work by Drs Petr Černý, David London, Axel Müller and others (all in the provided references). Pegmatites derived from granitic plutons have been described as *NYF* (niobium-, yttrium- and/or fluorine-bearing), *LCT* (lithium-, caesium- and/or tantalum-bearing) or *hybrid NYF/LCT* (containing aspects of both geochemical types). Descriptions of these pegmatites comprise most of the book. In general, NYF pegmatites contain topaz and beryl (aquamarine), while LCT pegmatites contain tourmaline (e.g. elbaite) and beryl (morganite) and sometimes spodumene (kunzite). In addition, there are non-granitic pegmatites (derived from low-Si nepheline syenites and related rocks), as well as altered or desilicated pegmatites or pegmatite-related deposits. The inclusion of altered pegmatites and related deposits allows the authors to discuss certain sources of emerald, alexandrite, gem corundum and amethyst.

Chapter 5 gives field descriptions of 30 pegmatite regions worldwide. For each deposit, the authors describe the location, history and geology, while also providing recent locality photographs. The chapter is profusely illustrated with images of mineral specimens, some photographed *in situ*. Also included are maps and other non-photographic illustrations that are primarily the work of cartographer William Besse. Most of the mentioned deposits are currently being exploited, or have been mined in the recent past, and the outlook for further production is included. Finally, a summary and, usually, images of fashioned gems from the deposit are typically provided. However, some of the choices of deposits covered in this chapter seem idiosyncratic. Would you begin a chapter on gem deposits with a locality known for zektzerite? Two other deposits are mainly notable for fluorite, which is not an important gem mineral.

The discussion of pegmatite minerals and gems in Chapter 6 could seem redundant if you have just finished reading Chapter 5, although it is convenient to have each gem mineral discussed in just one section (with exceptions; e.g. aegirine and zircon are both discussed twice, as they occur in two different pegmatite environments). Also, less-common minerals (such as beryllonite and pollucite) are

conveniently discussed in one place here. A section on causes of colour indicates that Fe and Mn are the most common chromophores in pegmatite-associated gems, whereas the most significant in terms of gem value are Cr, which colours emerald, ruby and alexandrite, and Cu, which colours Paraíba-type tourmaline.

Chapter 7 covers pegmatite formation, from the initial crystallisation of the melt to final decomposition into clays. (It is mostly based on the work of Dr David London and his collaborators, but other valid models also exist.) The crystallisation of rock-forming minerals in the pegmatite (mainly quartz and feldspars) excludes water, so the melt evolves into a hydrous fluid. Trace elements are also concentrated in the fluid, and they act as fluxes that allow crystallisation to continue at relatively low temperatures. The stage is then set (in a watery cavity) for the hydrothermal growth of crystals. As the temperature of the fluid decreases, conditions may shift from acidic to basic and back again, causing some minerals (e.g. beryl) to undergo dissolution or etching. Pressure changes can cause the pegmatite cavity to rupture and be exposed to groundwater, leading to partial or complete replacement of earlier-formed crystals (e.g. tourmaline) by kaolinite or clay.

Although *Pegmatites and Their Gem Minerals* is certainly an impressive work, there is room for improvement. It seems to have lacked a copy editor in the late stages of production. For example, although pegmatites are noted to form in greisens, the term *greisen* itself is not in the glossary. One photograph of fluorite is shown twice, with different captions, on pages 462 and 471; the latter caption appears to be the correct one. A few cited references are not in the reference list. There are occasional infelicities of language, such as this sentence from page 476 on fluorapatite: ‘Sizes are typically small, in the cm range, but range up to a few cm.’ (Perhaps the first ‘cm range’ refers to 1-cm crystals.) Finally, an index would be extremely helpful.

Anyone who appreciates gems and minerals of pegmatites will enjoy this book. Use it to plan your next field trip, or to take an armchair tour of fine specimens seen in museums and at mineral shows, or just to learn and dream about geology on blustery nights, like this reviewer did.

Dr Mary L. Johnson

Mary Johnson Consulting
San Diego, California, USA

Other Book Titles

DIAMOND

Flawless: Blue White & D Flawless

By P. C. Schneirla, 2023. Self-published by P. C. Schneirla Inc., 392 pages, ISBN 979-8986671123 hardcover, 979-8986671109 softcover or ASIN B0C1HG4KGW Kindle edn. USD32.99 hardcover, USD19.99 softcover or USD9.49 Kindle edn.

FAIR TRADE

Terrible Beauty: Elephant – Human – Ivory

By Nicholas J. Conard, 2021. Hirmer Verlag GmbH, Munich, Germany, 200 pages, ISBN 978-3777433639. EUR29.95 hardcover.

INSTRUMENTATION

Handbook of Mineral Spectroscopy,

Vol. 2: Infrared Spectra

By J. Theo Klopogge, 2023. Elsevier, Amsterdam, The Netherlands, 632 pages, ISBN 978-0128045206 or e-ISBN 978-0128045213. EUR310.65 hardcover or eBook.

JEWELLERY HISTORY

A History of Royal Britain in 100 Objects

By Gill Knappett, 2023. Rizzoli, New York, New York, USA, 216 pages, ISBN 978-1841659527. USD23.95 hardcover.

JEWELLERY AND OBJETS D'ART

The Art & Times of Daniel Jocz

Ed. by Sarah Davis, 2023. Arnoldsche Art Publishers, Stuttgart, Germany, 208 pages, ISBN 978-3897906655. USD65.00 softcover.

A Bit of Universe: The Jewelry of Luz Camino

By Luz Camino, 2023. Rizzoli, New York, New York, USA, 224 pages, ISBN 978-0847899203. USD85.00 hardcover.

Boghossian: Expertise, Craftsmanship, Innovation

By Vivienne Becker, 2023. Assouline Publishing, New York, New York, USA, 252 pages, ISBN 978-1649801197. USD195.00 hardcover.

Chanel High Jewelry

By Julie Levoyer and Agnès Muckensturm, 2023. Thames & Hudson, New York, New York, USA, 528 pages, ISBN 978-0500025239. USD200.00 hardcover.

Cora Sheibani: Jewels

By William Grant, 2023. ACC Art Books, Woodbridge, Suffolk, 228 pages, ISBN 978-1788842136. GBP40.00 hardcover.

Italian Jewels: Museo del Gioiello di Vicenza

By Livia Tenuta, 2021. Silvana Editoriale, Milan, Italy, 344 pages, ISBN 978-8836646463. EUR34.00 hardcover.

The Jewellery Collection of the Musée des Arts Décoratifs

By Dominique Forest, Karine Lacquemant and Évelyne Possémé, 2023. ACC Art Books, Woodbridge, Suffolk, 40 pages, ISBN 978-2383140061. GBP30.00 softcover.

Legendary Patania Jewelry:

In the Tradition of the Southwest

By Pat Messier and Kim Messier, 2023. Schiffer Publishing Ltd, Atglen, Pennsylvania, USA, 256 pages, ISBN 978-0764364464. USD60.00 hardcover.

Paul Brandt

By Bleue-Marine Massard, 2023. ACC Art Books, Woodbridge, Suffolk, 192 pages, ISBN 978-2376660699. GBP65.00 hardcover.

Symbolism in Global Jewelry

By Sindi Schloss, 2022. International Gemological Services, Scottsdale, Arizona, USA, 248 pages, ISBN 978-0578392684. USD34.95 softcover.

MISCELLANEOUS

Flawless Beauty: The Mineral World of Will Johnson

By Will Johnson, Wendell E. Wilson and Thomas Spann, 2023. Mineralogical Record Inc., Tucson, Arizona, USA, 314 pages, no ISBN. USD50.00 softcover.

Refined Elegance: The Small Treasures of Mineralogy

By Wendell E. Wilson, Jim Houran, Alexander G. Schauss and Robert M. Lavinsky, 2022. Mineralogical Record Inc., Tucson, Arizona, USA, 160 pages, no ISBN. USD38.00 softcover.

Literature of Interest

COLOURED STONES

Achate aus Rio Grande do Sol, Brasilien: Eine gemmologische Betrachtung hinsichtlich der Bedeutung des Achats als Schmuckstein [Agates from Rio Grande do Sul, Brazil: A gemmological review on the importance of the agate as gem material]. U. Henn, *Gemmologie: Zeitschrift der Deutschen Gemmologischen Gesellschaft*, **71**(3/4), 2022, 3–34 (in German with English abstract).

Archean age and radiogenic source for the world's oldest emeralds. R.W. Nicklas, J.M.D. Day and R. Alonso-Perez, *Geochemical Perspectives Letters*, **23**, 2022, 23–27, <https://doi.org/10.7185/geochemlet.2232>.*

Die Beryll-Gruppe – eine Übersicht zu den Varietäten Aquamarin, Morganit, Heliodor und Goldberyll [The beryl group – An overview of the varieties aquamarine, morganite, heliodor and golden beryl]. U. Henn, *Gemmologie: Zeitschrift der Deutschen Gemmologischen Gesellschaft*, **71**(1/2), 2022, 3–26 (in German with English abstract).

Chatoyance de la calcédoine [Chalcedony chatoyancy]. J. Fereire and J.-P. Gauthier, *Revue de Gemmologie A.F.G.*, No. 218, 2022, 7–9 (in French with English abstract).

Colored Stones Unearthed: Gems formed in magmatic rocks. A.C. Palke and J.E. Shigley, *Gems & Gemology*, **58**(4), 2022, 494–506, <https://www.gia.edu/gems-gemology/winter-2022-colored-stones-unearthed>.*

La découverte de la laurenthomasite, un nouveau minéral d'intérêt gemmologique [The discovery of laurenthomasite, a new mineral of gemological interest]. I. Pignatelli & C. Ferraris, *Revue de Gemmologie A.F.G.*, No. 217, 2022, 6–7 (in French).

Entre inclusions et illusions [Between inclusions and illusions]. I. Lerouyer and E. Fritsch, *Revue de Gemmologie A.F.G.*, No. 217, 2022, 16–17 (in French).

Fluorescence characteristics of two copper-diffused plagioclase feldspars: Labradorite and andesine.

Q. Zhou, C. Wang and A.H. Shen, *Gems & Gemology*, **58**(4), 2022, 424–237, <https://doi.org/10.5741/gems.58.4.424>.*

Sur la fracturation de l'opale [On the fracturing of opal]. B. Chauviré, *Revue de Gemmologie A.F.G.*, No. 217, 2022, 12–13 (in French).

Gemmological characterization of Montana sapphire from the secondary deposits at Rock Creek, Missouri River, and Dry Cottonwood Creek.

A.C. Palke, N.D. Renfro, J.R. Hapeman and R.B. Berg, *Gems & Gemology*, **59**(1), 2023, 2–45, <https://doi.org/10.5741/GEMS.59.1.2>.*

Die Handelsbezeichnungen Santa Maria und Santa Maria Africana [The trade terms Santa Maria and Santa Maria Africana]. C.C. Milisenda and S. Müller, *Gemmologie: Zeitschrift der Deutschen Gemmologischen Gesellschaft*, **71**(1/2), 2022, 61–65 (in German with English abstract).

Inclusions triphasées de CO₂, soufre (S) et orpiment (As₂S₃) dans un saphir [Three-phase inclusions of CO₂, sulfur (S) and orpiment (As₂S₃) in a sapphire]. F. Blumentritt, C. Caplan and F. Notari, *Revue de Gemmologie A.F.G.*, No. 218, 2022, 10–13 (in French with English abstract).

Les luminescences du corindon [The luminescence of corundum]. M. Vigier and E. Fritsch, *Revue de Gemmologie A.F.G.*, No. 217, 2022, 14–15 (in French).

Le marbre Picasso d'Utah, USA [Picasso marble from Utah, USA]. E. Thoreux, *Revue de Gemmologie A.F.G.*, No. 218, 2022, 21–22 (in French with English abstract).

Morphology of Colombian emerald: Some less common cases and their growth and dissolution history. K. Schmetzer and G. Martayan, *Gems & Gemology*, **59**(1), 2023, 2–45, <https://doi.org/10.5741/GEMS.59.1.46>.*

Our friends the inclusions. The detective at the party of inclusions. Thirteenth episode [emerald]. L. Costantini and C. Russo, *Rivista Italiana de Gemmologia/Italian Gemmological Review*, No. 15, 2022, 7–12.

A photomicrographic compilation of inclusions in quartzes. G. Pearson, *Australian Gemmologist*, **28**(2), 2022, 80–88.

Les pierres ornementales dans la joaillerie [Ornamental stones in jewellery]. M. Chabrol, *Revue de Gemmologie A.F.G.*, No. 217, 2022, 28–29 (in French).

Quelques éclaircissements sur la labradorescence. Partie I : État de l'art [A few clarifications on labradorescence. Part I: State of the art]. M. Cagnon Trouche, J.-C. Boulliard, I. Estève and P. Giura, *Revue de Gemmologie A.F.G.*, No. 218, 2022, 14–20 (in French with English abstract).

Spektrentypen und Farben von eisen- und manganhaltigen Beryllen [Spectra types and colour of iron- and manganese-bearing beryls]. T. Lind and T. Stephan, *Gemmologie: Zeitschrift der Deutschen Gemmologischen Gesellschaft*, **71**(1/2), 2022, 27–40 (in German with English abstract).

Spice of life: Shedding light on fluorite. L. Langeslag, *Gemmology Today*, March 2023, 62–65, <https://tinyurl.com/5h83s6kk>.*

A study of sapphire origin determination methods. J. Caldaron, *Gems&Jewellery*, 31(4), 2022, 36–39.

Update on ruby mining and gemology in Mozambique. K. Schollenbruch, *InColor*, No. 49, 2023, 24–26, <http://www.incolormagazine.com/books/vslz/#p=24>.*

CULTURAL HERITAGE

Les gemmes du livre d'heures de François 1^{er} conservé au Musée du Louvre [Gems from the Book of Hours of François I kept at the Louvre Museum]. G. Panczer. É. Romeo and G. Riondet, *Revue de Gemmologie A.F.G.*, No. 217, 2022, 30–31 (in French).

A hexagonal aquamarine gem with new hermeneutical glosses. R.D. Kotansky, *Le Muséon*, **35**(3–4), 2022, 285–322, <https://doi.org/10.2143/MUS.135.3.3291197>.

Le pendentif aux émeraudes du Cabinet des Médailles et des Antiques. Proposition d'interprétation [The emerald pendant from the Cabinet of Medals and Antiques. Interpretation proposal]. M.-L. Cassius-Duranton, *Revue de Gemmologie A.F.G.*, No. 217, 2022, 26–27 (in French).

DIAMONDS

Analýza polki diamantu z Indie / Analysis of polki diamond from India. J. Štubňa, *Gemologický spravodajca (Gemmological Newsletter)*, **12**(2), 2022, 9–13, <https://tinyurl.com/39mr2sbt> (in Slovak with English abstract).*

Argyle violet diamonds. J. Chapman, *Australian Gemmologist*, **28**(2), 2022, 98–102.

The color origin and evaluation of natural colored diamonds. F.K. Liu, Y. Guo, B. Zhao and X. Li, *Science of Advanced Materials*, **14**(2), 2022, 243–256, <https://doi.org/10.1166/sam.2022.4210>.

Nitrogen structure determination in treated fancy diamonds via EPR spectroscopy. I. Litvak, A. Cahana, Y. Anker, S. Ruthstein and H. Cohen, *Crystals*, **12**(12), 2022, article 1775 (13 pp.), <https://doi.org/10.3390/cryst12121775>.*

Plastic deformation: How and why are most diamonds slightly distorted? E.M. Smith, *Gems & Gemology*, **59**(1), 2023, 94–100, <https://tinyurl.com/vs89rke7>.*

The structures, synthesis, properties, and applications of diamond. S. Xie and F. Liu, in J. Ma & J. Xu, Eds., *Functional Carbon Materials*. IOP Publishing, Bristol, 2022, 7–1–7–27, <https://doi.org/10.1088/978-0-7503-4972-7ch7>.

FAIR TRADE

ESG [Environmental, social and governance] in the jewellery trade. I. Yan, *JNA*, No. 438, 2023, 10–16, <https://tinyurl.com/3uuc6h8u> (in English and Chinese).*

Ethics, law, and politics in palaeontological research: The case of Myanmar amber. E.M. Dunne, N.B. Raja, P.P. Stewens, Zin-Maung-Maung-Thein and Khin Zaw, *Communications Biology*, **5**(1), 2022, article 1023 (10 pp.), <https://doi.org/10.1038/s42003-022-03847-2>.*

Responsible sourcing in the coloured gemstone business. R.G. Sikri, *JNA*, No. 438, 2023, 18–24, <https://tinyurl.com/3uuc6h8u> (in English and Chinese).*

Talking supply-chain ethics with Virgu Gem. C. Unninayar, *InColor*, No. 49, 2023, 34–42, <http://www.incolormagazine.com/books/vslz/#p=34>.*

What is the real price of a gemstone? N. Zolotukhina, *Gemmology Today*, December 2022, 82–86, <https://tinyurl.com/36fr2n7s>.*

GEM LOCALITIES

Aventures gemmologiques au Groenland [Gemological adventures in Greenland]. V. Pardieu, *Revue de Gemmologie A.F.G.*, No. 217, 2022, 22–23 (in French).

Beryll aus der Region Chitral, Pakistan: Ein neues Smaragdorkommen [Beryl from the Chitral region, Pakistan: A new emerald deposit]. C.S. Hanser, B. Gul, T. Häger and R. Botcharnikov, *Gemmologie: Zeitschrift der Deutschen Gemmologischen Gesellschaft*, **71**(3/4), 2022, 35–56 (in German with English abstract).

Blue opal find in Chihuahua, Mexico. J. Heebner, *GemGuide*, **41**(6), 2022, 8–10.

Carving space and time. Interruptions and (un)predictability in infrastructural design of emeralds and the mining formalization in Colombia. V. Caraballo Acuña, *Journal of Latin American and Caribbean Anthropology*, **27**(1–2), 2022, 146–164, <https://doi.org/10.1111/jlca.12586>.

Connoisseur's Choice: Jeremejevite, Mile 72, Cape Cross area, Arandis Constituency, Erongo Region, Namibia. B. Cairncross, *Rocks & Minerals*, **98**(2), 2023, 160–170, <https://doi.org/10.1080/00357529.2023.2129301>.

Neue Funde von kobalthaltigem Spinell bei Mahenge, Tansania [New finds of cobalt-bearing spinel near Mahenge, Tanzania]. T. Stephan, U. Henn and S. Müller, *Gemmologie: Zeitschrift der Deutschen Gemmologischen Gesellschaft*, **71**(1/2), 2022, 57–64 (in German with English abstract).

An overview of Arizona's collector-quality quartz localities. L. Presmyk, *Rocks & Minerals*, **98**(1), 2023, 54–73, <https://doi.org/10.1080/00357529.2023.2126700>.

Pakistan's gems, mines, and markets. J. Bergman, *InColor*, No. 49, 2023, 44–51, <http://www.incolormagazine.com/books/vslz/#p=44>.*

INSTRUMENTATION AND TECHNOLOGY

Lab-grown diamond screening. G. Borenstein, *GemGuide*, **41**(5), 2022, 4–7.

Ruby stone light grade inspection system using CCD linear sensor – A review. F.M. Rahalim, J. Jamaludin, S.N. Raisin and F.A. Asuhaimi, *Journal of Physics: Conference Series*, **2312**(1), 2022, article 012061, <https://doi.org/10.1088/1742-6596/2312/1/012061>.*

JEWELLERY HISTORY

Mourning jewelry in late Georgian and Victorian Britain. J. Tsoumas, *Convergences – Journal of Research and Arts Education*, **15**(30), 2022, 121–134, <https://doi.org/10.53681/c1514225187514391s.30.150>.*

Thomas Gray of Sackville Street: Royal retail jeweller, goldsmith and sword-cutler. L. Southwick, *Jewellery Studies—The Journal of The Society of Jewellery Historians*, No. 2, 2022, 3–30, https://www.societyofjewelleryhistorians.ac.uk/JSO_2022_2.pdf.*

The trends and gems of Art Deco. I. Alexandris, *InColor*, No. 49, 2023, 56–60, <http://www.incolormagazine.com/books/vslz/#p=56>.*

LAPIDARY TOPICS

Decisive action: Measure twice, cut once [lapidary considerations for coloured stones]. *Gemmology Today*, March 2023, 34–45, <https://tinyurl.com/47nkyhk8>.*

Gemstone manufacturing: Process, practice & automation. TDi Sustainability, *Gemmology Today*, March 2023, 20–24, <https://tinyurl.com/z4svmaav>.*

Never stop innovating: Gem artist Chi Huynh. T. Hsu, A. Homkrajae and K. Schumacher, *Gems & Gemology*, **58**(4), 2022, 458–473, <https://doi.org/10.5741/gems.58.4.458>.*

True grit: Flirting with danger [cutting Ethiopian opal]. H. Sisay, *Gemmology Today*, March 2023, 72–74, <https://tinyurl.com/yd5tcsyc>.*

MISCELLANEOUS

The Alfie Norville Gem and Mineral Museum – A curator's view. S. Sargent, *InColor*, No. 49, 2023, 68–71, <http://www.incolormagazine.com/books/vslz/#p=68>.*

The Ferrara gemological conference. Bridging university and industry. P. Minieri and S. Coppola, *Rivista Italiana de Gemmologia/Italian Gemmological Review*, No. 15, 2022, 48–58.

Origin opinions: When gem labs agree to disagree. J. Bergman, *InColor*, No. 49, 2023, 12–22, <http://www.incolormagazine.com/books/vslz/#p=12>.*

Overpricing misreported gemstones is a threat. Gemologists and dealers have to come to terms with this issue. J. Bergman, *Rivista Italiana de Gemmologia/Italian Gemmological Review*, No. 15, 2022, 22–27.

The role of CIBJO. Anonymous, *Gemmology Today*, September 2022, 50–55, <https://tinyurl.com/kewz2ub8>.*

NEWS PRESS

Carlisle Roman baths: Gems recovered from drains. A. Giecco, BBC News, 31 January 2023, <https://www.bbc.com/news/uk-england-cumbria-64458322>.*

Jewellery worth hundreds of millions in the king's private collection. D. Pegg, *The Guardian*, 14 April 2023, <https://tinyurl.com/2py38fmd>.*

A 'stunning' 1,300-year-old gold necklace is unearthed in England. M. Levenson, *New York Times*, 8 December 2022, <https://tinyurl.com/mrzuta6h>.

Their world was the oyster: Oldest pearl town found in UAE. J. Gambrell, AP News, 20 March 2023, <https://tinyurl.com/3xt7vt4x>.*

ORGANIC/BIOGENIC GEMS

Coral color grading. Practical application cases. P. Minieri and S. Coppola, *Rivista Italiana de Gemmologia/Italian Gemmological Review*, No. 15, 2022, 37–45.

L'ivoire, hier et aujourd'hui [Ivory, yesterday and today]. I. Reyjal, *Revue de Gemmologie A.F.G.*, No. 218, 2022, 23–25 (in French with English abstract).

PEARLS

Pearls: A literature review. A. El-Refi, I. Gharib and N. Abdul Fatah, *International Design Journal*, **12**(4), 2022, 243–251, <https://doi.org/10.21608/idj.2022.245902>.*

Spectroscopic characteristic of natural and dyed yellow Akoya pearl. M. Lin and Y. Gao, *Journal of Gems & Gemmology*, **24**(5), 2022, 94–100, <https://tinyurl.com/23ycssss> (in Chinese with English abstract).*

Yellow pigmentation analysis of pearl oyster *Pinctada fucata martensii* shells through in situ micro-Raman spectroscopy. M. Xu, G. Zhang, Y. Shi, H. Zhang, W. Liu and M. He, *Journal of Shellfish Research*, **41**(2), 2022, 229–234, <https://doi.org/10.2983/035.041.0208>.

SYNTHETICS

Development status and application of diamond cultivation. F. Li, Y. Liu and J. Zhang, *Superhard Material Engineering*, **34**(4), 2022, 51–54, <https://tinyurl.com/372xj9ta> (in Chinese with English abstract).

The early history of synthetic diamond. J. Evans, *Australian Gemmologist*, **28**(2), 2022, 90–95.

Effect of external ambient temperature on synthesis of gem grade diamond. Q. Liu, L. Yi, X. Shen, H. Du, M. Qu, L. Hu, Z. Wu and C. Han, *Superhard Material Engineering*, **34**(3), 2022, 19–23, <https://tinyurl.com/3djz9xz3> (in Chinese with English abstract).

Synthetische Berylle [Synthetic beryls]. T. Stephan, S. Müller and Q. Wang, *Gemmologie: Zeitschrift der Deutschen Gemmologischen Gesellschaft*, **71**(1/2), 2022, 51–60 (in German with English abstract).

TREATMENTS

A canary in the ruby mine: Low-temperature heat treatment experiments on Burmese ruby. E.B. Hughes and W. Vertriebt, *Gems & Gemmology*, **58**(4), 2022, 400–423, <https://doi.org/10.5741/gems.58.4.400>.*

Composition and spectral characteristics of porcelain-treated turquoise. L. Huang, Q. Chen, Y. Li, Z. Yin, F. Xu, X. Gao and Y. Du, *Gems & Gemology*, **58**(4), 2022, 438–457, <https://doi.org/10.5741/gems.58.4.438>.*

Détection du traitement thermique à basse température des corindons [Detection of low-temperature heat treatment of corundum]. S. Karampelas, U. Hennebois and A. Delaunay, *Revue de Gemmologie A.F.G.*, No. 217, 2022, 4–5 (in French).

A discussion and identification of beryllium diffused sapphires. D. Srinivasa and R. Patil, *GemGuide*, **42**(1), 2023, 6–9.

The heat treatment of pink zoisite. C. Schwarzing, *Minerals*, **12**(11), 2022, article 1472 (13 pp.), <https://doi.org/10.3390/min12111472>.*

Identification characteristics of a type IaB irradiated green-blue diamond. P. Wu, *Superhard Material Engineering*, **34**(4), 2022, 55–58, <https://tinyurl.com/yc4whha8> (in Chinese with English abstract).

Künstliche Eigenschaftsveränderungen in der Beryllgruppe [Artificial enhancement in the beryl group]. T. Stephan, T. Lind and S. Müller, *Gemmologie: Zeitschrift der Deutschen Gemmologischen Gesellschaft*, **71**(1/2), 2022, 41–50 (in German with English abstract).

Money honey [overview of gem treatments]. Anonymous, *Gemmology Today*, December 2022, 58–75, <https://tinyurl.com/67bz9n2s>.*

Permanence: The liability of stability [gem treatments]. Anonymous, *Gemmology Today*, December 2022, 78–81, <https://tinyurl.com/4pv34afj>.*

COMPILATIONS

G&G Micro-World. Arsenopyrite in smoky quartz • Unusual inclusions in demantoid • ‘Galaxy’ in diamond • Omphacite in pink diamond • Aegirine in poudretteite from Myanmar • ‘Waveform’ in Mong Hsu ruby • Volcano-shaped feature in trapiche-like sapphire • Copper ‘confetti’ inclusions in chalcedony • Apatite in garnet • Etching on laurenthomasite. *Gems & Gemology*, **58**(4), 2022, 484–493, <https://tinyurl.com/2f7s534d>.*

G&G Micro-World. Three-phase inclusion in alexandrite • Apatite in hackmanite • Inclusions in chondrodite • ‘Flying insect’ in diamond • ‘Starry night’ in diamond • Xenomorphic garnet in diamond • Arrow-patterned negative crystals in sapphire • Solid inclusions in flame-fusion synthetic ruby • Columbite(?) in beryl. *Gems & Gemology*, **59**(1), 2023, 84–91, <https://tinyurl.com/acsuabaxx>.*

Gem News International. Grossular from Mogok with strong red fluorescence • Hellandite inclusion in Mogok ruby • Quartzite bangle with fuchsite inclusions • Natural, reconstructed and imitation ‘root’ amber • Synthetic quartz crystal cluster with natural-looking inclusions • Red-dyed spodumene imitating ruby • GSA 2022 annual meeting • Fall auction highlights • Dr Peter Keller obituary. *Gems & Gemology*, **58**(4), 2022, 508–526, <https://tinyurl.com/bp6yumvd>.*

Gem News International. Tucson 2023 report • Atypical bead cultured pearls from the UAE • Cultured abalone pearls from Chile • Microscopic shell nuclei in natural pearls • Color study of sapphires from Greenland • Liberian ruby • Purple spinel from Tanzania • Greyish blue CVD synthetic diamond • Phosphorescence of HPHT-grown synthetic diamond • Color-change synthetic wakefieldite • Heated purplish pink sapphire with monazite inclusions • Irradiated pink sapphire. *Gems & Gemology*, **59**(1), 2023, 102–162, <https://tinyurl.com/56ecyzh6>.*

Lab Notes. Four-rayed star chrysoberyl • Etch channels in diamond • 126 ct cat’s-eye emerald • ‘Cobalt blue’ gahnospinel • Calcite detected on a nacreous saltwater pearl • Black non-nacreous bead-cultured pearls from *Pinctada margaritifera* • Partially hollow natural blister pearl filled with foreign material • 2.32 ct pallasitic peridot. *Gems & Gemology*, **58**(4), 2022, 474–482, <https://tinyurl.com/frfumpzt>.*

Lab Notes. Purple anhydrite • Pink pyrope • Libyan Desert glass bangle • Atypical bead-cultured pearls • Treated freshwater non-bead cultured pearls with antique appearance • Heart-shaped golden South Sea cultured pearl • Gastropod shell in a shell blister • Ruby with synthetic overgrowth • 110.18 ct synthetic rutile. *Gems & Gemology*, **59**(1), 2023, 72–82, <https://tinyurl.com/56ecyzh6>.*

*Article freely available for download, as of press time



Gem-A
THE GEMMOLOGICAL ASSOCIATION
OF GREAT BRITAIN

**Save the
date** 05|11|23



Gem-A Conference 2023

Bringing together the greatest minds in Gemmology

November 5

etc.venues County Hall, London



